HOKKAIDO UNIVERSITY

Title	Remote sensing of microparticles by laser scattering for medical applications
Author(s)	Shimizu, Koichi
Citation	University of Washington. Ph.D.
Issue Date	1979
Doc URL	http://hdl.handle.net/2115/20123
Type	theses (doctoral)
File Information	thesis.pdf

Instructions for use

Remote Sensing of Microparticles by Laser Scattering

for Medical Applications:

Approach with Transport Theory and

Picosecond Optical Range-Gating

by

Koichi Shimizu

A dissertation submitted in partial fulfillment
of the requirements for the degree of

Doctor of Philosophy

University of Washington

1979

Approved by _____

Program Authorized
to Offer Degree _____

Date _____

Doctoral Dissertation

University of Washington

Abstract

REMOTE SENSING OF MICROPARTICLES BY LASER SCATTERING
FOR MEDICAL APPLICATIONS: APPROACH WITH TRANSPORT
THEORY AND PICOSECOND OPTICAL RANGE-GATING

By Koichi Shimizu

Chairperson of the Supervisory Committee: Professor Akira Ishimaru
Electrical Engineering

Three techniques were developed for the remote sensing of micro-
particles by laser scattering. They were applied to the non-invasive
probing of biological particles, namely bacteria in urine, cataracts
in the eye, and platelets in blood, respectively.

(1) The Fourier transform inversion technique determines the
size distribution of tenuous scatterers from the forward scattering
pattern. This technique consists of differentiating operations and
Fourier transforms. It does not require matrix-inversion or an a-
priori knowledge of functional forms of the size distribution, and
it can take advantage of other techniques in spectral analysis such
as the Fast Fourier Transform or digital filtering. Susceptibility
to noise was checked by adding the random noise to the scattered
intensity pattern simulated by the Rayleigh-Debye approximation.
Typical error for 10% noise was within a few percent for mean and
standard deviation in the estimation of Gaussian distribution using
1024 points FFT. Size distributions were determined for latex
spheres with known sizes and bacteria in homogeneous and highly

aggregated conditions. A resolution comparable to the wavelength of the probing light was demonstrated.

(2) The backward scattering pattern analysis technique determines an average size and variance of tenuous scatterers from the backward scattering pattern. With an optical range-gating technique, scattering patterns could be measured in backward angles while eliminating the extraneous scattering and corrections for the change of scattering volumes. Characteristic patterns for different sizes of scatterers were obtained with latex spheres with diameters less and more than the wavelength of the probing light.

(3) The pulse backscattering technique evaluates the scattering and absorption characteristics of scatterers in a dense medium by means of backscattered pulses. Using the Kerr effect ultrafast shutter, the shapes of backscattered pulses were observed with a resolution of picoseconds. The general pulse shape is characterized by a rapid rise followed by a slow asymptotic decay. When the scatterer is absorbing the decay part suffers noticeable attenuation. The shapes and magnitudes of the observed pulses were in excellent agreement with the theory. The feasibility for this technique to detect the aggregation of particles in a closed system was examined.

Along with the development of the above techniques, the following results were obtained.

(a) The scattering patterns calculated by the Rayleigh-Debye approximation are improved considerably, if the approximation is modified to include the relative refractive index of the scatterers in the Fourier Transform kernel.

(b) The equation of transfer was solved for the time-dependent specific intensity under the diffusion approximation and a closed form expression was obtained for the pulse beam wave incidence on a slab of dense media. This solution includes as its asymptotic cases, semi-infinite media, plane wave incidence and the point source.

(c) Four phases of scattering were observed in the scattering patterns, in the graph of scattered intensity as a function of scatterer density and in the visual observation of a collimated light beam in the scattering medium. They are single scattering, first order multiple scattering, multiple scattering and diffusion. According to this classification, the range of validity was clarified for the first order multiple scattering and diffusion approximations.

(d) The ratio between the velocities of pulse propagation in diffuse and non-diffuse media, or the slowing rate of light velocity due to the diffusing propagation was measured to be $\sqrt{3}$.

TABLE OF CONTENTS

LIST OF FIGURES

vii

xi

LIST OF TABLES

ACKNOWLEDGMENTS

Chapter I

INTRODUCTION

Remote sensing is generally defined as an acquisition of information about an object or phenomenon which is not in intimate contact with the sensing device. Radar and sonar are familiar examples. During the past decade, the rapid growth of technology has widened the horizon of applications of this methodology in various fields such as astronomy, meteorology, oceanography, etc. Among the remote sensing techniques, lidar (light detection and ranging) has become increasingly important due to its various advantages over the microwave radar.

Following the principle of bioengineering, this technique, developed in the physical sciences, has been applied as a non-invasive diagnostic technique in biomedical sciences, only recently. It may answer the strong need for the efficient detection or quantitative assessment of biological microparticles in vivo, such as bacteria in body fluids, blood cells in whole blood, etc. Since these natural media have microparticles randomly distributed in time and space, they are called random media and analyzed in their statistical descriptions. The object of this dissertation is the development of the techniques which apply the lidar method to the remote sensing of biological microparticles in random media.

The theory is mainly based on two concepts, namely transport theory and picosecond optical range-gating. Transport theory, also

called radiative transfer theory was initiated by Schuster in 1903. It deals with the transport of energy through the scattering medium rather than the propagation of the field given by Maxwell's equations. The basic differential equation is called the equation of transfer which is equivalent to Boltzman's equation or Maxwell-Boltzmann collision equation. Generally in random media, it is assumed that the correlation between fields is negligible and that the addition of powers holds rather than the addition of fields. Therefore, the equation of transfer is solved to obtain a mathematical description of the light scattering from biological random media.

Another concept, picosecond optical range-gating, first reported by Duguay and Mattick (1971), is an optical ranging technique which is capable of a distance resolution on the order of a millimeter (Bruckner, 1976). An ultrashort pulse of light, 5-10 psec in duration, generated by a mode-locked laser (DeMaria, 1969) is directed toward the target of interest and the backscattered pulses are recorded by means of an ultrafast shutter (Duguay, 1969) coupled to a suitable detector. By judicious gating of the shutter, extraneous backscattering from foreground or background clutter, which would otherwise obscure the desired echo pulses, can be blocked from the detector. Thus, an object imbedded in or obscured by a highly scattering medium can be made visible. In this thesis, we take advantage of the two aspects of range-gating, namely the ultrafast sampling and the picosecond time-resolution.

With these concepts, the following remote sensing techniques are

proposed, and their applicability is verified theoretically and experimentally.

(1) Fourier transform inversion technique: This technique determines a size distribution of tenuous scatterers from the forward scattering pattern. This is applied to probe the condition of bacteria in their living environments such as urine, water, etc.

(2) Backward scattering pattern analysis: With the range-gating technique, backward scattering patterns for tenuous media are measured and an average size of scatterers is estimated. This technique is applied to investigate the microstructure of cataracts.

(3) Pulse backscattering from dense media: This technique probes a dense media with an ultrashort pulse of a picosecond duration. From the backscattered pulse, information on the scattering media can be obtained, such as scatterer density, scattering characteristics of the constituent scatterers, etc. This is applied to assess the platelet aggregation in blood.

<u>Organization of the Thesis</u>

According to the subject to be discussed, this thesis can be divided into two parts. Chapters II-IV deal with light scattering from tenuous media and Chapters V-VIII from dense media.

Chapter II discusses the modification of Rayleigh-Debye approximation to extend its range of validity. It is shown that the

scattering patterns calculated by the Raleigh-Debye approximation are considerably improved by the modification. This modification widens the applicable range of the technique developed in the next chapter.

Chapter III presents the Fourier transform inversion technique which determines the size-distribution of scatterers (apertures) from the scattering pattern (diffraction pattern) of a collection of scatterers. With simulated data from a known size-distribution, the technique is tested for accuracy, resolution and susceptibility to error in input data. Then, this technique is applied to latex spheres of known sizes and bacteria of different shapes. Its sensitivity to the aggregation of bacteria is investigated.

Chapter IV deals with the measurement and analysis of backward scattering patterns. The experimental apparatus is described which enables the ultrafast sampling in a picosecond time-scale by the optical range-gating technique. The effectiveness of the picosecond sampling is shown in its noise-limiting capability and elimination of the correction for the observation geometry. The characteristic scattering patterns for different sizes of particles are measured and the applicability of this technique to the estimation of particle size is demonstrated.

Chapter V presents a solution of the diffusion equation for beam wave incidence on a slab of dense random media. It is shown that this general solution includes the cases of semi-infinite media, plane wave incidence and the point source, as its asymptotic cases. Using these

solutions, the scattered pulse shape for the impulse incidence is calculated and analyzed. The results of this chapter give a theoretical basis for Chapters VI, VII and VIII.

Chapter VI discusses a classification of different types of scattering into four groups, namely single scattering, first order multiple scattering, multiple scattering and diffusion. These four phases are demonstrated in scattering patterns, graphs of scattered intensity as a function of scatterer density, and visual observations of a collimated beam in the scattering media. The range of validity is investigated for the first order multiple scattering approximation and diffusion approximation.

Chapter VII discusses the measurement of light velocity in diffuse media. Off-axis backscattered pulse shapes are measured at different angles with tenuous and dense media. Pulse shapes from tenuous and dense media are analyzed. From the difference in the arriving-time of the pulse peak, the slowing rate of light velocity in dense media is obtained, and the theoretically predicted slowing rate $\sqrt{3}$ is verified.

Chapter VIII presents a remote sensing technique for dense media by picosecond pulse-backscattering. The range-gating technique is formulated and receiving pulse shapes are calculated using the diffusion solutions obtained in Chapter V. Experimental facility is described and observed pulse shapes are analyzed. The agreement between theory and measurement is shown both in the shape and the magnitude of the pulse. Sensitivity for scatterer absorption and

aggregation is discussed. Finally, the feasibility for the remote sensing of dense media is shown, particularly for the detection of platelet aggregates in transfusion blood.

Chapter IX summarizes the significant results of this thesis and indicates the areas to be further studied.

This research falls into the broad field of light scattering studies and the results presented in this thesis can be applied to other purposes, which include the optical properties estimation for particles in a fluid or gaseous surrounding such as microbial particles, physiological particles, chemical particles, air pollutants, rain, fog, ice particles, etc.

Chapter II

MODIFICATION OF RAYLEIGH-DEBYE APPROXIMATION

II.1. INTRODUCTION

Rayleigh-Debye approximation, also called Rayleigh-Gans or Born approximation, has been used in many fields with practical advantages such as mathematical simplicity, applicability to any shape and structure, etc. However, it is only valid under the following two conditions, i.e, the relative refractive index of the scatterer is close to 1 and the phase shift of the wave through the scatterer is much less than 1. See Eqs. (2-1) and (2-2). As these conditions are violated, the error of the approximation increases rapidly. The extensive study on the range of validity has been reported by Kerker (1969, p. 427).

As can be seen in the derivation, the scattering pattern, (Eq. (2-4) also called a form factor) calculated by this approximation is independent of the refractive index of the scatterer, which is not true. This chapter discusses the modification of the Rayleigh-Debye approximation to include the refractive index in the Fourier kernel of the form factor. The justification for this is given by two different derivations. The improvement due to this modification is demonstrated by comparing the scattering patterns calculated by modified approximation, regular approximation and Mie theory which is exact for spherical scatterers. This modification extends the valid range of the Fourier transform inversion technique presented in Chapter III.

II.2 THEORY

In the Rayleigh-Debye approximation, it is assumed that " . . . each volume element (of a scatterer) gives Rayleigh scattering, and does so independently of the other volume elements. The waves scattered in a given direction by all these elements interfere because of the different positions of the volume elements in space." (van de Hulst, 1957, p. 86). Therefore, with the conditions

$$| n_r - 1 | \ll 1 \qquad\qquad (2\text{-}1)$$

$$2k_0 D | n_r - 1 | \ll 1 \qquad\qquad (2\text{-}2)$$

the scattered intensity for perpendicular polarization is given by,

$$I_s = (k_0^4 V^2 / 4\pi^2 R^2) | n_r - 1 |^2 \, P(\Theta) \qquad\qquad (2\text{-}3)$$

$$P(\Theta) = (1/V^2) \, \left| \int \exp (i\delta) \, dV \right|^2 \qquad\qquad (2\text{-}4)$$

where n_r is the relative refractive index of the scatterer, k_0 is the propagation constant of the surrounding medium of the scatterer. D is a typical dimension of the scatterer such as its diameter, V is the volume of the scatterer, R is the distance from the scatterer to the observation point, Θ is the scattering angle, and δ is the phase delay of the volume element dV. The detailed discussion can be found elsewhere (Kerker , 1969, p. 415). $P(\Theta)$ in Eq. (2-4) is called a form factor and represents the interference effect mentioned above. Since the scattering pattern or the angular distribution of scattered intensity is of interest, the following discussion is mainly

concentrated on this form factor $P(\theta)$.

Fig. 2-1 illustrates the phase delay δ . Two wavelets are scattered by the volume elements at O and O'. $\hat{i}$ and $\hat{o}$ are unit vectors in the directions of propagation for incident wave and scattered wave, respectively. As shown in the figure, the difference in their path length is the distance B-O-C. Thus, the phase delay between the volume elements is given by

$$\delta = k (\hat{i} - \hat{o}) \cdot \bar{r} \qquad (2-5)$$

$$\text{where} \quad |\hat{i} - \hat{o}| = 2 \sin(\theta/2) \qquad (2-6)$$

If the shape of the scatterer is similar to a sphere, the phase delay occurs mostly <u>in the scatterer</u>. Therefore, for the propagation constant k in Eq. (2-5), the k of the scatterer $(n_r k_0)$ is a better approximation than that of the surrounding medium $(k_0 = 2\pi/\lambda)$. Note that in the R-D approximation, the latter has been used with the condition $|n_r - 1| \ll 1$.

This can also be shown in a different method of formulation of the R-D approximation. First we follow the formulation to make it clear where to modify it. Starting from Maxwell's equations, the scattered field $\bar{E}_s$ at an observation point $\bar{r}$, is given by

$$\bar{E}_s(\bar{r}) = \nabla \times \nabla \times \int_V \{\epsilon_r(\bar{r}') - 1\} E(\bar{r}') G_0(\bar{r},\bar{r}') \, dV' \qquad (2-7)$$

$$\text{where} \quad G_0(\bar{r},\bar{r}') = \exp (ik|\bar{r} - \bar{r}'|)/(4\pi|\bar{r} - \bar{r}'|) \qquad (2-8)$$

is the free space Green's function, $\epsilon_r(\bar{r}')$ is the relative dielectric constant at the position $\bar{r}'$ within the scatterer, and $E(\bar{r}')$ is the
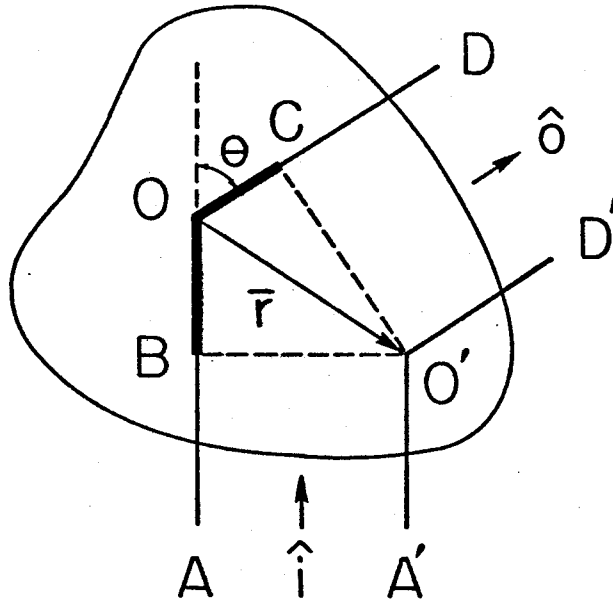
Fig. 2-1   Geometry for Rayleigh-Debye scattering:
Phase delay δ
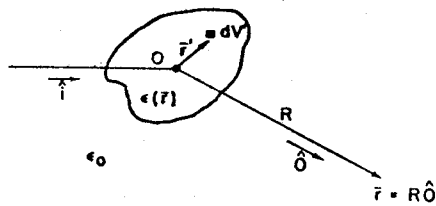
Fig. 2-2   Geometry for Rayleigh-Debye scattering:
Incident and scattered field

total electric field inside the scatterer. Assume that the phase term in the Green's function is approximated by

$$k|\bar{r} - \bar{r}'| \approx k_0(R - \bar{r}' \cdot \hat{o}) \quad \text{for } |\bar{r}| \gg |\bar{r}'| \tag{2-9}$$

where $\bar{r} = R\hat{o}$. Fig. 2-2 shows the geometry. The field inside the scatterer is approximated by the incident field, i.e.,

$$\bar{E}(\bar{r}) \approx \bar{E}_i(\bar{r}) = \hat{e}_i \exp(ik_0\bar{r} \cdot \hat{i}) \tag{2-10}$$

where $\hat{e}_i$ is the unit vector in the direction of polarization of the incident field. Then, we obtain the formula for the R-D approximation

$$\bar{E}_s(\bar{r}) = -\frac{\exp(ik_0R)}{R} \frac{k_0^2}{4\pi} \{\hat{o} \times (\hat{o} \times \hat{e}_i)\} VP^{1/2}(\theta) \tag{2-11}$$

$$P(\theta) = |1/V \int_V [\epsilon_r(\bar{r}') - 1] \exp\{ik_0(\hat{i} - \hat{o}) \cdot \bar{r}'\} dV'|^2 \tag{2-12}$$

Note that the propagation constant in Eq. (2-12) is that of the surrounding medium (k_0). In the following derivation, it is modified to be that of the scatterer ($n_r k_0$).

To satisfy the condition $|\bar{r}| \gg |\bar{r}'|$ in Eq. (2-9), the reference origin O must be located close to all the volume elements, most likely in the center for the sphere-like scatterers. Then, most of the phase difference $k\bar{r}' \cdot \hat{o}$ falls <u>inside the scatterer</u>. Thus, the phase of Green's function is better approximated by

$$k|\bar{r} - \bar{r}'| \approx k_0 R - n_r k_0 \bar{r}' \cdot \hat{o} \tag{2-13}$$

In addition, the field inside the scatterer is better approximated with the propagation constant of the scatterer, i.e.,

$$\bar{E}(\bar{r}) \approx \hat{e}_i \exp(in_r k_0 \bar{r} \cdot \hat{i}) \tag{2-14}$$

Therefore, the modified R-D approximation is given by

$$\bar{E}_s(\bar{r}) = - \frac{\exp(ik_0 R)}{R} \frac{k_0^2}{4\pi} \{ - \hat{o} \times (\hat{o} \times \hat{e}_i) \} V P^{1/2}(\theta) \tag{2-11}$$

$$P(\theta) = |1/V \int_V [\varepsilon_r(\bar{r}') - 1] \exp\{in_r k_0(\hat{i} - \hat{o}) \cdot \bar{r}'\} dV'|^2 \tag{2-15}$$

This modification may be well understood by comparison with other methods. In the regular R-D approximation, the incident and scattered wave are assumed to propagate with the constant k_0 to and from the scattering volume element, even in the scatterer. In the WKB approximation, the propagation constant for the incident wave in the scatterer is $n_r k_0$, and that of the scattered wave is k_0. While, in the modified R-D approximation, both of them are $n_r k_0$ in the scatterer.

II.3 RESULTS AND DISCUSSION

Fig. 2-3 shows the scattering patterns or the form factors cal-
culated by the modified R-D approximation (a), Mie theory (b), and
the regular R-D approximation (c). Mie theory gives exact solutions
for spherical scatterers. The scatterer in this case is a 1 μm
diameter dielectric sphere with the relative refractive index of
1.60/1.33. This corresponds to a latex sphere suspended in water,
and illuminated by He-Ne laser (n = 0.6328 μm). This is the case of
our experiment discussed in the next chapter. Although the conditions
of the R-D approximation given in Eqs. (2-1)(2-2) are not satisfied
$(n_r - 1 \approx 0.20$, $2k_oD(n_r - 1) \approx 5.3)$, Fig. 2-3(a) is very similar to
Fig. 2-3(b), especially in the small angle region. Comparison between
Figs. 2-3(a) and 2-3(c) shows the improvement due to the modification
proposed here. Note the closeness of the scattering angles of extrema
(1st minimum, 2nd maximum, etc.) which are important parameters for practi-
cal applications, such as size estimation of scatterers (Kerker, 1969,
p. 175, p. 344).

Figs. 2-4 and 2-5 show scattering patterns calculated by the same
theories as Fig. 2-3 but with different diameters and relative refrac-
tive indices. They are 1 μm and 1.60/1.0 for Fig. 2-4, and 2μm and
1.60/1.33 for Fig. 2-5, respectively. These parameters are well beyond
the range of validity of the R-D approximation, i.e., for Fig. 2-4,
$n_r - 1 \approx 0.60$, $2kD(n_r - 1) \approx 12$. And for Fig. 2-5, $n_r - 1 \approx 0.20$,
$2kD(n_r - 1) \approx 11$. In these cases, the scattering patterns of (a)'s
are not similar to (b)'s as much as in the case of Fig. 2-3. However,

the improvement by the modification is still evident, especially in the small angle region and in the angular positions of extrema. Note the completely different patterns of (c)'s given by the regular R-D approximation.

The error in a large angle region may be attributed to the refraction and reflection effects at the boundary of the scatterer which were neglected in the R-D approximations, both regular and modified. Inclusion of these effects is not as simple as the modification made here. Up to here, we have not taken into account the size distribution of the scatterers, which is common in practical applications particularly in the natural world. With the size distribution, the scattering pattern of the modified R-D approximation becomes very similar to that of the Mie theory. An example is shown in Fig. 2-6.

In conclusion, the modification proposed in the previous section was proved to be effective, at least for the scattering pattern of the latex microspheres in water, in the range of optical scattering. In order to justify the modification for general cases, further study is required.
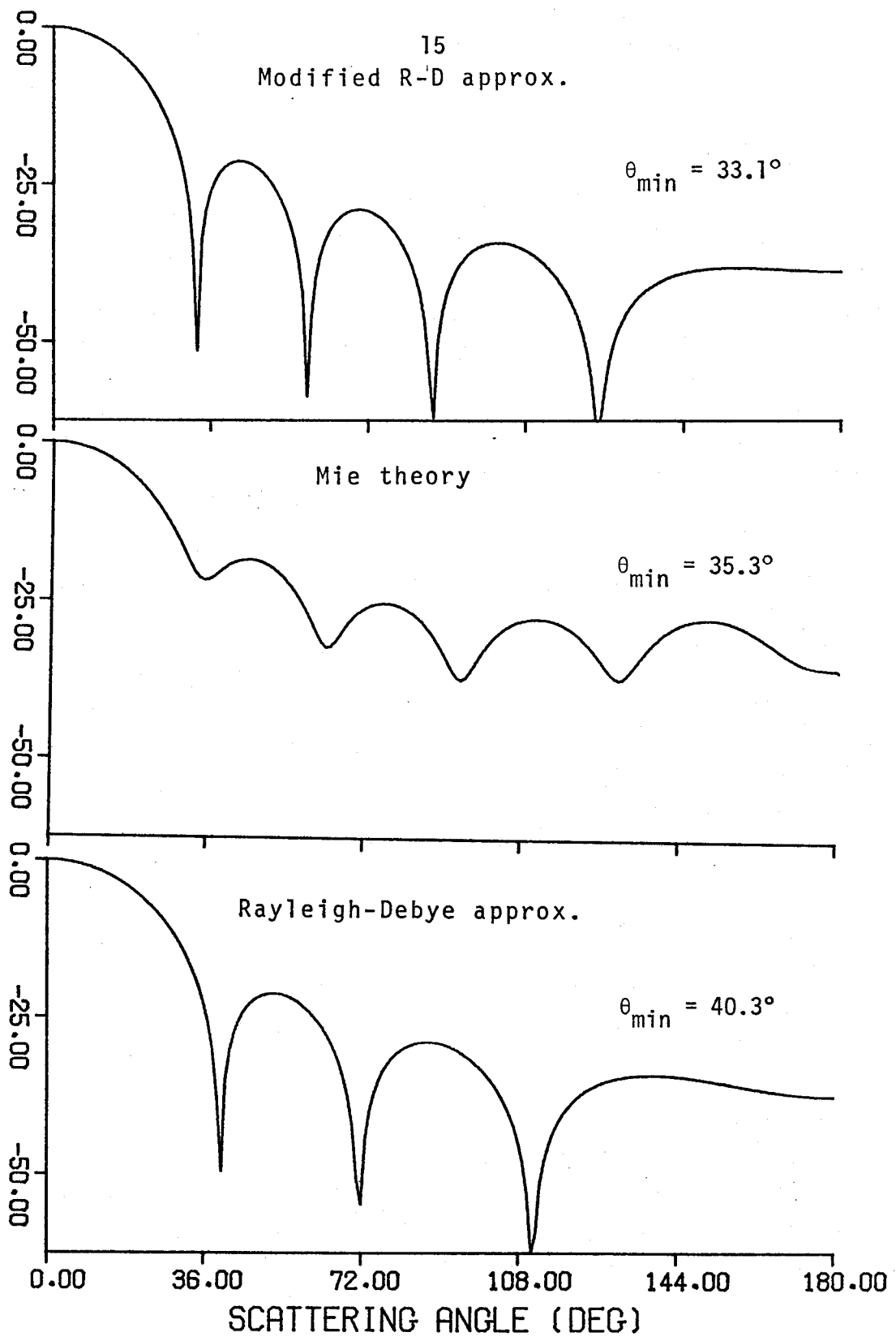
Fig. 2-3 Calculated scattering patterns of a sphere
with 1μm dia. and n_r=1.60/1.33

16

Fig.2-4 Calculated scattering patterns of a sphere
with 1μm dia. and n_r=1.60/1.00
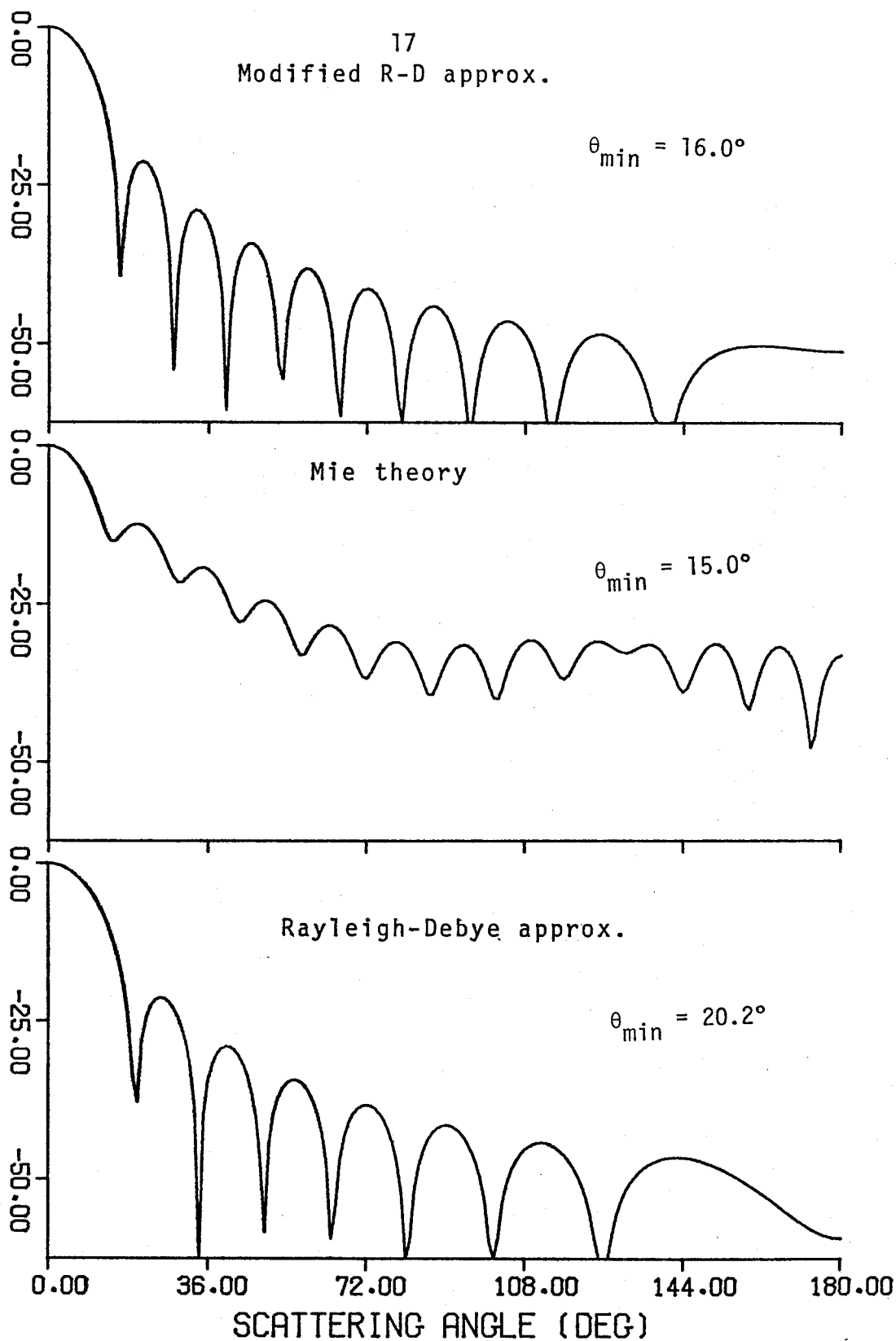
Fig.2-5 Calculated scattering patterns of a sphere
with 2μm dia. and n_r=1.60/1.33
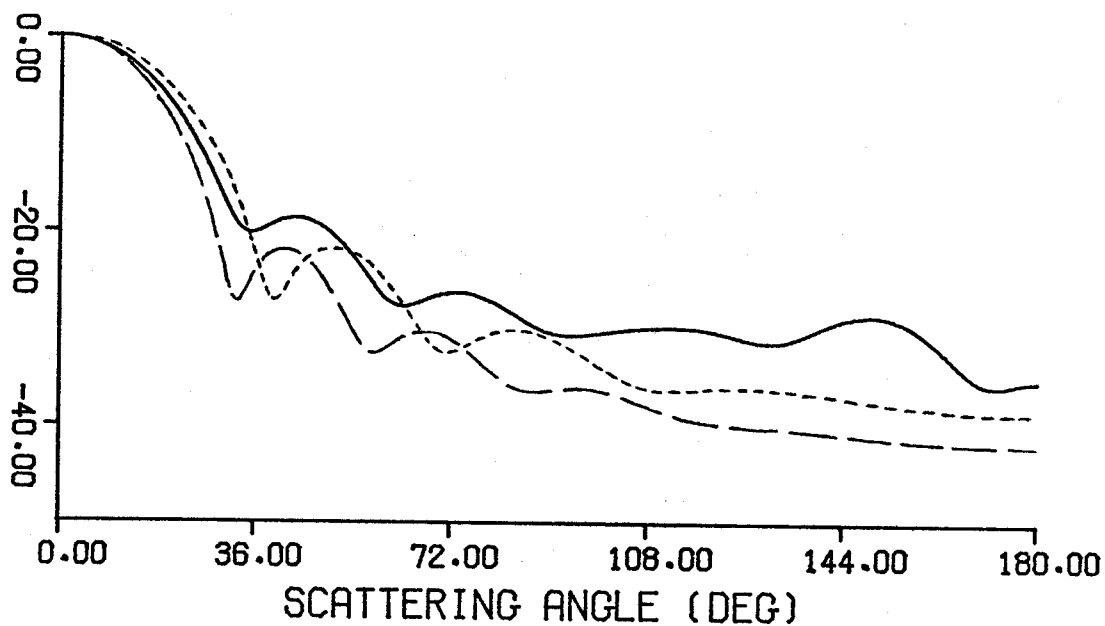
Fig. 2-6 Calculated scattering patterns of spheres
with size distributions: σ/d = 7%
Mie theory (solid line), modified R-D approx.
(dashed line), R-D approx. (dotted line)
with 1 m dia. and n_r=1.60/1.33

Chapter III

FOURIER TRANSFORM INVERSION TECHNIQUE:
ESTIMATION OF SIZE DISTRIBUTION OF BACTERIA

III.1   INTRODUCTION

According to the terminology of mathematical physics, problems

can be categorized into two groups, namely, direct problems and inverse

problems. The former seeks the consequences of given causes, while

the latter tries to obtain the unknown causes by means of observable

consequences. In the field of optical scattering, the direct problem

is to predict the propagation and scattering of light on the basis of

a known constitution of sources or scatterers, while the inverse pro-

blem is to deduce features of sources or scatterers from the scattered

light. The process of obtaining the solution of an inverse problem is

called inversion, and the technique to perform the inversion is called

the inversion technique. This chapter deals with the inversion tech-

nique which determines the size distribution of scatterers from a

scattering pattern.

Various techniques have been developed for the inverse scattering

problems, but every technique has some disadvantages. Some need a

large matrix-inversion, a judicious choice of parameters, a priori

knowledge of scatterers, initial guess of the distribution, etc.

(Ishimaru, 1978a, p. 508). Some techniques such as Backus-Gilbert

technique do not require these but use involved mathematics.

Using the Mellin transform, Shifrin has developed an inversion technique for Rayleigh-Debye scattering, which does not have the above disadvantages. (Shifrin, 1965, p. 131.) This technique is similar to the one developed by Schmidt for the small angle X-ray scattering (Schmidt, 1965, p. 169). Recently, Fymat has also reported an inversion technique for Rayleigh-Debye scattering using the Bateman-Titchmarsh-Fox integral transform (Fymat, 1979). All these techniques are based on the invertibility of the special mathematical form of the Rayleigh-Debye approximation. Therefore, their applicability is restricted by the conditions of the Rayleigh-Debye approximation (Shifrin, 1966).

In this chapter, an inversion technique is developed with a completely different derivation from those mentioned above. This technique is general and applicable to one, two, and three dimensional scatterings, such as the diffraction of slits and apertures, as well as the scattering of particles. The inversion formula for the three dimensional case is shown to reduce to the formula obtained by Schmidt (1965). It is also shown that the integral transform in the inversion formula can be converted to a Fourier transform, which facilitates the inversion process rather than using the special transforms mentioned above.

The idea of this technique is as follows. The scattering pattern of a single scatterer is approximately proportional to the Fourier transform of the auto-correlation of the dielectric constant of the scatterer. The auto-correlation function has discontinuities at the boundary of the scatterer. Therefore, transforming and differentiating

operations on the scattering pattern yield delta-functions at the boundary. Since the linear addition holds for the scattered intensity of randomly distributed scatterers, the operations turn the addition into the convolution of the delta-function and the size-distribution function. This technique is applied to one-, two- and three-dimensional cases using an appropriate combination of linear operations and transforms, such as Fourier, Hankel and spherical-Bessel transforms. The spherical-Bessel transform can be converted to Fourier transform. As can be seen in its derivation, this technique does not require matrix-inversion or a priori knowledge of functional forms of the size distribution, and it can take advantage of other techniques in spectral analysis such as the Fast Fourier Transform or digital filtering technique. Since the 3-dimensional case of this technique is based on the Rayleigh-Debye approximation, its range of validity is limited by the conditions of the R-D approximation. However, it is shown that the valid range is extended considerably if the modification discussed in Chapter II is taken into account.

Bacteria count in urine is now routine for clinical microbiologists, urologists and obstetricians. The current technique consists of the processes of dilution, incubation (~24 hours), colony count and identification by susceptibility to different agents. This technique is time consuming, expensive, and also likely to introduce errors through manual processes. Many attempts have been made to improve and automate the processes. However, none of them seems to have been widely accepted. Our ultimate goal is the development of a rapid automated technique which identifies and counts bacteria in urine.

This technique will allow the mass-screening of urine samples and could also be applied to the general microbiological problems, such as the detection of micro-organisms in water.

In recent years, the usefulness of differential light scattering technique has been recognized in biological research, particularly in cytology and microbiology. However, its application to the clinical practice has been restricted by the problems commonly associated with natural particles, namely their size distribution, aggregation and existence of impurities. In urine, there are many kinds of particles in addition to the bacteria of interest, i.e., other kinds of bacteria, cells, cell fragments, crystals and other impurities.

The technique presented in this chapter can count the bacteria of interest exclusively separated from others by their sizes.

III.2   THEORY

III.2.1   Inversion for Size Distribution Estimation

If the locations and sizes of scatterers are randomly distributed, the correlation between the scattered fields from individual scatterers can be neglected. Therefore, the total scattered intensity $I(\Theta,\lambda)$ is given by the sum of the intensity rather than the field (Ishimaru, 1978a, pp. 36, 504), i.e.,

$$I(\Theta,\lambda) = \int_0^\infty I(\Theta,\lambda,D)\, n(D)\, dD \qquad (3\text{-}1)$$

where $I(\Theta,\lambda,D)$ is the scattered intensity from the scatterer with the typical dimension D, such as the diameter. Θ is the scattering angle and λ is the wavelength of the incident light. $n(D)$ is the size distribution of scatterers, or $n(D)\, dD$ is the number of scatterers per unit volume having the dimensions between D and $D+dD$. The inverse problem is to obtain the size distribution $n(D)$ from the measurements $I(\Theta,\lambda)$ using the known function $I(\Theta,\lambda,D)$.

III.2.2   Scattered Field

In some scattering approximations, the scattered field is given by the Fourier transform of the field at the scatterer, namely Fraunhofer diffraction (Goodman, 1968, p. 61) and Rayleigh-Debye scattering (Ishimaru, 1978a, p. 22).

(a)   1-dimension, such as slits or rectangular apertures

$$E(k_x) = C_1 \int_{-\infty}^\infty E(x')e^{ik_x x'} dx' \equiv F[E(x')] \qquad (3\text{-}2)$$

(b) 2-dimension, such as holes

$$E(k_x, k_y) = C_2 \iint\limits_{-\infty}^{\infty} E(x',y') e^{i(k_x x' + k_y y')} dx'dy' \tag{3-3}$$

for circular symmetry

$$E(k\rho) = C_3 \int\limits_0^{\infty} E(\rho') J_0(k_\rho \rho') \rho' d\rho' \equiv \mathcal{B}[E(\rho')] \tag{3-4}$$

(c) 3-dimension, such as particles

$$E(\bar{k}_s) = C_4 \iiint\limits_{-\infty}^{\infty} E(\bar{r}') e^{i\bar{k}_s \cdot \bar{r}'} d\bar{r}' \tag{3-5}$$

for spherical symmetry

$$E(k_r) = C_5 \int\limits_0^{\infty} E(r') j_0(k_r r') r'^2 dr' \equiv \mathcal{S}[E(r')] \tag{3-6}$$

where $k_x = kx/z$, $k_y = ky/z$, $k_\rho = k\rho/z$, $k = 2\pi n/\lambda$

$$\bar{k}_s = k\bar{i}_s = k(\hat{i} - \hat{o}), \quad |\bar{i}_s| = 2\sin(\theta/2)$$

$\hat{i}$ and $\hat{o}$ are unit vectors in the direction of incidence and observation, θ is the scattering angle, and $C_1 \sim C_5$ are constants. See Fig. 3-1.
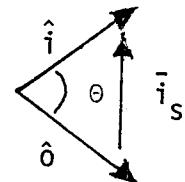
Fig. 3-1 Geometry of $\bar{i}_s$

In this chapter, the coordinates at the scatterer and at the observation point are distinguished by a prime (') such as x' and x respectively. In the cases of diffraction from the slits and apertures, n is the refractive index of the medium in which wave travels such as air or water. However, for the Rayleigh-Debye scattering, n is proved to be the refractive index of the scatterers.

It is discussed in Section III.5.4 and Chapter II. The operators

in Eqs. (3-2), (3-4), (3-6) are defined below.

III.2.3   Generalized Fourier Transform

(a)   Fourier Transform

$$F(k) = \int_{-\infty}^{\infty} f(x)e^{ikx} \, dx \equiv F[f(x)] \tag{3-7}$$

$$f(x) = \frac{1}{2\pi} \int_{-\infty}^{\infty} F(k)e^{-ikx} \, dk \equiv F^{-1}[F(k)] \tag{3-8}$$

(b)   Fourier-Bessel Transform (Hankel Transform)

$$F(k) = \int_{0}^{\infty} f(\rho) \, J_m(k\rho) \, \rho d\rho \equiv \mathcal{B}[f(\rho)] \tag{3-9}$$

$$f(\rho) = \int_{0}^{\infty} F(k) \, J_m(k\rho) \, kdk \equiv \mathcal{B}^{-1}[F(k)] \tag{3-10}$$

(c)   Spherical Bessel Transform

$$F(k) = \int_{0}^{\infty} f(r) \, j_m(kr) \, r^2 dr \equiv S[f(r)] \tag{3-11}$$

$$f(r) = \frac{2}{\pi} \int_{0}^{\infty} F(k) \, j_m(kr) \, k^2 dk \equiv S^{-1}[F(k)] \tag{3-12}$$

(d)   Generally, they can be written

$$F(\bar{k}) = \int_n f(\bar{r}) \, e^{i\bar{k} \cdot \bar{r}} \, d\bar{r} \equiv F[F(\bar{k})] \tag{3-13}$$

$$f(\bar{r}) = (2\pi)^{-n} \int_n F(\bar{k})e^{-i\bar{k} \cdot \bar{r}} \, d\bar{k} \equiv F^{-1}[f(\bar{r})] \tag{3-14}$$

(Kraut, 1967, p. 213)

III.2.4   Inversion Technique

Using Eq. (3-13), the scattered intensity is given as a Fourier Transform of an autocorrelation function $R_E(\bar{r}_0)$ of the field at the scatterer; that is

$$I(\bar{k}_s) = |F[E(\bar{r}')]|^2 = F[R_E(\bar{r}_d)] \tag{3-15}$$

where $R_E(\bar{r}_d) = \int_n E(\bar{r}_1) E^*(\bar{r}_1 - \bar{r}_d) d\bar{r}_1$,

The field at the discrete scatterers (e.g., holes, particles) has discontinuities at the boundary of the scatterers, such as a rectangular function. Thus its autocorrelation function also has discontinuities at the points corresponding to the boundary or the size of the scatterers. By applying a proper linear operation to the autocorrelation function, we can develop a delta function at the boundary. The delta function brings the unknown size-distribution-function out of the integral, thus giving a solution to the inverse problem, i.e.,

$$I(\bar{k}_s) = \int_0^\infty I(\bar{k}_s,D) \; n(D) \; dD$$

$$F^{-1}[I(\bar{k}_s)] = \int_0^\infty R_E(\bar{r}_d,D) \; n(D) \; dD$$

$$L[\,F^{-1}[I(\bar{k}_s)]\,] = \int_0^\infty \delta(D - r_d) \; n(D) \; dD = n(r_d) \tag{3-16}$$

where $L[R_E(\bar{r}_d,D)] = \delta(D - r_d)$.

The detailed procedures are as follows:

(a) 1-dimension

$$E(x',a) = \text{rect}(x',a) = \begin{cases} 1 & |x| \le a \\ 0 & \text{elsewhere} \end{cases}$$

$$R_E(x_d,a) = \Lambda(x_d,2a) = \begin{cases} 2a + x_d & -2a \le x \le 0 \\ 2a - x_d & 0 \le x \le 2a \\ 0 & \text{elsewhere} \end{cases}$$

$$\frac{\partial^2}{\partial x^2} R_E(x,a)\Big|_{x > 0} \propto \delta(x - 2a) \text{ ,where the region } x > 0 \text{ is}$$

considered to eliminate another delta-function at $x = 0$.

Therefore,

$$\frac{\partial^2}{\partial x^2} F^{-1}[I(k_x)]\Big|_{x > 0} \propto n\left(\frac{x}{2}\right) \tag{3-17}$$

(b) 2-dimension (circular symmetry)

$$E(\rho',a) = \text{circ}(\rho',a) = \begin{cases} 1 & 0 \le \rho' \le a \\ 0 & \rho' > a \end{cases}$$

$$R_E(\rho_d,a) = \begin{cases} 2a^2(\cos^{-1}\alpha - \alpha\sqrt{1 - \alpha^2}) & 0 \le \rho_d \le 2a \\ 0 & \rho_d > 2a \end{cases}$$

$$\approx \Lambda(\rho_d,2a)$$

where $\alpha = \rho_d/(2a)$

$$\frac{1}{\rho} \frac{\partial^2}{\partial \rho^2} R_E(\rho,a) \bigg|_{\rho > 0} \propto \begin{cases} (\sqrt{a^2 - (\rho/2)^2}\,)^{-1} & 0 \leq \rho \leq 2a \\ 0 & \rho > 2a \end{cases}$$

$$\simeq \delta(\rho - 2a)$$

Therefore approximately,

$$\frac{1}{\rho} \frac{\partial^2}{\partial \rho^2} B^{-1} [I(k_\rho)] \bigg|_{\rho > 0} \propto n(\tfrac{\rho}{2}) \qquad (3\text{-}18)$$

(c) 3-dimension (spherical symmetry)

$$E(r',a) = \text{sphr } (r',a) = \begin{cases} 1 & 0 \leq r' \leq a \\ 0 & r' > a \end{cases}$$

$$R_E(r_d,a) = \begin{cases} (r_d - 2a)^2 (r_d + 4a)/6 \quad {}^{six} & 0 \leq r_d \leq 2a \\ 0 & r_d > 2a \end{cases}$$

$$\frac{\partial}{\partial r} \frac{1}{r} \frac{\partial^2}{\partial r^2} R_E(r,a) \bigg|_{r > 0} \propto \delta(r - 2a)$$

Therefore

$$\frac{\partial}{\partial r} \frac{1}{r} \frac{\partial^2}{\partial r^2} S^{-1} [I(k_r)] \bigg|_{r > 0} \propto n(\tfrac{r}{2}) \qquad (3\text{-}19)$$

See Appendix III.A for the derivation. This formula was obtained by others for the small angle X-ray scattering problems (Schmidt, 1965). Noting that $I(k_r)$ is an even function of k_r, the spherical-Bessel transform in Eq. (3-19) can be converted into the regular Fourier

transform, i.e.,

$$\frac{\partial}{\partial r} \frac{1}{r} \frac{\partial^2}{\partial r^2} \frac{2i}{r} \; F^{-1} \; [k_r I(k_r)] \Big|_{r > 0} \propto n(\tfrac{r}{2}) \qquad (3\text{-}20)$$

In numerical calculation, the Eq. (3-20) is more convenient with the advantages of the Fast Fourier Transform technique than Eq. (3-19), which involves the evaluation of an infinite integral.

III.2.5   Elimination of Differentiation

By interchanging the linear operation and the transform, we can eliminate the differential operation which sometimes causes instability problems in numerical calculations:

$$n(\tfrac{x}{2}) \propto \frac{d^2}{dx^2} \; F^{-1} \; [I(k_x)] \Big|_{x > 0} = F^{-1}[- k_x^2 I(k_x)] \Big|_{x > 0} \qquad (3\text{-}21)$$

$$n(\tfrac{r}{2}) \propto \frac{\partial}{\partial r} \; \frac{1}{r} \frac{\partial^2}{\partial r^2} \; S^{-1}[I(k)] \Big|_{r > 0}$$

$$= F^{-1}[\{ (\frac{4k^2}{r^4} - \frac{k^4}{2r^2}) + i \, (\frac{2k^3}{r^3} - \frac{4k}{r^5}) \} I(k)] \Big|_{r > 0} \qquad (3\text{-}22)$$

where $i = \sqrt{-1}$ and k_r was replaced by k for simplification. Again in Eq. (3-22), the spherical-Bessel transform was converted into the regular Fourier transform.

See Appendix III.B for the proof of Eq. (3-22).

III.2.6   An Example of Inversion

As an example, we can demonstrate the inversion using Eq. (3-21).

The scattering pattern of a single slit with the width $2a$ is given by,

$$I(k_x, a) = \frac{(2a)^2}{\lambda z} \left\{ \frac{\sin(k_x a)}{k_x a} \right\}^2 \qquad \text{(Goodman, 1968, p. 63)}$$

and

$$-k_x^2 \, I(k_x, a) \propto 1 - \cos(2k_x a) .$$

Hence, $F^{-1}[- k_x^2 \, I(k_x, a)] \Big|_{x > 0} \propto \delta(x - 2a)$.

Substituting this into Eq. (3-1), we obtain the size distribution, i.e.,

$$I(k_x) = \int_0^\infty I(k_x, a) \, n(a) \, da$$

and

$$F^{-1}[- k_x^2 \, I(k_x)] \Big|_{x > 0} \propto \int_0^\infty \delta(x - 2a) \, n(a) \, da = n\left(\frac{x}{2}\right)$$

III.3   METHOD

III.3.1   Problems in the Inversion Technique

The Fourier Transform in the inversion technique presented in the previous section III.2 requires the scattered intensity $I(k_r)$ to be continuous between $k_r = 0$ and ∞, where $k_r = 2k \sin(\theta/2)$. However, in our experimental system, the scattered intensity was measured at about 50 discrete angles between $\theta = 5° \sim 70°$, which corresponds to $k_r = 1.15 \sim 15.2$ for $\lambda = 0.6328\,\mu m$. The discreteness and the small number of data points causes an "aliasing" problem of the transformed function, and the finiteness of the range k_r causes the "leakage" problem (Brigham, 1974, pp. 83, 105). In addition, the differential operation tends to exaggerate various errors, such as numerical and measurement noises.

III.3.2   Countermeasures

To overcome these problems, the following measures were taken.

(a) An FFT was used which provides efficient transforms and avoids the aliasing (IMSL, 1978).

(b) Applying a cubic spline interpolation (IMSL, 1978) to the measured data, the input function $I(k_r)$ was sampled at a closer interval in k_r. With the interpolation we can take a specific number of sample points (2^n) which makes the FFT more efficient.

(c) A digital filter (Blackman Window) was applied to the input function to moderate the leakage problem. (Oppenheim, 1975, p. 242).

(d) Since the noises mentioned above tend to have high-frequency

components, the Eq. (3-20) was used instead of Eq. (3-22). The latter exaggerates the noise and makes the following transformation erroneous. In our méthod based on Eq. (3-20), we know beforehand if the function to be differentiated is monotonically increasing or decreasing. Therefore, each time after the first order derivative was applied, the sign of the differentiated function was checked and improper parts were set to zero. In this way, we can discard a part of the leakage as well as the noises.

The outline of the algorithm is as follows. An example of the program is shown in Appendix P.

1. Read in measured data $I(\Theta)$.

2. Interpolate $I(k_r)$ at 2^M points, where $k_r = 2k \sin(\Theta/2)$.

3. Apply FFT to $k_r I(k_r)$, i.e., $F^{-1}[k_r I(k_r)]$.

4. Calculate a spherical Bessel transform, i.e.,

$$S^{-1}[I(k_r)] = \frac{2i}{r} F^{-1}[k_r I(k_r)]$$

   and take a real part.

5. Differentiate it with respect to r to get

$$\frac{\partial}{\partial r} S^{-1}[I(k_r)] .$$

6. Take the negative parts and set the positive parts zero, because

$$\frac{\partial}{\partial r} S^{-1}[I(k_r)] = \frac{1}{2} \int_0^\infty (r^2 - 4a^2) \, \text{rect}(r,2a) \, n(a) \, da < 0 .$$

7. Differentiate it again, divide by r , and take the positive parts, because

$$\frac{1}{r} \frac{\partial^2}{\partial r^2} \; S^{-1}[I(k_r)] = \int_0^\infty \text{rect}(r,2a) \; n(a) \; da > 0 \quad .$$

8. Differentiate it, take the negative parts, and discard the huge value at the origin, thus getting

$$\left. \frac{\partial}{\partial r} \frac{1}{r} \frac{\partial^2}{\partial r^2} \; S^{-1}[I(k_r)] \right|_{r > 0} \propto n\!\left(\frac{r}{2}\right)$$

III.4   EXPERIMENTS

III.4.1   Scattering Pattern

The scattered intensity $I(k_r)$ defined in previous sections was measured as a function of a scattering angle Θ , and is called an "(angular) scattering pattern," where $k_r = 2k \sin(\Theta/2)$. In our experiments, the scattering patterns were obtained by measuring the angular intensity distribution of a perpendicularly polarized component of the scattered light with respect to the scattering plane. The incident light was assumed to be a perpendicularly polarized plane wave.

Fig. 3-2 illustrates the scattering pattern measurement schematically.
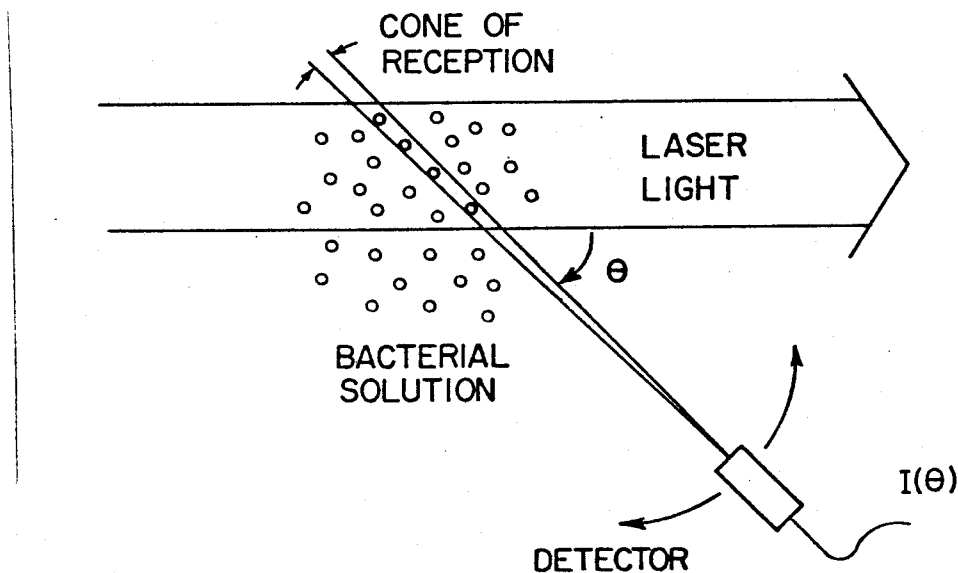
Fig. 3-2 Schematic diagram of light scattering measurement

III.4.2 Samples

Experiments were conducted with latex spheres and bacteria. In the measurement, the concentration of scatterers was kept low (optical distance < 0.1) and a detector with a very narrow cone of reception (0.3°) was used to minimize multiple scattering effects and to attain high angular resolution.

Sample solutions of spherical particles were prepared by diluting a concentrated solution of latex spheres (10 volume percent) with 0.01% detergent water. The detergent, sodium dodecyl sulfate, was added to double distilled and deionized water as surfactant to prevent aggregation of particles.

As sample solutions of bacteria, Staphylococcus aureus (ATCC 25923) and Escherichia coli (ATCC 25922) were suspended separately in isotonic saline solutions (0.85%) and were killed by filtered formalin solution (30%). The concentrations of bacteria in sample solutions were approximately $10^6/cm^3$. This is one of the clinically significant ranges of concentrations for the examinations of urine.

III.4.3 Measurement

Light intensities were measured by changing the angular position of a detector over 5° to 70° from the direction of incident light. The measurement which covers a wide range of light intensity ($\sim$ 50 db) was attained by the combination of high intensity light source (laser), sensitive detector (PMT) and attenuators (neutral density filters). Measured data were plotted in a scattering pattern after the correction for the effects of the glass-liquid interface, geometrical factors

of the experimental system, and the scattering caused by the background solution of the scatterers.

In these corrections, the theory of radiative transfer was applied successfuly (Shimizu, 1976), rather than the conventional $\sin\Theta$-correction ($V = V_0/\sin\Theta$), which corrects only the change of the scattering volume V with respect to the scattering angle Θ .

Experiments were conducted several times and the results showed excellent reproducibility.

III.4.4   Experimental Facility

Fig. 3-3 shows a schematic diagram of our experimental set-up. The principal optical and electronic system was developed by Dr. J. Molcho.

Particles suspended in a solution are contained in a cylindrical scattering cell (S.C.). One end of the cell is flat glass and the other end is hemispherical glass. A beam of He-Ne laser light (λ = 632.8 nm) is mechanically chopped by a chopper (CHOP.) for a phase-lock technique. The beam is shifted from the center line of the scattering cell so that the part of the beam which illuminates the particles is brought within the view range of a detector (D_3). The detector which has a very narrow angle of acceptance ($0.3°$) transmits the scattered light to a photomultiplier (PMT) through fiber optics (F.O.). The signal is amplified by the lock-in amplifier (LIA), which is a phase responsive amplifier with a narrow effective bandwidth, in order to reduce the noise. An auxiliary beam which is generated at a beam splitter (BS) is directed by the mirror (M) toward a transmittance

cuvette (T.C.) and a detector (D_2, acceptance angle 0.1°) for a turbidity measurement. The scattering signal ($I(\theta)$) and the transmittance signal (T) are sent to a mini-computer (PDP-12). In the computer, the signals are normalized for changes in the incident intensity (N) sampled through a detector (D_1).

The computer samples the signals in time, calculates simple statistics (mean, median, standard deviation, etc.) and displays the information in real time. The median is less affected by impulse-type noise than the mean. The computer stores all the data obtained for further processes, such as plotting, noise extraction, parameters estimation, etc. It also monitors automatic measurements and controls their mechanisms, which involves controlling an integration time for the lock-in amplifier, sampling frequency, thickness of the scattering cell, and X-Y plotter.
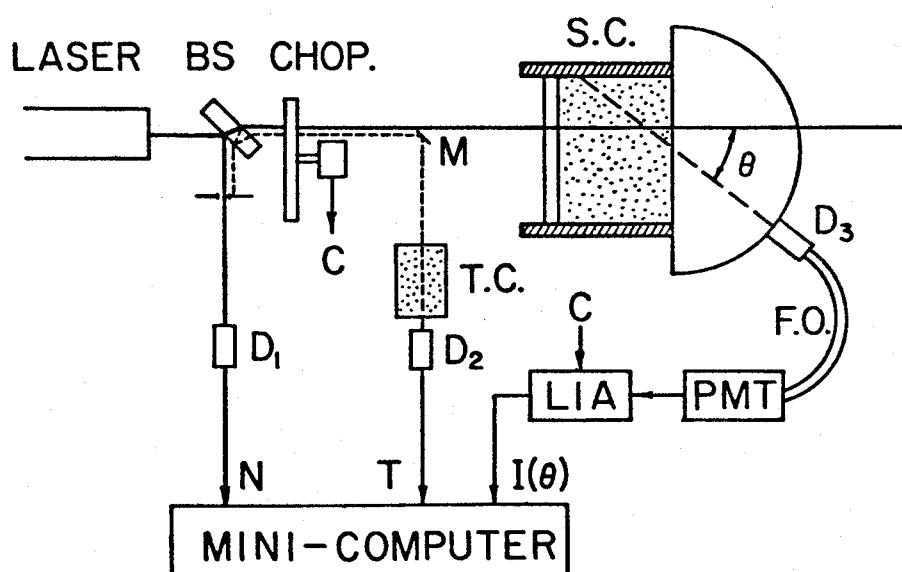
Fig. 3-3 Schematic diagram of experimental system

More detailed discussions of the experimental system, method, and materials are given in (Shimizu, 1976), (Molcho, 1975).

III.5   RESULTS AND DISCUSSION

III.5.1   Advantage of the Inversion Technique

The effectiveness of the proposed technique is investigated using the simulated data calculated with a known size distribution. Figs. 3-4 and 3-5 show the advantage of the inversion technique over the empirical curve-fitting technique.

Figs. 3-4(a) and 3-5(a) are the sampled scattering patterns calculated by the Rayleigh-Debye approximation with the size distribution shown in the upper right corners of the figures. The scattering patterns appear to be very similar despite the different size distributions. Without a priori knowledge, it is difficult or time-consuming to find such size distributions by the regular curve-fitting technique.

Figs. 3-4(b) and 3-5(b) show the size distributions estimated by the inversion technique proposed here. The noisy outline is due to the discreteness of the sampled scattering pattern (number of samples N_s = 64) and the finiteness of the scattering angle (θ = 0 ~ 60° or k_r = 0 ~ k where k = $2\pi n/\lambda$). Although the shapes of the estimated size distributions are not as smooth as the given ones, the distinction of the two different distributions is well recovered. Note that this technique does not require any a priori knowledge. The accuracy of this technique can be seen in the relative heights of the two peaks in Fig. 3-5(b). They agree well with those of the given distribution.
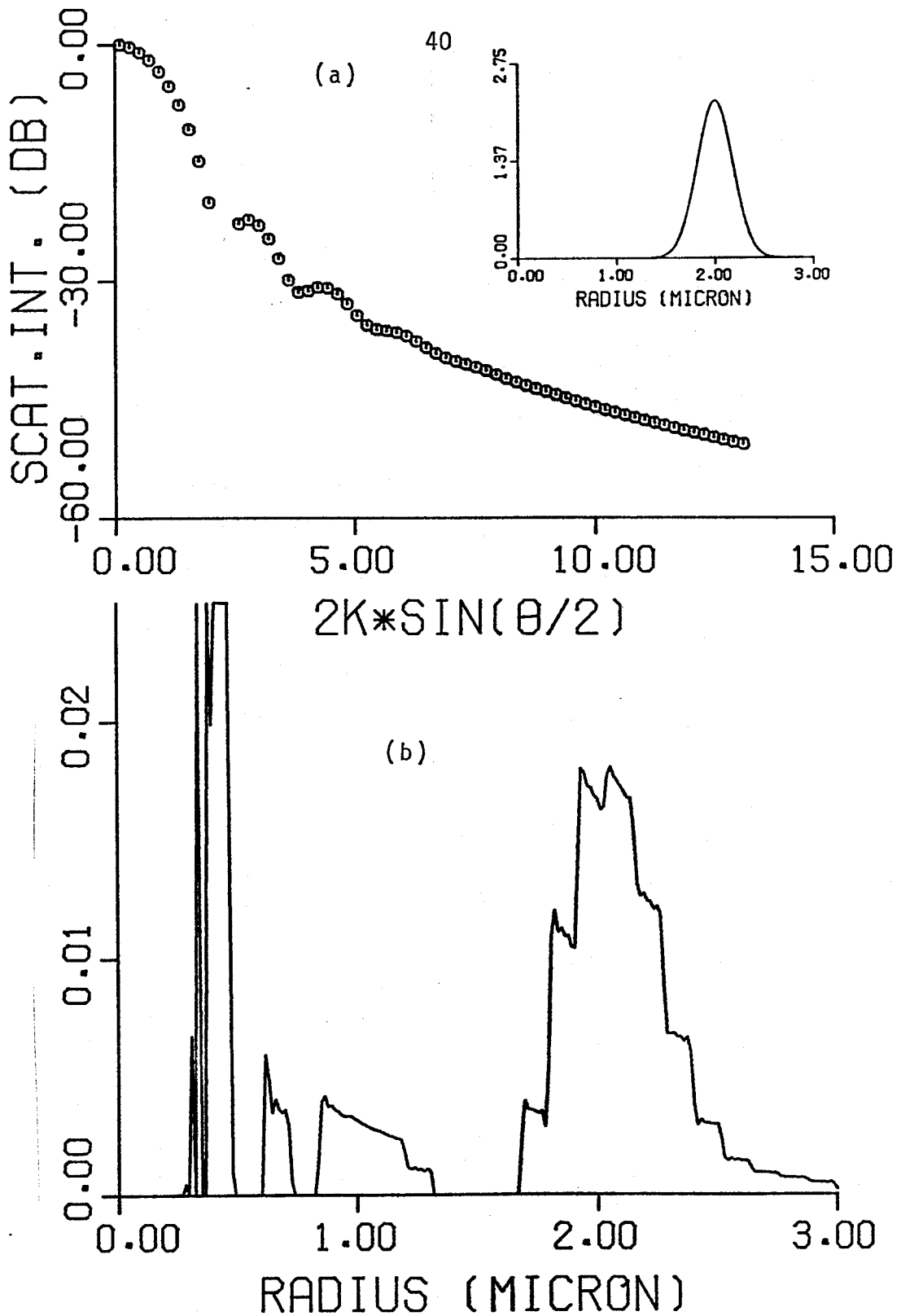
Fig. 3-4   Advantage of the inversion technique;
           Gaussian size distribution (μ = 2.0,
           σ = 0.18) from simulated data
           (a) scattering pattern, (b) size dist.
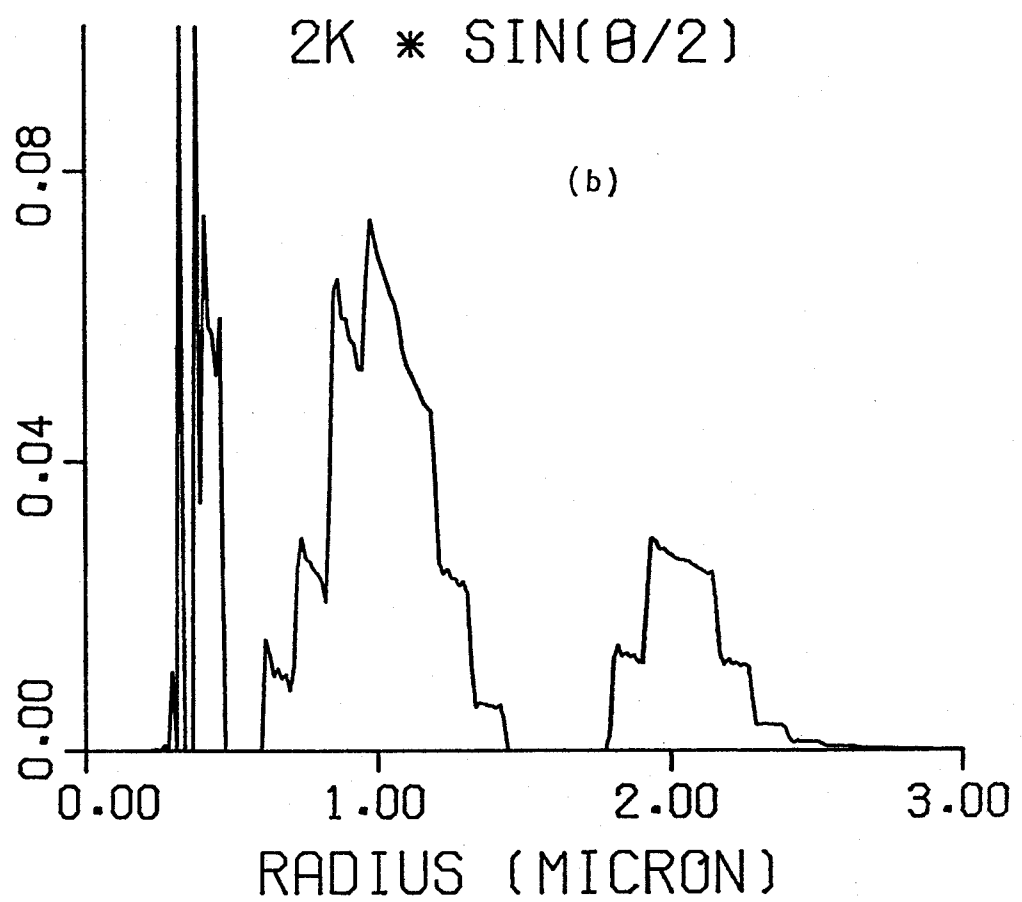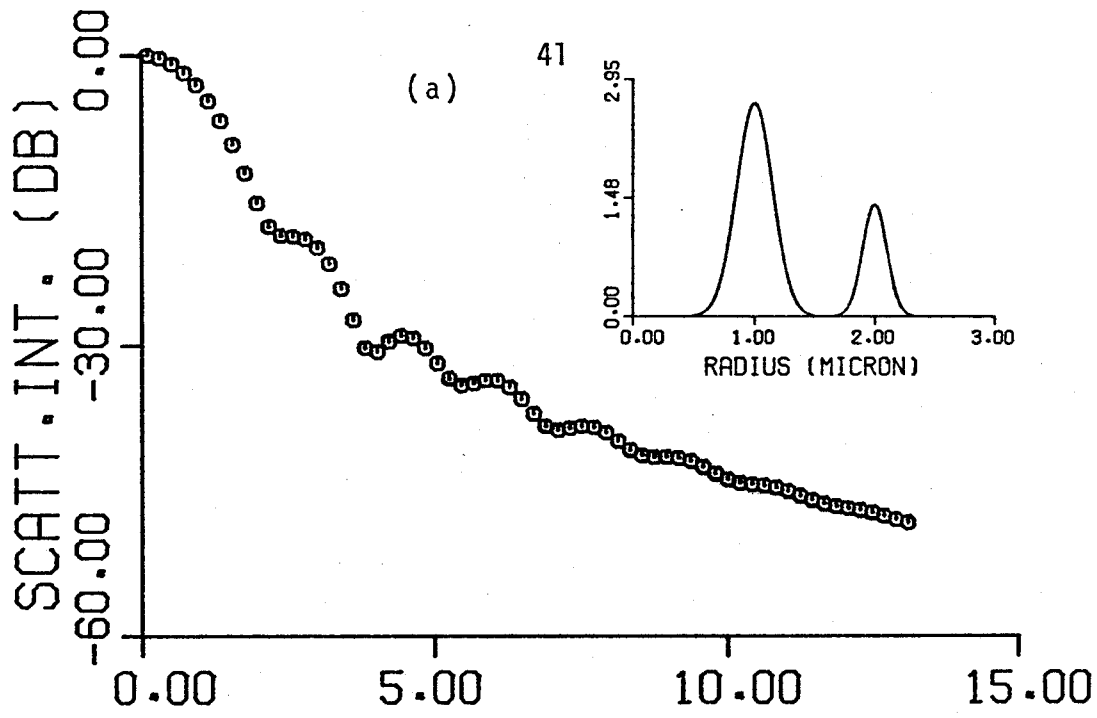
Fig.3-5 Advantage of the inversion technique:
size distribution with two peaks
(μ_1 = 1.0, σ_1 = 0.15, μ_2 = 2.0, σ_2 = 0.1)

(a) scattering pattern, (b) size dist.

III.5.2   Resolution

The accuracy of the proposed technique was shown above with the Gaussian distribution. Another important factor in inversion problems is resolution—how closely we can recover the detailed shape of the given distribution. Since the core of this technique is the Fast Fourier Transform, the frequency and the range in one domain corresponds to the range and the frequency in the transformed domain. In other words, with the fixed range of the scattering angle, the more frequent sampling in the scattering angle gives the distribution estimated in the wider range of scatterer's size. On the contrary, with a fixed rate of sampling, if the scattering pattern is sampled in a wider range of the scattering angle, the estimated size distribution contains higher frequency components, that is, more resolution is attained.

In order to examine the resolution of our technique, a rectangular function was chosen as the given function to be estimated. Although such a distribution rarely appears in the natural world, we can check with this function the recovery of the wide range of frequency components, i.e., flat top, sharp edge, etc. Fig. 3-6(a) and (b) show the estimated distributions using the calculated scattering pattern sampled in $\Theta = 0° \sim 60°$ ($k_r = 0 \sim k$) and $\Theta = 0° \sim 180°$ ($k_r = 0 \sim 2k$), respectively. The sampling rate is the same for both cases ($\Delta k_r = k/64$).

As expected, the data at larger angles improves the resolution, giving better recovery for the higher frequency components. The

43
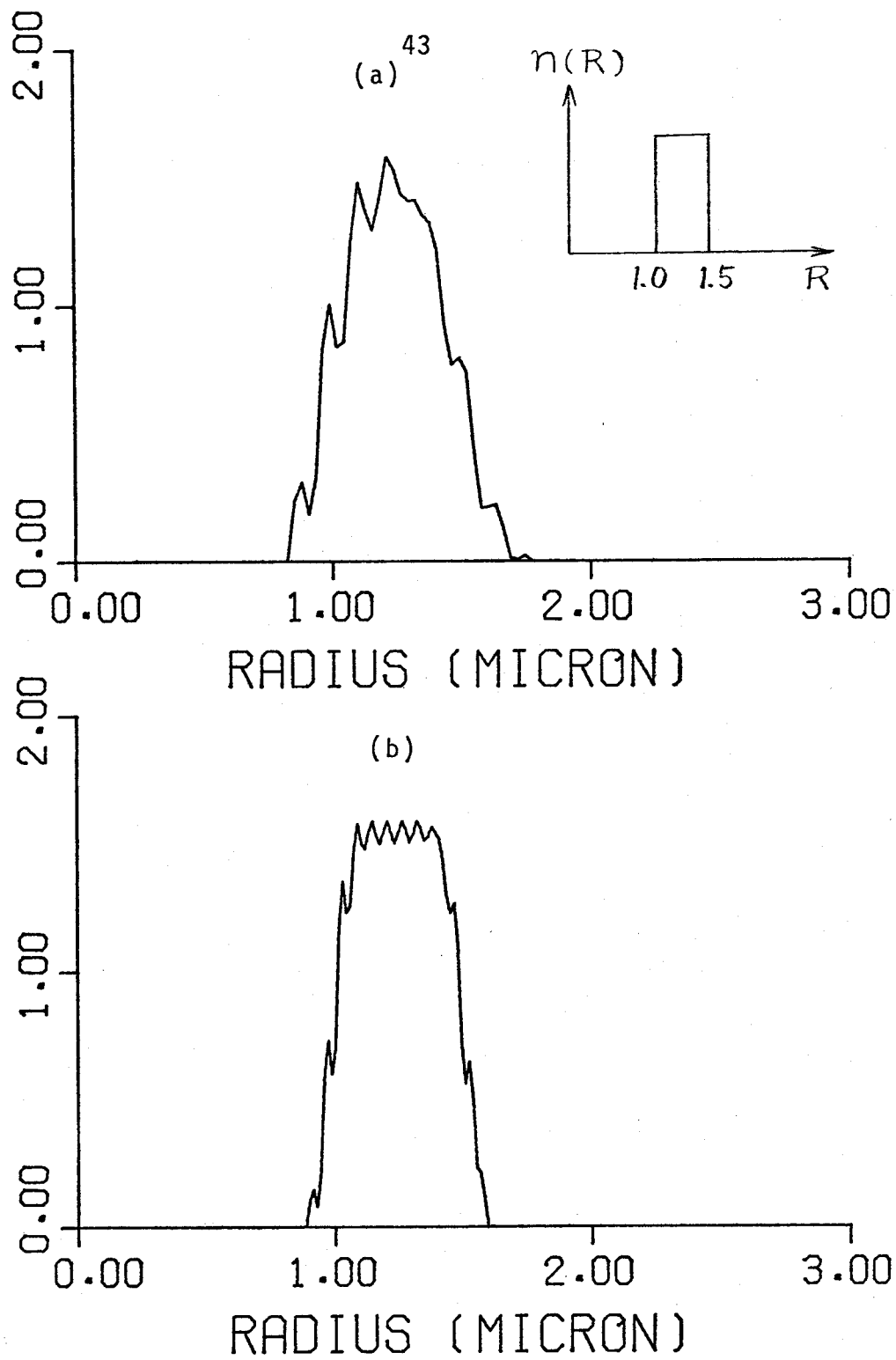
Fig.3-6 Resolution of the inversion technique:
rectangular size distribution from
simulated data; (a) θ = 0° – 60°
(b) θ = 0° – 180°

distortion by ripple which is due to the discrete sampling in the finite range, is reduced in the latter case. It should be noted also that the location of the estimated curve in the size-axis is not affected much by the expansion of the sampling range.

III.5.3 Noise Analysis

The determination of particle size distribution is an ill-posed problem (Franklin, 1970), (Ishimaru, 1978a, p. 504), which means the small error in the measured data cuases the large error in the estimation resulting in instability or divergence. In this section, the effect of the measurement error on the estimation by our technique is investigated. To simulate the error or noise in measurements, a random number weighted by a given factor is added to the calculated scattering pattern.

Figs. 3-7 ~ 3-11 show the calculated scattering patterns with the noise added and the estimated size distributions. The weighting factors for the random number are 0% (noise free), 5%, 10%, 30% and 50%, respectively. The given distribution is inlayed in Fig. 3-7. The mean and the standard deviation of the estimated distribution are shown in each figure. As can be seen, this technique is fairly stable in relation to the random additive noise. Note the accuracy in the case of 10% noise, which is typical in many practical situations. The estimation errors are within a few % for the mean and the standard deviation of the estimated distributions.

The cause of the noisy peaks at 0.4 ~ 0.5 µm is not fully understood. Since they appear in the error-free case too, they may be

attributed to the noise originated in the process of inversion, such as the discrete periodic sampling, Truncation errors in computation, etc. The 50% error induces another peak with a pointed top at the smaller size ($\sim$ 0.8 μm) than the true peak.

III.5.4   Latex Spheres

This technique is applied to the measured data obtained from the scatterers with known sizes. Fig. 3-12 show the measured scattering pattern and the estimated size distribution of the latex microspheres with a radius of 0.5055 μm. Two well-defined peaks are obtained at $\sim$ 0.5 μm and $\sim$ 0.35 μm. The latter with the characteristic pointed top may be considered as the erroneous estimate discussed in the previous section. This result shows the resolution or the minimum sizes to be determined is comparable to the wavelength of the probing light (λ = 0.6328 μm).

Fig. 3-13 is the case for the latex spheres with a radius of 1.01 μm. Now the true peak at $\sim$1 μm is separated from the erroneous one at $\sim$ 0.6 μm. The standard deviation of the true peak ($\sim$ 4% of the mean) is larger than the manufacturer's claim ($\sim$ 0.7%) which was measured in the electronmicroscopy. This tendency of the estimation of wide distribution may be attributed to the following. As can be seen in Fig. 2-3 in the previous chapter, the exact scattering pattern (b) appears as if the size distribution of scatterers were slightly wider than the scattering pattern (a) which is calculated by the Rayleigh-Debye approximation. That is, from the standard of the Rayleigh-Debye approximation, the size distribution looks wider

than the true one. Since this inversion technique is based on the
Rayleigh-Debye approximation, the estimated distribution can be
wider than the true distribution. It should be also noted that in
optical scattering measurements, the wider distribution has been
reported by others with various methods of measurements (Kratohvil,
1965), (Cooke, 1973),(Shimizu, 1978).

The Rayleigh-Debye approximation which this inversion technique
is based on is the modified one discussed in Chapter II. Note that
the refractive index of the latex spheres ($\sim$ 1.6 for λ = 0.6328 μm)
is beyond the range of validity of the Rayleigh-Debye approximation.
If the technique is based on the regular Rayleigh-Debye approximation,
the estimated size distribution is shifted by the ratio of refractive
indices of the scatterers and the surrounding medium (1.6/1.33). This
is shown in Fig. 3-14.

III.5.5 Bacteria

Finally, this technique is applied to estimate the size distribu-
tion of bacteria. Fig. 3-15 shows the measured scattering pattern
and estimated size distribution for Staphylococcus aureus. This is
a spherical bacteria with average radius of 0.4 $\sim$ 0.5 μm (Cohen, 1972,
p. 5). Under the microscope, they appear mostly in singlets with
uniform size. Some doublets are observed too, but not many higher
multiplets. Their photographs are given elsewhere (Shimizu, 1976).
The estimated distribution shows these characteristics well. Note
the small but evident distribution at $\sim$ 0.9 μm which is considered
to be the distribution of the doublets. The left peak with the pointed

top might be the erroneous peak discussed above. Fig. 3-16 shows the estimated size distribution for the large radius using the same data as in the case of Fig. 3-15. No significant distribution appears except for the predominant peak at 0.4 ~ 0.5 μm and the secondary peak at ~ 0.9 μm.

Fig. 3-17 shows the results for Escherichia coli. This is rod-shape or prolate spheroidal bacteria with the minor and major axis of ~ 0.5 μm and 2 ~ 3 μm respectively (Wolfgang, 1972, p. 27), (Wyatt, 1972). As shown elsewhere (Shimizu, 1976), the shape of the scattering pattern of the prolate spheroidal particles is similar to that of spheres with the radius equal to the minor axis of the spheroids. See Appendix III.C for more discussion. Thus, the slightly wider peak at 0.45 ~ 0.6 μm shown in Fig. 3-17(b) is reasonable. This is confirmed in microscopy. See the reference (Shimizu, 1976) for detailed discussion and for their micrographs.

III.5.6   Aggregated Bacteria

To examine the sensitivity of this technique to the change in the condition of scatterers, dye chemicals are added to the sample solution and part of the bacteria were aggregated. See the references (Shimizu, 1978, 1976) for the procedures and their appearances under microscope.

Figs. 3-18, 3-19 and 3-20 show the measured scattering patterns and the estimated size distributions for the Staphylococcus aureus, with no chemical, with safranine, and with methylene blue added, respectively. (a)'s of the figures are size distributions in large

48

scale with the scattering patterns inlayed and (b)'s are those in small scale.

The former ones show the major and the secondary peaks for singlets and doublets. As discussed elsewhere (Shimizu, 1978, 1976), scattering patterns contain the information of the single scatterer, even if the characteristic pattern of the single scatterer is degraded considerably by the aggregation of the scatterers. Figs. 3-19(a) and 3-20(a) show the effectiveness of this technique in extracting the information from the degraded scattering pattern.

Figs. 3-19(b) and 3-20(b) show interesting periodic structures. Comparing them with Fig. 3-18(b), they are considered to be the distribution of the multiplets, i.e, doublets, triplets, . . . etc. We can see the degree of aggregation increases in Figs. 3-18(b), 3-19(b) and 3-20(b).
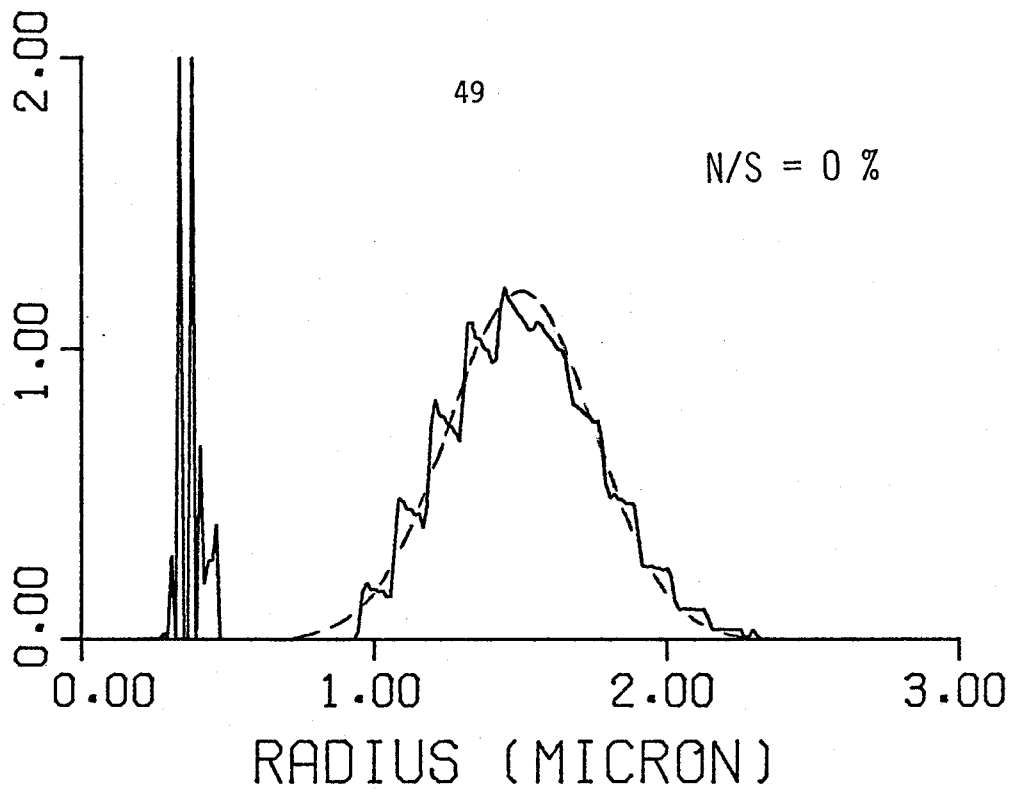
Fig.3-7 Noise analysis : simulated data with 0 %
random noise added
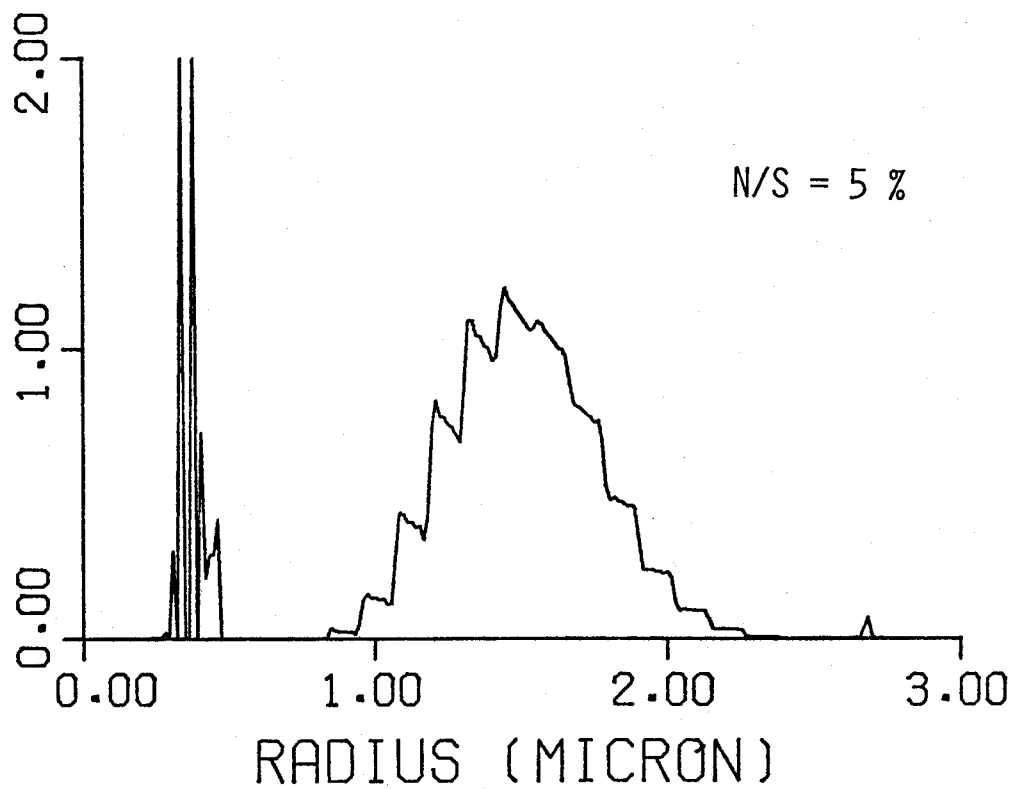
Fig.3-8 Noise analysis : simulated data with 5 %
random noise added
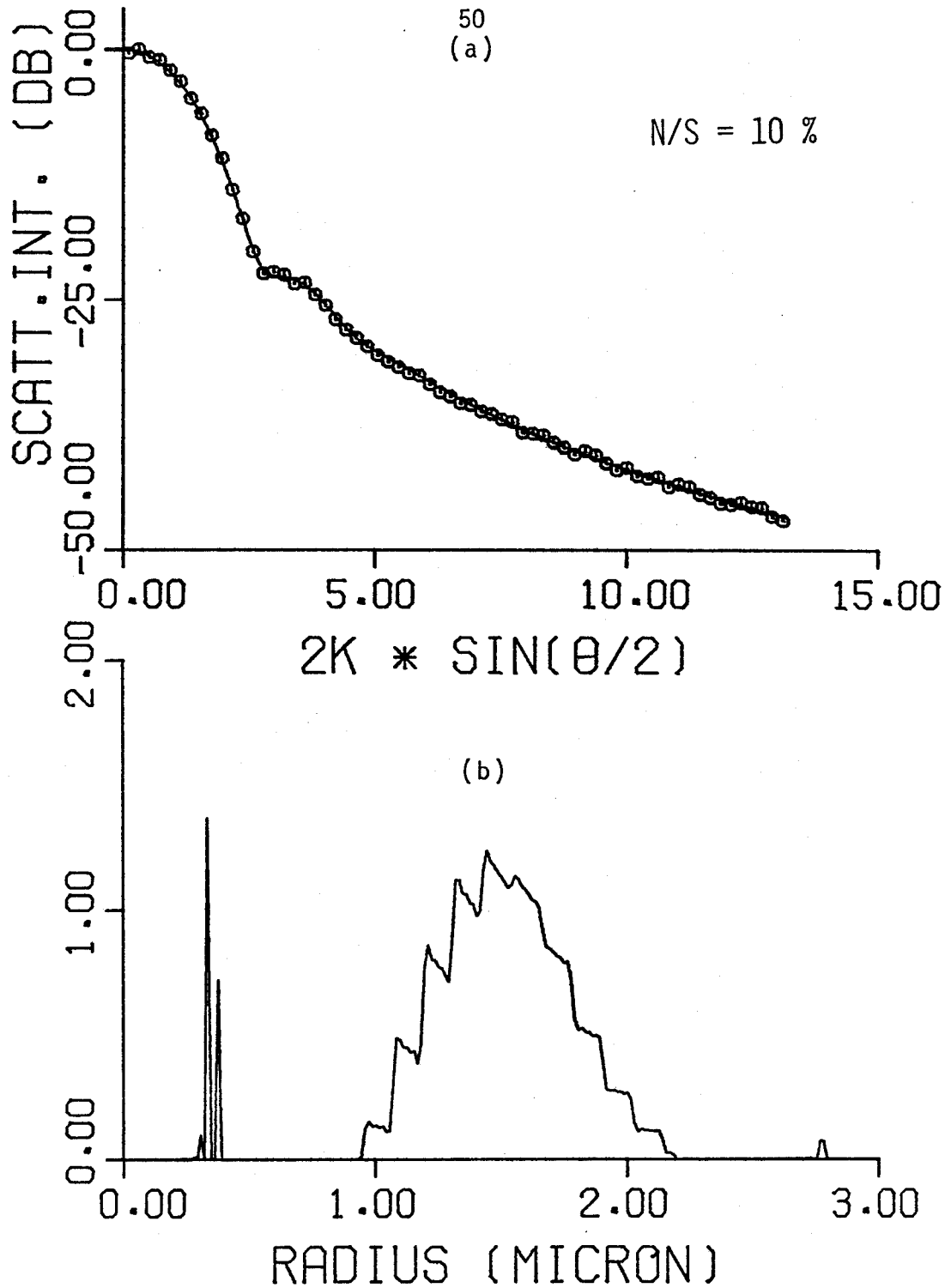
Fig.3-9 Noise analysis : simulated data with 10 %
random noise added

(a)

N/S = 30 %

(b)
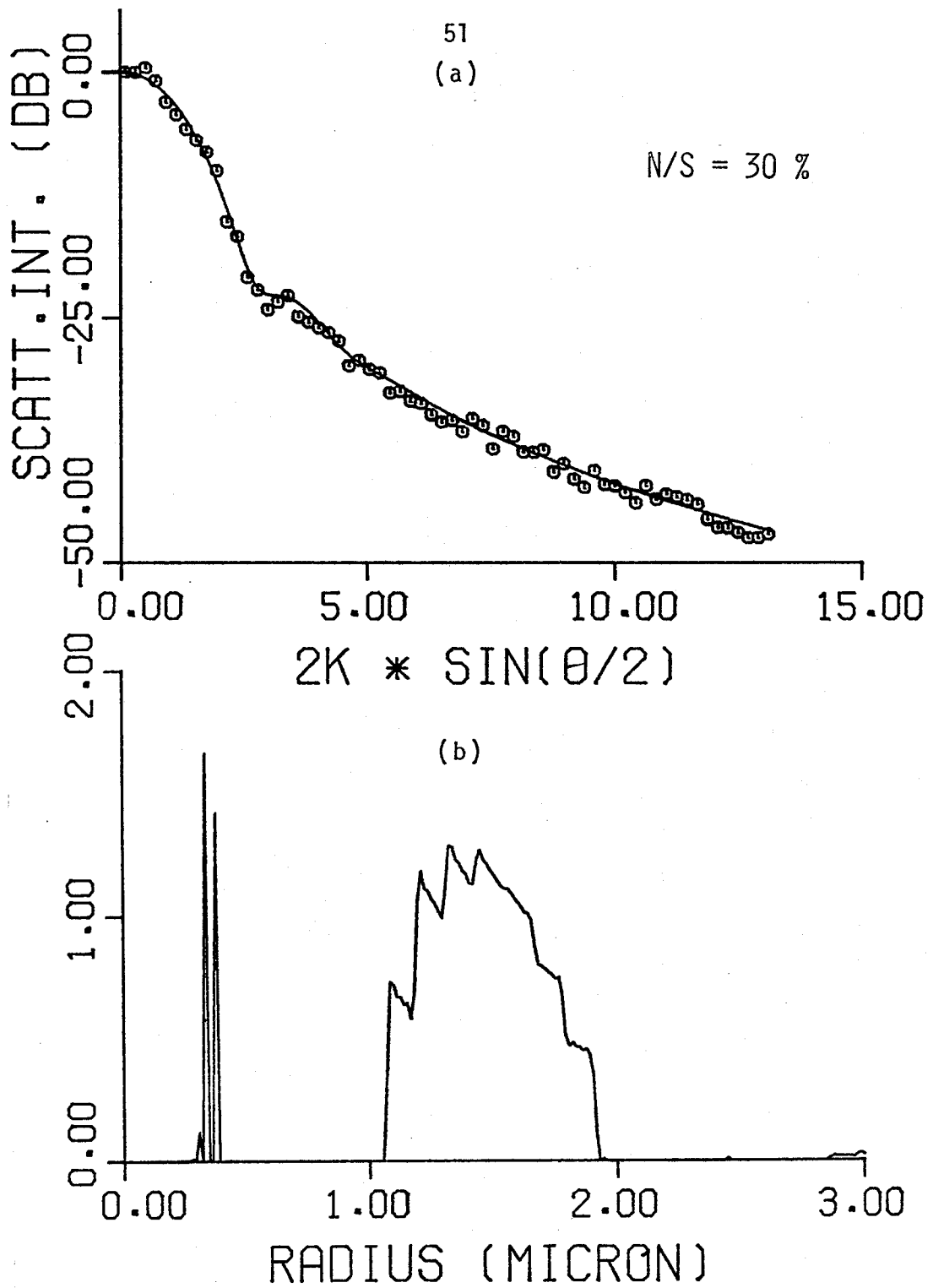
Fig.3-10 Noise analysis : simulated data with 30 %
random noise added

52
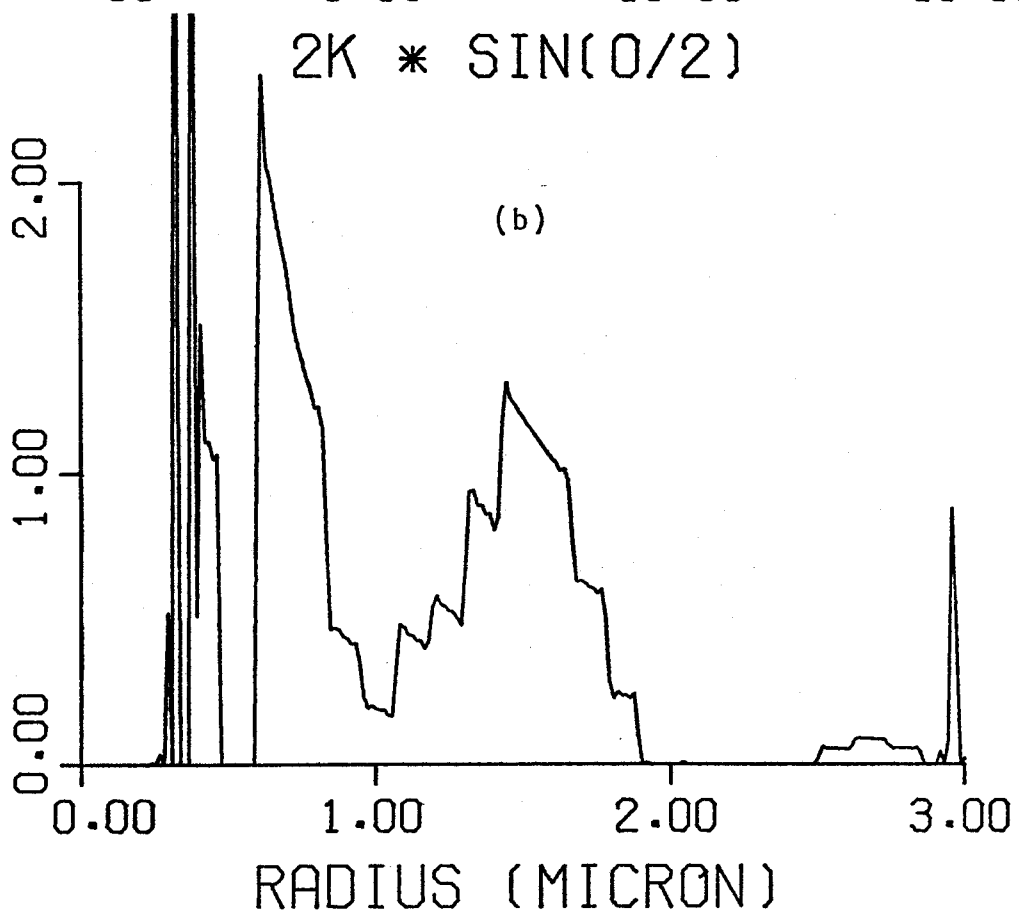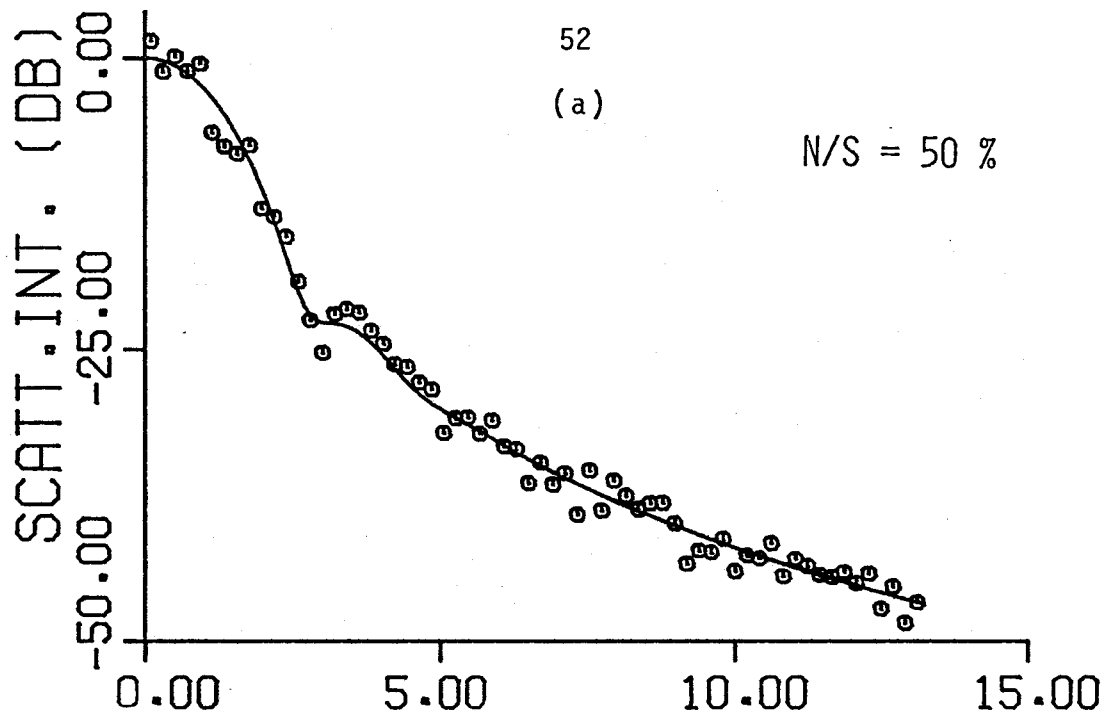
Fig.3-11 Noise analysis : simulated data with 50 %
                            random noise added

(a)

(b)
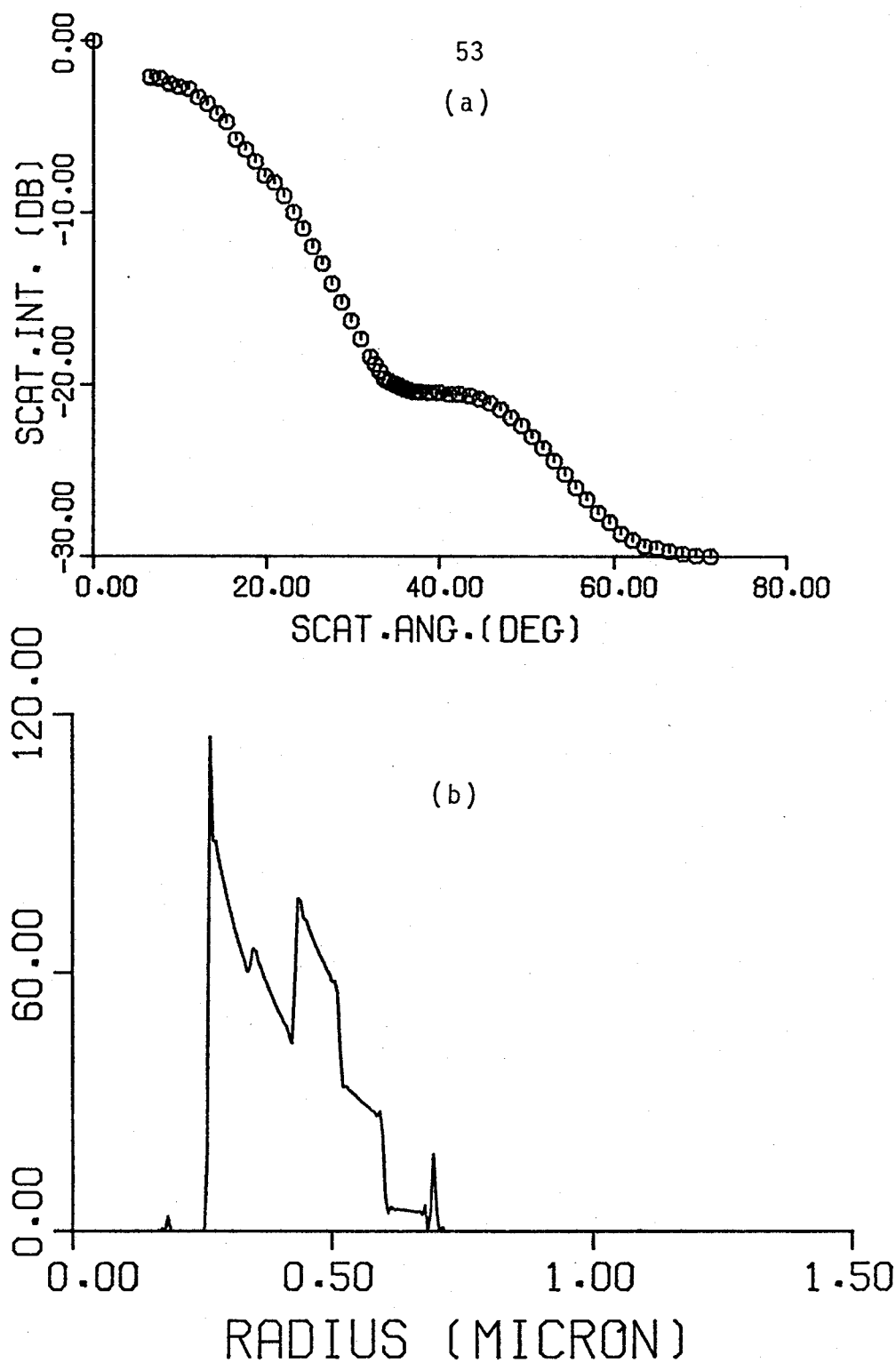
Fig.3-12 Size distribution of 0.5055 μm latex spheres ;
(a) measured scattering pattern (b) size dist.
N = 512, Θ = 0° – 71.2°, n_r = 1.588
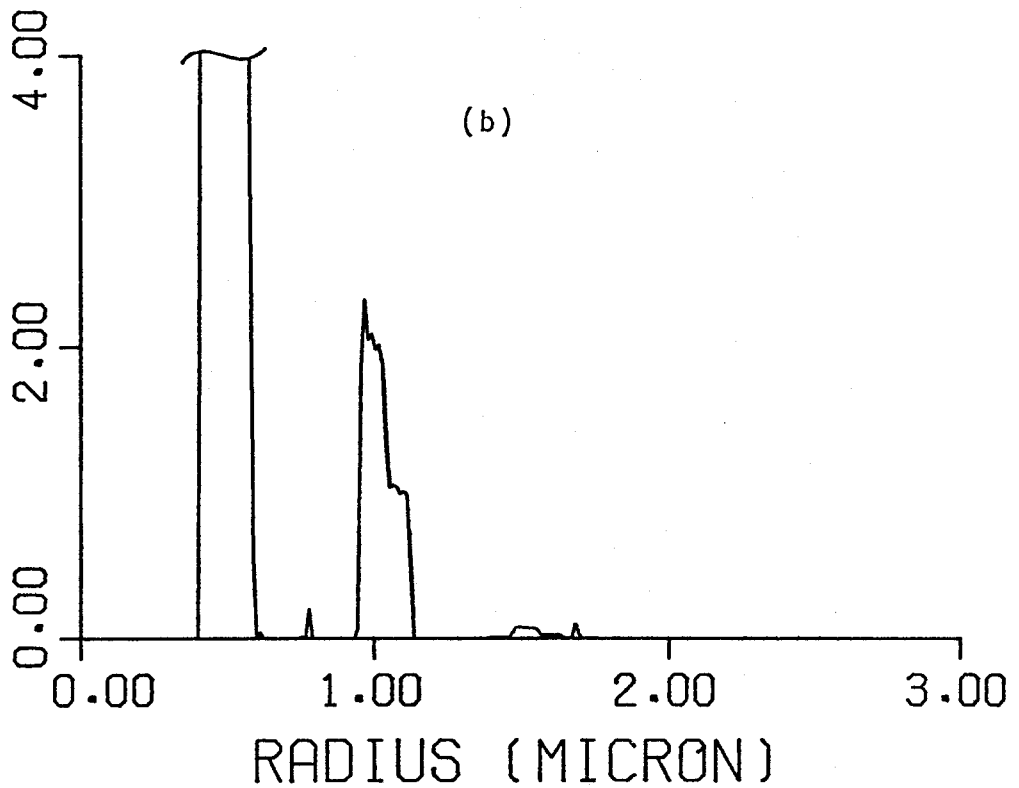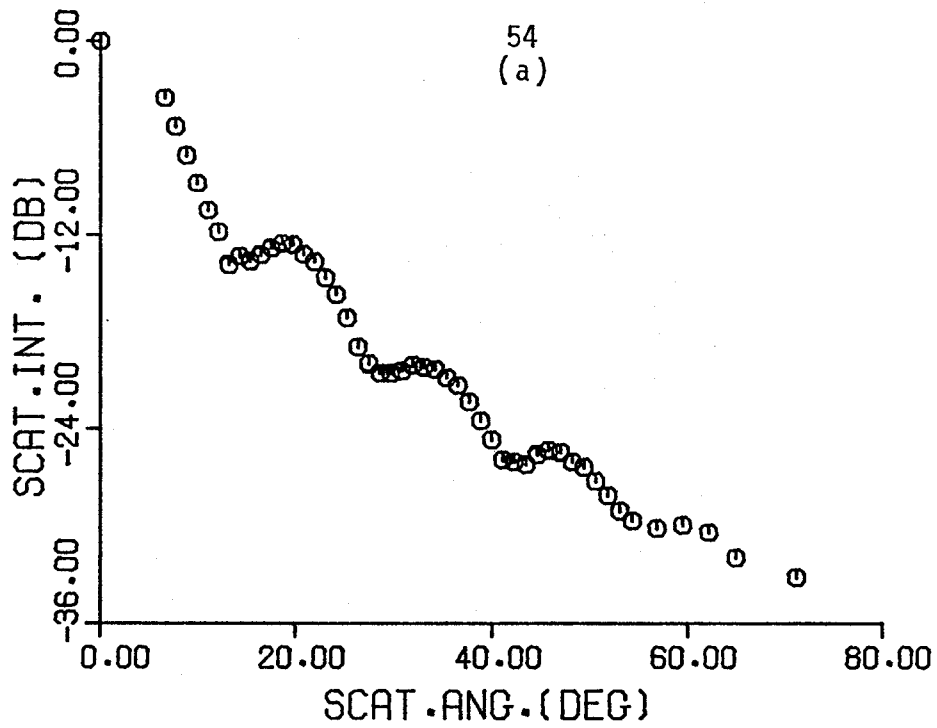
Fig.3-13 Size distribution of 1.01 μm latex spheres ;
(a) measured scattering pattern, (b) size dist.
N = 512, θ = 0° – 71.2°, n_r = 1.577
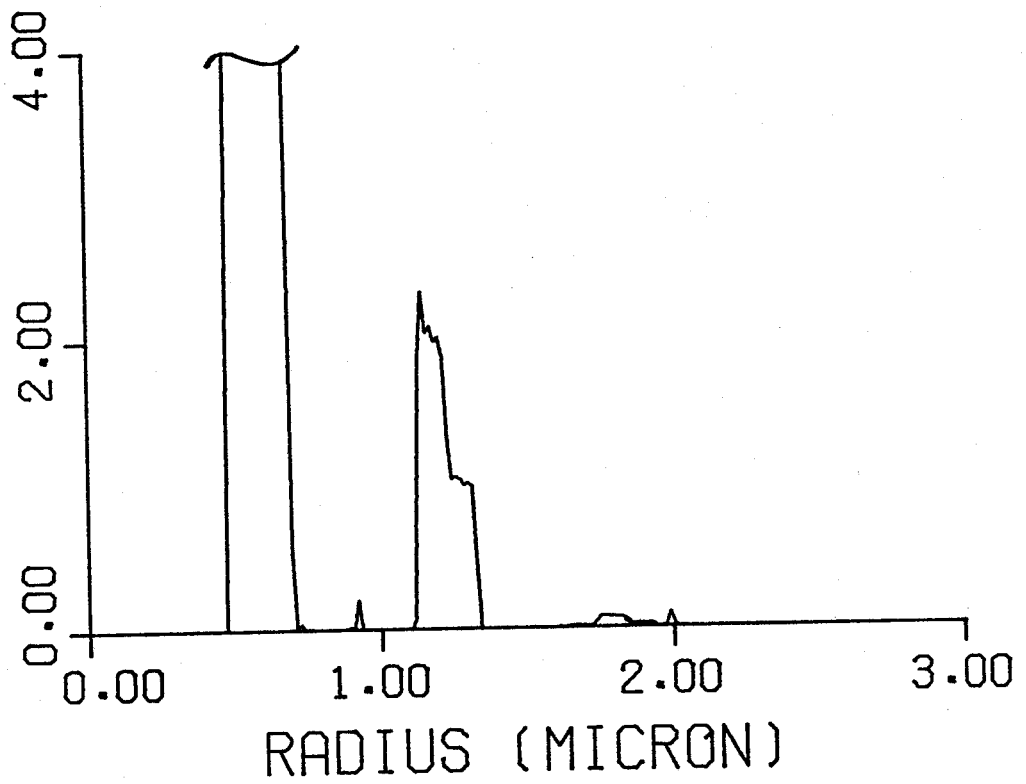
Fig.3-14 Without the modification of Rayleigh-Debye approximation :
measured data of 1.01 μm latex spheres

56

(a)

(b)
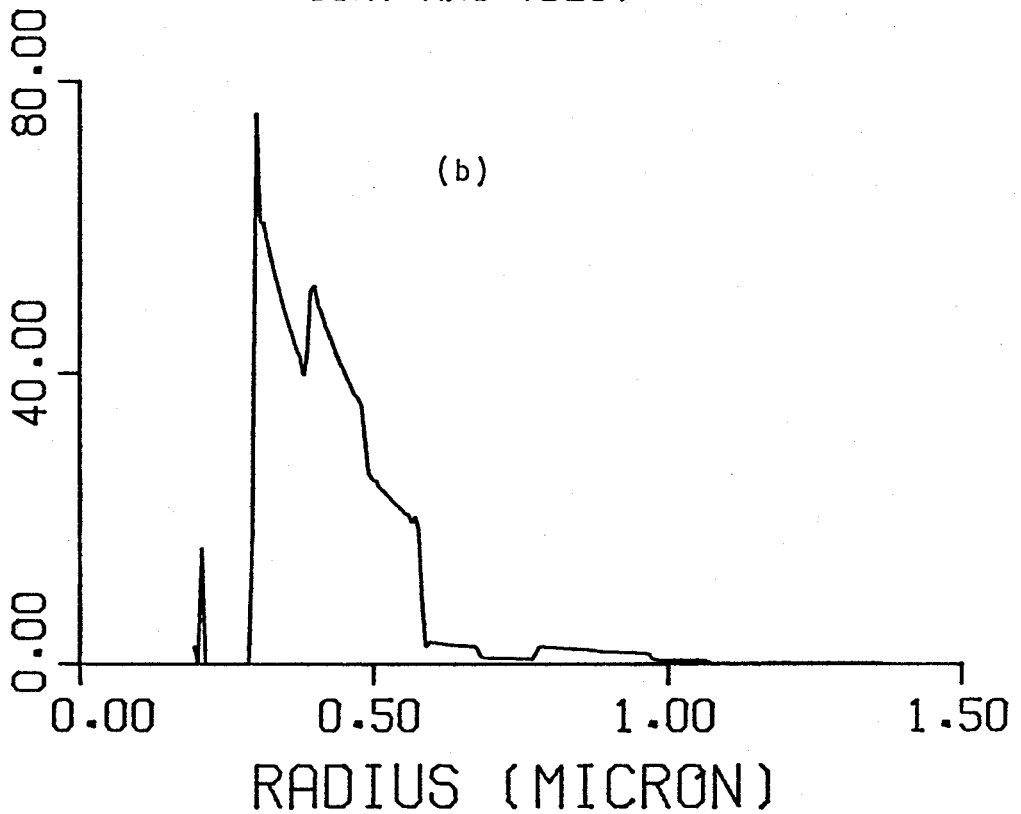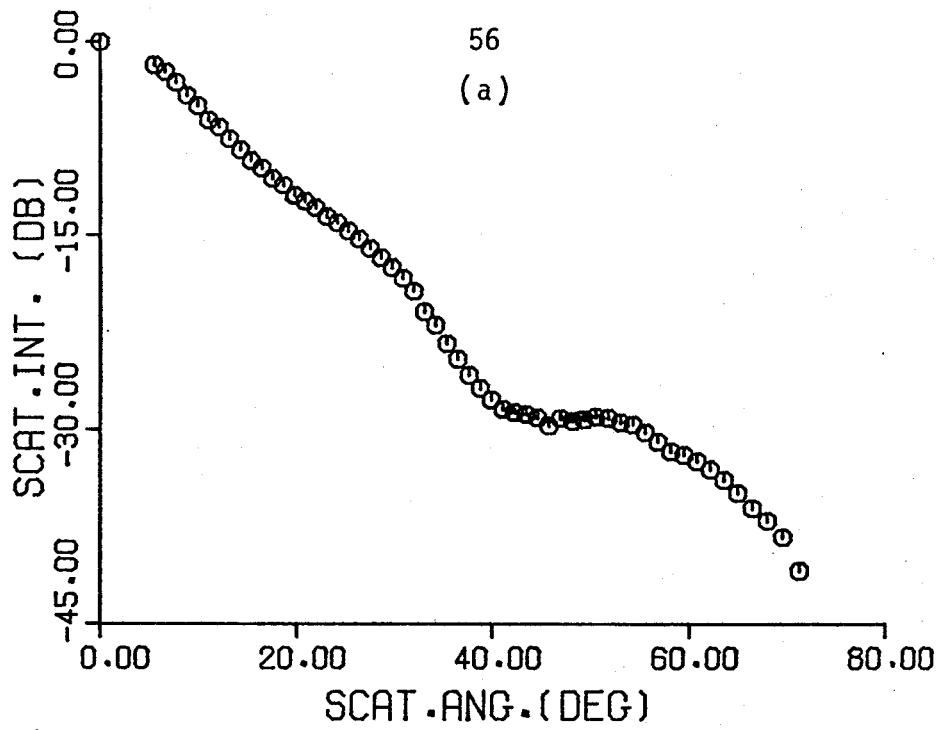
Fig.3-15 Size distribution of spherical bacteria,
Staphylococcus aureus : (a) measured
scattering pattern, (b) size dist.
N = 512, θ = 0° − 71.2°, n_r = 1.40
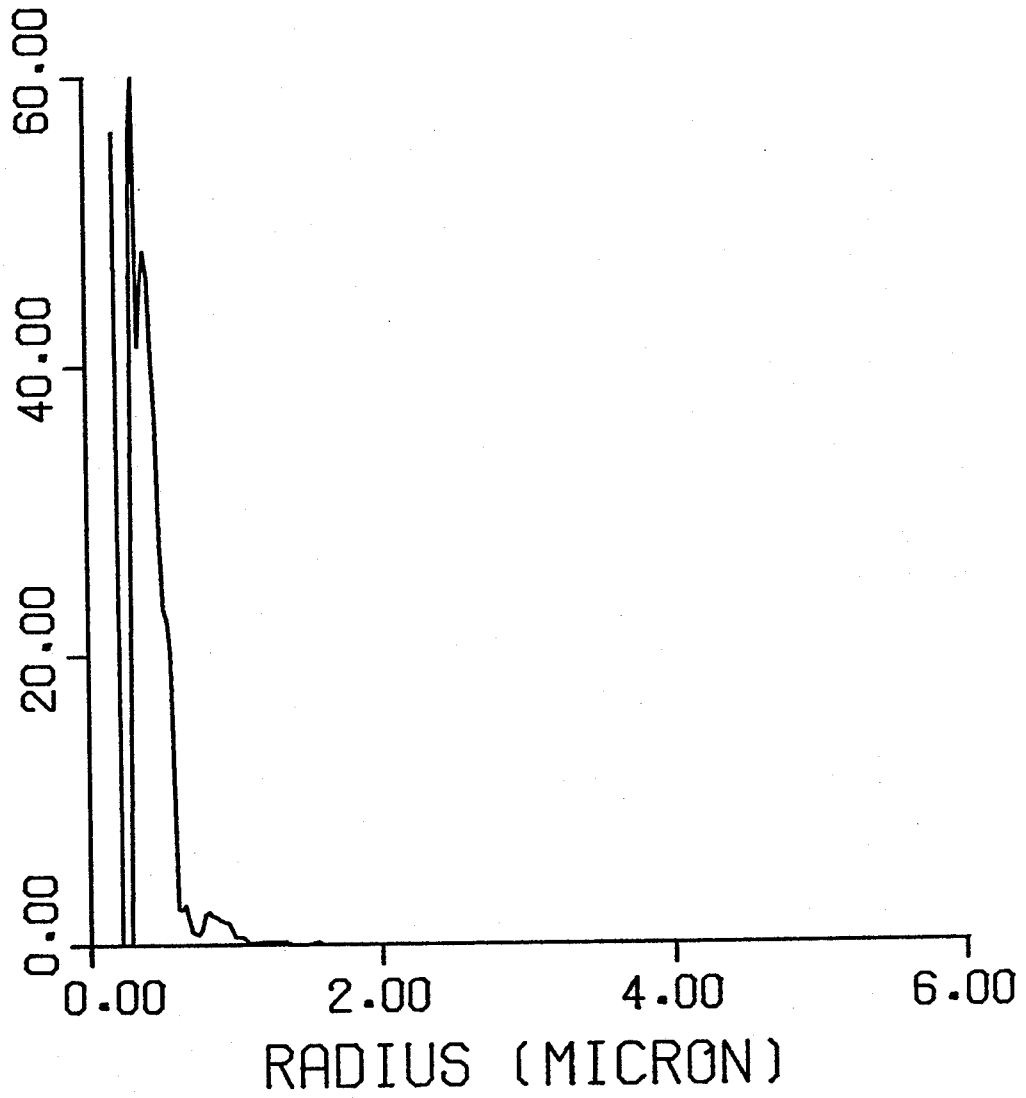
Fig.3-16 Large size region of *Staphylococcus aureus*
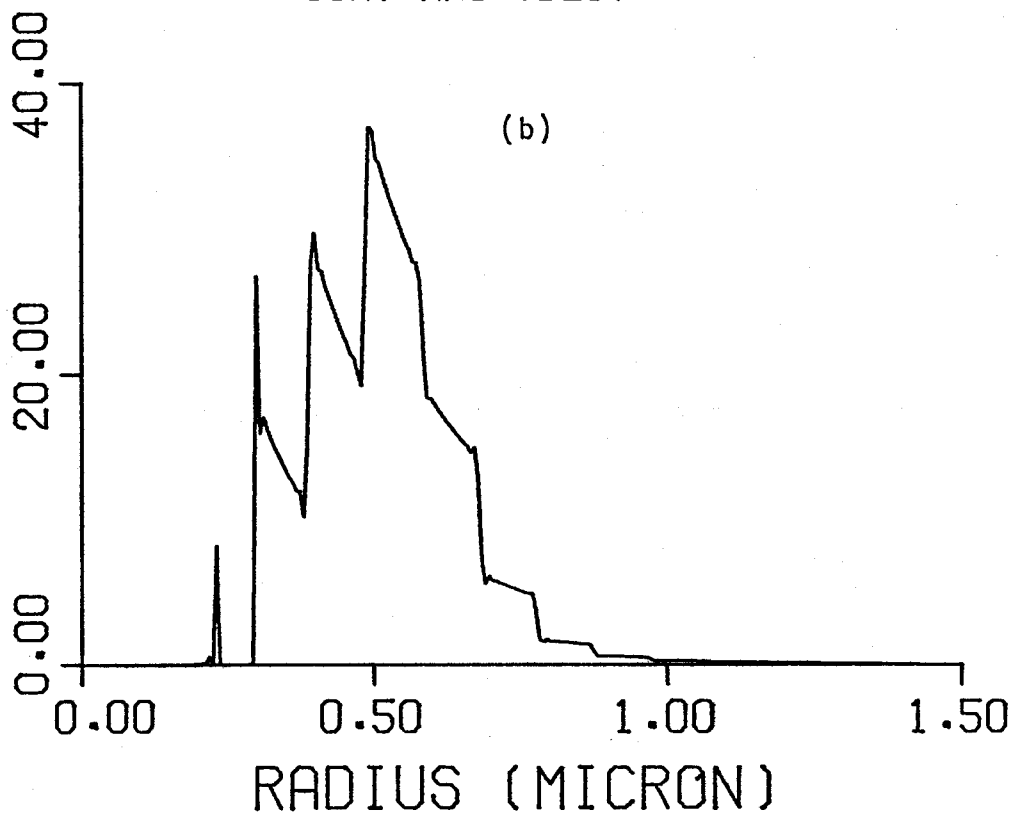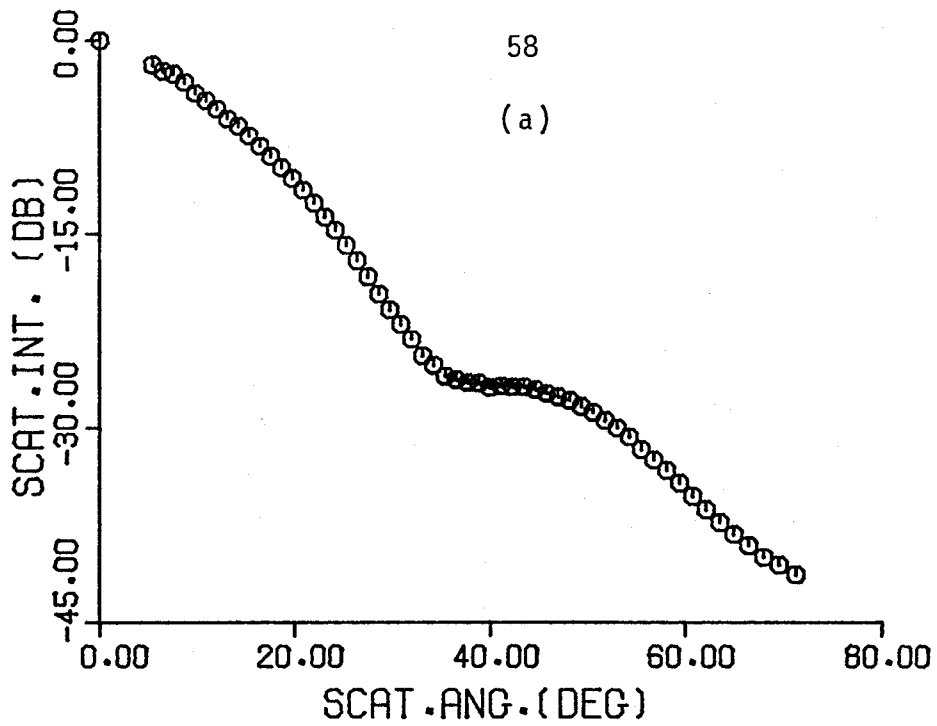
Fig.3-17 Size distribution of non-spherical bacteria,
Escherichia coli : (a) measured scattering
pattern, (b) size distribution
N = 512, Θ = 0° - 71.2°, n_r = 1.40
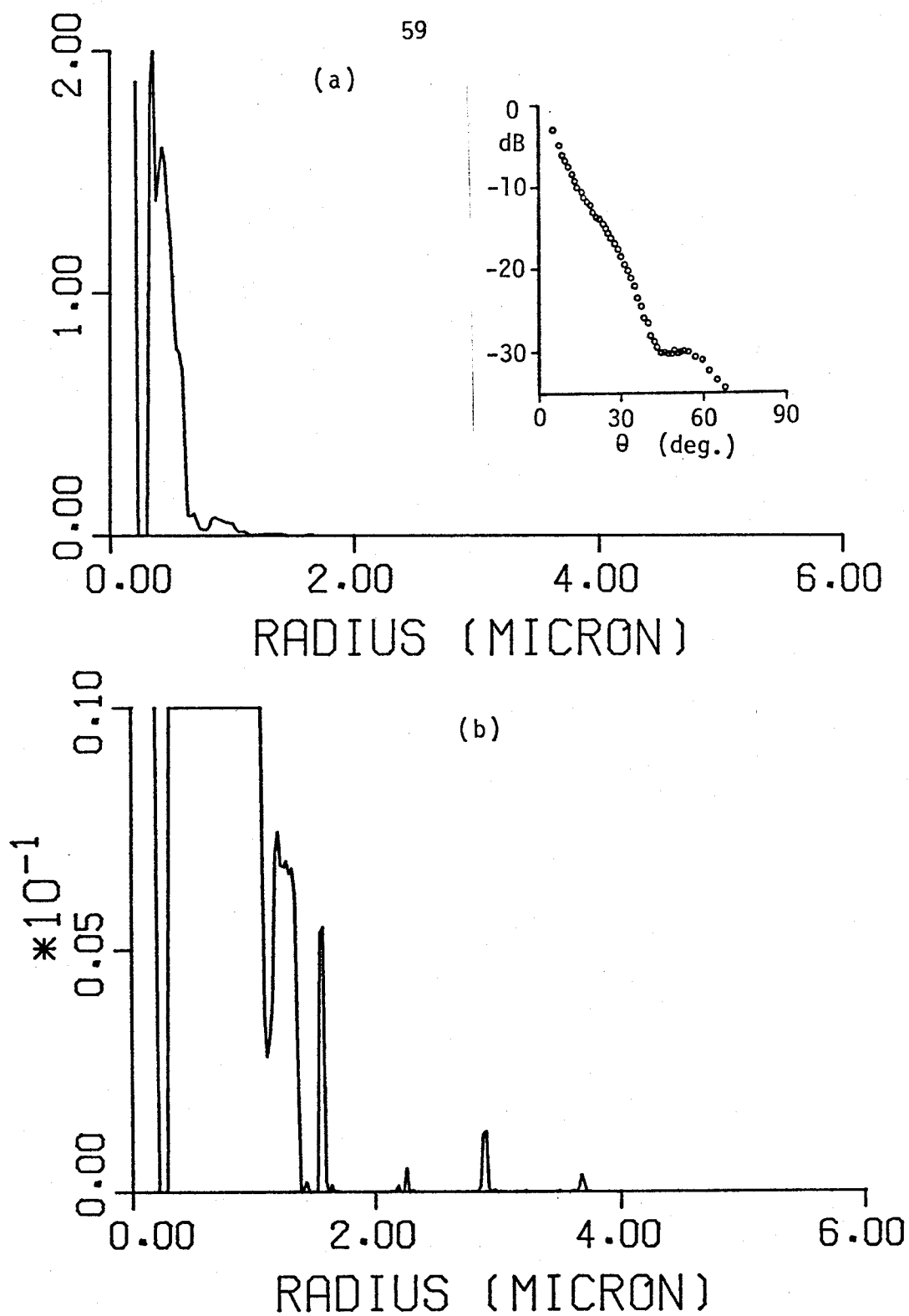
Fig.3-18 Effect of aggregation, *Staphylococcus aureus*
non-aggregated case :
(a) large scale, (b) small scale

60
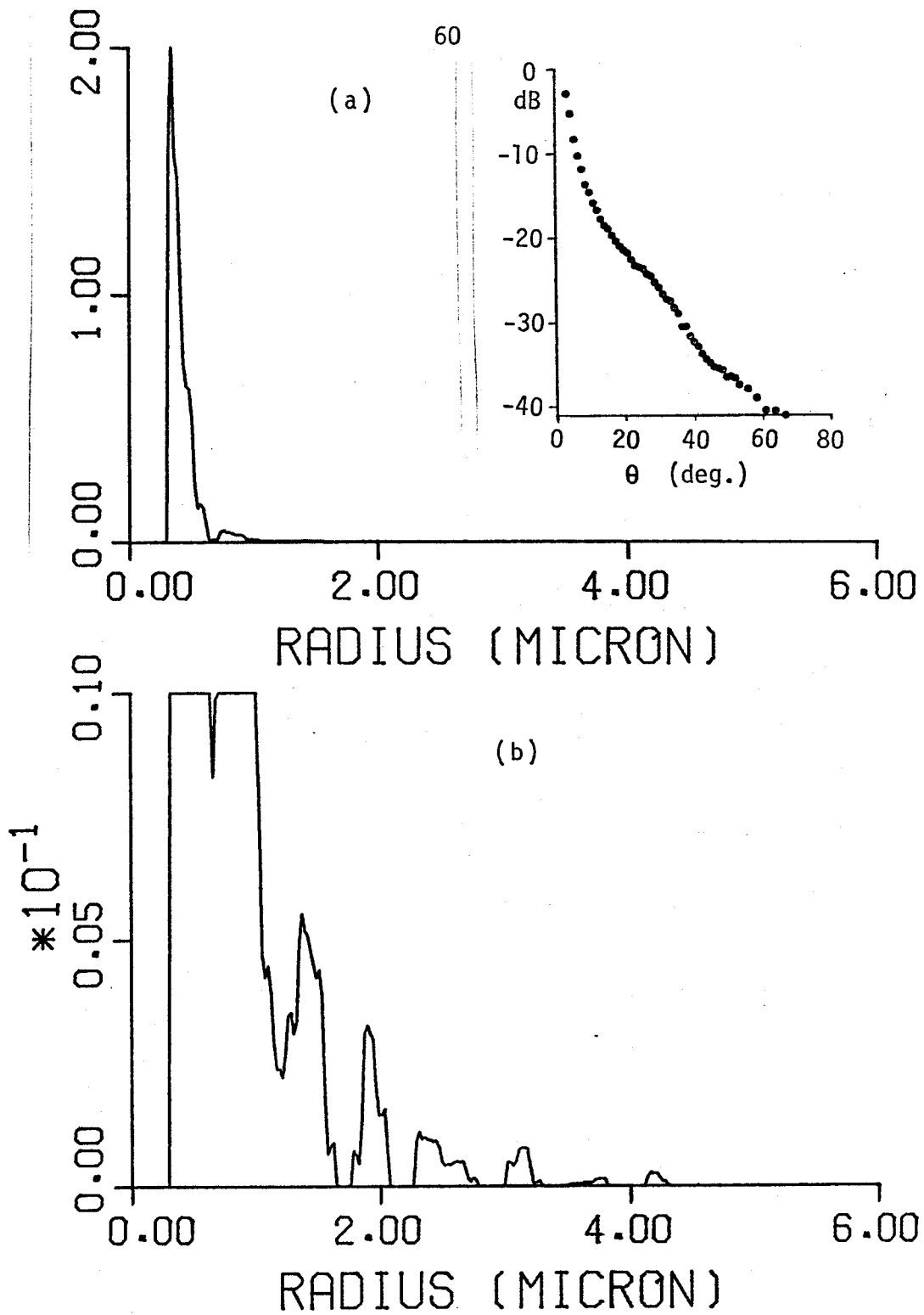
Fig.3-19 Effect of aggregation, *Staphylococcus aureus* aggregated by safranin :

(a) large scale, (b) small scale
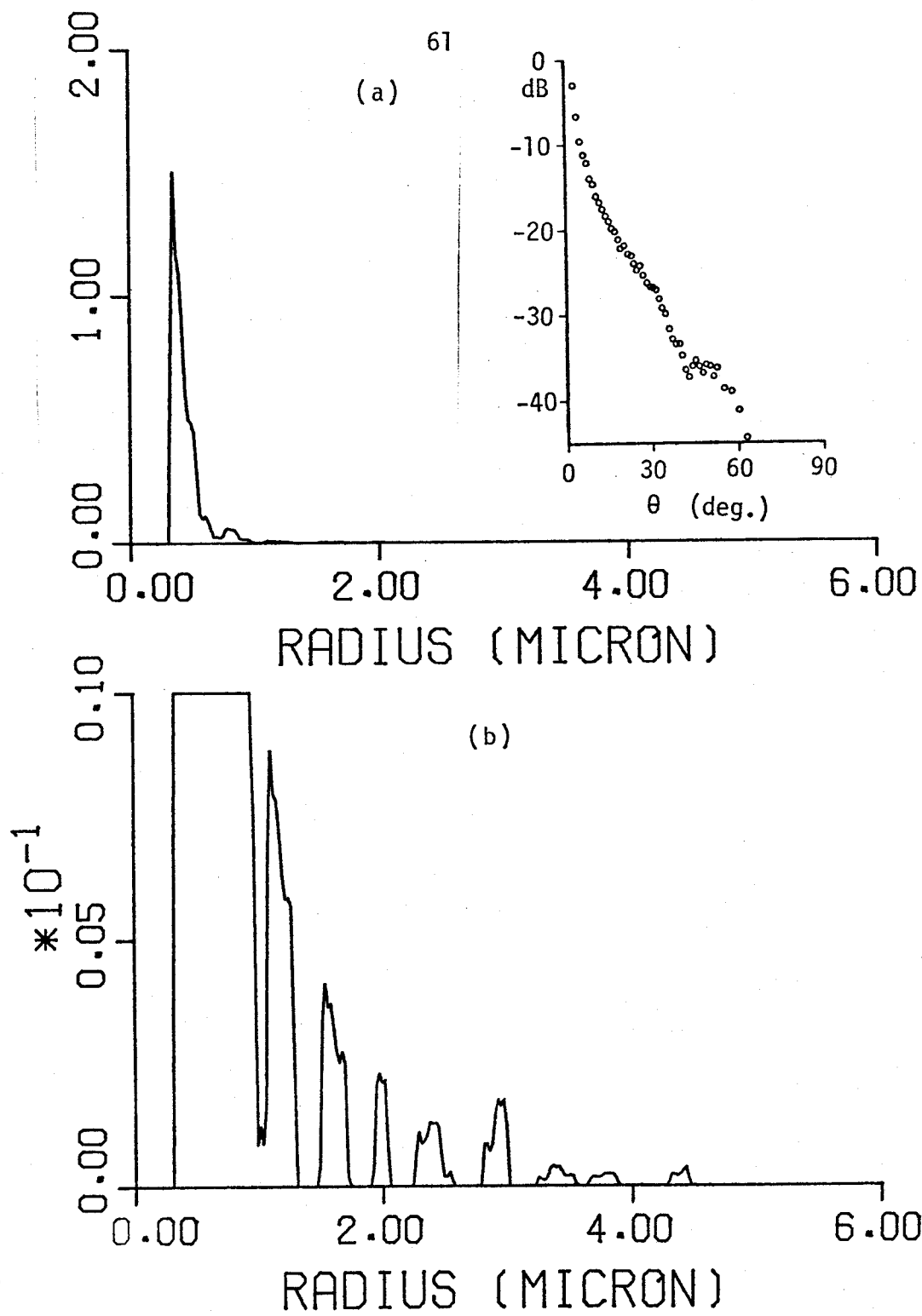
Fig.3-20 Effect of aggregation, *Staphylococcus aureus*
aggregated by methylene blue :
(a) large scale, (b) small scale

CHAPTER IV

BACKWARD SCATTERING PATTERN ANALYSIS WITH RANGE-GATING TECHNIQUE

IV.1   INTRODUCTION

During the past few decades, the usefulness of scattering pattern analysis for the size estimation of scatterers has been recognized and various applications have been devised (Kerker, 1969, p. 311). However, as was discussion in Section III.1, there are many areas left for further progress, which include the facilitation of the backward scattering pattern analysis.

In Chapter III, we discussed an inversion technique which determines the size distribution of scatterers from the scattering pattern in the forward angles. In practice, however, backward scattering pattern (θ = 90° - 180°) is often preferable to the forward scattering pattern (θ = 0° - 90°) due to the geometrical restrictions of the object such as an eye, atmosphere at high altitude, ocean, stars, etc. Although it is useful, the measurement of backscattering has its own difficulties. They are, for example, the low-signal level, specular reflections, susceptibility to extraneous or spurious scatterings, etc. The ultrafast sampling capability of the optical range-gating technique is applied to overcome these difficulties and utilize the advantages of the backward scattering pattern analysis.

As discussed in detail in Chapter I, the optical range-gating technique is a technique whereby the separation between scattering or reflecting objects can be measured at a distance, with a resolution

of the order of a millimeter (Duguay, 1971), (Bruckner, 1976). If the scatterers are cataract particles in an eye, a variety of back-scattered pulses will be observed. The refractive index changes characteristic of the various tissue layers give rise to specularly reflected pulses.

Cataracts and other opacities consist of microscopic random fluctuations in the index of refraction of the lens tissue, with dimensions on the order of the wavelength of light. The intensity of light scattered at a given angle by these fluctuations is a function of the mean size of the scattering inhomogeneities and the shape and width of the size distribution. By application of Mie scattering theory the size parameters of the scattering particles in the cataract or other opacity can be determined (Kerker, 1969, p. 311). The picosecond gating technique allows one to observe the scattering from only the desired depth in the eye while rejecting light scattered by foreground or background tissue.

In this chapter, the application of the range-gating technique to the backward scattering pattern measurement is discussed with a view toward the remote sensing of the cataract microstructure. This technique has been successfully applied to the investigation of microwave induced cataracts (Bruckner, 1978a, 1978b).

IV.2   THEORY

IV.2.1   Range-Gating for Tenuous Medium

The integral equation formulation for the equation of transfer
has been obtained by (Ishimaru, 1978a, p. 161). For pulse propaga-
tion problems in a tenuous medium, it can be modified so as to include
the time dependence, i.e.,

$$I(\bar{r},\hat{s};t) = I_{ri}(\bar{r},\hat{s};t) + I_d(\bar{r},\hat{s};t) \tag{4-1}$$

$$I_{ri}(\bar{r},\hat{s};t) = I_i(\bar{r}_o,\hat{s})e^{-\rho\sigma_t s} \tag{4-2}$$

$$I_d(\bar{r},\hat{s};t) = \int_0^s ds_1 e^{-\rho\sigma_t(s-s_1)} \rho \int_{4\pi} d\Omega' \mid \bar{f}(\hat{s},\hat{s}') \mid^2$$
$$\times I(\bar{r}_1,\hat{s}';t - \frac{s-s_1}{C}) \tag{4-3}$$

where I, I_{ri} and I_d are the total (specific) intensity, the reduced
incident intensity and diffuse intensity, respectively. They are func-
tions of the position $\bar{r}$, direction of the unit vector $\hat{s}$, and time t .
$I_i(\bar{r}_o,\hat{s})$ is the incident intensity at the point of incidence $\bar{r}_o$, ρ
is the number density of scatterers, σ_t is the total cross section,
s is the distance along the detection line, $d\Omega'$ is the elementary solid
angle in the direction $\hat{s}'$, C is the velocity of light in the medium,
and $\bar{f}(\hat{o},\hat{i})$ is the scattering amplitude vector when a wave is incident
and scattered in the direction of unit vectors $\hat{i}$ and $\hat{o}$.

Note that the inclusion of the time-dependence here is different
from what is to be discussed in the later chapter (Chapter V) for the
dense medium. Here, since the medium is tenuous, it is assumed that

the pulse propagates without the significant change in its spectral composition. In other words, the incident pulse propagates with the attenuation due to absorption and scattering but not with the change in the shape such as pulse broadening and tailing. Throughout this thesis, the equation of transfer for each case is distinguished by the terms "time-dependent" and "two-frequency," respectively.

Fig. 4-1 shows the geometry of the problem. An incident light propagates in the $\hat{z}$-direction and the light scattered is observed by the detector in the backward direction at the angle θ. Since the detector is designed to have a very narrow receiving pattern, the received signal is proportional to the specific intensity I_d.

If the incident wave is a plane wave impulse, the reduced incident intensity is given by

$$I_{ri}(\bar{r},\hat{s};t) = F_i \; \delta(z - ct)e^{-\rho\sigma_t z} \; \delta(\hat{s} - \hat{z}) \tag{4-4}$$

where F_i is the flux density. According to the first order multiple scattering approximation, the total intensity in Eq. (4-3) is approximated by I_{ri}. Then we get the diffuse intensity

$$I_d(\bar{r},\hat{s};t) = F_i \frac{\rho|\bar{f}(\hat{s},\hat{z})|^2}{1 + \cos\theta} \; e^{-\rho\sigma_t ct} \tag{4-5}$$

The range-gating shutter is synchonrized so that it samples the light intensity scattered at the crossing point of the propagation path of the incident pulse and the line (actually the cone) of acceptance of the detector. The signal intensity we receive is given by the
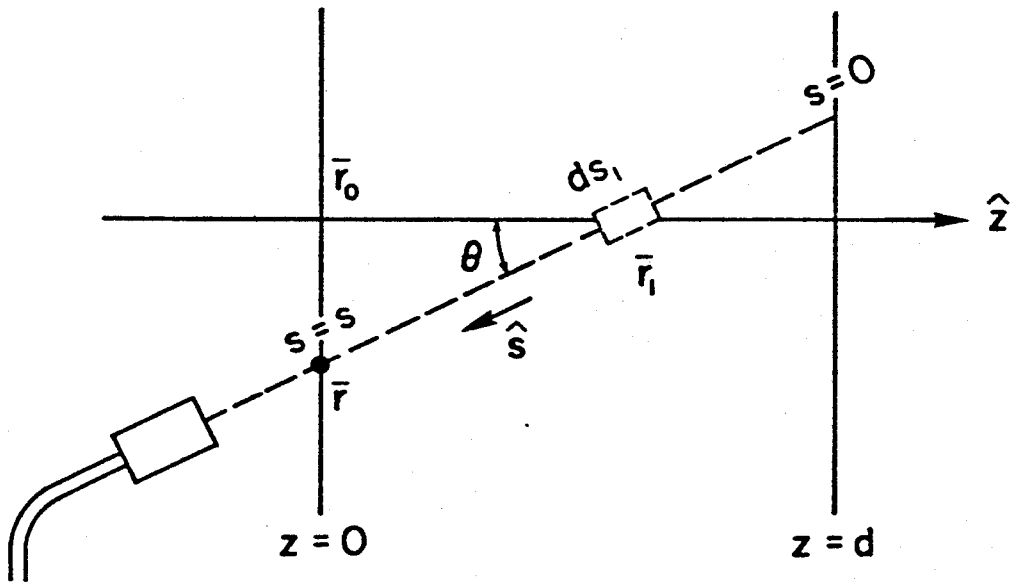
Fig.4-1 Geometry of the problem
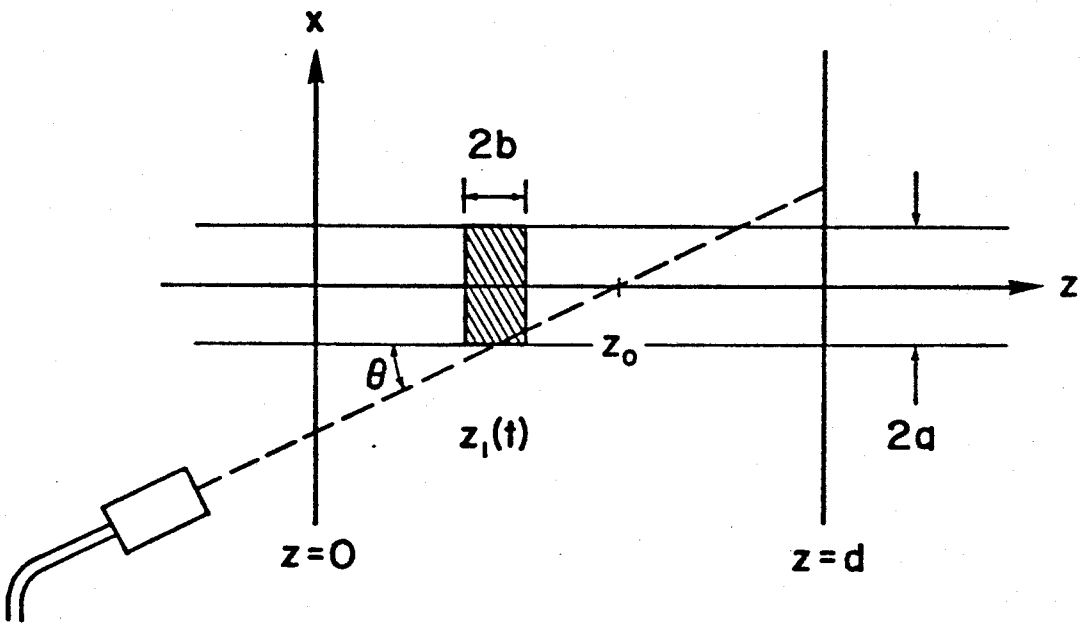
Fig.4-2 Geometry of measurement systm

convolution of the diffuse intensity I_d and the function of the shutter opening time. Assuming that the sampling time of the shutter is the delta function at t_o , we get the receiving intensity

$$I_{rec}(\bar{r},\hat{s}) = \int_0^\infty I_d(\bar{r},\hat{s};t)\delta(t - t_o)dt = F_i \frac{\rho|f(\hat{s},\hat{z})|^2}{1 + \cos\theta} e^{- \rho\sigma_t ct_o} \quad (4-6)$$

If the range-gating is not applied, or the shutter is kept open, the receiving intensity becomes

$$I_{rec}(\bar{r},\hat{s}) = \int_0^{t_d} I_d(\bar{r},\hat{s};t)dt = F_i \frac{|\bar{f}(\hat{s},\hat{z})|^2}{1 + \cos\theta} \frac{1}{\sigma_t c} (1 - e^{- \rho\sigma_t ct_d}) \quad (4-7)$$

where t_d = d/c , the time when the incident pulse leaves the slab of scatterers.

VI.2.2   Scattering Pattern Measurement with Range-Gating

Fig. 4-2 illustrates the geometry of the measurement system. A beam of an incident pulse impinges on a slab of tenuous scatterers with the thickness d . The incident pulse is approximated by a rectangular parallelopiped with the beamwidth 2a and the pulse length 2b . Then, the reduced incident intensity is given by

$$I_{ri}(\bar{r},\hat{s};t) = F_i \text{ rect}(x,a) \text{ rect}(z - ct,b) e^{- \rho\sigma_t z} \delta(\hat{s} - \hat{z}) \quad (4-8)$$

where rect (x,a) = 1 for $|x| \le a$ and 0 for $|x| > a$. By the first order multiple scattering approximation, we get the diffuse intensity

$$I_d(\bar{r},\hat{s};t) = F_i \rho |\bar{f}(\hat{s},\hat{z})|^2 \int_0^s ds_1 \, rect(x_1,a) rect(z_1 + s - s_1$$

$$- ct,b) exp\{ - \rho\sigma_t(z_1 + s - s_1)\}$$

$$= F_i \rho |\bar{f}(\hat{s},\hat{z})|^2 \int_{z_0-b}^{z_0+b} \frac{dz_1}{cos\Theta} exp\{ - \rho\sigma_t(1 + \frac{1}{cos\Theta})z_1\}$$

$$= F_i \frac{|\bar{f}(\hat{s},\hat{z})|^2}{\sigma_t(1 + cos\Theta)} 2e^{-\rho\sigma_t ct} sinh\{\rho\sigma_t(1 + \frac{1}{cos\Theta})b\} \quad (4-9)$$

where z_0 is the sampling position. As can be seen in Fig. 4-2, Eq. (4-9) holds only when the propagating pulse is in the view of the detector. That duration is, from the geometry:

$$t_0 - \Delta t \le t \le t_0 + \Delta t \qquad (4-10)$$

where $t_0 = \frac{z_0}{c} (1 + \frac{1}{cos\Theta}) \quad \Delta t = \frac{a}{c} \frac{1 + cos\Theta}{sin\Theta}$

Otherwise, $I_d(\bar{r},\hat{s};t) = 0$.

Therefore, when the range-gating is not used or the shutter is kept open, the receiving intensity is

$$I_{rec}(\bar{r},\hat{s}) = \int_0^\infty I_d(\bar{r},\hat{s};t)dt = \int_{t_0-\Delta t}^{t_0+\Delta t} I_d(\bar{r},\hat{s};t)dt \qquad (4-11)$$

This same equation also applies to the range-gated case, if the time duration $[t_0 - \Delta t, t_0 + \Delta t]$ is considered as the gating time. In the range-gated case, the shutter is synchornized so that the sampling time

$t_o = \dfrac{z_o}{c}(1 + \dfrac{1}{\cos\Theta})$ and $2\Delta t$ is the shutter open period. Usually,

$\Delta t \ll a(1 + \cos\Theta)/c\sin\Theta$. Thus, the received intensity is given by

the same equation for both the range-gated and the non-range-gated

cases, but with the different definitions for the parameter Δt.

That is,

$$I_{rec}(\bar{r},\hat{s}) = F_i \dfrac{4|\bar{f}(\hat{s},\hat{z})|^2}{\rho\sigma_t^2 c(1 + \cos\Theta)} e^{-\rho\sigma_t ct_o} \sinh\{\rho\sigma_t(1 + \dfrac{1}{\cos\Theta})b\}$$

$$\sinh(\rho\sigma_t c\Delta t) \qquad\qquad (4\text{-}12)$$

where $\Delta t = a(1 + \cos\Theta)/c\sin\Theta$ for the non-range-gated case and Δt

is half the shutter open period for the range gated case. The former

is typically $20 \sim 100$ psec for $\Theta = 5° \sim 30°$ and the latter is $5 \sim 10$

psec.

Since $\rho\sigma_t(1 + \dfrac{1}{\cos\Theta})b \ll 1$ and $\rho\sigma_t c\,\Delta t \ll 1$ for the tenuous

medium. Eq. (4-12) can be approximated by

$$I_{rec}(\bar{r},\hat{s}) = F_i \dfrac{\Delta t}{\cos\Theta} 4b\rho|\bar{f}(\hat{s},\hat{z})|^2 e^{-\rho\sigma_t ct_o} \qquad\qquad (4\text{-}13)$$

where $\sinh x \approx x$ for $|x| \ll 1$. Here, $|\bar{f}(\hat{s},\hat{z})|^2 = \sigma_d(\Theta)$ is the

differential cross section or the scattering pattern of the scatterers.

Therefore, with the correction for the term $\Delta t/\cos\Theta$, the scattering

pattern is obtained by measuring the signal intensity varying the angle

of the detector Θ. It should be noted that for the measurements of

$\Theta = 2° \sim 30°$, the effect of the correction factor is large in the

non-range-gated case ($\Delta t/\cos\theta = a(1 + \cos\theta)/(c\ \sin\theta\ \cos\theta) = 57.3\ a/c$ $\sim 4.31\ a/c$) but little in the range-gated case ($1.00\ \Delta t \sim 1.15\ \Delta t$).

IV.3   EXPERIMENTS

IV.3.1   Experimental Facility

The experimental apparatus is illustrated schematically in Fig. 4-3. The principal parts of the system were designed by Dr. A. P. Bruckner. An outline of its operation is as follows. A mode-locked Nd:glass laser generates a train of horizontally polarized infrared pulses (λ = 1.06 μm), each of ~10 psec duration and carrying a peak power density of up to ~500 MW/cm^2. Frequency doubling occurs in a KDP crystal adjusted to yield ~0.1% conversion efficiency. This limits the energy of the resulting green pulse train to ~1 mJ. The green pulses (0.53 μm) are separated from the infrared pulses by a dichroic beam splitter, DBS. The vertically polarized green pulses are directed toward the scatterers contained in the scattering cuvette, SC. Filter GF absorbs residual infrared and neutral density filter NF_1 reduces the intensity to the desired level. Lens L_1 (f.l. 20 cm) focuses the green beam to a point in front of the SC such that the beam diverges slightly to a 2 mm spot size at the SC.

An array of fiber-optic light guides FO, mounted in a goniometer, collects the light scattered from the scatterers at several selected angles to the incident illuminating beam. The scattered light is coupled into the individual fibers and directed to the ultrafast Kerr shutter, SHUT. A part of the incident beam is sampled by a beam splitter, BS_1, and directed by a mirror M_1 toward one of the light guides to provide a reference signal of the incident power. Using
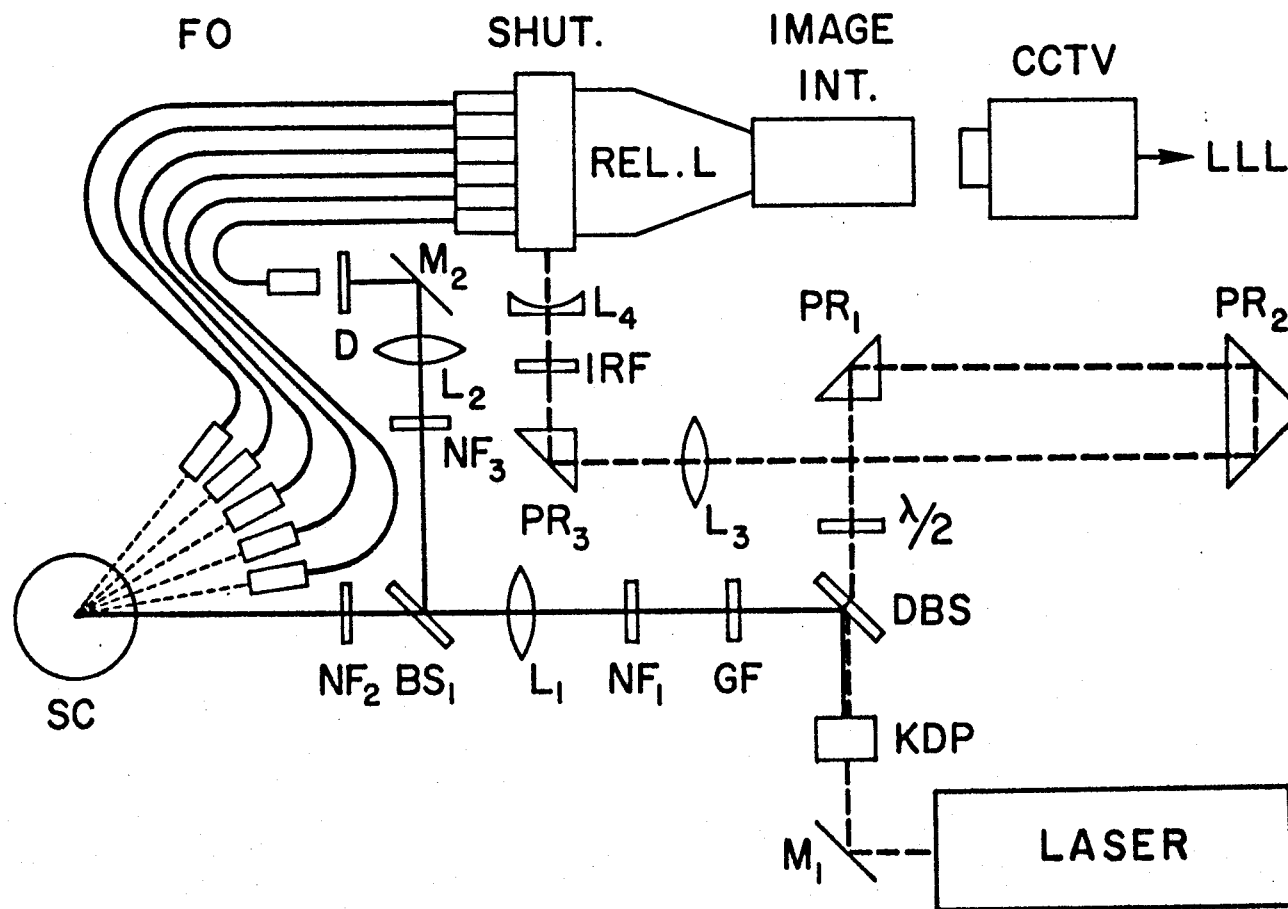
Fig.4-3 Schematic of range-gated backward scattering pattern measurement

three neutral density filters NF_1, NF_2 and NF_3, the intensities of incident and reference beams can be controlled appropriately. The lens L_2(f.1. 3.9 cm) focuses the reference beam on the translucent diffuser D placed in front of the reference fiber. They minimize the error in measuring the reference signal due to a spatial fluctuation of the reference beam. The output of all the fibers are fed to the ultrafast shutter SHUT.

The shutter is driven by the vertically polarized infrared pulses generated by the laser. These pulses, after passing through KDP, DBS and $\lambda/2$, traverse a variable optical delay line, PR_1-PR_3 to equalize the infrared and green pathlengths and thus assure proper gating synchronization. A half-wave retardation plate $\lambda/2$ rotates the polarization of the infrared pulses into the vertical plane. Lenses L_3 (f.1. 20 cm) and L_4(f.1.-5.3 cm) collimate the pulses to ~2 mm diameter in the shutter cell. The filter IRF prevents stray light from coming in the shutter. The shutter consists of a rectangular quartz cell containing carbon disulfide (CS_2) placed between two crossed polarizers. The electric field associated with each infrared pulse induces a narrow zone of birefringence in the CS, which makes a narrow transparent zone through the crossed polarizers. This transparent zone travels across the lines of sight of the fiber-optics at the speed of light. Thus, the shutter produces a streak record of the light pulses incident at right angles to the infrared path.

The shortest fiber is 50 cm long and the lengths of the remaining fibers are staggered by 5.8 mm, such that the arrival of a scattered

pulse from a given location in the scattering medium coincides with the arrival of the infrared gating pulse at the appropriate location along the shutter. This synchronization is attained by adjusting the movable prism PR_2 to vary the delay of the infrared gating pulse.

The shutter output is detected and processed by the low-light-level video system LLL, which includes relay lens REL.L, image intensifier IMAG.INT., CCTV camera and so on. The output of LLL is recorded on polaroid film. Fig. 4-4 is an example of the recorded signal. Each peak is the gated signal from the corresponding optic fiber. The heights of the peaks represent the incident (--Ref) and scattered intensities ($---\Theta_i$) at the corresponding scattering angle.

IV.3.2   Specifications of Apparatus

(a) Optical Bench

All the components shown in Fig. 4-3 are mounted on a 2'x4' stainless steel honeycomb table manufactured by Newport Research Corp.

(b) Laser System

As a source of the infrared pulses, Nd:glass laser system (Apollo Laser, Inc., Model 42) is used. The water-cooled laser head contains a 6" long helical flashlamp which pumps a 1/2" dia x 8" long brewster-cut, Owens-Illinois type ED-2 Nd:Glass rod. Coolant circulation is accomplished by a Neslab RTE-4 refrigerated circulator. The resonant cavity consists of a 35%R flat output reflector and a 4.65 m radius concave 99%R rear reflector, spaced approximately 70 cm apart. Mode-locking is accomplished by Eastman 9860 dye in contact with the rear
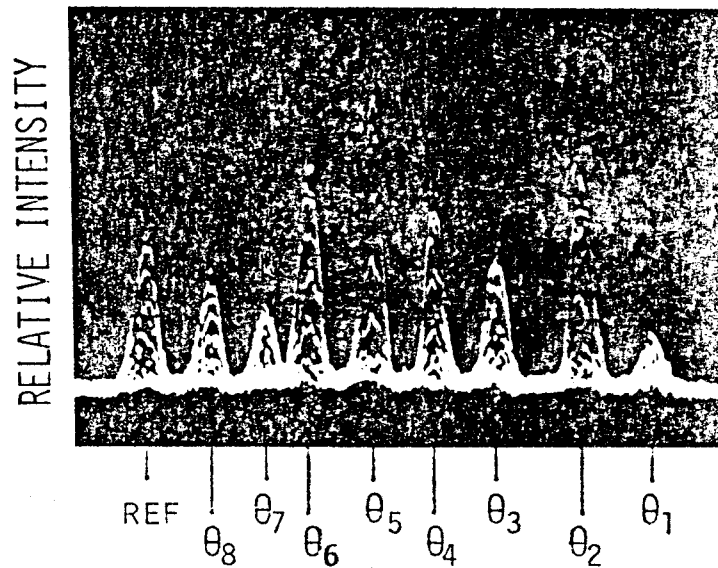
Fig.4-4   Typical data format :   Each peak is the gated signal
from the corresponding fiber optic. The target in
this case is a white diffusing reflector which serves
as a calibration standard. Unequal signal amplitudes
result from inequalities in fiber optic coupling
coefficients. This picture is used to normalize all
other scattering data. ; $\lambda = 0.53$ m, $\theta_1 = 178.25°$,
$\Delta\theta = -1.75°$.

reflector. Dye thickness is 1 mm. A temperature controlled dye pumping system circulates the dye through the dye cell. This flowing contacted dye configuration produces the most reproducible output and prolongs the useful life of the dye.

As delivered, the laser had the dye cell at the front (output) reflector. However, in this configuration the mode-locking was highly irreproducible. The 1.06 μm output of the laser consists of a train of 50-100 pulses, each of 10-20 psec duration, spaced at 4.6 nsec intervals. The peak power density per pulse is of the order of 300-500 MW/cm^2.

(c) Fiber Optic Light Guides

The fibers are multimode clad quartz, with 100 μm core diameter and 0.14 numerical aperture. They are protected in stainless steel hypodermic tubing. Input and output couplers are brass cylinders supporting coupling lenses of 4 mm diameter and 21 mm focal length. The input couplers are mounted on a goniometer as a detector array and observe a scattering volume at 15 cm from the array. The angular separation of the detectors are 1.83°. The output couplers feed the light signal to the ultrafast shutter. In later experiments the number of the light guides was decreased from 9 to 6 by eliminating the guides with poor performance. The observable scattering angle extends from 178° to 150° by rotating the goniometer in which the detector array was mounted.

(d) Ultrafast Shutter

The Kerr shutter assembly consists of the CS_2 cell between crossed

polarizers put in a 2.75" x 2.75" x 1" black painted steel box. The CS_2 is contained in a 50 mm pathlength quartz spectrophotometric cell which has been annealed to minimize residual stress birefringence in the walls. A mask is interposed between the fiber-optic output couplers and the quartz cell. It has a series of vertical slots, with 2 mm widths and 4 mm heights, through which the signals to be gated must pass. Its purpose is to improve the temporal gating resolution of each fiber output by decreasing the horizontal aperture of the pulses to be gated.

The peak transmission factor is approximately proportional to the square of the infrared intensity, and has been measured to be $\sim 1\%$, with an on-off contrast ratio of > 1000 in the present case. The output couplers of the fiber-optic light guides are arranged on 5.2 mm centers at the shutter; thus the sampling interval between adjacent fibers is ~ 28 psec.

The sampling time resolution of the ultrafast shutter is governed by the duration and transverse dimension of the infrared gating pulse (Bradley, 1974) and by the apertures of the fiber-optic output lenses in the direction parallel to the IR path. The convolution of the birefringent zone induced by a 2 mm dia, 10 psec gating pulse with the 2 mm effective aperture of each output coupler results in a sampling time of ~ 15 psec per signal. This permits a ranging resolution of ~ 1.7 mm in an aqueous medium, i.e., only light scattered within a volume element ~ 1.7 mm long is transmitted by the shutter. Pulse broadening in the fibers is well under 10 psec (Sunak, 1974) and does not

significantly affect this resolution.

(e) Low-Light-Level Video System

A schematic diagram of the LLL system is shown in Fig. 4-5. The output of the shutter is relayed by a 135 mm f.1. lens to a three-stage, 18 mm RCA 4550 image intensifier tube. The intensifier output is imaged by a Telemation TMC-1100 video camera equipped with an RCA 4532A silicon vidicon tube. The video signal is processed by a control unit built in-house. An image of the gated signals, with a superimposed rectangular frame of variable height and width, appears on a CCTV monitor. The intensity profile of each TV line within the frame is displayed on an oscilloscope. The video system is operated in the single-shot mode, in which only a single sweep of the vidicon and display oscilloscope occurs. A trigger output pulse from the control unit fires the laser at the start of the vidicon sweep. The dynamic range of this detector system is greater than 100. This is not high by present standards, but has proved to be adequate for our purpose.

(f) Scattering Cell

As scatterers, an aqueous suspension of latex spheres are contained in glass spectrophotometric cells. The cells of two types of geometry are used. One type is a vertical cylinder with 28.6 mm internal diameter and 30 mm height. With this cell a collimated beam impinges upon the curved side wall of the cylinder. Its incidence is normal and the beamwidth ($\sim$ 2.5mm) is much smaller than the radius of curvature of the wall (14.3 mm). Thus the refraction and the focusing effect of the incident beam is negligible. As for the
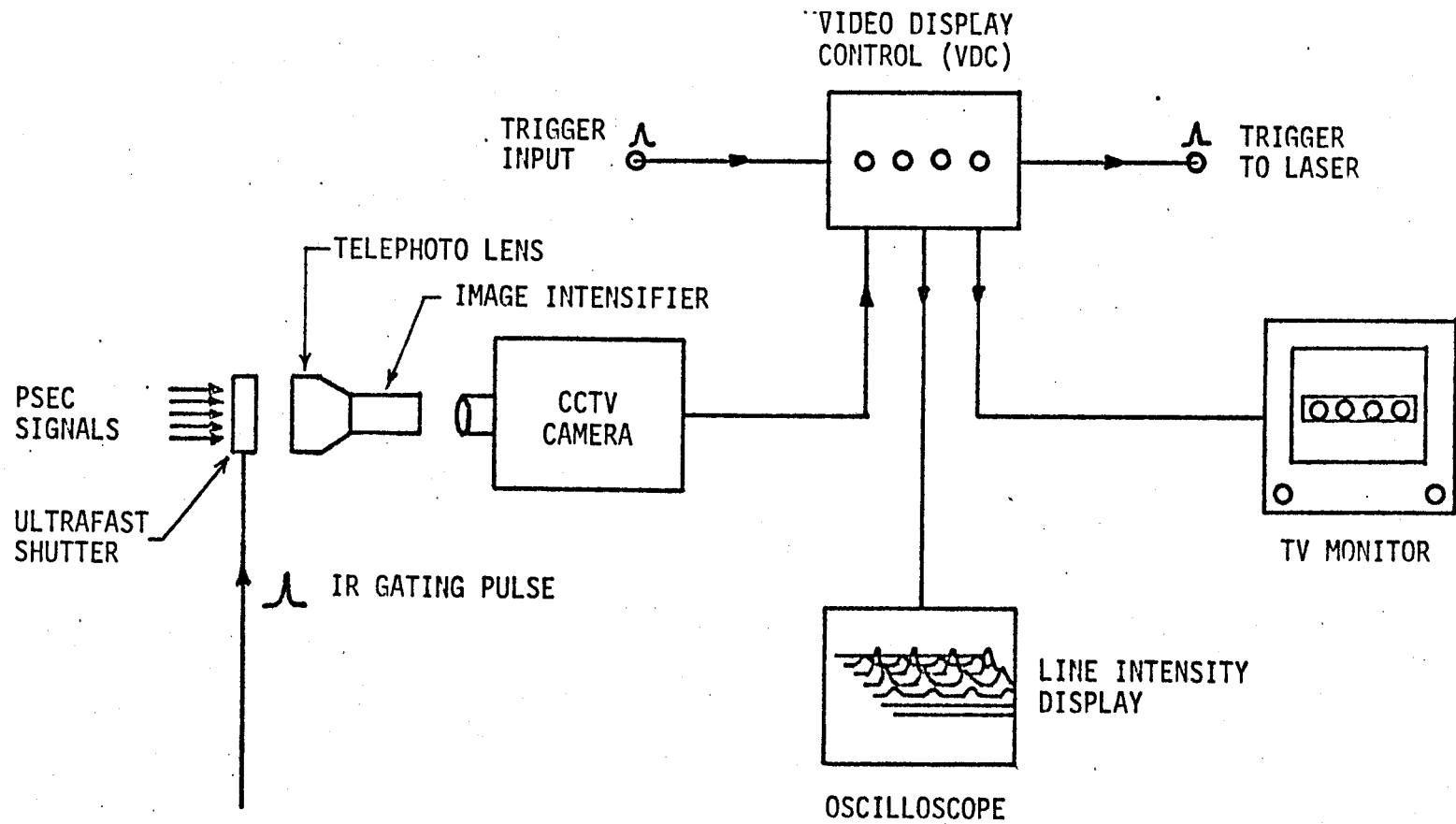
Fig.4-5 Schematic of Low-Light-Level video detector system

scattering angles, due to the circular circumference, the correction for the refraction at the air-glass-liquid interfaces is not necessary, either. Therefore, this cell is used for the scattering pattern measurements discussed in Chapters IV and VI.

Another type of the cell is a standard flat window horizontal cylinder with 20 mm internal diameter and 50 mm pathlength. An incident wave impinges normally upon the flat end of the cylinder. Although it needs the correction for the refraction of the scattering angles, the simple geometry makes the analysis easier, particularly for the dense medium. It also enables the plane wave incidence. Thus, this cell is used for the experiments in Chapters VII and VIII.

IV.3.3   Tuning of System

The "tuning" of the system consists of adjusting the path lengths of the IR and green beams such that the IR gating pulses arrive in the shutter at the proper time to sequentially gate the scattered green pulses emerging from the fiber optics. A white diffusely reflecting plane target was placed 15 cm from the detector array and normal to the incident light path. The relative signal delays of the light guides were fine-tuned by moving the output couplers toward or away from the shutter in small increments until the gated signal from each fiber was maximized. The IR pulse delay was adjusted by means of the movable prism, PR_2 , shown in Fig. 4-3. To avoid saturation of the image intensifier, the incident train of green pulses was attenuated by a factor of 10^{-3} by means of neutral density filters.

IV.3.4 Calibration of System

The system is calibrated with the same plane diffuse target. Fig. 4-4 shows a typical result from a calibration test. The first eight peaks from the right are the gated signals from the corresponding fiber-optics. The ninth peak on the extreme left is the signal from the reference fiber. The unequal amplitudes of the signals from the collecting fibers are primarily a result of inequalities in the fiber-optic coupling coefficients. These data, corrected for Lambert's law, are used to normalize the angular scattering data obtained with other scattering media. The method of the normalization is described quantitatively in a later section (IV.3.7).

IV.3.5 Linearity of System Response

The linearity of the overall detection system, including the shutter, was tested by varying the intensity of the green pulses incident on the plane diffuse target by means of neutral density filters. Both with and without range-gating, the response to the signals from each fiber-optic was found to be essentially linear over a two order of magnitude range below the saturation level of the vidicon tube. Departures from linearity below this range are not severe.

IV.3.6 Turbidity Measurement

In order to assure the correct dilution of the sample solutions of the scatterers, the turbidity of each sample was measured. The procedures and the principle of the measurement are given in Sections VI.2.3 and VI.3.4.

IV.3.7 Method of Normalization

As can be seen in the recorded signals shown in Fig. 4-4, the overall sensitivity of each signal channel is not uniform over the channels. To correct the nonuniformity, the following normalization method was employed. Fig. 4-6 illustrates the parameters necessary for the derivation. The heights of the recorded peaks for the signal and reference channels are given by

$$H_i = C_1 \, I_s(\Theta_i) \, \alpha_i \qquad i = 1, 2, 3 \ldots 8 \qquad (4\text{-}14)$$

$$H_r = I_0 \, k \, NF_3 \, \alpha_r \qquad (4\text{-}15)$$

where C_1 is a constant, I_s and I_0 are the scattered and original intensity respectively, Θ is the scattering angle, α is the attenuation coefficient of the light guide system, k is the reflection coefficient of the beam splitter, and NF_3 is the attenuation factor of the neutral density filter in the reference channel. The subscripts i and r represent the i-th channel and the reference channel.

The incident intensity I_{inc} impinging on the scatterers is related to the original intensity I_0 by,

$$I_{inc} = I_0(1 - k) \, NF_2 \qquad (4\text{-}16)$$

where NF_2 is the attenuation factor of the neutral density filter between the beam splitter and the scatterers.
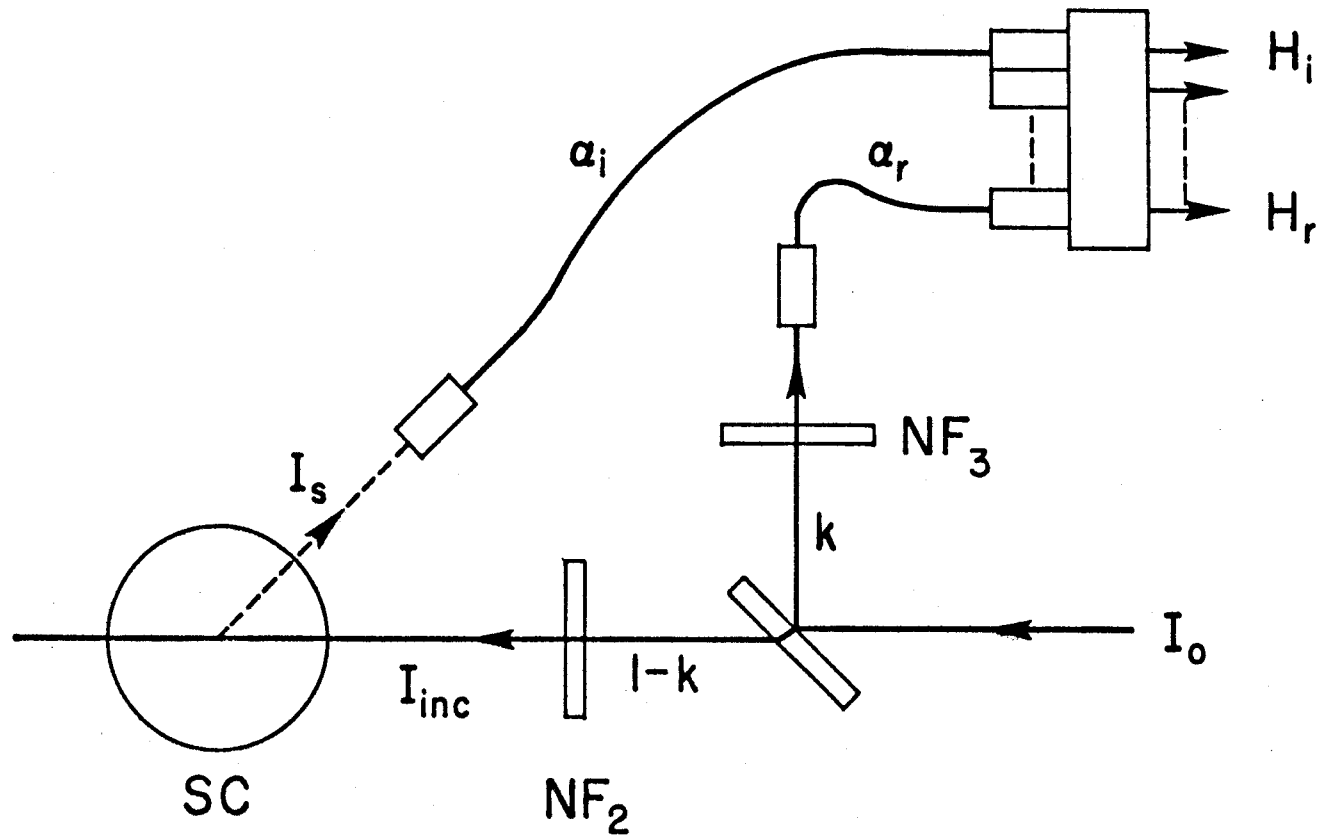
Fig.4-6 Parameters for normalization method

Substituting Eq.(4-16) into Eq.(4-15), relative scattered intensity can be written

$$\frac{I_s(\theta_i)}{I_{inc}} = \frac{H_i}{H_r} \frac{NF_2}{NF_3} \left/ \left(\frac{1-k}{k} \frac{\alpha_i}{\alpha_r} \right) \right.$$ (4-17)

Since the direct measurement of k and α's above is not as easy as that of the H's and NF's, the following two-step-normalization process was developed.

First, the denominator of Eq.(4-17) is obtained by measuring the scattered intensity from a white, diffusely reflecting plate. Assuming the plate is a uniform diffuser (Keitz, 1971, p. 106), the scattered intensity is given by Lambert's law,

$$I_s(\theta) = C_2 I_{inc} \cos\theta$$ (4-18)

where C_2 is a constant.
Substitution of Eq.(4-18) in Eq.(4-17) gives the denominator of Eq.
. It is called a channel attenuation ratio, CAR, i.e.,

$$C_2 \frac{1-k}{k} \frac{\alpha_i}{\alpha_r} = \frac{H_i}{H_r} \frac{NF_2}{NF_3} \left/ \cos\theta_i \right. \triangleq (CAR)_i$$ (4-19)

After determining the CAR, the relative scattered intensity from the sample scatterers is obtained in terms of the ratio of the recorded peaks' heights H_i/H_r , ratio of the neutral density filter NF_2/NF_3 , and the $(CAR)_i$:

$$\frac{I_s(\theta_i)}{I_{inc}} = \frac{H_i}{H_r} \frac{NF_2}{NF_3} \frac{1}{(CAR)_i} \qquad i = 1, 2, 3 \ldots 8 \qquad (4\text{-}20)$$

IV. 4   RESULTS AND DISCUSSION

IV. 4.1   Background Scattering

Prior to the scattering experiments with the particles the cell being used was filled with distilled water only, and the system was tested with this target to check on possible spurious background signals.

Fig 4-7(a) and (b) show the signals from the background solution with and without range-gating, respectively. See Section IV.3.1 for the interpretation of the recorded signal. They show the effectiveness of the ultrafast sampling technique to suppress the spurious scatterings. Note that the sensitivity for the range-gated case is 100 times as high as the non-range-gated case. The signals of observable intensity are confined in the angles near to the backward normal (180°). They may be attributed to the discontinuities of the refractive index at the air-glass-water interfaces. The specular reflection was eliminated already by tilting the scattering cell before the measurements.

The measured data presented in the subsequent discussions are those from which this background scattering has been subtracted. For most of the cases, the background signal is negligible compared with the scattered intensity from the particles.

IV.4.2   Backward Scattering Pattern

A representative set of angular scattering results obtained with particles of diameters 0.481 μm, 2.02 μm and 3.2 μm is shown in Figs. 4-8, 4-9 and 4-10, respectively. The particle concentrations

investigated in each case extend to considerably higher values than plotted in the figures, however only those are shown which retain the characteristic scattering patterns. The data obtained at higher concentrations are presented in Chapter VI. The graphs in the figures display the relative scattered intensity for vertical polarization as a function of the scattering angle for the indicated concentrations. The intensity scale is referenced to the unattenuated signal at the reference fiber. The scale in each case is relative and arbitrary and no comparisons between the intensities for different sizes is to be made. Each set of experimental points is the average of 3 to 5 shots of the laser. The standard deviation in intensity is approximately 10% for each point, while the uncertainty in scattering angle is ± 0.7°.

The solid curves superimposed on the data in each figure corresponds to the best-fit Mie theory modified for the size distribution of scatterers (Shimizu, 1978). This fit was obtained by assuming a Gaussian size distribution with a standard deviation σ , in the diameter d , of 0.37%, 7.0% and 5.9% for the 0.481, 2.02 and 3.20 μm latex spheres. The σ/d provided by the manufacturer is 0.37%, 0.67% and 5.9% respectively. The parameter m is the ratio of the refractive index of the particles to that of the water at λ = 0.53 μm.

In spite of the difficulties of backward scattering measurements mentioned before, the general agreement between the measurements and the Mie calculations are good. It should be emphasized that no special precautions had to be taken to minimize stray light during the

above experiments. The combination of ultrafast sampling and the sharply pointed receiving pattern of the detector block out all signals not originating in the region of interest. The effectiveness of this temporal and spatial noise-limiting function is further demonstrated in the next section.

In conclusion, these results suggest the applicability of this technique to the estimation of an average size of scatterers from the backward scattering pattern.

IV.4.3   Suppression of Spurious Scattering

To examine the effect of the range-gating, the scattering pattern measurements discussed above were repeated with the shutter kept open continuously by a quarter-wave plate to simulate the conditions of continuous wave (CW). Since, however, the incident wave is still a pulse, this non-range-gating case is called "quasi-CW" case. In this case, considerable difficulty was experienced with stray light, especially at lower concentrations and at the angles close to the backward normal.

A set of results for the quasi-CW case with 3.2 μm particles is shown in Fig. 4-11. The geometrical factor discussed in Section IV.2.2 was corrected already. It is seen by comparison with the range-gated case of Fig. 4-10 that the experimental data for the two different cases do not correlate with each other and that the non-range-gated case does not agree with Mie theory. This discrepancy is found to be attributed to the spurious reflections within the scattering cell.

In the range-gated case, only light within the desired focal volume at the selected depth in the scattering medium is sampled. In the non-range-gated case, since the shutter is open continuously, the light reflected at the far wall of the cell is forward scattered and this "forward scattered reflection" is picked up by the collection optics. Thus the observed results are a superposition of direct back-scattering and indirect forward scattering. Since the reflectivity at the far wall is ~4% (air-glass interface) the spurious forward scattering is only a few % of what it would be under direct illumination. However, since forward scattering cross sections are much greater than backscattering cross-sections, the forward scattering from the reflected light is sufficient to seriously distort the backscattering data.

In Fig. 4-11, is shown a corrected theoretical Mie scattering curve which takes this effect into account, i.e., backscattering + 4% forward scattering. It can be seen that the agreement with the experimental results is much better than if only backscattering is assumed.

IV.4.4 Reduction of Multiple Scattering Effect

The ultrafast sampling of the scattered pusles also has the benefit of reducing some of the effects of multiple scattering. At a given observation angle, light which is scattered more than once travels a path-length different from that of singly scattered light. For a low number of scatterings, the multiple scattered light can have a path-length less than or greater than singly scattered light. If the number of scatterings is large, the path length will in general tend to be greater than that for single scattering. Thus, multiple

scattered light arrives at the shutter either early or late for sampling and is consequently attenuated. The shorter the sampling time, the more effective is this discrimination against multiple scattered signals.

A comparison is made with the results of non-range-gated case. Fig. 4-12, 4-13, and 4-14 show the behavior of relative scattered intensity at certain selected angles as a function of particle concentration for 0.481 μm, 2.02 μm, and 3.2 μm particles, respectively, for both the range-gated and non-range-gated cases. For the 0.481 μm particles, 10% solid density corresponds to a particle concentration of 1.64 x 10^{12} cm^{-3} , for the 2.02 μm particles to 2.26 x 10^{10} cm^{-3} , and for the 3.2 μm particles to 5.605 x 10^9 cm^{-3} . In each case the solid line represents linear behavior corresponding to single scattering theory. Deviations from linearity are caused by multile scattering. It should be noted that significant deviation from linear behavior occurs at nearly an order of magnitude lower concentration in the non-range-gated case, attesting to the usefulness of range-gating in the suppression of multiple scattering. At shorter pulse durations this effect would be considerably more pronounced. With our present equipment, however, we are not able to achieve sampling times under 15 psec.

The decrease in intensity at higher particle concentration is due to the attenuation of the incident beam and the scattered signal along their propagation paths. This has been analyzed theoretically in Section IV.2 as the first order multiple scattering. The results of

the calculation are shown in Fig. 4-15, compared to experimental results for 0.481 µm particles at an angle of 169°. The open circles represent the range-gated data while the crosses represent the non-range-gated (i.e., quasi-CW) data. The solid circles are pseudo-theoretical points calculated using measured values of turbidity as an attenuation factor for the single scattering extrapolation. See Sections VI.3.1 and VI.3.4 for the detailed discussions on the turbidity measurements.

As can be seen in the figure, the range-gated data fit the theoretical curve more closely than the non-range-gated data, showing that range-gating does suppress some of the higher order effects of multiple scattering. From another point of view, the valid range of the first order multiple scattering approximation is expanded by the range-gating technique.

The open and solid circles coincide almost exactly even at the concentration of 10^{-2}% by weight, where the theoretical curve fails to fit. The difference between the theoretical curve and the solid circles is due to the assumption of constant turbidity of the former and decreasing turbidity of the latter caused by multiple scattering. This result suggests that the first order multiple scattering approximation is still valid at this concentration-range by simply including the multiple scattering effect in one of the parameters which is measured as the turbidity.

IV.4.5   Simplification of Geometric Correction

The advantage of the range-gating technique in simplifying the geometrical corrections is demonstrated. The correction factors for the change of the scattering volume was obtained in Section IV.2.2 as a function of the scattering angle Θ. They are $(1 + \cos\Theta)/(\sin\Theta \cos\Theta)$ for the non-range-gated case and $1/\cos\Theta$ for range-gated case. When Θ is small, the former reduces to the conventional "$\sin\Theta$-correction" and the latter to the correction-free.

This advantage is illustrated in Fig. 4-16 which shows the scattered intensities measured as a function of the particle concentrations at the angles of $\Theta = 1.83°$, $11.0°$, $20.2°$ and $29.3°$. Fig. 4-16(a), (b) and (c) corresponds to the cases of non-range-gating without the $\sin\Theta$-correction, non-range-gating with $\sin\Theta$-correction and range-gating with no correction. They show that the correction is not required at these angles if the range-gating is applied.

(a)
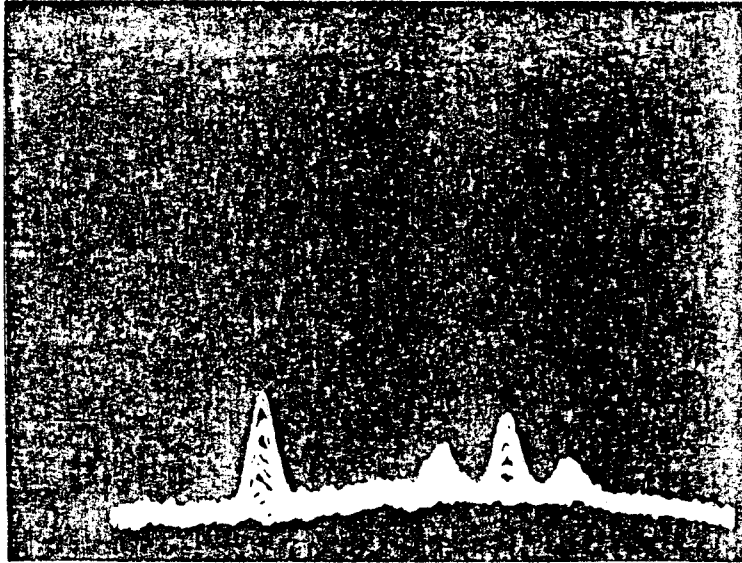
(b)
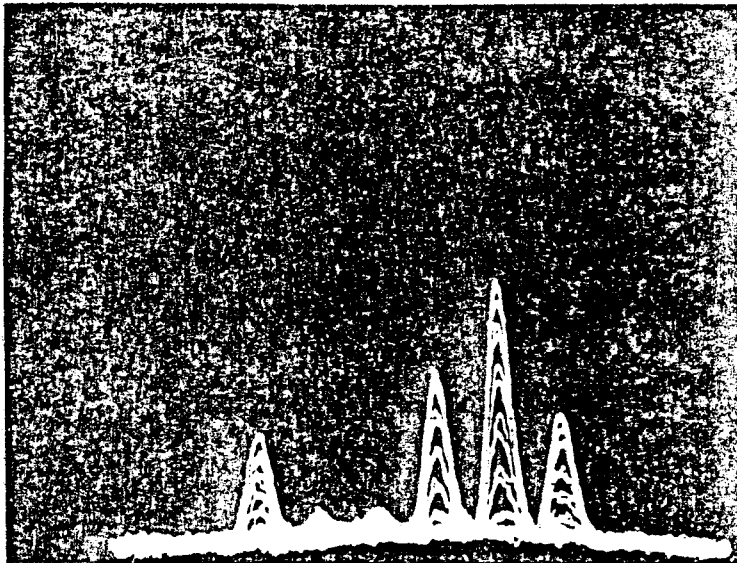
Fig.4-7 Suppression of background scattering :
        recorded signals (a) with range-gating (x100),
        (b) without range-gating
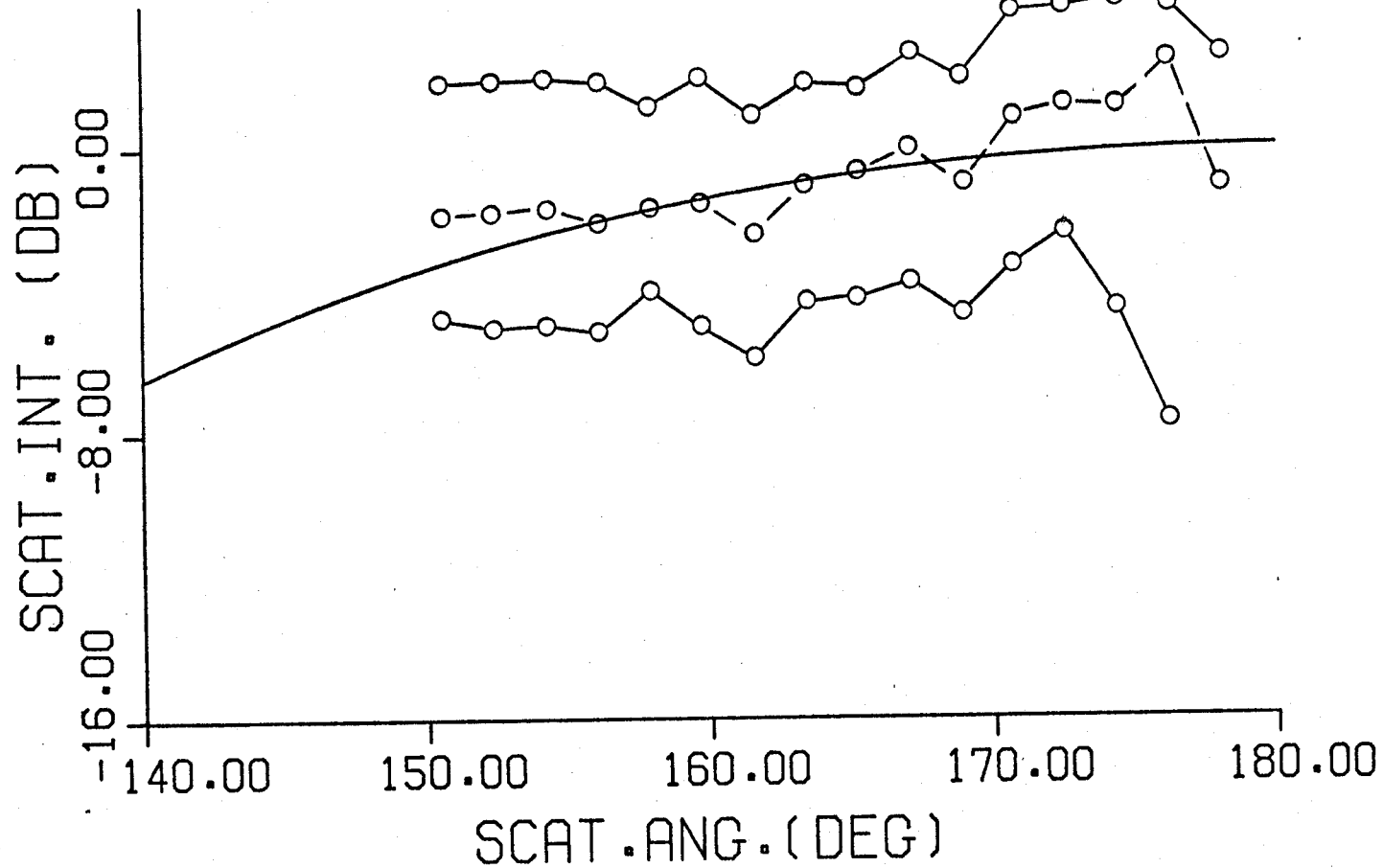
Fig.4-8 Backward scattering patterns of 0.481 μm latex spheres :
measurement (circles), best-fit Mie calculation (solid
line); d = 0.481 μm, m = 1.20, σ/d = 0.35 %
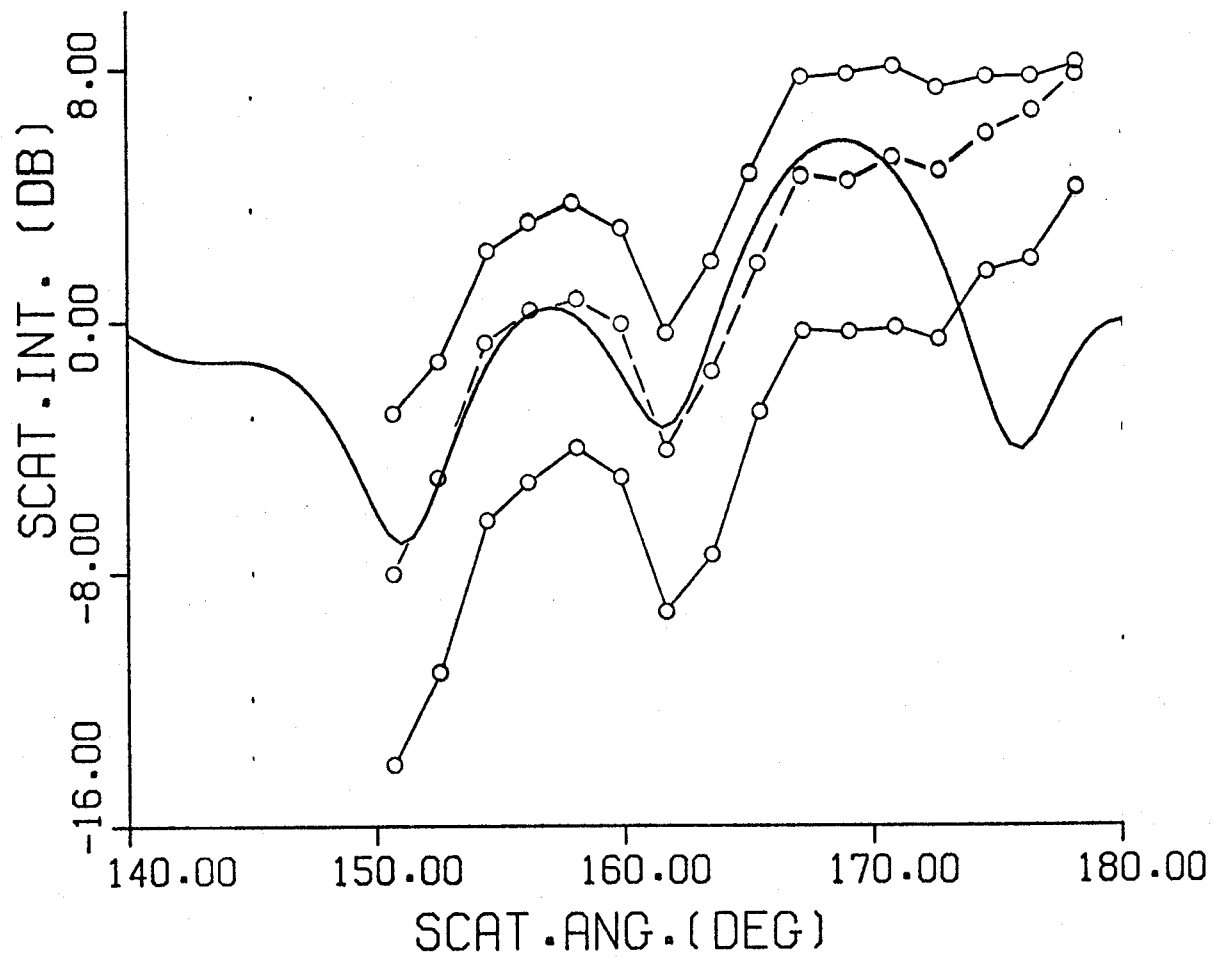
fig.4-9　Backward scattering patterns of 2.02 μm latex spheres :
measurement (circles), best-fit Mie calculation (solid
line); d = 2.02 μm, m = 1.19, σ/d = 1.4 %
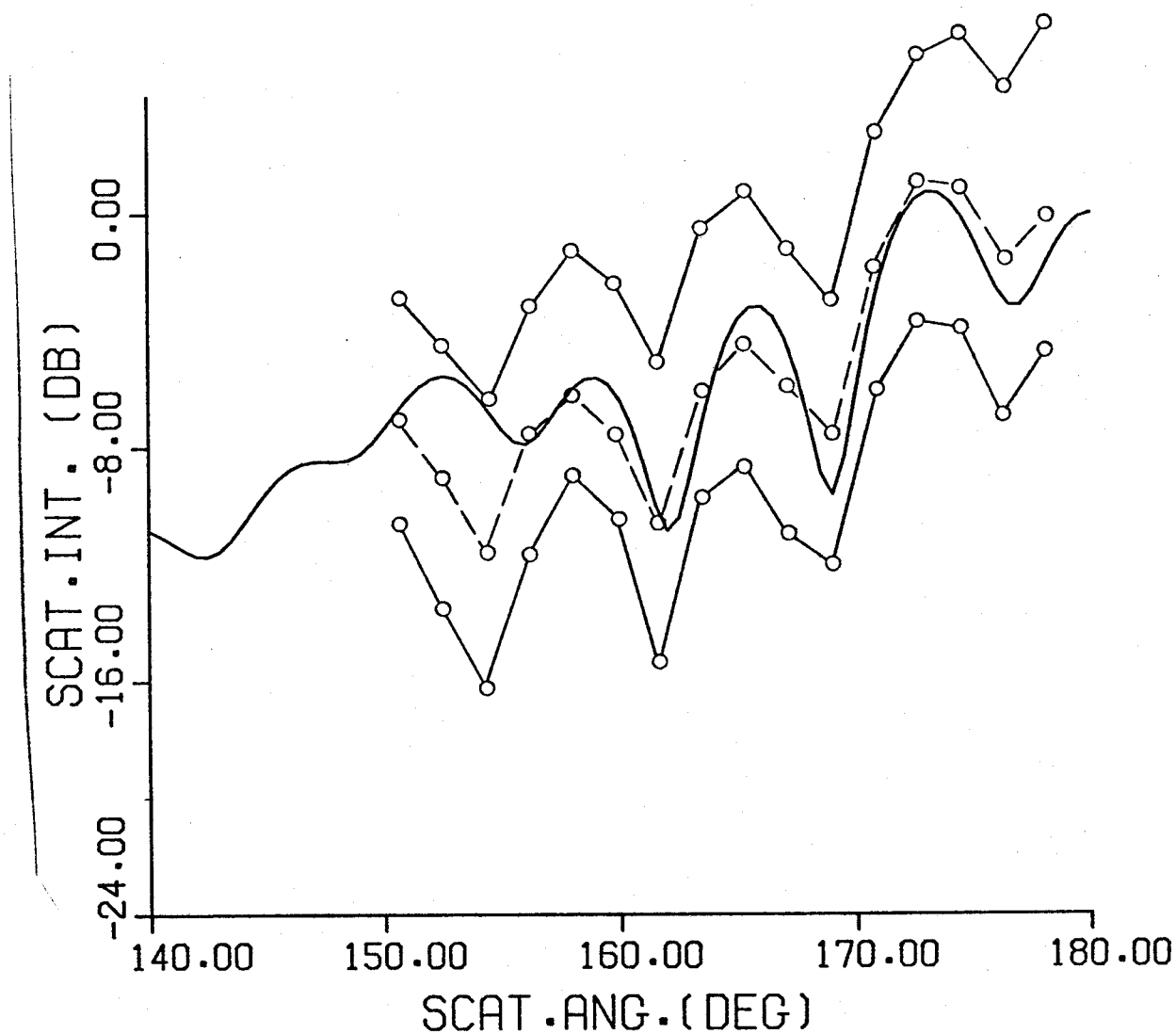
Fig.4-10 Backward scattering patterns of 3.20 μm latex spheres :
measurement (circles), best-fit Mie calculation (solid
line); d = 3.20 μm, m = 1.20, σ/d = 5.9 %

QUASI – CW

PARTICLE
CONCENTRATION
(cm^{-3})

5.6 x 10^6
1.68 x 10^6

5.6 x 10^5

1.68 x 10^5

5.6 x 10^4

RELATIVE SCATTERED INTENSITY

1.0

10^1

10^2

10^{-3}

150°   160°   170°   180°

SCATTERING ANGLE, θ

MIE THEORY
(BACKSCATTERING
+ 4% FORWARD
SCATTERING)
d = 3.2 μ
σ/d = 3 %
λ = 0.53μ
m = 1.2
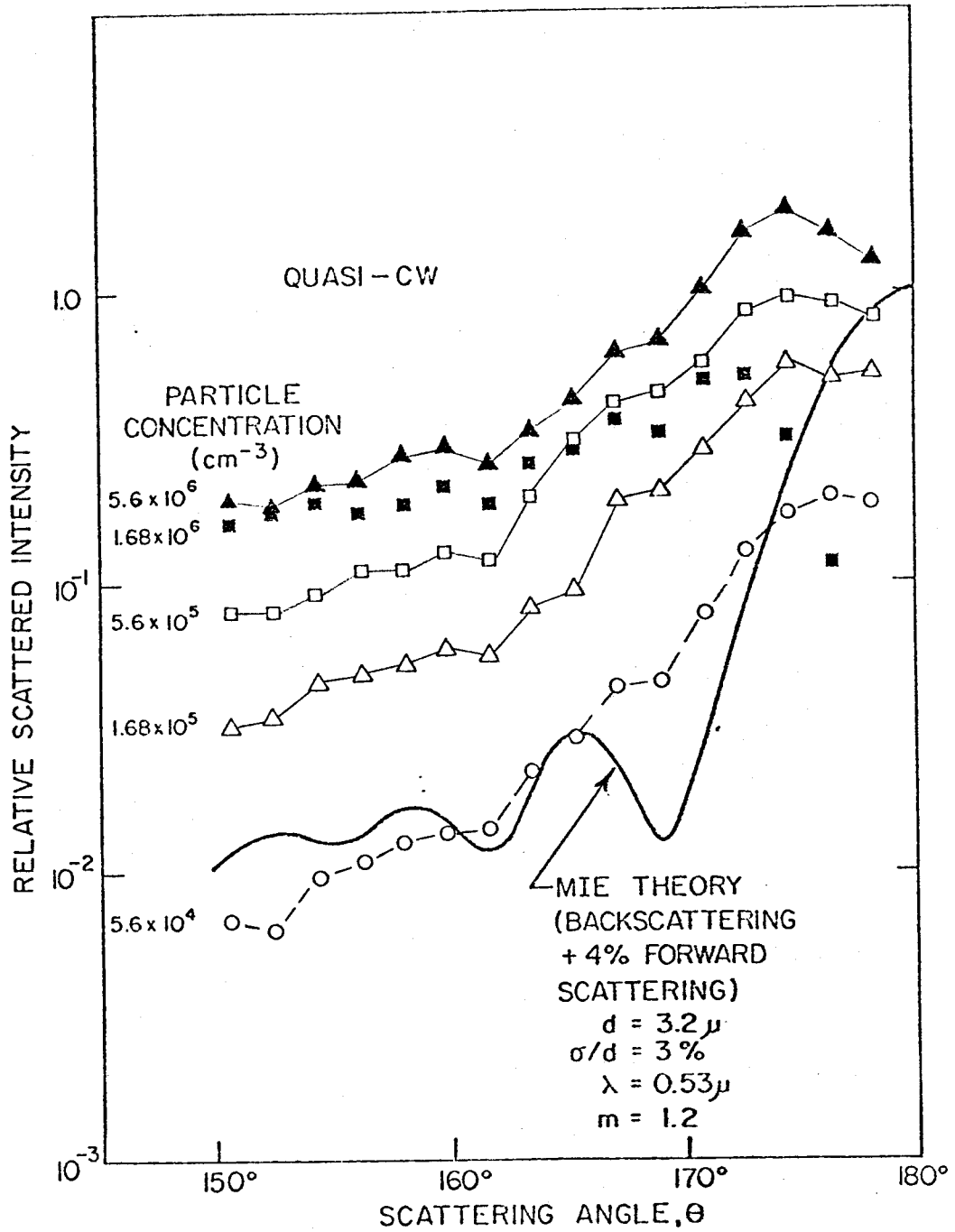
Fig.4-11   Scattering patterns of quasi-CW (non-range-gated) case,
d = 3.20 μm
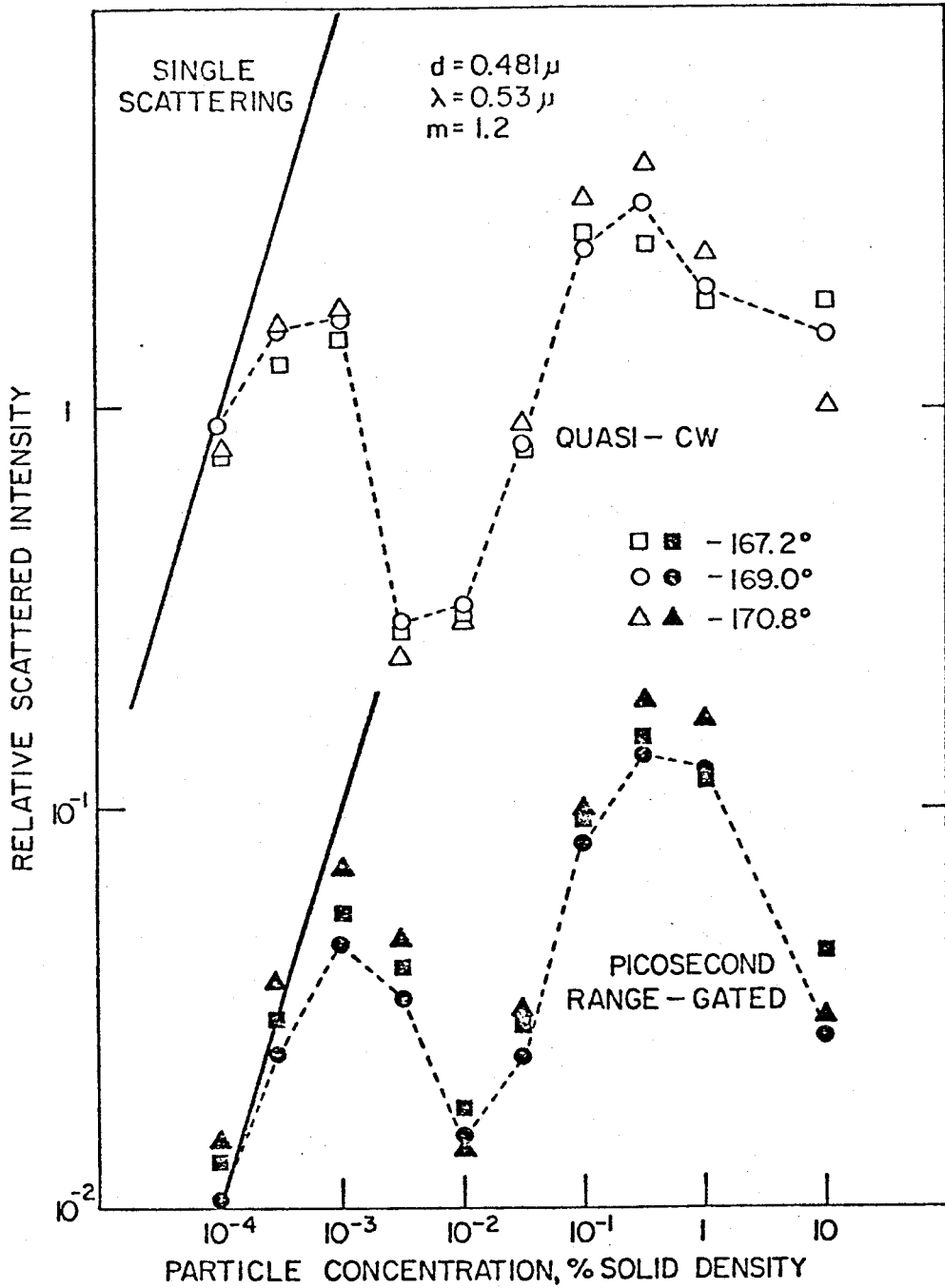
Fig.4-12 Reduction of multiple scattering effect : relative
scattered intensity vs. particle concentration,
d = 0.481 μm
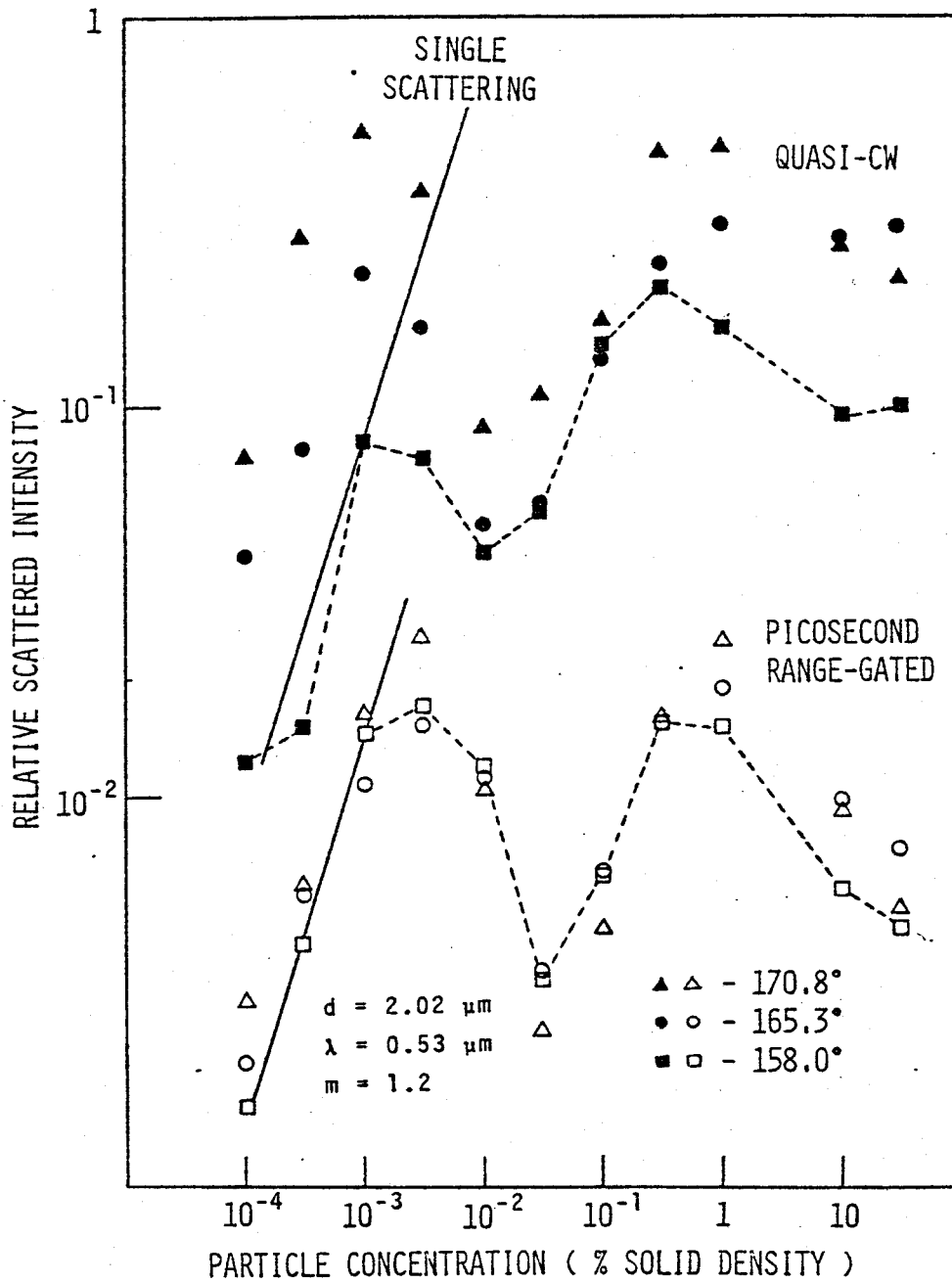
Fig.4-13 Reduction of multiple scattering effect : relative
scattered intensity vs. particle concentration,
d = 2.02 μm
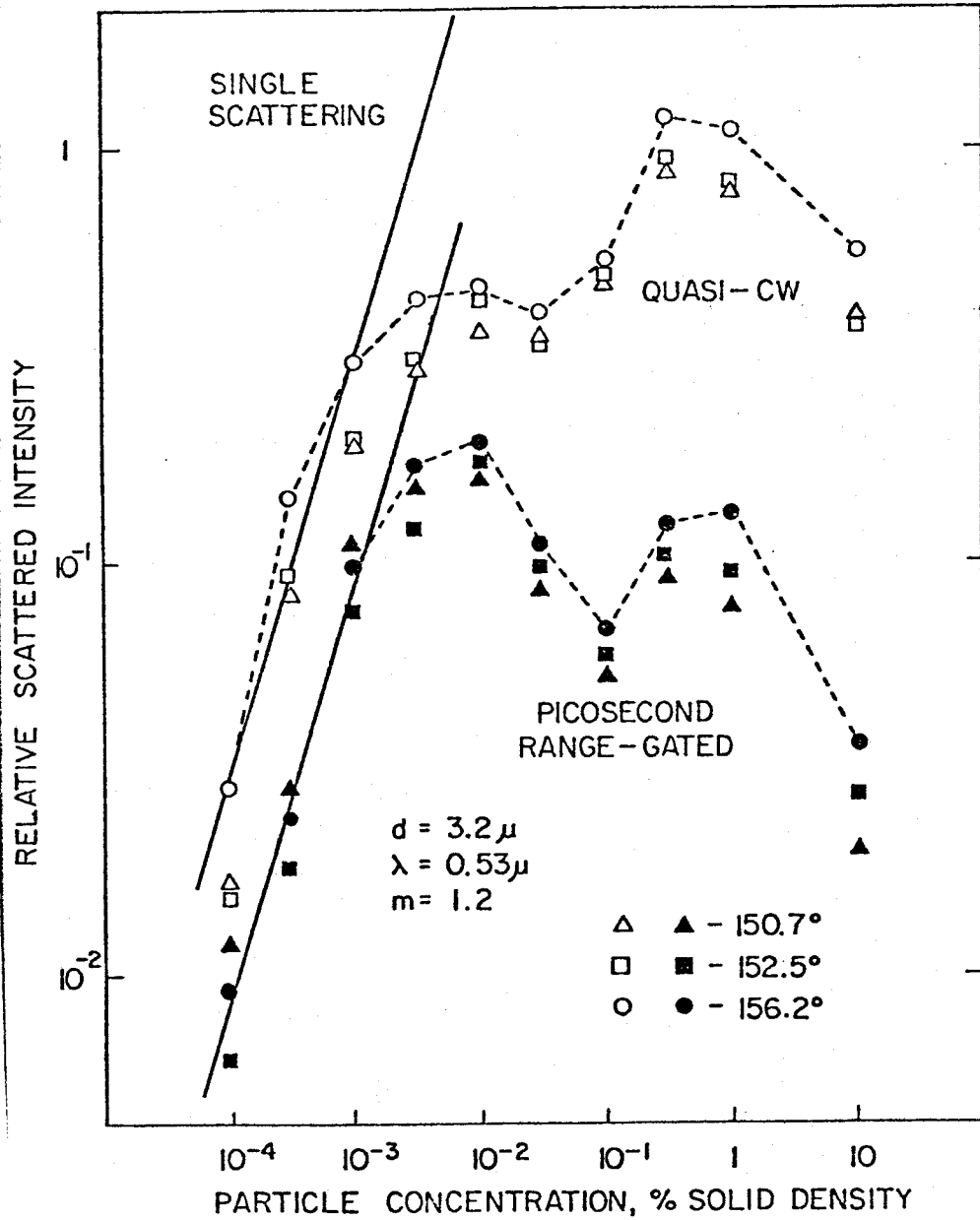
Fig.4-14 Reduction of multiple scattering effect : relative
scattering intensity vs. particle concentration,
d = 3.20 µm
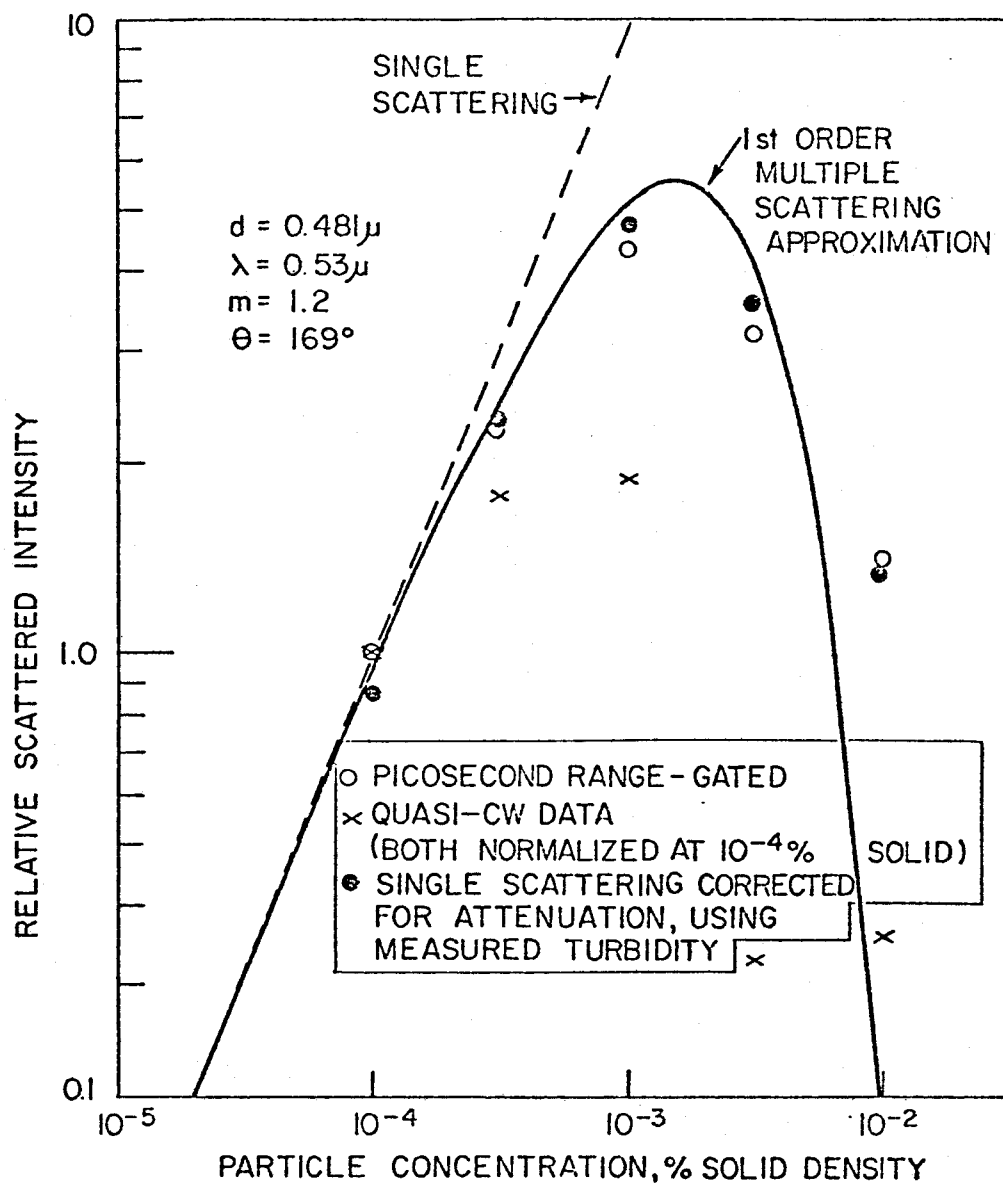
Fig.4-15   Comparison of first order multiple scattering theory
with picosecond range-gated and quasi-CW data
d = 0.481 μm
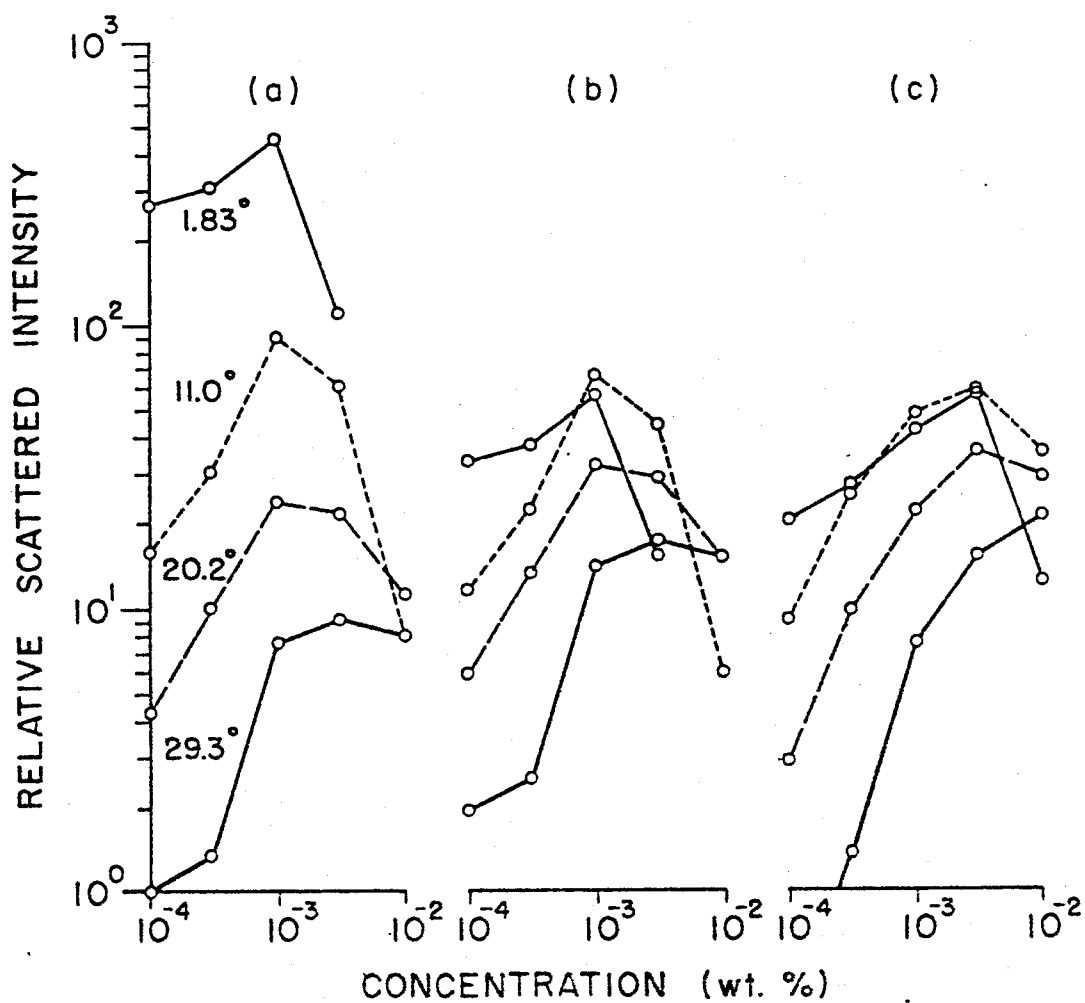
Fig.4-16 Simplification of geometrical correction by range-gating :
    (a) non-range-gated without geometrical correction
    (b) non-range-gated with geometrical correction
    (c) range-gated without geometrical correction
    observation angles are 1.83°, 11.0°, 20.2°, 29.3°

Chapter V

SOLUTION OF DIFFUSION EQUATION FOR BEAM WAVE

INCIDENCE ON DENSE RANDOM MEDIA

V.1.   INTRODUCTION

There has been an increasing interest in the propagation and scattering characteristics of a short optical pulse in a random medium. The practical application ranges widely in various fields such as meteorology, astronomy and biology.

Ishimaru (1975), Hong (1976) (1977) and Sreenivasiah (1976) obtained general formulations for line-of-sight pulse propagation in randomly distributed scatterers as well as turbulence, and considered optical pulse propagation in fog and clouds. These and other studies (Liu, 1975), (Uscinski, 1974), (Erhukumov, 1973), (Bucher, 1973) were directed to the study of line-of-sight propagation of a pulse under the forward scattering assumption which is applicable for tenuous media and large scatterers compared with the wavelength.

Although CW studies in dense media have been reported (Ishimaru, 1978a, p. 174)(Reynolds, 1976), very few attempts have been made to treat the problem of backscattering of a short optical pulse from a dense distribution of scatterers. Recently, Ishimaru (1978b) derived the diffusion equation for pulse propagation by applying the diffusion approximation to the two-frequency equation of transfer. He also obtained the solution of the diffusion equation for the point source and plane wave cases.

In the preceding chapters (Chapters II-IV), we dealt with the remote-sensing technique for a tenuous medium. In general, they are applicable only when the single scattering or the first order multiple scattering approximation is valid, which corresponds to scatterer volume density considerably smaller than 0.1%. If the volume density is much greater than 1%, a diffusion approximation must be used (Ishimaru, 1978a, p. 175). The range of these approximations will be discussed in detail in Chapter VI.

In this chapter we derive the beam wave solution to the diffusion equation, and analyze the scattered pulse shape from dense media. Also, the combination of the first order multiple scattering and diffusion approximations is attempted. A new parameter, diffusion optical distance is defined and its usefulness is demonstrated. The range of validity of the diffusion approximation is examined as well.

V.2   THEORY

V.2.1   Diffusion Equation for Pulse Propagation

The two-frequency equation of transfer (Ishimaru, 1978b) is given by

$$\frac{dI(\bar{r},\hat{s})}{ds} = i(K_1 - K_2^*)I(\bar{r},\hat{s}) + \rho\int f_1(\hat{s},\hat{s}')f_2^*(\hat{s},\hat{s}')I(\bar{r},\hat{s})d\Omega'$$

$$+ \ \varepsilon(\bar{r},\hat{s}) \qquad (5\text{-}1)$$

$$K_1 = k_1 + \{2\pi\rho f_1(\hat{i},\hat{i})\}/k_1$$

$$(5\text{-}2)$$

$$K_2 = k_2 + \{2\pi\rho f_2(\hat{i},\hat{i})\}/k_2$$

where $I(\bar{r},\hat{s},\omega_1,\omega_2)$ and $\varepsilon(\bar{r},\hat{s},\omega_1,\omega_2)$ are two-frequency specific intensity and source function at the position $\bar{r}$ in the direction of the unit vector $\hat{s}$ at frequencies ω_1 and ω_2, $f_1(\hat{o},\hat{i})$ and $f_2(\hat{o},\hat{i})$ are scattering amplitudes at ω_1 and ω_2 respectively when a wave is incident and scattered in the directions of the unit vectors $\hat{i}$ and $\hat{o}$, $d\Omega'$ is the elementary solid angle in the direction $\hat{s}'$, ρ is the number density, $k_1 = \omega_1/c$, $k_2 = \omega_2/c$ and c is the velocity of light. The scalar variable s represents a distance in space.

The specific intensity I can be expressed as a sum of the reduced incident intensity I_{ri} and the diffuse intensity I_d.

$$I(\bar{r},\hat{s},\omega_1,\omega_2) = I_{ri}(\bar{r},\hat{s},\omega_1,\omega_2) + I_d(\bar{r},\hat{s},\omega_1,\omega_2)$$

$$\frac{dI_{ri}}{ds} = i(K_1 - K_2^*)I_{ri} \tag{5-3}$$

$$\frac{dI_d}{ds} = i(K_1 - K_2^*)I_d + \rho\int_{4\pi} f_1 f_2^* I_d d\Omega' + \varepsilon_{ri} + \varepsilon \tag{5-4}$$

where $\quad \varepsilon_{ri} = \varepsilon_{ri}(\bar{r},\hat{s},\omega_1,\omega_2) = \rho\int_{4\pi} f_1 f_2^* I_{ri} d\Omega' \tag{5-5}$

The diffusion approximation is given by the first two terms of the series expansion of I_d in terms of the scattering angle, i.e.,

$$I_d(\bar{r},\hat{s}) = U_d(\bar{r}) + (3/4\pi) \bar{F}_d(\bar{r}) \cdot \hat{s} \tag{5-6}$$

where the average intensity U_d and the flux vector $\bar{F}_d$ are defined by

$$U_d(\bar{r},\omega_1,\omega_2) = \frac{1}{4\pi} \int_{4\pi} I_d(\bar{r},\hat{s},\omega_1,\omega_2)d\Omega \tag{5-7}$$

$$\bar{F}_d(\bar{r},\omega_1,\omega_2) = \int_{4\pi} I_d(\bar{r},\hat{s},\omega_1,\omega_2) \, \hat{s} \, d\Omega \tag{5-8}$$

$\bar{F}_d$ can be related to U_d as

$$\bar{F}_d(\bar{r}) = -\frac{4\pi}{3\alpha_{tr}} \text{ grad } U_d(\bar{r}) + \frac{1}{\alpha_{tr}} \int_{4\pi} \varepsilon_{ri}(\bar{r},\hat{s})\hat{s} \, d\Omega$$

$$+ \frac{1}{\alpha_{tr}} \int_{4\pi} \varepsilon(\bar{r},\hat{s})\hat{s} \, d\Omega \tag{5-8'}$$

Applying the diffusion approximation to the equation of transfer given in Eq. (5-4), we obtain the diffusion equation for the average intensity.

$$(\nabla^2 - q^2)U_d = \frac{3}{4\pi} \{ -\rho\sigma_s\alpha_{tr} \int_{4\pi} I_{ri}(\bar{r},\hat{s})d\Omega + \text{div} \int_{4\pi} \varepsilon_{ri}(\bar{r},\hat{s})\hat{s} \, d\Omega$$

$$- \alpha_{tr} \int_{4\pi} \varepsilon(\bar{r},\hat{s})d\Omega + \text{div} \int_{4\pi} \varepsilon(\bar{r},\hat{s})\hat{s} \, d\Omega \} \qquad (5-9)$$

where $q^2 = 3\alpha_a\alpha_{tr}$, $\alpha_a = \rho\sigma_a - iK_d$, $\alpha_{tr} = \rho\sigma_{tr} - iK_d$

$$K_d = R_e[K_1 - K_2^*], \quad \sigma_a = \sigma_t - \sigma_s, \quad \sigma_{tr} = (1 - \bar{\mu}) \sigma_s + \sigma_a$$

$$\sigma_t = I_m[K_1 - K_2^*]/\rho \quad, \quad \sigma_s = \int_{4\pi} f_1(\hat{s},\hat{s}')f_2^*(\hat{s},\hat{s}') \, d\Omega' \quad.$$

and

σ_a, σ_s, σ_t and σ_{tr} shown above are two-frequency-absorption, -scattering, -total and -transport cross sections of the scatterer. They are functions of ω_1 and ω_2. If $\omega_1 = \omega_2$, they become the usual cross sections of the particle at the frequency $\omega = \omega_1 = \omega_2$. $\bar{\mu}$ is a mean cosine of the scattering angle $\Theta = \cos^{-1}(\hat{s} \cdot \hat{s}')$ and is given by

$$\bar{\mu} = (\int_{4\pi} f_1 f_2^* \hat{s} \cdot \hat{s}' \, d\Omega')/(\int_{4\pi} f_1 f_2^* \, d\Omega')$$

The boundary condition for the diffusion equation is given by

$$U_d(\bar{r}_s) - \frac{2}{3\alpha_{tr}} \frac{\partial}{\partial n} U_d(\bar{r}_s) + \frac{\hat{n} \cdot \bar{Q}_1(\bar{r}_s)}{2\pi} = 0 \qquad (5\text{-}10)$$

where $\bar{Q}_1(\bar{r}_s) = (\int_{4\pi} \varepsilon_{ri} \hat{s} \, d\Omega)/\alpha_{tr}$, $\bar{r}_s$ is a position on the surface of boundary and $\hat{n}$ is a unit vector normally directed into the region containing scatterers. Note this boundary condition is approximate (Ishimaru, 1978a, p. 179).

In the following sections, solutions of the diffusion equation are given in terms of the average intensity $U_d(\bar{r})$. Once $U_d(\bar{r})$ is found, the flux $\bar{F}_d(\bar{r})$ can be calculated from Eq. (5-8') and the specific intensity $I_d(\bar{r},\hat{s})$ can be approximated by Eq. (5-6). Another type of approximation for $I_d(\bar{r},\hat{s})$ is given in a later section (V.2.8).

V.2.2   Solution for Beam Wave Incidence

Fig. 5-1 shows the geometry of the problem. A collimated beam wave is normally incident upon a slab of dense random medium. Considering the axial symmetry of the geometry, a cylindrical coordinate system (r,ϕ,z) is employed.

From Eq. (5-3), we get the two-frequency reduced incident intensity.

$$I_{ri}(\bar{r},\hat{s},\omega_1, \omega_2) = F_0(r) \exp(-\alpha_t z)\delta(\hat{s} - \hat{z}) \qquad (5\text{-}11)$$

where $F_0(r)$ is the function of intensity variation in the transverse plane, $\alpha_t = \rho\sigma_t - iK_d$, $\bar{r} = r\hat{r} + z\hat{z}$, $\hat{r}$ and $\hat{z}$ are unit vectors
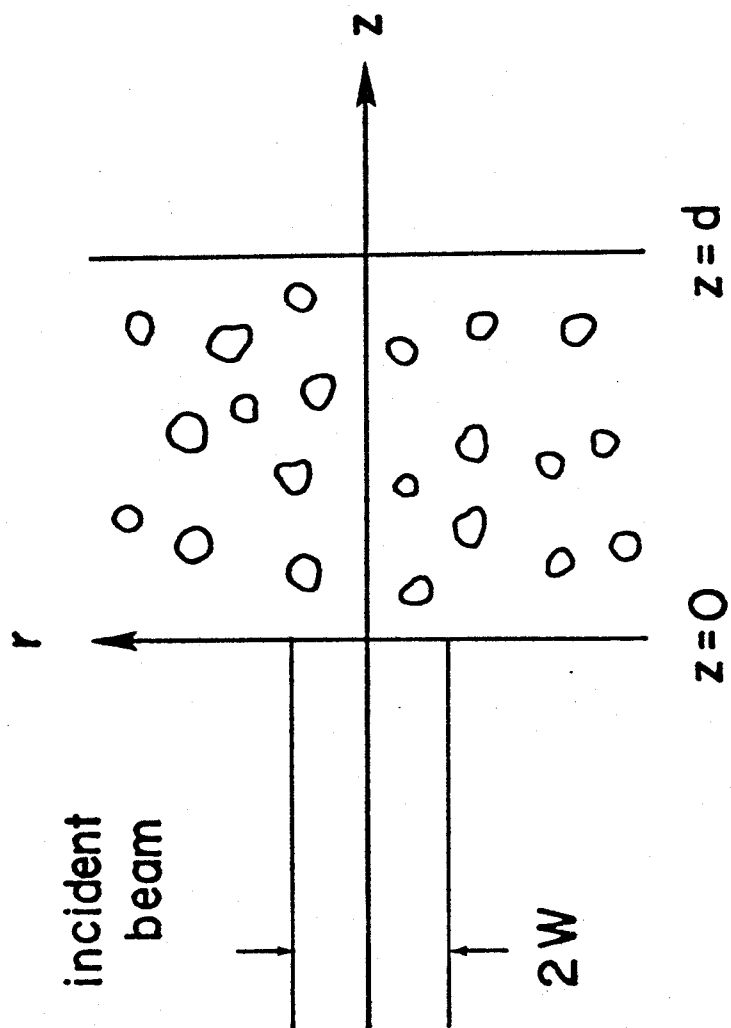
Fig.5-1 Geometry of the problem

in the radial and z directions. In the following discussion, $F_0(r)$ is assumed to be Gaussian, i.e.,

$$F_0(r) = \exp(-r^2/w^2) \tag{5-12}$$

where w is an e^{-1} half beam width.

Substituting Eqs. (5-11) and (5-12) in Eqs. (5-5) and (5-9), the problem is formulated in the following boundary value problem.

$$(\nabla^2 - q^2)\, U_d(\bar{r}) = -\, Q_0(\bar{r}) \tag{5-13}$$

$$U_d(\bar{r}) - h\, \frac{\partial}{\partial z} U_d(\bar{r}) + \frac{Q_1(\bar{r})}{2\pi} = 0 \qquad\qquad \text{at } z = 0 \tag{5-14}$$

$$U_d(\bar{r}) + h\, \frac{\partial}{\partial z} U_d(\bar{r}) - \frac{Q_1(\bar{r})}{2\pi} = 0 \qquad\qquad \text{at } z = d \tag{5-15}$$

where $q^2 = 3\alpha_a \alpha_{tr}$, $h = 2/3\alpha_{tr}$, d is the thickness of the slab of scatterers,

$$Q_0(\bar{r}) = \frac{3}{4\pi}\, \rho\sigma_s (\alpha_{tr} + \bar{\mu}\alpha_t)\, \exp(-r^2/w^2)\exp(-\alpha_t z)$$

$$\triangleq C_0\, \exp(-r^2/w^2)\exp(-\alpha_t z) \tag{5-16},$$

and

$$Q_1 = (\bar{\mu}\rho\sigma_s/\alpha_{tr})\, \exp(-r^2/w^2)\exp(-\alpha_t z)$$

$$\triangleq C_1\, \exp(-r^2/w^2)\exp(-\alpha_t z) \tag{5-17}.$$

This can be solved by the Green's function method, i.e.,

$$U_d(\bar{r}) = \int_V G(\bar{r},\bar{r}') \, Q_0(\bar{r}')dV' - \frac{1}{2\pi h} \int_S G(\bar{r},\bar{r}')Q_1(\bar{r}')dS' \qquad (5\text{-}18)$$

where

$$(\nabla^2 - q^2)G(\bar{r},\bar{r}') = -\delta(\bar{r} - \bar{r}') \qquad (5\text{-}19)$$

$$G(\bar{r},\bar{r}') - h \frac{\partial}{\partial z} G(\bar{r},\bar{r}') = 0 \qquad\qquad \text{at } z = 0 \qquad (5\text{-}20)$$

$$G(\bar{r},\bar{r}') + h \frac{\partial}{\partial z} G(\bar{r},\bar{r}') = 0 \qquad\qquad \text{at } z = d \qquad (5\text{-}21)$$

The solution $G(\bar{r},\bar{r}')$ can be written as a sum of the particular solution $G_p(\bar{r},\bar{r}')$ and the homogeneous solution $G_h(\bar{r},\bar{r}')$. They correspond to the primary wave or the "incident wave" and the secondary wave or "the scattered wave," respectively (Ishimaru, 1974, p. 505).

$$G(\bar{r},\bar{r}') = G_p(\bar{r},\bar{r}') + G_h(\bar{r},\bar{r}') \qquad (5\text{-}22)$$

$$G_p(r,r') = \frac{1}{4\pi} \int_0^\infty J_0(\lambda r) \, J_0(\lambda r') \, e^{-\gamma|z - z'|} \frac{\lambda d\lambda}{\gamma} \qquad (5\text{-}23)$$

$$G_h(r,r') = \frac{1}{4\pi} \int_0^\infty J_0(\lambda r) \, J_0(\lambda r') \, \{ \, g_1(\lambda)e^{-\gamma z}$$

$$+ g_2(\lambda)e^{\gamma z} \, \} \, \frac{\lambda d\lambda}{\gamma} \qquad (5\text{-}24)$$

where $\gamma = (\lambda^2 + q^2)^{1/2}$. Eqs. (5-23) and (5-24) are obtained from the Green's function for the Helmholtz equation, simplified for the axial symmetry (Kraut, 1967, p. 386). The coefficient functions $g_1(\lambda)$ and $g_2(\lambda)$ are determined by applying the boundary conditions

Eqs. (5-20) and (5-21). They are

$$g_1(\lambda) = \{(h^2\gamma^2 - 1)e^{\gamma(d-z')} + (h\gamma - 1)^2 e^{-\gamma(d-z')}\}/\Delta$$

$$g_2(\lambda) = \{(h^2\gamma^2 - 1)e^{-\gamma(d-z')} + (h\gamma - 1)^2 e^{-\gamma(d+z')}\}/\Delta$$

where $\Delta = (h\gamma + 1)^2 e^{\gamma d} - (h\gamma - 1)^2 e^{-\gamma d}$. $\hspace{2cm}$ (5-25)

Rearranging them for future convenience, the Green's function is given by

$$G(r,z;r',z') = \frac{1}{4\pi} \int_0^\infty \frac{\lambda d\lambda}{\gamma} J_0(\lambda r) J_0(\lambda r') \{e^{-\gamma|z-z'|}$$

$$+ g_{11}e^{-\gamma(z+z')} + g_{12}e^{-\gamma(z-z')} + g_{21}e^{\gamma(z+z')}$$

$$+ g_{22}e^{\gamma(z-z')} \hspace{3cm} (5-26)$$

where

$$g_{11} = (h^2\gamma^2 - 1)e^{\gamma d}/\Delta \hspace{2cm} g_{12} = (h\gamma - 1)^2 e^{-\gamma d}/\Delta$$

$$g_{21} = (h^2\gamma^2 - 1)e^{-\gamma d}/\Delta \hspace{2cm} g_{22} = (h\gamma - 1)^2 e^{-\gamma d}/\Delta$$

Finally, substitution of Eq. (5-26) into Eq. (5-18) yields the solution for the original boundary value problem (Eqs. (5-13) $\sim$ (5-15)), i.e.,

$$U_d(r,z) = \int_0^\infty \frac{\lambda d\lambda}{\gamma} J_0(\lambda r) \frac{w^2}{2} e^{-\frac{w^2}{4}\lambda^2} \{\frac{C_0}{2} A(z) + \frac{C_1}{4\pi h} B(z)\} \hspace{1cm} (5-27)$$

$$A(z) = \frac{1}{\gamma - \alpha}(e^{-\alpha z} - e^{-\gamma z}) - \frac{1}{\gamma + \alpha}(e^{\gamma z - \gamma d - \alpha d} - e^{-\alpha z})$$

$$- \frac{g_{11}}{\gamma + \alpha}(e^{-\gamma z - \gamma d - \alpha d} - e^{-\gamma z}) + \frac{g_{12}}{\gamma - \alpha}(e^{-\gamma z + \gamma d - \alpha d} - e^{-\gamma z})$$

$$+ \frac{g_{21}}{\gamma - \alpha}(e^{\gamma z + \gamma d - \alpha d} - e^{\gamma z}) - \frac{g_{22}}{\gamma + \alpha}(e^{\gamma z - \gamma d - \alpha d} - e^{\gamma z}) \qquad (5\text{-}28)$$

$$B(z) = e^{\gamma z - \gamma d - \alpha d} - e^{-\gamma z} + g_{11}(e^{-\gamma z - \gamma d - \alpha d} - e^{-\gamma z}) + g_{12}(e^{-\gamma z + \gamma d - \alpha d}$$

$$- e^{-\gamma z}) + g_{21}(e^{\gamma z + \gamma d - \alpha d} - e^{\gamma z}) + g_{22}(e^{\gamma z - \gamma d - \alpha d} - e^{\gamma z}) \qquad (5\text{-}29)$$

where $\alpha = \alpha_t = \rho\sigma_t - iK_d$, C_0 and C_1 are defined in Eqs. (5-16) and (5-17).

V.2.3   Beam Wave Incidence on Semi-Infinite Medium

If we take the infinite limit of the slab thickness ($d \rightarrow \infty$) in Eqs. (5-28) and (5-29), we get the solution for a semi-infinite medium, i.e.,

$$U_d(r,z) = \int_0^\infty \frac{\lambda d\lambda}{\gamma} J_0(\lambda r) \frac{w^2}{2} e^{-\frac{w^2}{4}\lambda^2} \{ \frac{C_0}{2} A_\infty(z) + \frac{C_1}{4\pi h} B_\infty(z) \} \qquad (5\text{-}30)$$

$$A_\infty(z) = \frac{e^{-\alpha z} - e^{\gamma z}}{\gamma - \alpha} + \frac{e^{-\alpha z}}{\gamma + \alpha} + \frac{h\gamma - 1}{h\gamma + 1} \frac{e^{-\gamma z}}{\gamma + \alpha} \qquad (5\text{-}31)$$

$$B_\infty(z) = \frac{-2h\gamma}{h\gamma + 1} e^{-\gamma z} \qquad (5\text{-}32)$$

Note that the solution is simplified considerably when the effect from the backwall is eliminated.

If we replace the boundary condition, Eq. (5-15), by

$$U_d(\bar{r}) = 0 \qquad \text{at} \quad z = \infty \qquad\qquad (5\text{-}33)$$

and solve the boundary value problem (Eqs. (5-13), (5-14) and (5-33)), we get the same solution as above. The agreement was confirmed. See Fig. 5-2.

V.2.4   Plane Wave Incidence on Slab of Medium

A plane wave can be considered to be a beam wave with an infinite beam width. Therefore, the solution for plane wave incidence is obtained by taking an infinite limit of the beam width ($w \to \infty$) in Eq. (5-27). Since

$$\lim_{w \to \infty} \int_0^\infty f(\lambda) \, \frac{w^2}{2} \, e^{-\frac{w^2}{4}\lambda^2} \, \lambda d\lambda \;=\; f(0) \qquad\qquad (5\text{-}34)$$

Eq. (5-27) becomes

$$U_d(z) = \frac{1}{q} \left\{ \frac{C_0}{2} A_p(z) + \frac{C_1}{4\pi h} B_p(z) \right\} \qquad\qquad (5\text{-}35)$$

where $A_p(z)$ and $B_p(z)$ are given by replacing all the γ's by q's in Eqs. (5-28) and (5-29) respectively. This solution agrees with the one obtained by Ishimaru (1978b), who set up the diffusion equation and boundary conditions for the plane wave and solved it. It is outlined in Section VIII.2.2.

$$\begin{cases} \nabla^2 U - q^2 U = -Q \\[2mm] U - h\frac{\partial U}{\partial z} + \frac{Q_1}{2\pi} = 0 \Big|_{z=0} \\[2mm] U + h\frac{\partial U}{\partial z} - \frac{Q_1}{2\pi} = 0 \Big|_{z=d} \end{cases} \qquad\qquad \begin{cases} \nabla^2 U - q^2 U = -Q \\[2mm] U - h\frac{\partial U}{\partial z} + \frac{Q_1}{2\pi} = 0 \Big|_{z=0} \\[2mm] U = 0 \Big|_{z=\infty} \end{cases}$$

Green's function method $\downarrow$ Green's function method $\downarrow$

Collimated Wave   +   Slab of Medium

$[F_0 e^{-(r/w)^2}]$

$\xrightarrow{\quad d \to \infty \quad}$

Collimated Wave   +   Semi-Infinite Media

$w \to \infty \downarrow$ $\downarrow w \to \infty$

Plane Wave   +   Slab of Medium

$\xrightarrow{\quad d \to \infty \quad}$

Plane Wave   +   Semi-Infinite Media

$\uparrow$ Particular Sol. & Compl. Sol. $\uparrow$ Particular Sol. & compl. sol.

$$\begin{cases} \frac{\partial^2}{\partial z^2} U - q^2 U = -Q \\[2mm] U - h\frac{\partial}{\partial z} U + \frac{Q_1}{2\pi} = 0 \Big|_{z=0} \\[2mm] U + h\frac{\partial}{\partial z} U - \frac{Q_1}{2\pi} = 0 \Big|_{z=d} \end{cases} \qquad\qquad \begin{cases} \frac{\partial^2}{\partial z^2} U - q^2 U = -Q \\[2mm] U - h\frac{\partial U}{\partial z} + \frac{Q_1}{2\pi} = 0 \Big|_{z=0} \\[2mm] U = 0 \Big|_{z=\infty} \end{cases}$$

Fig.5-2   Relation of beam wave solution for slab of medium to other solutions

Note that in Eq. (5-35), the r-dependence, and the integral appearing in Eq. (5-27) were removed.

V.2.5   Plane Wave Incidence on Semi-Infinite Medium

In the same way as the previous section ($w \to \infty$), the solution for beam wave incidence on a semi-infinite medium (Eqs. (5-30) ~ (5-32)) reduce to the solution for the plane wave incidence, i.e.,

$$U_d(z) = \frac{1}{q} \left\{ \frac{C_0}{2} A_{p\infty}(z) + \frac{C_1}{4\pi h} B_{p\infty}(z) \right\} \tag{5-36}$$

$$A_{p\infty}(z) = \frac{e^{-\alpha z} - e^{-qz}}{q - \alpha} + \frac{e^{-\alpha z}}{q + \alpha} + \frac{hq - 1}{hq + 1} \frac{e^{-qz}}{q + \alpha} \tag{5-37}$$

$$B_{p\infty}(z) = \frac{-2hq}{hq + 1} e^{-qz} \tag{5-38}$$

The same results are obtained by taking an infinite limit of the slab thickness ($d \to \infty$) in Eq. (5-35), or starting from the diffusion equation with an appropriate boundary condition such as Eq. (5-33). These agreements were confirmed. See. Fig. 5-2.

V.2.6   Point Source in the Medium

Another asymptotic case of the beam wave incidence is a point source. We take a zero limit of the beam width ($w \to 0$) in the beam wave solution for a semi-infinite medium (Eq. (5-30)), while keeping the total incident energy constant ($\pi w^2 = $ const.). Then, we get

$$U_d(r,z) = C_2 \int_0^\infty \frac{\lambda d\lambda}{\gamma} J_0(\lambda r)\{(\alpha_{tr} + \bar{\mu}\alpha_t)A_\infty(z) + \bar{\mu}B_\infty(z)\} \tag{5-39}$$

where

$$C_2 = \frac{3}{16\pi^2} \rho\sigma_s C_3$$

$$C_3 = \int_0^\infty \exp(-r^2/w^2)2\pi r \, dr = \pi w^2 = \text{const.}$$

and A_∞, B_∞ are given in Eqs. (5-31), (5-32).

For the dense random media, the optical distance is much larger than unity ($\rho\sigma_t z \gg 1$), and $e^{-\alpha z}$ is negligible if it is compared with $e^{-\gamma z}$. Then, Eq. (5-39) can be written in the following form:

$$U_d(r,z) = C_3 \int_0^\infty \frac{\lambda d\lambda}{\gamma} J_0(\lambda r) \, f(\gamma) \, e^{-\gamma z} \tag{5-40}$$

where $f(\gamma) = (\alpha_{tr} + \bar{\mu}\alpha_t)A'(z) + \bar{\mu}B'(z)$ and using Eqs. (5-31) and (5-32)

$$A_\infty(z) = \frac{e^{-\alpha z} - e^{-\gamma z}}{\gamma - \alpha} + \frac{e^{-\alpha z} + e^{-\gamma z}}{\gamma + \alpha} - \frac{2}{h\gamma + 1}\frac{e^{-\gamma z}}{\gamma + \alpha}$$

$$\simeq \left(\frac{-1}{\gamma - \alpha} + \frac{1}{\gamma + \alpha} - \frac{2}{h\gamma + 1}\frac{1}{\gamma + \alpha}\right)e^{-\gamma z} \triangleq A'(z)e^{-\gamma z} \tag{5-41}$$

$$B_\infty(z) = \frac{-2h\gamma}{h\gamma + 1}e^{-\gamma z} \triangleq B'(z)e^{-\gamma z} \tag{5-42}$$

The integral in Eq. (5-40) is evaluated by the method of steepest descents (saddle point technique), giving

$$U_d(r,z) = C_4 \frac{e^{-qR}}{R} f(q\frac{z}{R}) \tag{5-43}$$

where $R = (r^2 + z^2)^{1/2}$. Detailed discussion is given in Appendix V.A.

Finally, the beam wave solution, Eq. (5-30) reduces to

$$U_d(r,z) = C_3 \frac{3}{4\pi} \alpha_{tr} \frac{e^{-qR}}{4\pi R} A_{ps} \left(\frac{z}{R}\right) \tag{5-44}$$

where

$$A_{ps}(x) = \rho\sigma_s \frac{qx(2\alpha_t + 3\alpha_{tr} + 3\bar{\mu}\alpha_t + 6\bar{\mu}\alpha_a x^2)}{(qx - 3\alpha_{tr}/2)(q^2x^2 - \alpha_t^2)} \tag{5-45}$$

Ishimaru (1978b) solved the following diffusion equation for a point source in the scatterers,

$$(\nabla^2 - q^2) U_d(\bar{r}) = - \frac{3}{4\pi} \alpha_{tr} \tag{5-46}$$

and obtained

$$U_d(\bar{r}) = \frac{3}{4\pi} \alpha_{tr} \frac{e^{-qR}}{4\pi R} \tag{5-47}$$

On the z-axis or $r = 0$ and $R = z$, Eq. (5-44) agrees with Eq. (5-47) at least in the spatial dependence.

V.2.7   Impulse Response

The output power in time domain can be expressed

$$P(t) = \int_{-\infty}^{\infty} P_{in}(t') G(t - t') dt' \tag{5-48}$$

where $P_{in}(t)$ is the input power and $G(t)$ is the response due to the delta function input power or $P_{in}(t) = \delta(t)$. $G(t)$ is called the impulse response.

In the previous sections, the solutions of the diffusion equation were presented in terms of the two-frequency average intensity $U_d(\bar{r};\omega_1,\omega_2)$ in the frequency domain. It is defined by

$$U_d(\bar{r}\ ;\omega_1,\omega_2) = \frac{1}{4\pi} \int_{4\pi} I_d(\bar{r},\hat{s};\omega_1,\omega_2)\ d\Omega \qquad (5\text{-}49)$$

It has been shown that the impulse response $G(t)$ is given by the Fourier transform of the two-frequency mutual coherence function $\Gamma_0(\omega_d)$, i.e.,

$$G(t) = \frac{1}{2\pi} \int_{-\infty}^{\infty} \Gamma_0(\omega_d)\ e^{-i\omega_d t}\ d\omega_d \qquad (5\text{-}50)$$

where $\Gamma_0(\omega_d)$ is the mutual coherence function which represents the correlation function between the output fields due to the time-harmonic inputs at two different frequencies $\omega_0 + \omega_1$ and $\omega_0 + \omega_2$ evaluated at the same time t and at the same point $\bar{r}$, and $\omega_d = \omega_1 - \omega_2$ (Ishimaru, 1978a, p. 96, p. 313).

Since

$$\Gamma_0(\bar{r};\omega_d) = \int_{4\pi} I(\bar{r},\hat{s};\omega_d)\ d\Omega = 4\pi\ U_d(\bar{r};\omega_d) \qquad (5\text{-}51)$$

we get the impulse response as a Fourier transform of the U_d, i.e.,

$$G_1(\bar{r};t) = \int_{-\infty}^{\infty} U_d(\bar{r};\omega_d)\ e^{-i\omega_d t}\ d\omega_d \qquad (5\text{-}52)$$

As can be seen in Eqs. (5-52) and (5-49), the impulse response $G_1(t)$ represents the signal averaged over all directions. Thus, it

is applicable when the receiving pattern of the detector is isotropic
(no directivity) or the directivity of the incoming signal is sharply
peaked to be confined in the receiving pattern of the detector. In
practice, these conditions are not always easy to satisfy. In fact,
our system uses the detector with a very narrowly peaked receiving
pattern to obtain the directional information of the (diffusely)
scattered intensity. Therefore, in the following analysis, the impulse
response $G(t)$ refers to the $G_2(t)$ which is given as the Fourier
transform of the specific intensity I_d, i.e.,

$$G(t) \equiv G_2(\bar{r},\hat{s};t) = \int_{-\infty}^{\infty} I_d(\bar{r},\hat{s};\omega_d) \, e^{-i\omega_d t} \, d\omega_d \qquad (5-53)$$

The specific intensities to be used for the analyses in the later
sections are listed below. They are obtained by substituting the
each solution U_d for semi-infinite media into Eqs. (5-6), (5-8').

(1) Beam wave incidence

incident flux: $F(r;\omega_1,\omega_2) = F_o \, e^{-\frac{r^2}{w^2}}$

where F_o is the flux at $r = o$, r is the radial distance in
cylindrical coordinate system (r,θ,z), and w is the e^{-1} half
beam width.

$I_d(r,o,\hat{s};\omega_1,\omega_2)$

$$= -\frac{3}{4\pi} F_o \rho \sigma_s \left[\int_0^{\infty} \lambda d\lambda \, J_0(\lambda r) w^2 e^{-\frac{w^2}{4\lambda^2}} \frac{\mu\gamma - \alpha_{tr}}{(2\gamma + 3\alpha_{tr})(\gamma + \alpha)} \right.$$

$$+ \hat{r} \cdot \hat{s} \int_0^\infty \lambda^2 \, d\lambda \, J_1(\lambda r) w^2 e^{-\frac{w^2}{4\lambda^2}} \frac{\mu\gamma + \alpha_{tr}}{(2\gamma + 3\alpha_{tr})(\gamma + \alpha)\alpha_{tr}}$$

$$+ \hat{z} \cdot \hat{s} \int_0^\infty \lambda d\lambda \, J_0(\lambda r) w^2 \, e^{-\frac{w^2}{4\lambda^2}} \frac{1}{2\gamma + 3\alpha_{tr}} \{ \frac{3(\alpha_{tr} + \mu\alpha)}{2(\gamma + \alpha)}$$

$$+ \mu \frac{\gamma}{\alpha_{tr}} \} - \hat{z} \cdot \hat{s} \frac{\mu}{\alpha_{tr}} e^{-\frac{r^2}{w^2}}] \tag{5-54}$$

Previous sections (V.2.1, V.2.2) should be consulted for the definitions of parameters.

(2) Plane wave incidence

incident flux: $F(\omega_1, \omega_2) = F_0$ (const.)

$$I_d(z = 0, \hat{s}; \omega_1, \omega_2)$$

$$= - \frac{3}{4\pi} F_0 \, \rho\sigma_s \frac{\mu q - \alpha_{tr}}{(2q + 3\alpha_{tr})(q + \alpha)} (2 - 3\hat{s} \cdot \hat{z}) \tag{5-55}$$

(3) Quasi-spherical wave (point source at the boundary)

$$I_d(R, \phi, \hat{s}; \omega_1, \omega_2)$$

$$= - \frac{3}{4\pi} E_{tot} [\alpha_{tr} \frac{e^{-qR}}{4\pi R} f(\cos\phi)$$

$$+ \frac{e^{-qR}}{4\pi R^2} \{(qR + 1)f(\cos\phi)\hat{R} \cdot \hat{S} + \sin\phi \, f'(\cos\phi)\hat{\phi} \cdot \hat{s}\}] \tag{5-56}$$

where

$$f(x) = \rho\sigma_s \frac{2\mu}{\alpha_{tr}} \frac{x(x^2 + C_1)}{(x + C_2)(x^2 - C_3)}$$

$$f'(x) = \frac{d}{dx} f(x) = \rho\sigma_s \frac{2\mu}{\alpha_{tr}} \left\{ \frac{3x^2 + C_1}{(x + C_2)(x^2 - C_3)} \right.$$

$$\left. - \frac{x(x^2 + C_1)(3x^2 + 2C_2 x - C_3)}{(x + C_2)^2 (x^2 - C_3)^2} \right\}$$

$$C_1 = \alpha_{tr}(2\alpha + 3\mu\alpha + 3\alpha_{tr})/2\mu q^2 \ , \quad C_2 = 3\alpha_{tr}/2q \ ,$$

$C_3 = (\alpha/q)^2$ and the spherical coordinate system (R,Θ,ϕ)

was used. $\phi = 90°$ at the boundary.

(4) Point source in the medium

$$I_d(R,\hat{R};\omega_1,\omega_2) = \frac{3}{4\pi} \frac{e^{-qR}}{4\pi R} \left(\alpha_{tr} + q + \frac{1}{R}\right) \tag{5-57}$$

V.2.8   Improvement for Plane Wave Backscattering

As will be discussed in the next section, the diffusion solution
is not applicable for the scattering from the region near the boundary
of the scattering medium. Since, in this region, optical distance is
not high enough to satisfy the conditions of diffusion, the first order
multiple scattering (FOMS) is taken into account. Note that this
approach is not a simple addition of the solution for the FOMS to that
of the diffusion equation.

We start from the two-frequency equation of transfer for the diffuse intensity $I_d(\bar{r},\hat{s};\omega_1,\omega_2)$, i.e.,

$$\frac{d}{ds} I_d = i(K_1 - K_2^*)I_d + \rho \int f_1 f_2^* I_d \, d\Omega + \rho \int f_1 f_2^* I_{ri} \, d\Omega \qquad (5\text{-}58)$$

Definitions of parameters are given in Section V.2.1.

The equation of transfer is formulated into the integral equation as

$$I(\bar{r},\hat{s};\omega_1,\omega_2) = I_{ri}(\bar{r},\hat{s};\omega_1,\omega_2) + I_d(\bar{r},\hat{s};\omega_1,\omega_2) \qquad (5\text{-}59)$$

$$I_{ri}(\bar{r},\hat{s}) = I_i(\bar{r}_0,\hat{s}) \, e^{-\alpha s}$$

$$I_d(\bar{r},\hat{s}) = \int_0^\infty e^{-\alpha(s-s_1)} \frac{\rho \sigma_t}{4\pi} \int_{4\pi} p(\hat{s},\hat{s}')I(\bar{r}_1,\hat{s}')d\Omega' + \varepsilon(\bar{r}_1,\hat{s}) \}ds_1$$

where I_i is the incident intensity at the incidence point $\bar{r} = \bar{r}_0$,

s is the distance from $\bar{r}_0$ in the direction $\hat{s}$, $\alpha = \rho\sigma_t - iK_d$ and

$p(\hat{o},\hat{i};\omega_1,\omega_2) = \frac{4\pi}{\sigma_t} f_1(\hat{o},\hat{i}) \, f_2^*(\hat{o},\hat{i})$ is the two-frequency phase function.

To this point, no approximation has been made.

If the unknown total intensity $I(\bar{r}_1,\hat{s})$ in the integrand is approximated by the reduced incident intensity I_{ri}, we get the ordinal FOMS approximation (Ishimaru, 1978a, p. 169). Here instead, we approximate the $I(\bar{r}_1,\hat{s})$ by the I_{ri} plus the diffusion solution $\tilde{I}_d$, i.e.,

$$I(\bar{r},\hat{s};\omega_1,\omega_2) = I_{ri}(\bar{r},\hat{s};\omega_1,\omega_2) + \tilde{I}_d(\bar{r},\hat{s};\omega_1,\omega_2) \tag{5-60}$$

$$\tilde{I}_d(\bar{r},\hat{s};\omega_1,\omega_2) = U_d(\bar{r};\omega_1,\omega_2) + \frac{3}{4\pi}\bar{F}_d(\bar{r};\omega_1,\omega_2)\cdot\hat{s}$$

Comparing Eqs. (5-59) and (5-60), if $\tilde{I}_d = I_d$ the solution is exact. In other words, the accuracy of this approach depends on that of the diffusion solution. For convenience in further calculations, the solution I_d is written as a sum of the I_{d1} and I_{d2} which represents the contributions from I_{ri} and $\tilde{I}_d$ respectively, i.e.,

$$I_d(\bar{r},\hat{s};\omega_1,\omega_2) = I_{d1}(\bar{r},\hat{s};\omega_1,\omega_2) + I_{d2}(\bar{r},\hat{s};\omega_1,\omega_2) \tag{5-61}$$

$$I_{d1}(\bar{r},\hat{s}) = \int_0^S e^{-\alpha(s-s_1)}\{\frac{\rho\sigma t}{4\pi}\int_{4\pi}p(\hat{s},\hat{s}')I_{ri}(\bar{r}_1,\hat{s}')d\Omega'\}\ ds_1 \tag{5-62}$$

$$I_{d2}(\bar{r},\hat{s}) = \int_0^S e^{-\alpha(s-s_1)}\{\frac{\rho\sigma t}{4\pi}\int_{4\pi}p(\hat{s},\hat{s}')\tilde{I}_d(\bar{r}_1,\hat{s})d\Omega' + \epsilon(\bar{r}_1,\hat{s})\}\ ds_1 \tag{5-63}$$

After these general formulations, we consider the geometry of our problem shown in Fig. 5-1. A beam of a pulse with the intensity I_i is incident normally on the slab of scattering medium with the thickness d, i.e.,

$$I_i(\bar{r}_0,\hat{s};\omega_1,\omega_2) = F_0\ e^{-\frac{r^2}{w^2}}\delta(\hat{s}-\hat{z}) \tag{5-64}$$

where $\bar{r} = r\hat{r} + z\hat{z}$. From Eq. (5-59) the reduced incident intensity is given by

$$I_{ri}(r,\hat{s};\omega_1,\omega_2) = F_0\ e^{-\frac{r^2}{w^2}}e^{-\alpha z}\ \delta(\hat{s}-\hat{z}) \tag{5-65}$$

Substituting Eq. (5-65) in (5-62) we have

$$I_{d1}(r,z,\hat{s};\omega_1,\omega_2) = \int_z^d e^{-\alpha z_1} \, F_o \, e^{-\frac{r^2}{w^2}} \frac{\rho\sigma_t}{4\pi} p(\hat{s},\hat{z}) \, e^{-\alpha z_1} \, dz_1$$

The backscattering $(\hat{s} = -\hat{z})$ from the semi-infinite medium $(d = \infty)$ observed at the boundary $(z = o)$ is therefore given by

$$I_{d1}(r,o,-\hat{z};\omega_1,\omega_2) = F_o \, e^{-\frac{r^2}{w^2}} \frac{\rho\sigma_b}{4\pi} \frac{1}{2\alpha} \tag{5-66}$$

where σ_b is the backscattering cross section defined by

$$\sigma_b = 4\pi \, \sigma_d(-\hat{i},\hat{i}) = \sigma_t \, p(-\hat{z},\hat{z})$$

where $\sigma_d(\hat{o},\hat{i})$ is the differential cross section.

In the backscattering case, I_{d2} also reduces to the simpler expression. The term in the bracket $\{\cdot\}$ of Eq. (5-63) becomes

$$\frac{\rho\sigma_t}{4\pi} \int_{4\pi} p(-\hat{z},\hat{s}')\tilde{I}_d(\bar{r},\hat{s}')d\Omega' = \rho\sigma_s \left\{ U_d(\bar{r}) - \frac{3}{4\pi} \mu \, F_d(\bar{r}) \right\}$$

where $\int_{4\pi} p(\hat{s},\hat{s}')d\Omega' = 4\pi\sigma_s/\sigma_t$, $\int_{4\pi} p(\hat{s},\hat{s}')\hat{s} \cdot \hat{s}'d\Omega' = -4\pi\mu\sigma_s/\sigma_t$,

$\bar{F}_d(\bar{r}) = F_d(\bar{r})\hat{z}$, and no source, $\varepsilon(\bar{r},\hat{s}) = 0$.

Therefore, for the semi-infinite medium

$$I_{d2}(r,o,-\hat{z};\omega_1,\omega_2) = \int_0^\infty e^{-\alpha z_1} \rho\sigma_s\{U_d(r,z_1) - \frac{3}{4\pi} \mu F_d(r,z_1)\} \, dz_1 \tag{5-67}$$

Finally, substitution of Eqs. (5-66) and (5-67) to (5-61) yields the solution to the equation of transfer which includes the effects of the FOMS and diffusion.

In the case of plane wave incidence, it is given by

$$I_d(z = 0, -\hat{z} ; \omega_1, \omega_2) = I_{d1} + I_{d2}$$

$$= \frac{3}{4\pi} F_0 [\frac{\rho\sigma_b}{6\alpha} + (\rho\sigma_s)^2 \frac{\mu q - \alpha_{tr}}{q^2 - \alpha^2} \{ \frac{2\alpha + 3\mu\alpha + 3\alpha_{tr} + 6\mu\alpha_a}{(2q + 3\alpha_{tr})(q + \alpha)} - \frac{\mu q + \alpha_{tr}}{2\alpha\alpha_{tr}} \}] \quad (5-68)$$

V.2.9   Sign of Diffusion Solutions at Time-Origin

As mentioned before, the diffusion approximation is not valid for the scattering from the region close to the boundary of the scattering medium. This corresponds to the uncertainty of the impulse response near the time origin. In fact, the diffusion solutions can be negative near t = 0 . Therefore, by checking the behavior of the diffusion solutions at the time origin, we can obtain the conditions in which the diffusion solutions should not be used.

According to the initial value theorem of the Laplace transform,

$$\lim_{t \to 0+} f(t) = \lim_{s \to \infty} sF(s) \qquad (5-69)$$

where the function $F(s)$ is the Laplace transform of the function $f(t)$. Defining a new variable

$$s \equiv - i \frac{\omega_d}{\rho\sigma_{tr}c} \qquad \text{where} \quad \omega_d = \omega_1 - \omega_2 \qquad (5-70)$$

we have

$$\lim_{s \to \infty} (\alpha_t / s\rho\sigma_{tr}) = \lim_{s \to \infty} (1 + \sigma_t / s\sigma_{tr}) = 1$$

$$\lim_{s \to \infty} (\alpha_a / s\rho\sigma_{tr}) = \lim_{s \to \infty} (1 + \sigma_a / s\sigma_{tr}) = 1$$

$$\lim_{s \to \infty} (\alpha_{tr} / s\rho\sigma_{tr}) = \lim_{s \to \infty} (1 + 1/s) = 1$$

$$\lim_{s \to \infty} (q / s\rho\sigma_{tr}) = \lim_{s \to \infty} \{3(1 + \sigma_a / s\sigma_{tr})(1 + 1/s)\}^{1/2} = \sqrt{3}$$

$$\lim_{s \to \infty} (\gamma / s\rho\sigma_{tr}) = \lim_{s \to \infty} \sqrt{\lambda^2 + q^2} / s\rho\sigma_{tr} = \sqrt{3}$$

Thus, applying this theorem to the specific intensity for the beam wave incidence on the semi-infinite medium given in Eq. (5-54), we get

$$\lim_{t \to 0+} G(t) = \lim_{s \to \infty} s I_d(s)$$

$$= -\frac{3}{4\pi} F_o \frac{\sigma_s}{\sigma_{tr}} e^{-(\frac{r}{2})^2} \frac{\sqrt{3} \mu - 1}{(2\sqrt{3} + 3)(\sqrt{3} + 1)} (2 - 3 \hat{z} \cdot \hat{s}) \quad (5-71)$$

Therefore, the impulse response at $t = 0+$ is positive, when

$$0 < \mu < 1/\sqrt{3} \quad \text{and} \quad \hat{z} \cdot \hat{s} < 2/3 \quad (\Theta > 48.2°) \quad \text{or}$$

$$\quad (5-72)$$

$$1/\sqrt{3} < \mu < 1 \quad \text{and} \quad \hat{z} \cdot \hat{s} > 2/3 \quad (\Theta < 48.2°)$$

The interpretation of this result is as follows. The former condition implies that diffusion cannot be expected in the large angles ($\Theta > 48.2°$) unless the scattering pattern of each constituent

particle is fairly isotropic ($0 < \mu < 1/\sqrt{3}$). The latter condition implies that if the scattering pattern is peaked in the forward angles ($1/\sqrt{3} < \mu < 1$), diffusion cannot be expected in the large angles ($\Theta > 48.2°$). Thus, the impulse response based on the diffusion approximation is not valid near the time-origin, if the above conditions are not satisfied. It should be emphasized that the above conditions do not guarantee the validity of the solution even if they are satisfied. They just show the conditions under which the solution is not reliable.

The same method is applied to the point source case given in Eq. (5-57):

$$\lim_{t \to 0+} G(t) = \lim_{s \to \infty} s\, I_d(s) = \infty \tag{5-73}$$

where

$$\lim_{s \to \infty} s(s + 1)\, \exp\{-\sqrt{3s(s + 1)}\, R\} = \lim_{s \to \infty} \left[\frac{\exp\{\sqrt{3s(s+1)}\, R\}}{s(s + 1)} \right]^{-1}$$

$$= \lim_{s \to \infty} \left[\frac{1}{s(s + 1)} \left\{ 1 + \sqrt{3s(s + 1)}\, R + \frac{1}{2!}\, 3s(s + 1)R^2 + \ldots \right\} \right]^{-1}$$

This result is reasonable, since in the case of the point source, the time origin of the scattered wave corresponds to the spatial origin where the source is concentrated in a point.

As expected from the similarity in the geometry, the results for the plane wave and the quasi-spherical wave are the same as those for the beam wave given in Eq. (5-71) and the point source, Eq. (5-73),

respectively.

There is an interesting equivalence seen in the derivation of Eq. (5-71) to that of Eq. (5-55). Note the similarity in the final forms shown in Eqs. (5-71) and (5-55). This is attributed to the following. As can be seen in the definition given in Eq. (5-70), an increase in s corresponds to an increase in the frequency ω_d, and a decrease in the wavelength λ. A decrease in λ is equivalent to a relative increase in the beam width w of the incident wave. Thus, taking the infinite limit in s corresponds to the same limit in w which reduces the diffusion solution for the beam wave incidence to that for the plane wave incidence. It is shown in Section V.2.4.

V.2.10   Diffusion Optical Distance

The "optical distance" (Ishimaru, 1978a, p. 157) or the "optical thickness" (Chandrasekhar, 1950, p. 9) has been defined as

$$\tau = \int \rho \sigma_t \, ds \qquad (5\text{-}74)$$

where ρ, σ_t and ds is the particle concentration, the total cross section and the distance element. If the scattering medium is homogeneous and the wave travels in the z direction, it becomes

$$\tau = \rho \sigma_t \, z \qquad (5\text{-}75)$$

This parameter represents the attenuation characteristics of the medium due to scattering and absorption, i.e.,

$$I(z) = I_o \, e^{-\tau} \tag{5-76}$$

where $I(z)$ is the intensity at the position z and I_o is the incident intensity.

As can be seen in the following definition, the transport cross section σ_{tr} includes the effect of the unisotropic scattering, and therefore represents the scattering characteristic of the diffusive media better than other cross sections.

$$\sigma_{tr} \equiv (1 - \mu)\sigma_s + \sigma_a \tag{5-77}$$

where μ is the average cosine of the scattering angle. $\mu = 0$ and 1 corresponds to isotropic and purely forward scattering, respectively. Using σ_{tr}, a new parameter is defined and called a "diffusion optical distance":

$$\tau_d = \int \rho\sigma_{tr} \, ds = \rho\sigma_{tr}z \quad \text{for homogeneous media} \tag{5-78}$$

In the following analysis with diffusive media, parameters and functions are normalized by $\rho\sigma_{tr}$ or $\rho\sigma_{tr}C_{med}$ where C_{med} is the group velocity of light in the scattering medium.

It is demonstrated in later sections (V.4.1, VIII.4.3) that diffusive scattering depends mostly on τ_d and that the choice of the above normalization constant is appropriate. It is also verified experimentally in Section VIII.4.3.

V.3   NUMERICAL ANALYSIS

The theoretical discussions presented in the previous section (V.2) are examined by numerical analysis. The diffusion solutions in the time domain or the impulse responses are calculated and their pulse-shapes are analyzed. The values of parameters are chosen within a practical range. Most of them are those used in the experiments which are discussed in subsequent chapters. The calculations are made with 16 digits precision.

The outline of the algorithm developed for this analysis is as follows.

1. Initiate the program, i.e., read the given parameters, calculate necessary constants, etc.

2. Set the frequency in a given range, ω_i (i = 1, 2, . . . N)

3. Calculate the spectrum of the specific intensity $I_d(\omega_i)$. If numerical integrations are involved such as in the beam wave case, check the convergence of the integration. If necessary, apply the tapering window on the high-frequency tail to prevent the leakage phenomena in the following FFT.

4. Take Fourier transform of the spectrum by the Fast Fourier Transform technique.

5. Output the results in graphs.

V.4   RESULTS AND DISCUSSION

V.4.1   Diffusion Solution for Beam Wave Incidence

Fig. 5-3 shows the impulse response of a semi-infinite diffusive medium calculated by Eqs. (5-53) and (5-54). This is the intensity profile of the scattered signal in time, where the incident wave is assumed to be a beam of an impulse whose dimension is longitudinally infinitesimal and laterally Gaussian. The abscissa is the time normalized by $(\rho \sigma_{tr} C_{med})^{-1}$ and the ordinate is the intensity of the impulse response normalized by $\rho \sigma_{tr} C_{med}$, where ρ, σ_{tr} and C_{med} are the particles concentration, the transport cross section and the group velocity of light in the medium, respectively. As to the choice of this normalization constant, more discussion is given elsewhere (V.2.10, V.4.2, VIII.4.3). The time-origin is defined as the instant when the incident impulse passes the first boundary of the scattering medium. Through this chapter, impulse responses are presented in a linear scale unless otherwise specified.

We can see in Fig. 5-3, the typical characteristics of the impulse response of the diffuse media, namely the rapid rise and slow asymptotic decay. As mentioned before, the diffusion approximation is not valid for the scattering from the region near the boundary of the scattering medium. This corresponds to the uncertainty of the impulse response in the normalized time $t' \lesssim 1$. The part of the asymptotic decay, however, should be reliable. In the following analysis, this part is referred to as a "diffusion tail" due to its origin.

Fig. 5-4 is the same impulse response as Fig. 5-3, plotted in dB . Its linear decrease implies that the asymptotic decay can be approximated by $\exp(-C\tau_d)$, where C is a constant and τ_d is the diffusion optical distance defined in Section V.2.10.

V.4.2   Effect of Observation Geometry

The geometry of observation is illustrated in Fig. 5-5. The backward scattered pulse for the beam wave incidence is observed at the radial distance r and at the scattering angle Θ .

Fig. 5-6 shows the effect of the radial distance r . As r increases, the scattered intensity is rapidly attenuated, but pulse broadening does not occur, at least in the range examined. The pulse keeps its relative shape as it is attenuated.

Fig. 5-7 shows the effect of the observation angle Θ . Again, as Θ increases the magnitude of the pulse decreases, but the relative shape of the pulse is preserved. The angular dependence of the magnitude seems to be $(1 + \cos\Theta)/2$. According to Lambert's cosine law, the dependence would be $\cos\Theta$ if the medium is an ideal diffuse reflector.

V.4.3   Effect of Scatterers

Fig. 5-8 shows the effect of the sizes of scatterers. They are latex spheres with 0.481 μm, 5.7 μm and 45.4 μm diameters. Their relative refractive indices to water are 1.59/1.33 for λ = 0.53 μm. Average cosines $\bar{\mu}$ which represent the degree of anisotropy are 0.85, 0.90 and 0.93 respectively. Their concentrations are set in

10% by weight or 1.64×10^{12} cm^{-3}, 9.87×10^8 cm^{-3}, and 1.95×10^6 cm^{-3}.

The curve of 45.4 μm spheres shows the highest magnitude and the fastest decay in the diffusion tail due to the large $\bar{\mu}$ or high anisotropy. Except for these points, there is no significant difference observed among their shapes.

Fig. 5-9 shows the effect of the absorption of scatterers. The absorption is characterized in terms of the ratio of scattering and total extinction or the albedo, $w_0 = \sigma_s/\sigma_t$. Now, the shape of the impulse response changes significantly for the different w_0. The pulse width (FWHM) for absorbing scatterers ($w_0 = 0.85$) is ~60% of that for non-absorbing scatterers ($w_0 = 1.0$). This is due to the suppression of the diffusion tail caused by the absorption of the scatterers. This effect is demonstrated experimentally in a later chapter (VIII.4.2). The separation in the starting points of the rising part of the impulse response is not fully understood. It may take more time for the absorbing scatterers to start the diffusion.

Except for the above case of absorption, the curves presented in this and previous sections show general and common features. This can be attributed to the proper choice of the normalization constant $\rho\sigma_{tr}c$ discussed in Section V.2.10. If we use a different kind of normalization constant such as $\rho\sigma_t c$, $\rho\sigma_s c$, etc., the curves appear to be very different for different situations. Therefore, these results suggest the possibility of the universal curve which is applicable

to a variety of physical situations.

V.4.4   Comparison of Different Solutions

In Section V.2, diffusion solutions were obtained for different types of incident waves, namely the beam wave, plane wave and point source cases. The beam wave solution reduces precisely to the plane wave solution by taking the infinite limit of the beam width. By taking the zero limit, the beam wave solution reduces to a solution similar to that of the point source, but is not exact. This asymptotic solution is called a "quasi-spherical wave" solution. Fig. 5-10 illustrates these concepts.

In this section, the impulse responses calculated by these solutions are analyzed. They are the plane wave, beam wave, and quasi-spherical wave incidences on semi-infinite media calculated by Eqs. (5-55), (5-54) and (5-56) respectively, and the point source by Eq. (5-57). They are shown in Figs. 5-11, 5-12, 5-13 and 5-14 respectively. The impulse responses were calculated for two sizes of scatterers, namely 2.02 μm and 45.4 μm in diameter. These two sizes correspond to the diameters of the spherical equivalents of a RBC and a platelet aggregate which are used in our applications (Ishimaru, 1976). In the point source case, the analysis with the average intensity U_d is sometimes more practical than with the specific intensity I_d . However, no significant difference is found in the impulse responses calculated from U_d and I_d by Eqs. (5-47) and (5-57).

Comparing Figs. 5-11 ~ 5-14, first we note the difference in time scales. In the case of 2.02 μm spheres, the difference amounts

to four orders of magnitude between the plane wave case and point source cases. The quasi-spherical wave case lies in between and close to the point source case. The same argument applies for the 45.4 μm spheres as well, although the difference is a little smaller. This may be attributed to the dimensional difference of the diffusion model. In the plane wave case, the diffusion is considered in only one dimension, while in the point source case it is in three dimensions. Thus, in the latter case, photons are supposed to suffer more collisions against the scatterers than the former case and the effect of diffusion appears enhanced. The result of quasi-spherical wave is also reasonable if we consider the similarity in the geometry of the source point.

V.4.5 Diffusion Tales

By comparing the two curves for 2.02 μm and 45.4 μm spheres in Figs. 5-11 ∼ 5-14, we can see the following. In the plane wave case, there is no difference between the diffusion tales of the two curves. While for the point source, the diffusion tale for the 2.02 μm spheres develops three orders of magnitude larger than that of the 45.4 μm spheres. This three orders of magnitude difference can be seen in the quasi-spherical wave case as well. Although the difference is very small, the larger tail for 2.02 μm spheres appears in the beam wave case, which is otherwise almost identical to that of the plane wave. This is reasonable, since the beam wave case is categorized between the plane wave and the quasi-spherical wave cases, and is closer to the former in the dimension of diffusion discussed above.

These differences in the diffusion tails are attributed to the difference in the degree of diffusivity which is represented by the diffusion optical distance $\tau_d = \rho\sigma_{tr}z$. The larger the τ_d is, the more diffusion occurs resulting in the larger diffusion tale. The τ_d's per unit distance ($\rho\sigma_{tr}$) for 2.02 μm spheres and the 45.4 μm spheres are 204 cm^{-1} and 5.39 cm^{-1} respectively, where the density is 10% by weight for both cases.

Based on these theoretical analyses we can conclude the following points which will be useful for the practical applications. The aggregation of platelets in dense medium can be detected by observing the changes in the diffusion tales of the scattered pulses. This is confirmed experimentally in Chapter VIII. Note that in the above analysis, the fractional weight of the scatterers were kept constant (10%) for 2.02 μm spheres and 45.4 μm spheres, thus simulating the condition of aggregation in which the size of each scatterer grows large but the fractional weight does not change.

Furthermore, the above analysis shows that in the detection of aggregation, a point source or a narrow beam incidence is more effective than the wide wave incidence, such as the plane wave.

V.4.6   Inclusion of First Order Multiple Scattering

Fig. 5-15 shows backscattered (180°) impulse responses for the plane wave incidence. Fig. 5-15(a) is calculated by the diffusion solution for the plane wave incidence given in Eq. (5-55) and Fig. 5-15(b) is by the improved solution Eq. (5-68) obtained in Section V.2.8.

They look almost identical but a closer look reveals an improvement near the origin. A magnified view of this region is inlayed in the same figure. There is a peak originated by the first order multiple scattering (FOMS). Since the FOMS is attenuated rapidly in a short optical distance, it looks like an impulse. The peak shown is that of the 45.4 μm spheres. The one for 2.02 μm spheres is too small to see. The effect of the FOMS peak is shown in Table 5-1 in terms of the areas of the peak normalized by the area under the impulse response curve. The area in the time domain corresponds to the value of the spectrum at the frequency origin. The method of the calculation is shown in Table 5-1, where I_{d1} and I_{d2} are the specific intensities due to the FOMS and the diffusion discussed in Section V.2.8, respectively. As can be seen in the table, the effect of FOMS is negligible for small latex spheres, but it becomes comparable to that of diffusion in the cases of 3.20 μm and larger spheres. This is demonstrated in experiments discussed in Section VIII.4.1.

Another difference between Figs. 5-15(a) and (b) is the separation of the rising points apearing in the latter. This is to be expected since the 45.4 μm spheres are less diffusive ($\rho\sigma_{tr}$ = 5.39 cm^{-1}) than the 2.02 μm spheres ($\rho\sigma_{tr}$ = 204 cm^{-1}), because it takes more time for the former to start the diffusion.
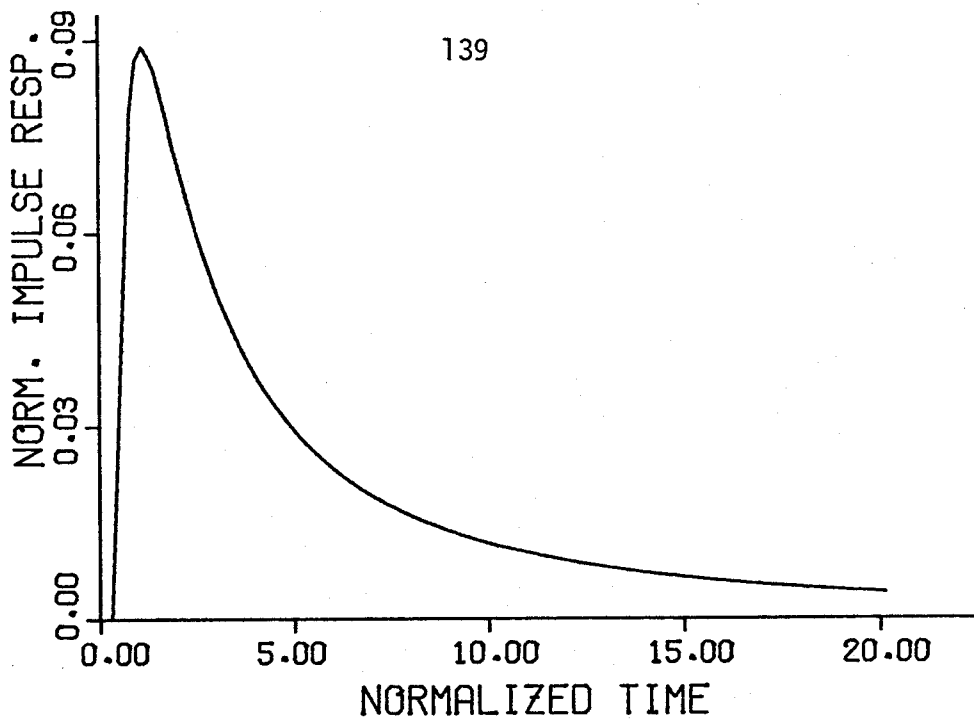
Fig.5-3 Impulse response of beam wave incidence on
semi-infinite medium : linear scale
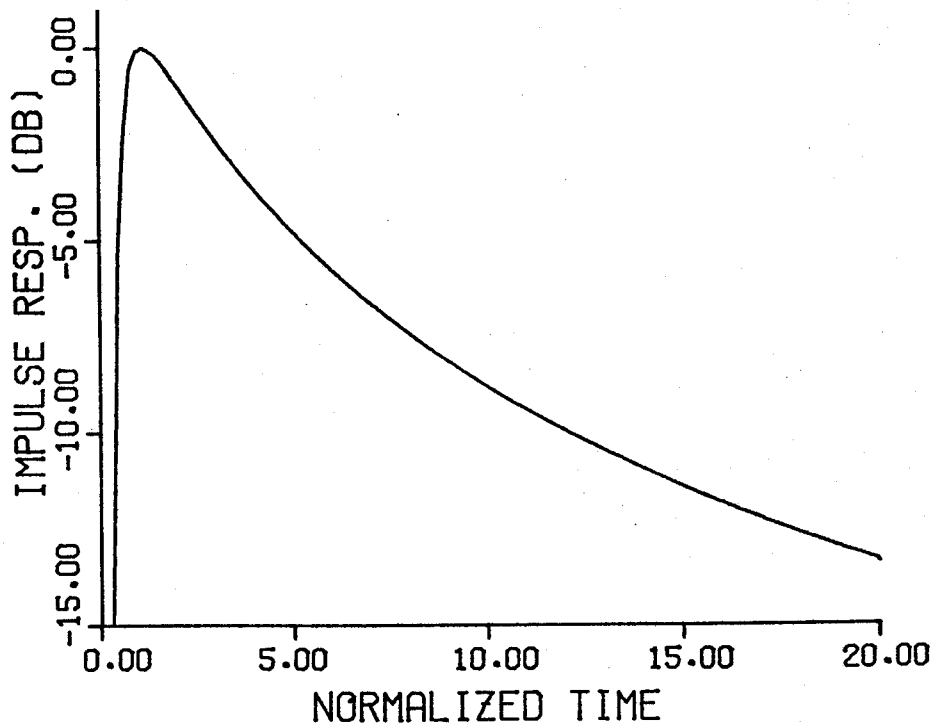
Fig.5-4 Impulse response of beam wave incidence on
semi-infinite medium : log-scale (dB)
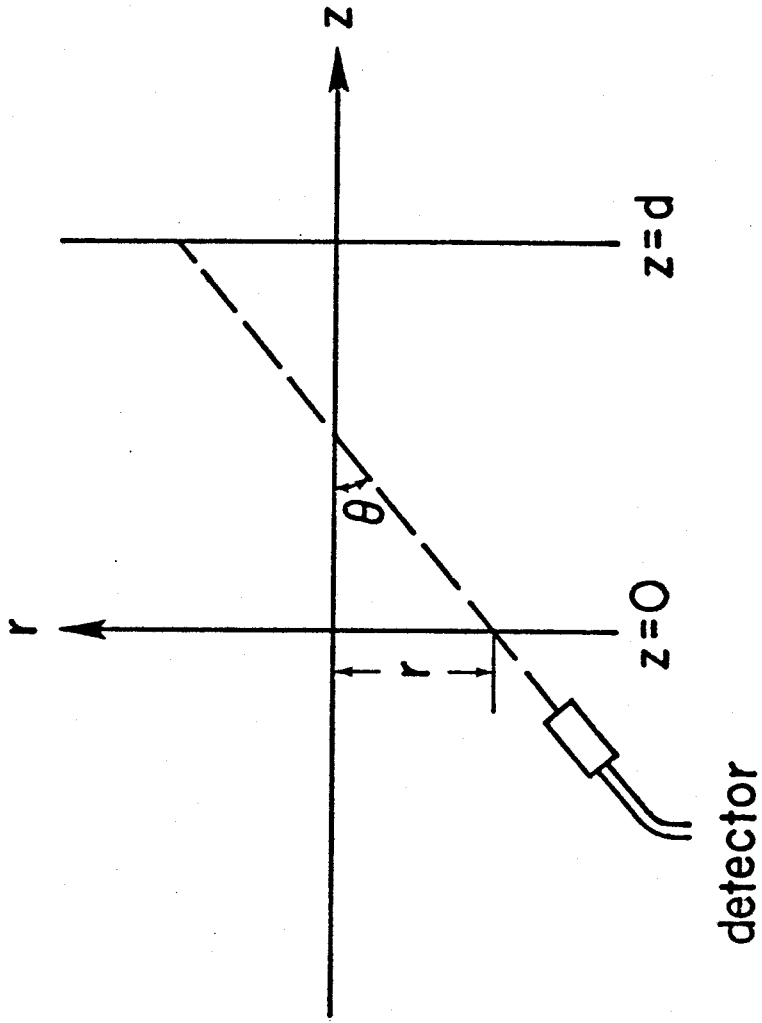
Fig.5-5 Geometry of observation

Fig.5-6 Effect of radial distance (r) of detector :
from the top, r = 0.1, 1.0, 1.5, θ = 150°,
beam width W = 1.0, 2.02 μmφ spheres

Fig.5-7 Effect of observation angle (θ) of detector :
from the top θ = 180°, 150°, 120°, 90°,
2.02 μmφ spheres, r = 1.0, W = 1.0

142

d (μmφ)	μ̄
45.4	0.930
5.7	0.901
0.481	0.849
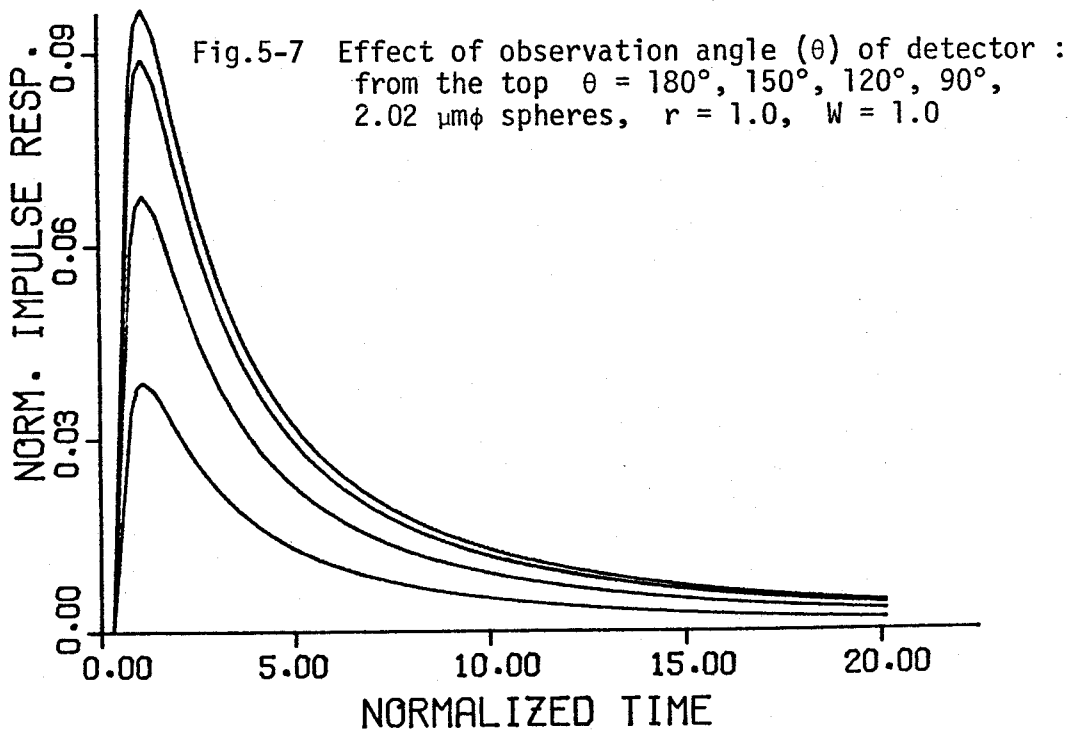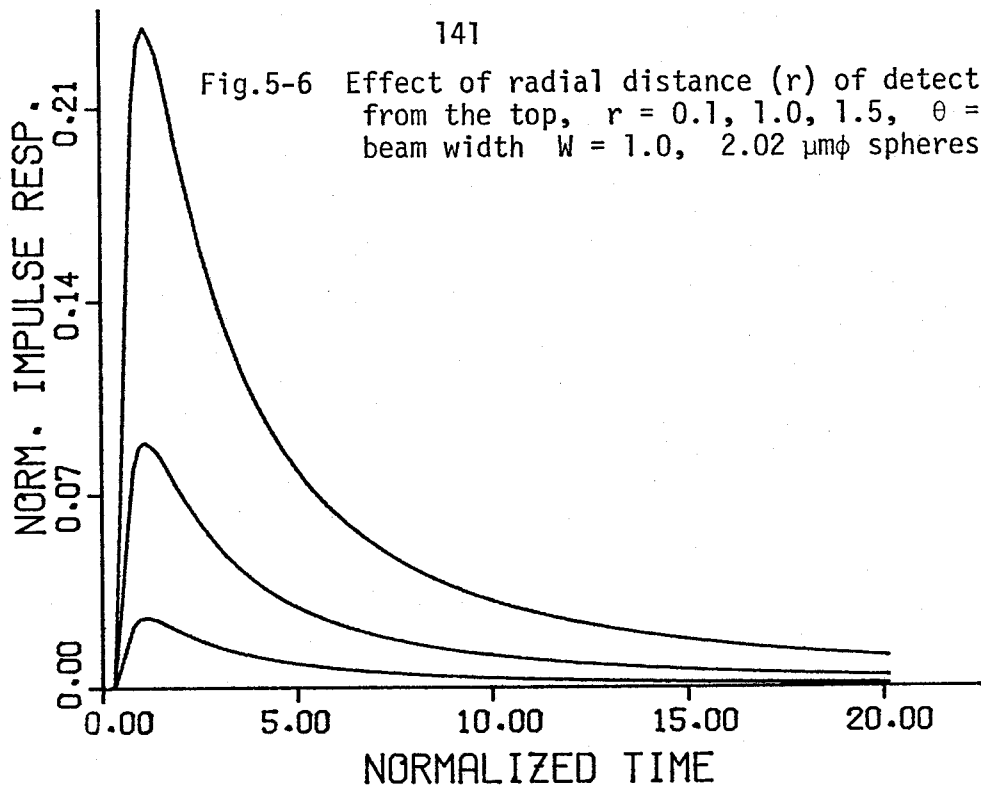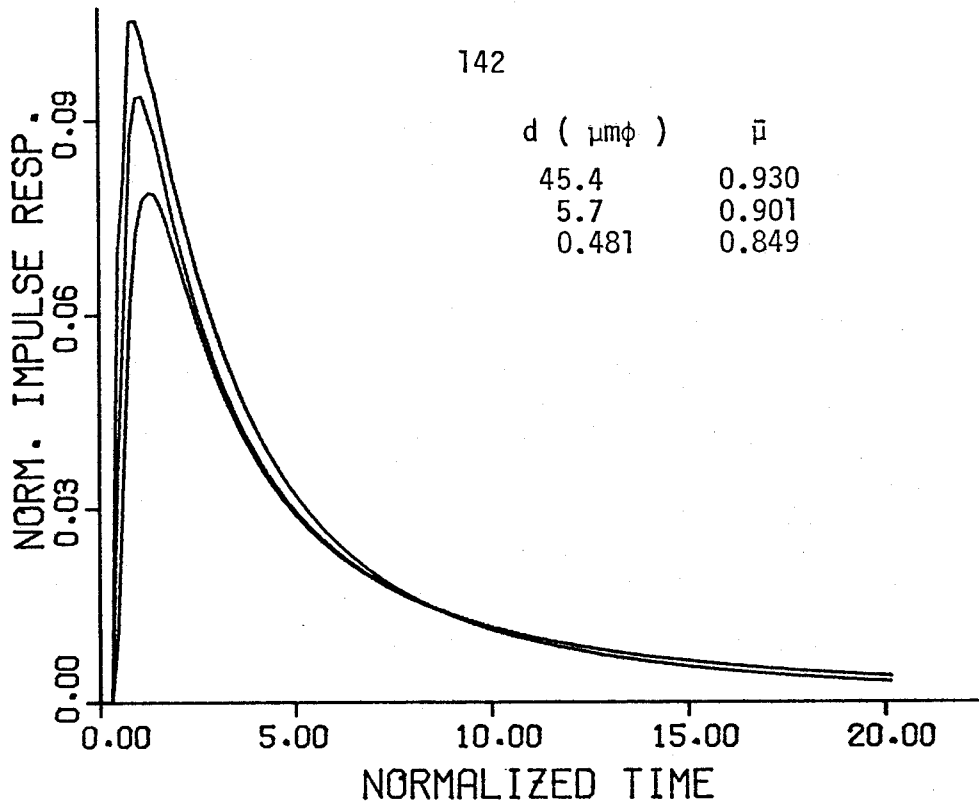
Fig.5-8 Effect of sizes of scatterers :
d = diameter, μ̄ = average cosθ
θ = 150°, r = 1.0, W = 1.0

W_0 =	1.00
	0.95
	0.90
	0.85
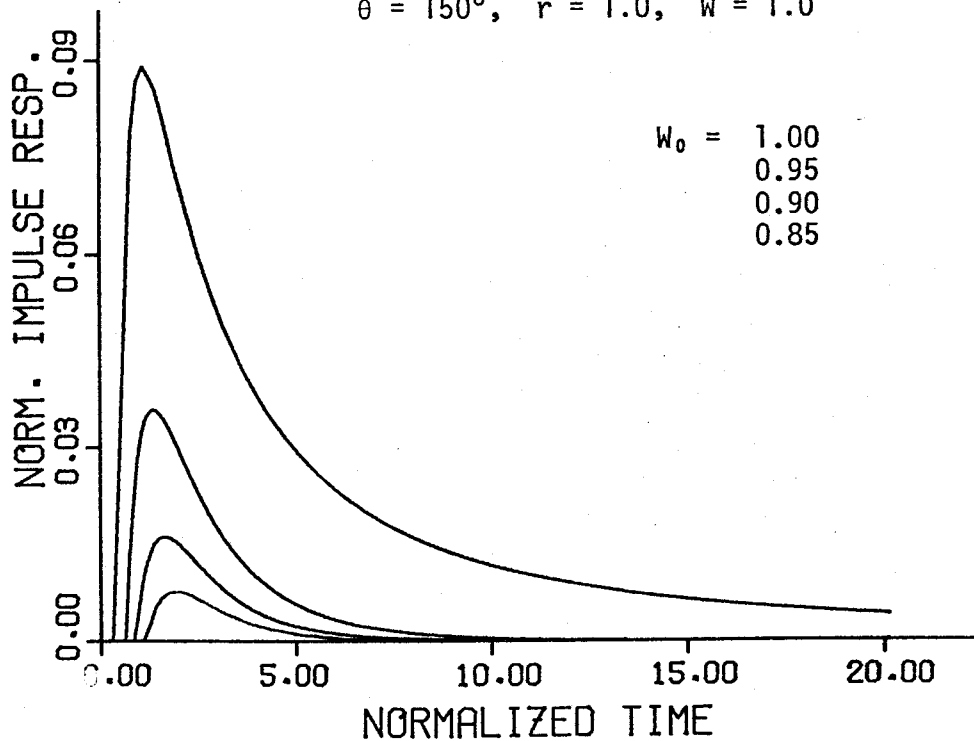
Fig.5-9 Effect of absorption of scatterers : 2.02 μmφ spheres,
W_0 = σ_s / σ_t = albedo, θ = 150°, r = 1.0, W = 1.0

BEAM WAVE[143]
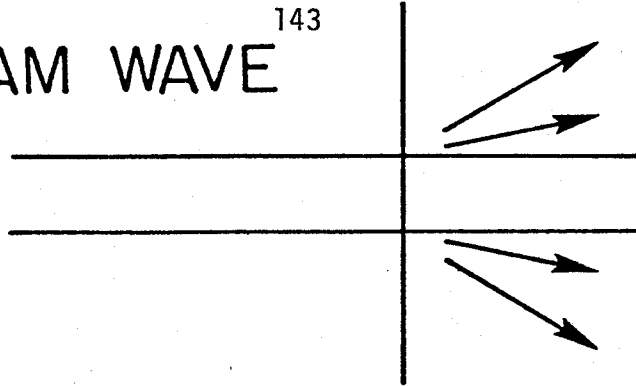
QUASI-
SPHERICAL
WAVE
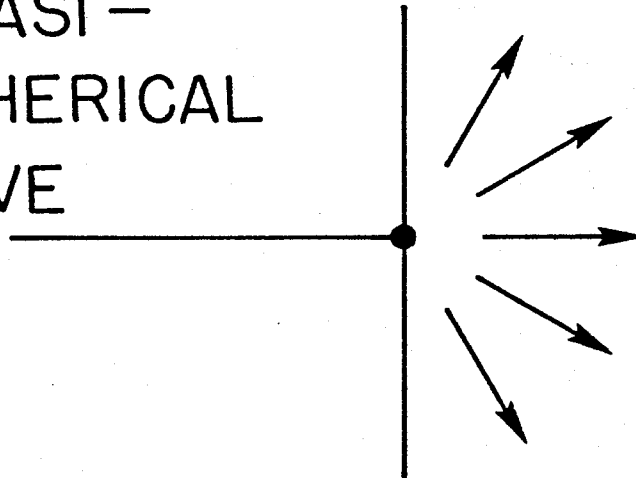
POINT
SOURCE
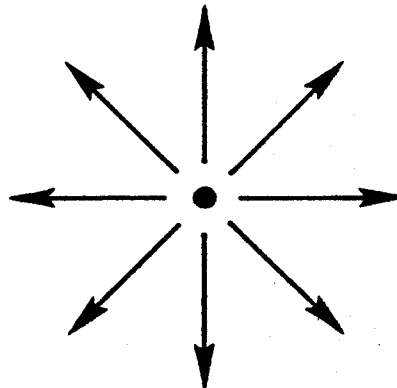
Fig.5-10   Concept of quasi-spherical wave
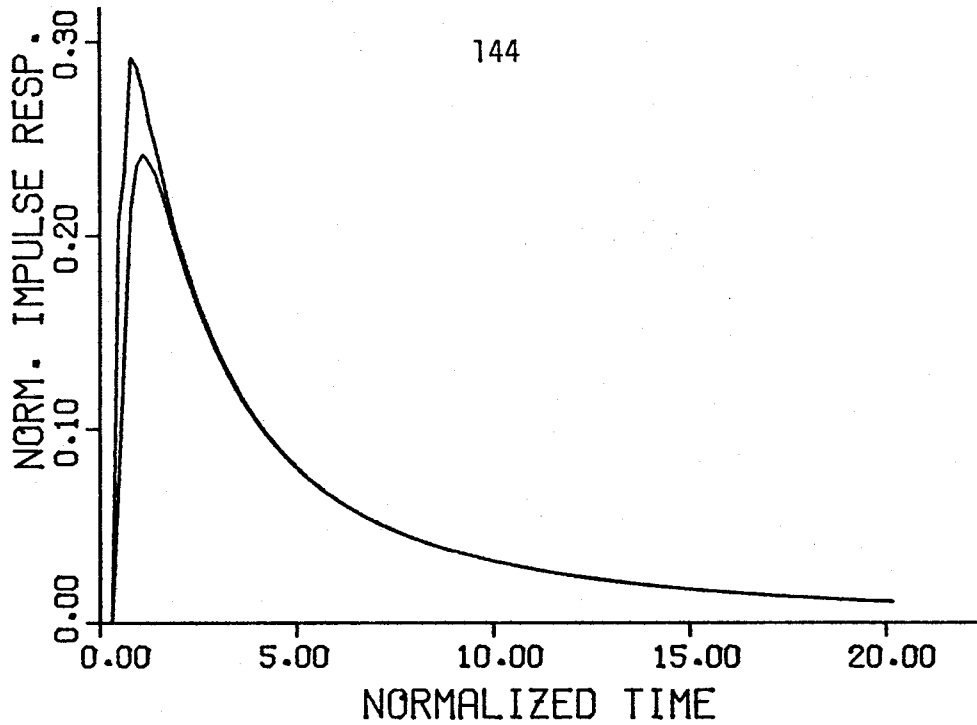
Fig.5-11   Impulse responses of plane wave incidence on
           semi-infinite medium : 45.4 $\mu m\phi$ and 2.02 $\mu m\phi$
           spheres, θ = 150°
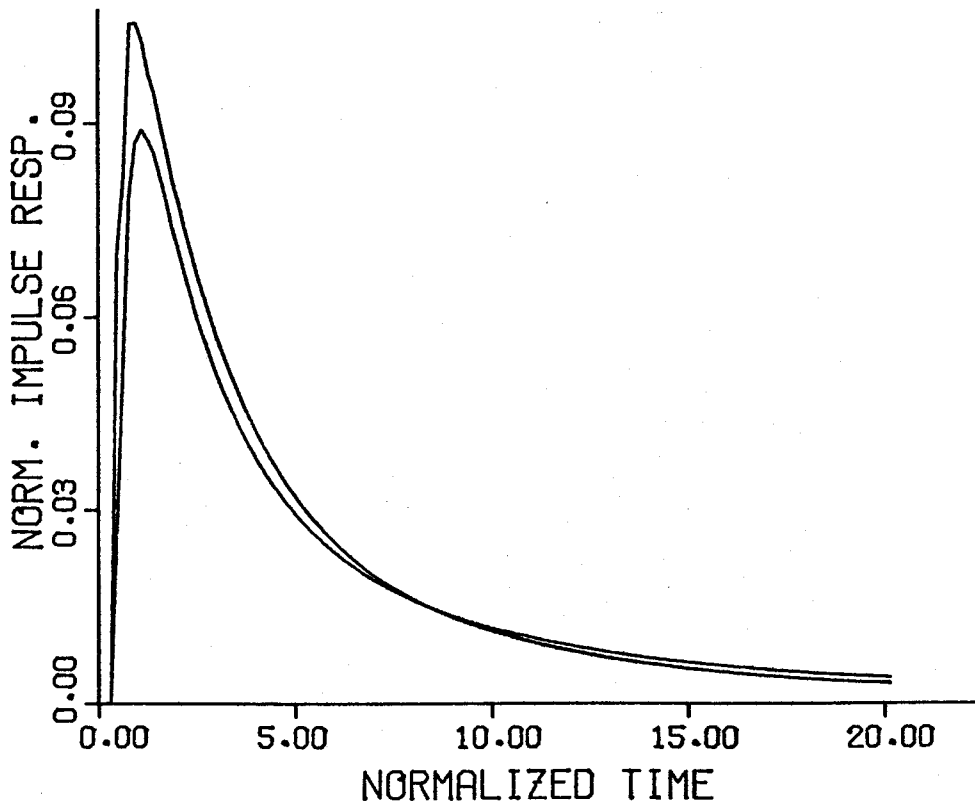
Fig.5-12   Impulse responses of beam wave incidence on
           semi-infinite medium : 45.4 $\mu m\phi$ and 2.02 $\mu m\phi$
   spheres, θ = 150°,   r = 1.0,   W = 1.0
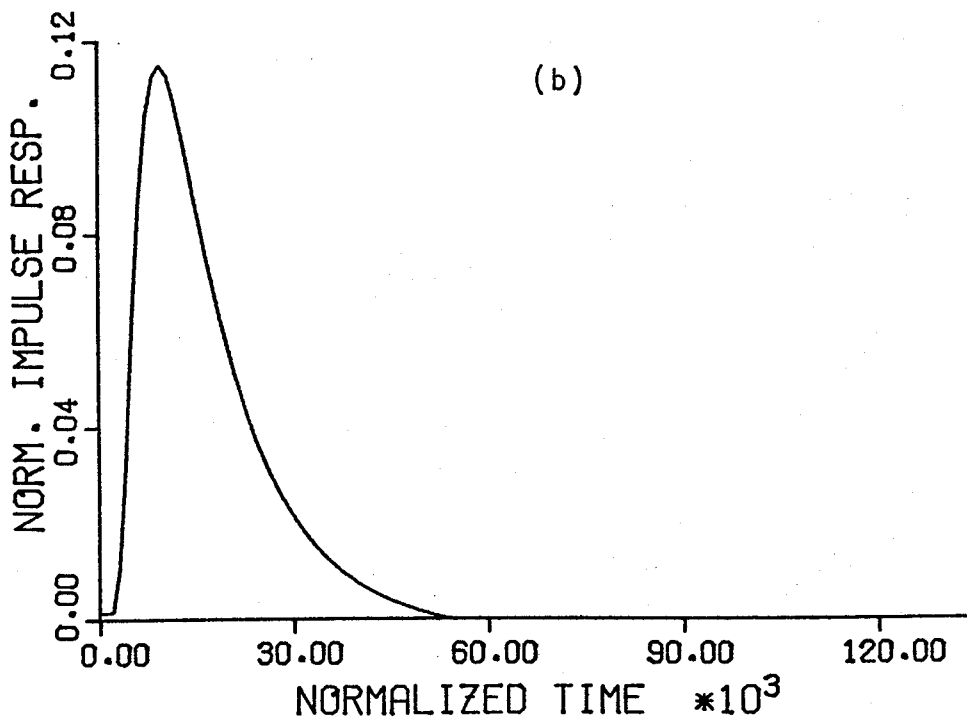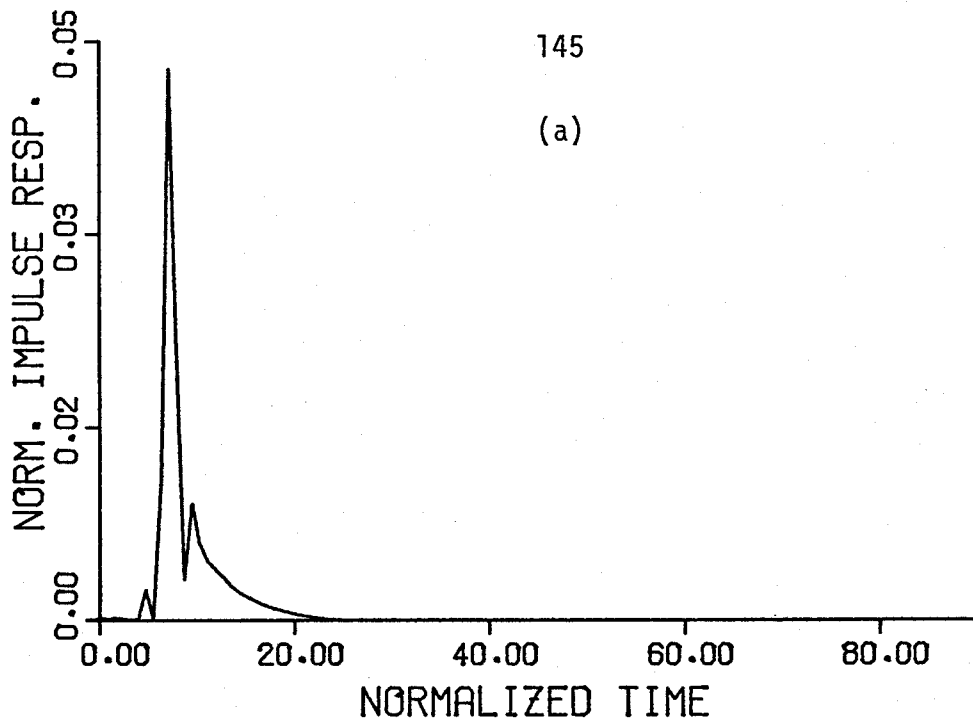
Fig.5-13   Impulse responses of quasi-spherical wave incidence
           on semi-infinite medium :   r = 1.0, ϕ = 90°,
 θ = 150°,   (a) 45.4 μmϕ spheres,   (b) 2.02 μmϕ
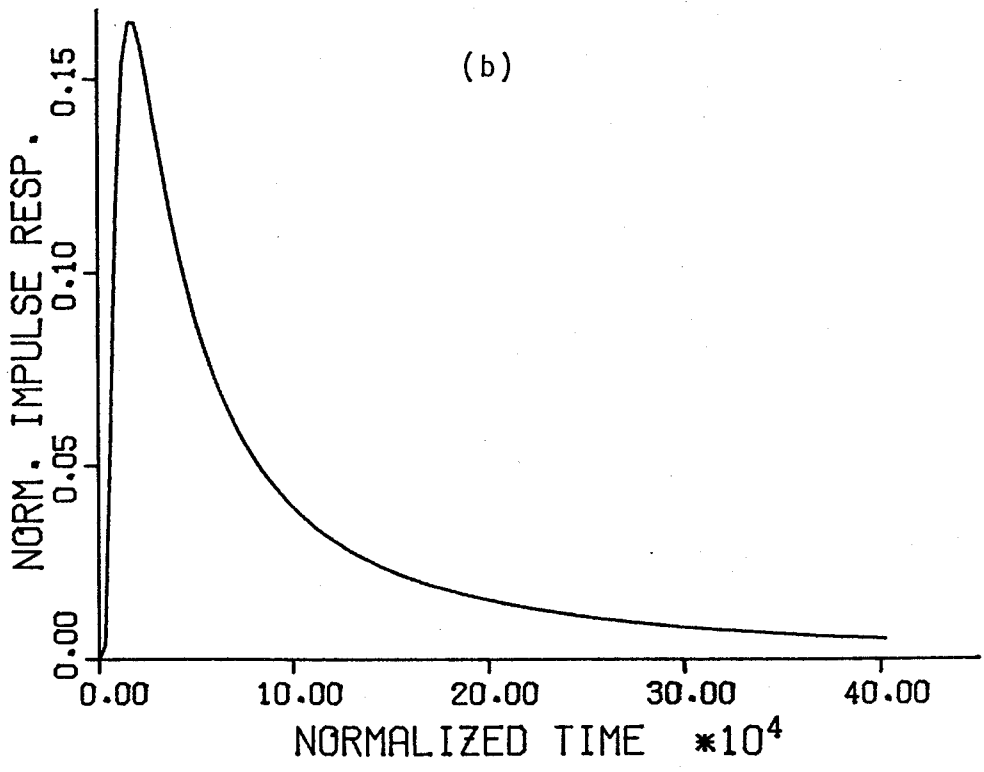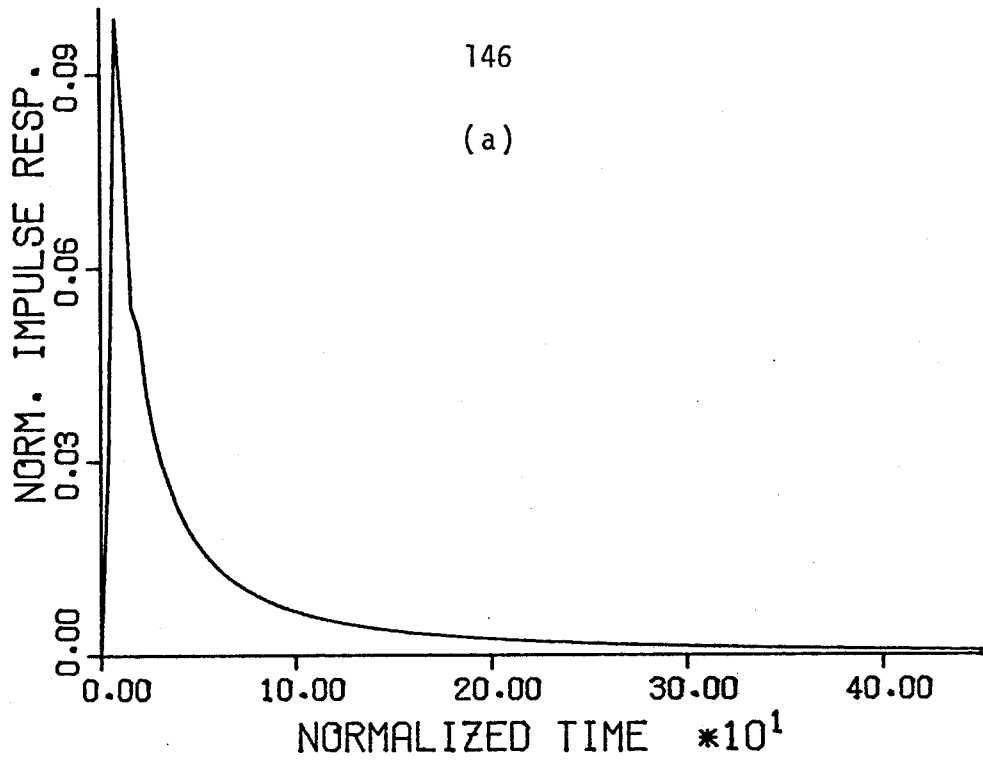
Fig.5-14 Impulse responses of point source at the origin :
r = 1.0, (a) 45.4 μmφ spheres, (b) 2.02 μmφ
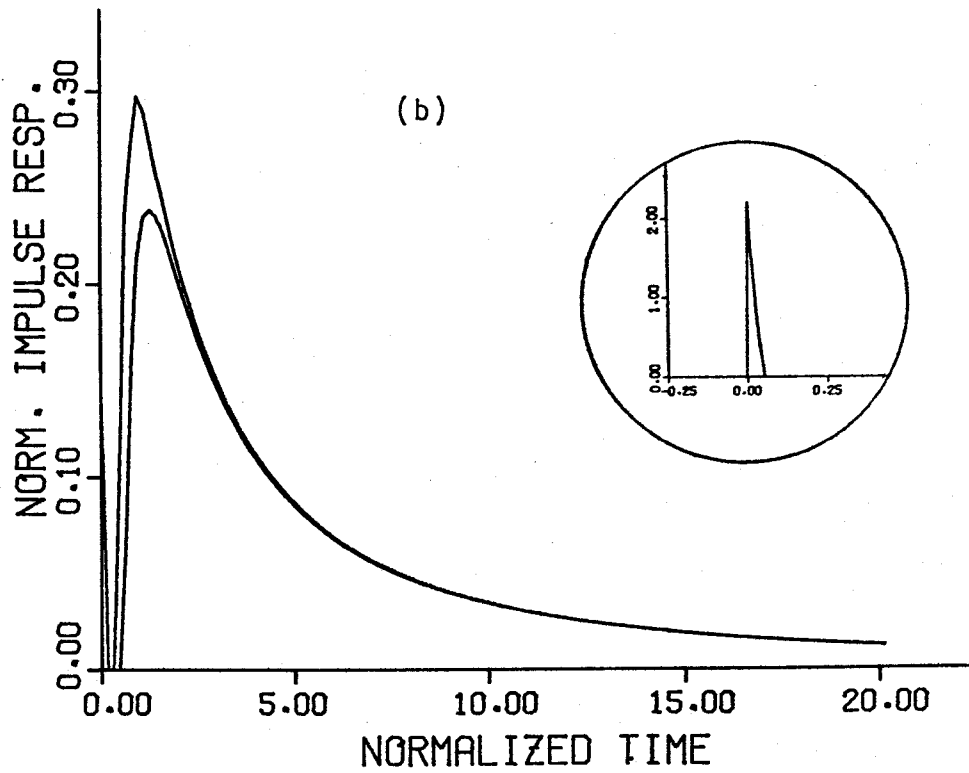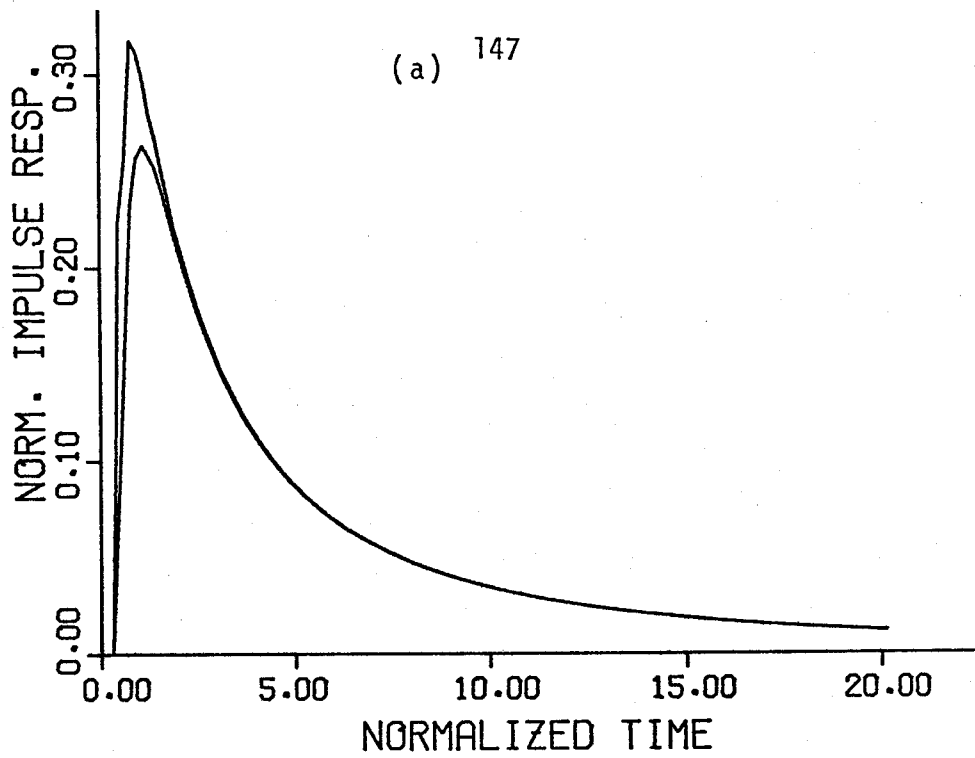
Fig.5-15 Inclusion of first order multiple scattering effect :
(a) diffusion only, (b) modified to include FOMS .

dia.	std. dev. mean	σ_b	σ_s	$\bar{\mu}$	$\dfrac{I_{d1}}{I_{d2}}$
(μm)	(%)	(μm^2)	(μm^2)		
0.481	0.374	0.0176	0.186	0.849	9.94E-3
2.02	0.668	0.253	7.96	0.886	3.29E-3
3.20	5.94	11.3	20.1	0.871	5.86E-2
5.7	26.3	88.4	59.4	0.890	1.54E-1
5.7 abs.	26.3	85.2	59.4	0.891	1.48E-1
45.4	19.6	3945.	3428.	0.928	1.18E-1

Table 5-1

Effect of First Order Multiple Scattering Relative to Diffusion

since

$$I_d(\omega=0) = \int_0^\infty I_d(t)\, e^{i\omega t}\, dt \,\big|_{\omega=0} = \int_0^\infty I_d(t)\, dt$$

$$= \text{energy of the pulse},$$

$I_{d1}(\omega=0) \,/\, I_{d2}(\omega=0)$ gives the energy ratio between the scattered signals due to FOMS and diffusion,

where

$$I_{d1}(\omega=0) \,/\, I_{d2}(\omega=0) = \frac{\sigma_b}{6\sigma_s} \,/\, \left(\frac{7}{6} + \frac{\bar{\mu}}{2}\right)$$

for $\sigma_a = 0$.

Chapter VI

FOUR PHASES OF SCATTERING

VI.1   INTRODUCTION

Although light scattering is an old subject dating back to the
study of the blue color of the sky in the late nineteenth century,
there is no exact solution available which describes the propagation
and scattering through the entire spectrum of scatterer densities.
Various theories and approximations have been developed for each
specific density region and have been used successfully (Ishimaru,
1978a, p. 69) (Ishimaru, 1977). However, the boundaries of their
valid range are not always clear.

In Chapter V, the solutions to the diffusion equation were ob-
tained for different geometries. Their behavior at time-origin could
give some idea on the inapplicable range but a more rigorous analysis
is required to determine the range of validity.

In this chapter, one method is proposed to classify the different
types of scattering according to the scatterer density. The justifi-
cation for this classification is shown in scattering patterns, the
graphs of scattered intensity as a function of scatterers density, and
visual observations of collimated light beam in the scattering medium.
Based on these results, the correlation between measurement and theory
is investigated on the first order multiple scattering and diffusion
approximations.

VI.2   THEORY

VI.2.1 ρ-dependence of Tenuous Medium

Assume that a plane wave impulse is incident on a slab of scatterers and that the scattered intensity is range-gated in the impulse shuttering time $\delta(t - t_o)$. The received intensity was obtained in Eq. (4-6), which is

$$I_{rec}(\bar{r},\hat{s}) = F_i \frac{\rho |\bar{f}(\hat{s},\hat{z})|^2}{1 + \cos\Theta} e^{-\rho\sigma_t c t_o} \qquad (6\text{-}1)$$

where ρ is the number density of the scatterers. See Fig. 6-1 and Section IV.2.1 for the definitions of other parameters. Considering ρ as an independent variable, Eq. (6-1) has a maximum at

$$\rho_{max} = \frac{1}{\sigma_t c t_o} \qquad (6\text{-}2)$$

When range-gating is not applied, or the shutter is kept open, the received intensity is given by Eq. (4-7), which is

$$I_{rec}(\bar{r},\hat{s}) = F_i \frac{|f(\hat{s},\hat{z})|^2}{1 + \cos\Theta} \frac{1}{\sigma_t c} (1 - e^{-\rho\sigma_t c t_d}) \qquad (6\text{-}3)$$

This equation shows the ρ-dependence in the form of the function $f(x) = 1 - \exp(-x)$.

If we take account of the finiteness of the beam width, pulse length and the range-gating shutter open period, the received intensity is given by Eq. (4-12), which is
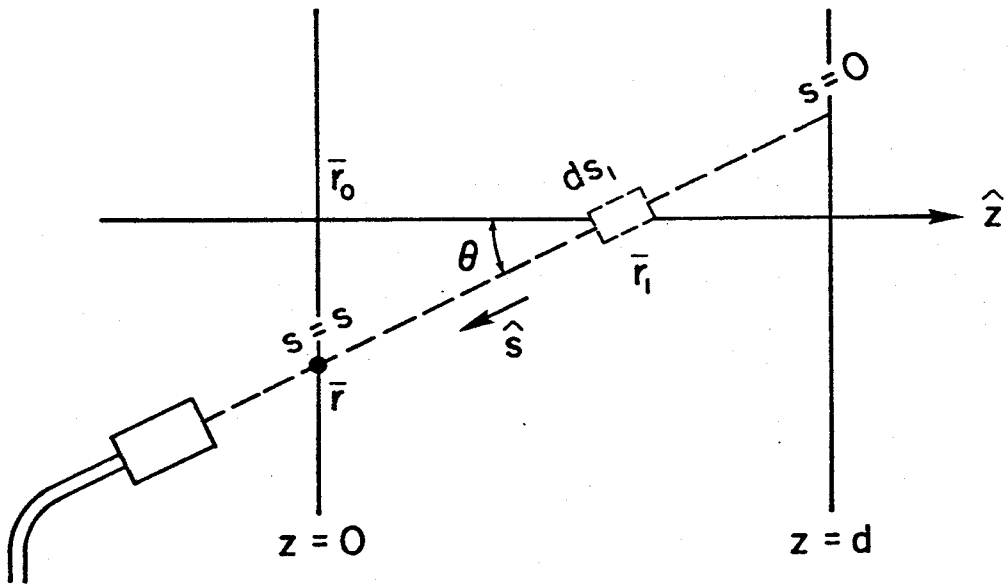
Fig.6-1   Geometry of the problem
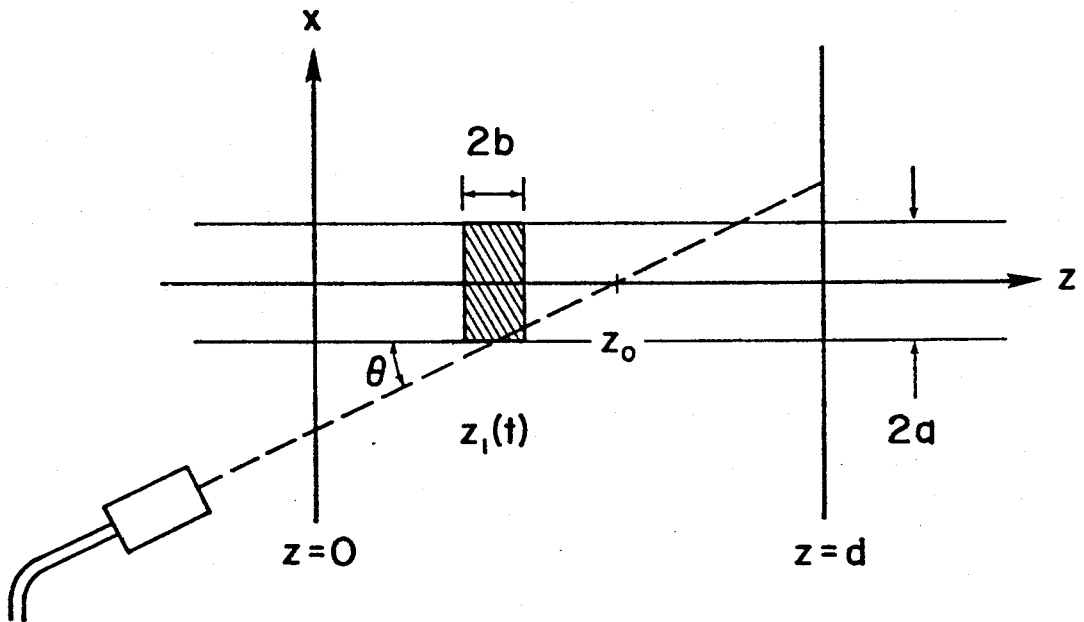
Fig.6-2   Geometry of measurement system

$$I_{rec}(\bar{r},\hat{s}) = F_i \frac{4|\bar{f}(\hat{s},\hat{z})|^2}{\rho\sigma_t^2 c(1 + \cos\Theta)} e^{-\rho\sigma_t c t_o} \sinh\{\rho\sigma_t(1 + \frac{1}{\cos\Theta})b\}$$

$$\times \sinh(\rho\sigma_t c \Delta t) \qquad (6\text{-}4)$$

As was shown in Chapter IV, Eq. (6-4) applies to both the range-gated case and the non-range-gated case with the different definitions of Δt . That is, Δt is half the shutter open period for the range-gated case and $\Delta t = a(1 + \cos\Theta)/c \sin\Theta$ for the non-range-gated case. See Fig. 6-2 and Section IV.2.2 for the definitions of parameters.

Eq. (6-4) has a maximum at

$$\rho_{max} = \frac{1}{2\sigma_t c \Delta t} \ln \left(\frac{t_o + \Delta t}{t_o - \Delta t} \right) \qquad (6\text{-}5)$$

where the following approximation is made use of

$$\sinh \{\rho\sigma_t(1 + \frac{1}{\cos\Theta})b\} \simeq \rho\sigma_t(1 + \frac{1}{\cos\Theta})b$$

since $\rho\sigma_t b \ll 1$ for the tenuous medium. If the sampling point z_o is not close to the front surface of the slab ($z = 0$), the sampling time t_o is much larger than the shutter open period Δt ($t_o \gg \Delta t$). Then the natural-log in Eq. (6-5) is approximated by

$$\ln \left(\frac{t_o + \Delta t}{t_o - \Delta t} \right) = \ln \left(1 + \frac{2 \Delta t}{t_o - \Delta t} \right) \simeq \frac{2 \Delta t}{t_o - \Delta t} \simeq \frac{2\Delta t}{t_o} \qquad (6\text{-}6)$$

and Eq. (6-5) reduces to Eq. (6-2) which was obtained above for the impulse-incident and impulse-shuttering case.

VI.2.2 ρ-dependence of Dense Medium

With dense media, the narrow beam incidence can be approximated by a point source located at the impinging point of the incident beam. The solution of the diffusion equation for the point source case was given in the previous chapter, i.e.,

$$U_d(\bar{r};\omega_1,\omega_2) = \frac{3}{4\pi} \; \alpha_{tr} \frac{e^{-qR}}{4\pi R} \tag{6-7}$$

See Chapter V for the definitions of parameters. The intensity at $\bar{r}$ due to a delta function input pulse at the origin is called the impulse response $G(t)$. It is given by the Fourier transform of the two-frequency mutual coherence function which is proportional to the average intensity U_d (Ishimaru, 1978b), i.e.,

$$G(t) = \int_{-\infty}^{\infty} U_d(\bar{r};\omega_1,\omega_2) \; e^{-i\omega_d t} \; d\omega_d$$

$$= \frac{3}{8\pi Rc} \; e^{-bt}\{ \; a\delta(t - t_0) + \delta'(t - t_0)$$

$$+ a^3 t_0 \frac{I_1(Z)}{Z} + a^4 t t_0 \frac{I_2(Z)}{Z} \; \} \tag{6-8}$$

for $t \geq t_0$. $G(t) = 0$ for $t < t_0$

where $\omega_d = \omega_1 - \omega_2$, $a = \rho\sigma_s(1 - \bar{\mu})c/2$, $b = \rho(\sigma_{tr} + \sigma_a)c/2$

$= a + \rho\sigma_a c$, $t_0 = \sqrt{3} \; R/c$, I_1 and I_2 are modified Bessel functions, and $Z = a(t^2 - t_0^2)^{1/2}$.

With the range-gating synchronized at the time t_1, the received intensity is approximately proportional to $G(t_1)$, if the input pulse and the gating time are short enough to be considered as an impulse. Note that, without range-gating, the received intensity is proportional to $\int_0^\infty G(t)dt$ which is a constant.

To examine the ρ-dependence of the impulse response $G(t)$, Eq. (6-8) can be rewritten as

$$G(t) = A \, \rho^{3/2} \exp(- B\rho) \qquad\qquad \text{for } t > t_0 \qquad (6-9)$$

where

$$A = \frac{3}{8\pi Rc} \frac{t_0}{(2\pi)^{1/2}} \frac{(t^2 - t_0^2)^{1/2} + t}{(t^2 - t_0^2)^{5/4}} \left\{ \frac{\sigma_s(1 - \bar{\mu})c}{2} \right\}^{3/2}$$

$$B = \frac{1}{2} \sigma_s(1 - \bar{\mu})c \left\{ t - (t^2 - t_0^2)^{1/2} \right\} + \sigma_a ct$$

and the asymptotic form $I_n(x) \sim \dfrac{e^x}{(2\pi x)^{1/2}}$ was used. Calculating $\dfrac{\partial}{\partial t} G(t) = 0$, we obtain the number density ρ at which $G(t)$ has a maximum

$$\rho_{max} = 3[\, \sigma_s(1 - \bar{\mu})c \left\{ t - (t^2 - t_0^2)^{1/2} \right\} + 2\sigma_a]^{-1} \qquad (6-10)$$

Since $t - (t^2 - t_0^2)^{1/2} \simeq t_0^2/2t$ for $t \gg t_0$ or $ct \gg \sqrt{3}\, R$, Eq. (6-10) is simplified for the non-absorbing case $(\sigma_a = 0)$ as

$$\rho_{max} = \frac{2ct}{\sigma_s(1 - \bar{\mu})R^2}$$

where c is the velocity of light, t is the sampling time of the

range-gating shutter, and R is the distance of the observation point from the source point at the origin.

If we start from Eq. (5-44) which was obtained by taking the zero limit of the beam width (w→o) in the solution for beam wave incidence, we get a similar result

$$P_{max} = \frac{14}{3} \frac{ct}{\sigma_x(1 - \bar{\mu})R^2}$$

VI.2.3   Normalization for Turbidity Measurement

Although we use matched spectrophotometric cells to contain the sample solution,the matching is not perfect. In addition, the output power of the light source (He-Ne laser) fluctuates during experiments. To overcome these problems, the following normalization technique is developed.

First, we measure the transmission of the suspending medium of the scatterers in two cells. Here, the scatterers are latex microspheres and the suspending medium is the water with surfactant. Their transmissions are given by

$$T(w,a,t_1) = I(t_1) \; \alpha_a \; \exp\{- \tau_w(t_1)\}$$

$$(6\text{-}13)$$

$$T(w,b,t_1) = I(t_1) \; \alpha_b \; \exp\{- \tau_w(t_1)\}$$

where $T(w,a,t_1)$ is the transmission of the water (w) in the cell (a) at the time (t_1), $T(w,b,t_1)$ is the same for the cell (b), $I(t_1)$ is the incident light intensity at t_1, α_a and α_b are

attenuation constants of the cells a and b respectively and
$\tau_w(t_1)$ is the turbidity of the water at t_1 .

Next, the content of the cell b is replaced by the solution
of scatterers. Their transmissions become

$$T(w,a,t_2) = I(t_2) \ \alpha_a \ \exp \ \{ \ - \ \tau_w(t_2) \ \}$$

$$\text{(6-14)}$$

$$T(s,b,t_2) = I(t_2) \ \alpha_b \ \exp \ \{ \ - \ \tau_w(t_2) \ \} \ \exp \{ \ - \ \tau_s(t_2) \ \}$$

where $\tau_s(t_2)$ is the turbidity of the scatterers at the time t_2 .
The ratio of above quantities yields

$$\frac{T(s,b,t_s)/T(w,a,t_2)}{T(w,b,t_1)/T(w,a,t_1)} \ = \ \exp \ \{ \ - \ \tau_s(t_2) \ \} \qquad \text{(6-15)}$$

Finally, we obtain the desired turbidity, free from those problems
mentioned above.

$$\tau_s(t_2) \ = \ - \ \ln \ \{ \ \frac{T(s,b,t_2)/T(w,a,t_2)}{T(w,b,t_1)/T(w,a,t_1)} \ \} \qquad \text{(6-16)}$$

With this technique, the turbidity measurements can be calibrated
over different scatterers as well as over the different times.

VI.3   EXPERIMENTS

VI.3.1   Experimental Facility

The range-gating system described in Section IV.3.1 was used.

In addition, a turbidity measurement system was developed. Fig. 6-3

is a schematic diagram of the system. A beam of He-Ne laser light

(λ = 0.6328 μm) is mechanically chopped by the chopper (CHOP) for

the phase-lock technique. The chopping signal (C) is sent to the

lock-in amplifier (LIA). The lateral and angular position of the

beam is finely controlled by the beam manipulator (BEAM MAN) which

consists of three mirrors actuated by four micrometers. (Molcho,

1975). Intensity of the incident beam is adjusted by two attenuators.

They are the variable neutral density filter (NF_1) and the calibrated

neutral density filter (NF_2). By the combination of these two, the

signal intensity is kept under the saturation level of the detector

and at the same time the measurable range of the lock-in amplifier is

expanded. After passing through the scatterers contained in a spec-

trophotometric cell (SC), the transmitted light is received by the

detector (DET). The detector has a very narrow angle of acceptance

($\sim$ 0.1°) attained by a focusing lens and a field stop pinhole. The

electrical signal from the detector is sent to the lock-in amplifier,

LIA. It is a phase responsive amplifier with a narrow effective

bandwidth. It suppresses various noises by the phase-lock technique

and through signal averaging.

DET   SC   NF$_2$ NF$_1$ C

BEAM   CHOP   LASER
MAN.

LIA → T

C
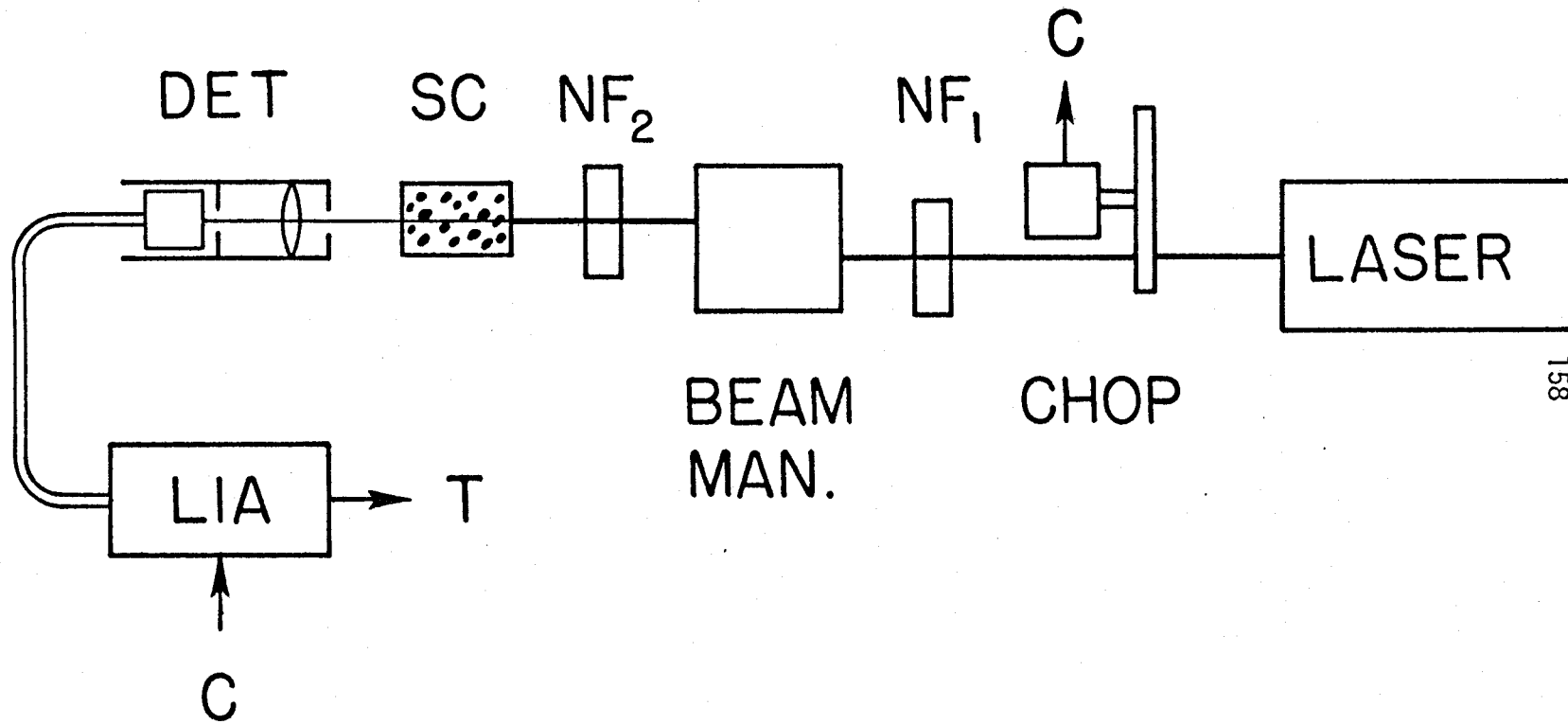
Fig.6-3 Schematic diagram of turbidity measurement

VI.3.2   Backward Scattering Pattern Measurement

Fig. 6-4 illustrates the measurement of the scattering pattern

of backward angles. See Section IV.3 for the detailed discussion.

The scattered intensity is measured at the scattering angle Θ =

$1.83° \sim 29.7°$ with and without range-gating. The method of the

measurement follows the same as that in Section IV.3 except for the

concentration of the scatterers. Here, the concentration is varied

from 10^{-4}% to 10% in weight, which spans from very tenuous to dense

cases. 30% solution is available only for the spheres with 2.02 μm

diameter.

The scattering volume observed by the detecting system is a

1mm diameter cylinder with the length of 2mm in the range-gated

case and about $5 \sim 30$mm for Θ = $30° \sim 5°$ in the non-range-gated

case.

While changing the concentration of the scatterers from tenuous

to dense, the conditions of experiments are kept the same, including

the synchronization time of the range-gating shutter. Thus, when the

scattering medium becomes dense or diffusive, it results in measuring

the tailing part of the scattered pulse where our theory is supposed

to be more accurate than near the peak.

VI.3.3 ρ-dependence Measurement

By the normalization method described in Section IV.3.6, the

scattered intensity can be calibrated over the different measurements.

Therefore, the scattering patterns obtained above for different con-

centrations give us the ρ-dependence of the scattered intensity, as
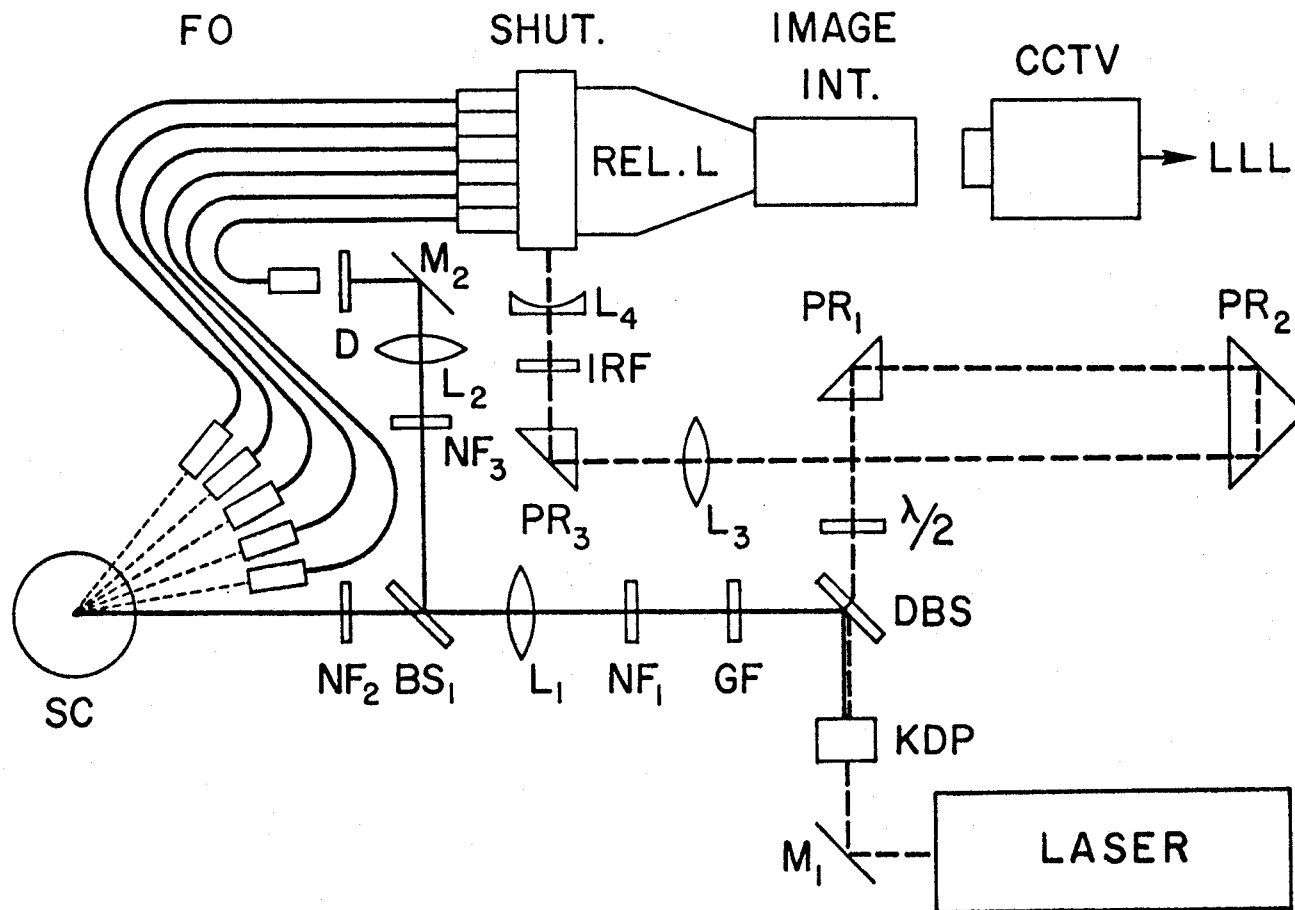
Fig.6-4 Schematic of range-gated backward scattering pattern measurement

well. It should be noted again that the measured intensity of the dense medium is not the peak value of the scattered pulse.

VI.3.4   Turbidity Measurement

In every experiment, the turbidity of the scattering sample is measured, to provide the parameters necessary for the theoretical calculations and to insure that the dilution of the sample solution is done properly.

The short-term stability of the laser within each measurement ($\sim$ a few min.) was fairly good. The long-term instability of the laser and the mismatch among the spectrophotometric cells are calibrated by the normalization technique described in Section VI.2.3. After the normalization, the turbidity of the scatterers is obtained by subtracting the turbidity of the background which is mostly that of the suspending medium.

VI.4   RESULTS AND DISCUSSION

VI.4.1   Backward Scattering Patterns of Tenuous and Dense Media

Fig. 6-5, 6-6 and 6-7 show the backward scattering patterns of latex spheres with 0.481 μm, 2.02 μm and 3.20 μm diameters, respectively. The concentrations of the scatterers vary from 10^{-4}% to 10% by weight. 30% wt. solution was available only for 2.02 μm spheres. Each data point is the average of $3 \sim 7$ shots of the laser. The standard deviation is within 10% of the average, and uncertainty in the scattering angle is ±0.7°.

Each figure shows an interesting transition in the shapes of the patterns as the concentration changes. According to the shape, we can classify the concentrations into four groups. Following the terminology used by Ishimaru (1978a, p. 69), they are referred to as "single scattering," "first order multiple scattering (FOMS)," "multiple scattering" and "diffusion" regions. Fig. 6-8 illustrates the concept. As can be seen in the Figs. 6-5, 6-6 and 6-7, the border of each region is not necessarily clear, but the difference in the patterns is evident. A further justification for this classification is given in the next section.

In the single scattering region, the curves show the patterns characteristic to each size of scatterers. Detailed discussions on the characteristic patterns are given in Chapter IV. The concentration of scatterers is 10^{-4}% $\sim 10^{-3}$% by weight. The optical distance per unit distance $(\rho\sigma_t)$ is $0.02 \sim 0.2$ cm^{-1} . Since the single

scattering approximation is valid in this range, the patterns closely follow the calculations obtained from Mie theory.

In the FOMS region, the patterns become smoothed. However, they still carry the vestiges of the characteristic patterns buried in the smoothed curves. Thus, they are considered as the single-scattering patterns smoothed by the multiple scattering effect. The concentration of scatterers is $10^{-3}\% \sim 10^{-2}\%$ by weight and $\rho\sigma_t$ is $0.2 \sim 2.0$ cm^{-1}.

In the multiple scattering region, the patterns are more smoothed and the vestiges of the characteristic patterns disappear. They have lost the distinction between the different sizes of scatterers. This loss of identity marks the dividing point of this region from the FOMS region. The dividing point is shown clearly in an alternate way of presenting the scattered intensity, which is discussed in the next section.

This strong smoothing is attributed to the multiple scattering effect which, by the randomness of the scatterers in both position and movement, cancels the orientational effect of each scatterer. Thus, the patterns in this region are characterized by the flat shape or an isotropic scattering. The concentration of scatterers is $10^{-2} \sim$ 1% and $\rho\sigma_t$ is $2.0 \sim 200$.

In the diffusion region, the scattering patterns start peaking up in the small angles. (Hereafter in this chapter, the small angle refers to the angle close to the backward normal.) This phenomena can be explained in the following way. In a dense medium, incident light is attenuated rapidly due to scattering and absorption as it

diffuses. Therefore, when the incident beam is narrow, the light diffuses as if from a point source at the impinging point of the incident beam. Then the scattered intensity is proportional to r^{-2}, where r is the radial distance measured from the impinging point. Since r is proportional to the observation angle Θ if Θ is small, the scattered intensity is proportional to Θ^{-2} which explains the peaking phenomena in the small angles of the scattering pattern. However, if the point source approximation mentioned above is valid, the scattered intensity received should be much smaller, especially in the larger angles. This may be due to the propagation of light through the air-glass-water interfaces or in the glass wall.

The scattering pattern of 10% wt. and 30% wt. concentrations show an interesting local minimum and maximum at $\sim 170°$ and $\sim 165°$ respectively. These correspond to the existence of concentric dark and bright bands around the incident beam. In fact, they can be observed with the naked eye when a beam of continuous wave laser is incident on a dense medium. The dark band can be seen also on the side of the scattering cell. Their appearance is shown in Fig. 6-9, where a beam of a He-Ne laser incident on the face of the scattering cell. They are compared with the case of 1% solution.

VI.4.2   Four Phases of Scattering

Fig. 6-10 shows the scattered intensity as a function of the scatterers density (ρ) with the different focal depths (f.d.) of the receiver. The curves in the figure are the measurements with latex

spheres (2.02 μm dia) at a fixed scattering angle (θ = ~11°). Here, the classification proposed in the previous section is clearly shown. See Fig. 6-11 also in the following discussion.

From the left, the linearly rising part of the curves corresponds to the single scattering region (①, ρ = 10^{-4}% ~10^{-3}% wt.). In this region, scattered intensity is proportional to the density of the scatterers and the curve is close to the straight line with a slope of 1. As the density increases, the curve separates from the linear increase, reaches a maximum, and decreases. This is due to the attenuation of incident light and scattered light along their propagation paths. Thus, this part corresponds to the FOMS region (②, ρ = 10^{-3}% ~10^{-2}% wt.). As can be seen in the figure, the deeper the focal depth is (the longer is the propagation path), the more attenuation is suffered by the scattered intensity. In the lower two cases (f.d. = 1.04 cm and 1.43 cm), the scattered intensity went down below the level of measurement noise. The upper two curves (f.d. = 0.497 cm and 1.04 cm) were obtained with the old facility (Bruckner, 1978a), the lowest measurable level of which is one order of magnitude higher than the present facility (Shimizu, 1979).

As the density increases, the scattered intensity becomes observable again. Now, multiple scattering becomes predominant and the light observed does not follow the same path as in the previous case. The photons are scattered back and forth between the scatterers and lose their original directionality. Thus, they reach the receiver through various paths. Since the more scatterers send more photons

to the receiver through this mechanism, the received intensity

increases almost linearly as the density of scatterers increases.

This part corresponds to the multiple scattering region (③, ρ =

$10^{-1} \sim 1\%$ wt.).

As the density of scatterers increases further, the light starts

diffusing. Since photons encounter many scatterers in a short dis-

tance, the scattering becomes isotropic and as a whole, light propagates

in a diffusing manner. In this phase, the light is attenuated rapidly

due to the many scattering as it propagates. Thus, it results in the

decrease of the received intensity as the density of scatterers

increases. This part corresponds to the diffusion region. (④,

$\rho > 1\%$ wt.). The difference of the scattering can be observed in a

visual observation with naked eyes. Their appearances are shown in

Fig. 6-11.

VI.4.3 ρ-Dependence of Dense Media

Figs. 6-12, 6-13, and 6-14 show the ρ-dependence of the scattered

intensity for latex spheres with 0.481, 2.02 and 3.20 μm diameters,

respectively. Each figure consists of a measurement with range-gating

(a), theoretical calculations (b), and measurement without range-gating

(c). Each data point is the average of $3 \sim 7$ shot of the laser. The

standard deviation is within 10% of the average.

First, we compare the measurements with range-gating for different

sizes of scatterers, i.e., Figs. 6-12(a), 6-13(a) and 6-14(a). In the

single scattering and the FOMS regions, the curves appear different

for different sizes of scatterers, while in the multiple scattering

and the diffusion regions, they are much similar. This is attributed to the following. In the latter regions, the multiple scattering averages out the characteristics of microscopic scattering from each particle, and the macroscopic scattering from a collection of particles becomes similar. While in the former regions, the difference in the microscopic scattering appears also in the macroscopic scattering.

Next, a comparison is made between the cases with and without range-gating, i.e., (a)'s and (c)'s in Figs. 6-12, 6-13 and 6-14. The non-range-gated case corresponds to the quasi-CW case discussed before (IV.4.3). The incident wave is a pulse but the range-gating shutter is kept open by the quarter-wave plate. Thus, the measured intensity is the time-integration of the received pulse intensity.

The difference in the magnitude of the curves for different receiving angles (1.83°, 11.0°, 20.2° and 29.3°) is much larger in the non-range-gated case than the range-gated case. Note that in Figs. 6-13(c) and 6-14(c), the curves for $\theta = 1.83°$ were shifted down by the amount shown in the captions. The difference is more evident in the lower density $(\rho < 10^{-2}\%$ wt.) than in the higher one. This difference is attributed to the change in the scattering volume as the receiving angle θ changes. $(\sim 1/\sin\theta)$. With range-gating, a constant scattering volume is sampled regardless of the receiving angle, thus eliminating the factor $1/\sin\theta$. Detailed discussion on this effect of range-gating is given in Section IV.4.5. When the density of scatterers is high, the scattering volume is

located along the boundary and the change in the scattering volume ($1/\cos\Theta$) is negligible if the receiving angle Θ is small. Thus, little difference can be seen between the cases with and without range-gating.

Lastly, the measurements with range-gating and theoretical calculations are compared, i.e., (a)'s and (b)'s in Figs. 6-12, 6-13 and 6-14. The theoretical curves in the low density region ($\rho < 10^{-2}$% wt.) were calculated by Eq. (6-4) and those in the high density region ($\rho > 10^{-2}$% wt.) by Eq. (6-9). The equations are based on the FOMS approximation and the diffusion solution for a point source, respectively. The point source solution was chosen on consideration of the beam width (1mm radius) and the radial distance of the observation points (0.46, 2.7, 5.0 and 7.3 mm for 1.83°, 11.0°, 20.2°, and 29.3°). Since, in the low density region, there is little difference among the curves for different angles (almost within the thickness of the line), only the one for $\Theta = 11°$ was shown. The vertical position of the calculated curve in the low density region was adjusted so that its maximum coincide with the center of the maxima of measurements for $\Theta = 11.0°$ and 20.2°. The vertical positions of the calculated curves in the high density region were adjusted so that the center of maxima for $\Theta = 11.0°$ and 20.2° coincides with that of the measurement. Therefore, the relative magnitude between the curves of low density and high density region is not exact. However, in the high density region, the relative magnitude among the curves of different observation angles is exact.

The theoretical calculations and the measurements agree well in the low density region. More discussion is given in Section IV.4.4. In the high density region, the agreement between theory and measurement is poor in the location of maxima and the attenuation of scattered intensity in higher density.

The locations of maxima in the low density region and the high density region are given in Tables 6-1 and 6-2. The theoretical values were obtained by Eqs. (6-5) and (6-11) based on the FOMS approximation and the diffusion solution for a point source, respectively. In Table 6-1, the agreement between the theory and the measurement is very good. In Table 6-2, the calculated values are consistently larger than those measured, however, the difference is within an order of magnitude. Note the agreement in large angles. This discrepancy in the small angles can be attributed to the impropriety of the point source assumption.

Fig. 6-15 shows the diffusion solutions for a point source and for a plane wave incidence along with the measurements observed at an angle $\theta = 11°$. All three curves were normalized by their peak values. As expected, the peak of the measurement lies between the two solutions which are two asymptotic cases of the beam wave solution. See Sections V.2.4 and V.2.6 for the detailed discussions. As a whole, the measurement follows the plane wave solution better than the point source solution. This corresponds to the similarity of the impulse responses between the beam wave case and the plane wave case discussed in Section V.4.4. Note their agreement in the slope of the curve at

~10% wt. density.

Although the plane wave solution describes well the density-dependence at each receiving angle independently, it cannot show the effect of the radial distance of the observation point which is a function of the receiving angle in our geometry. Therefore, in Figs. 6-12, 6-13 and 6-14, the point source solutions are compared against measurement to see the general behavior of the scattered intensity for different receiving angles. The curves calculated for the different angles by the plane wave solution, lie very close each other, while by the point source solution, they lie more separated than the measurements. This suggests again that our experiment falls in between these two extreme cases.
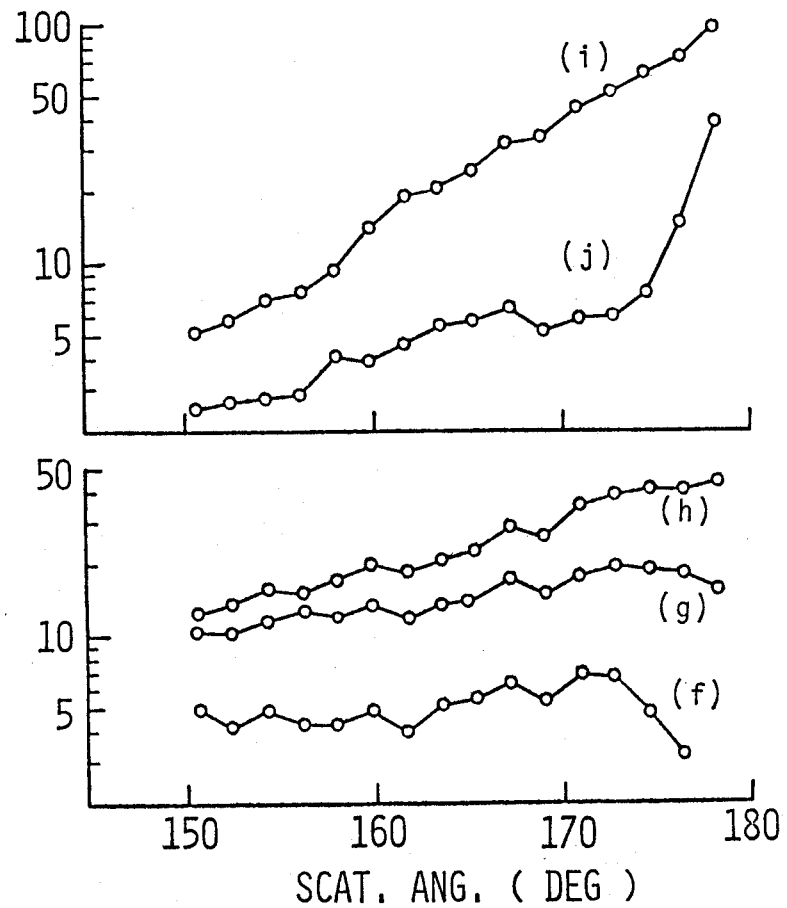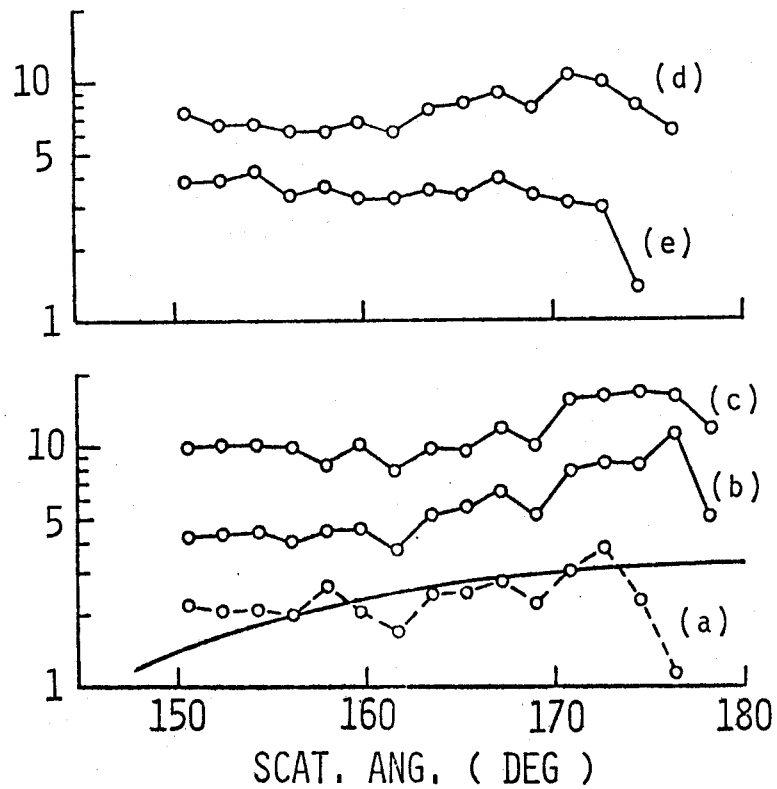
Fig.6-5 Backward scattering patterns of 0.481 μmφ latex spheres :
particle concentrations in weight %, (a) 0.0001,
(b) 0.0003, (c) 0.001, (d) 0.003, (e) 0.01, (f) 0.03,
(g) 0.1, (h) 0.3, (i) 1.0, (j) 10.0

171
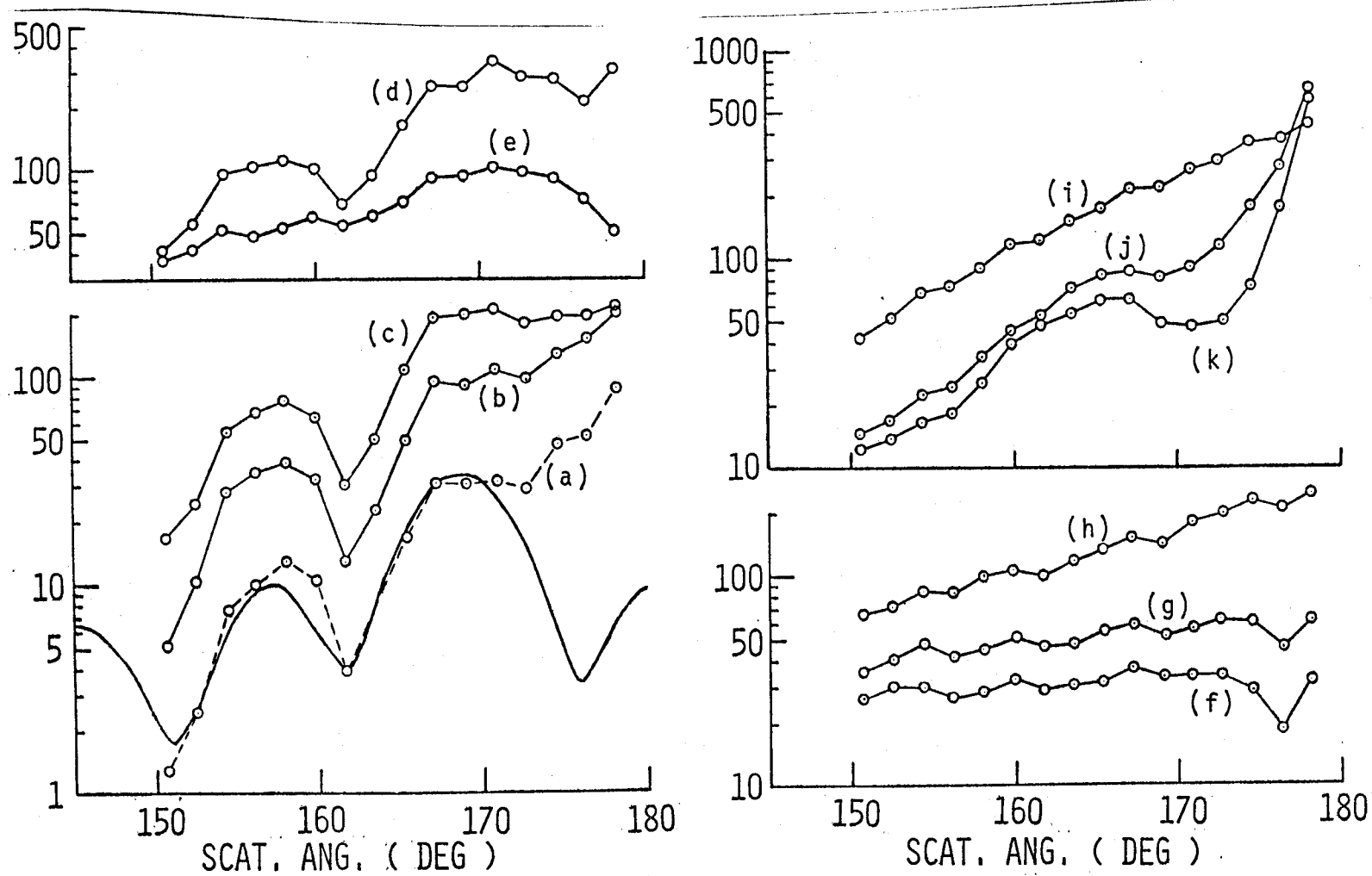
Fig.6-6 Backward scattering patterns of 2.02 μmφ latex spheres :
particle concentrations in weight %, (a) 0.0001,
(b) 0.0003, (c) 0.001, (d) 0.003, (e) 0.01, (f) 0.03,
(g) 0.1, (h) 0.3, (i) 1.0, (j) 10.0, (k) 30.0

172
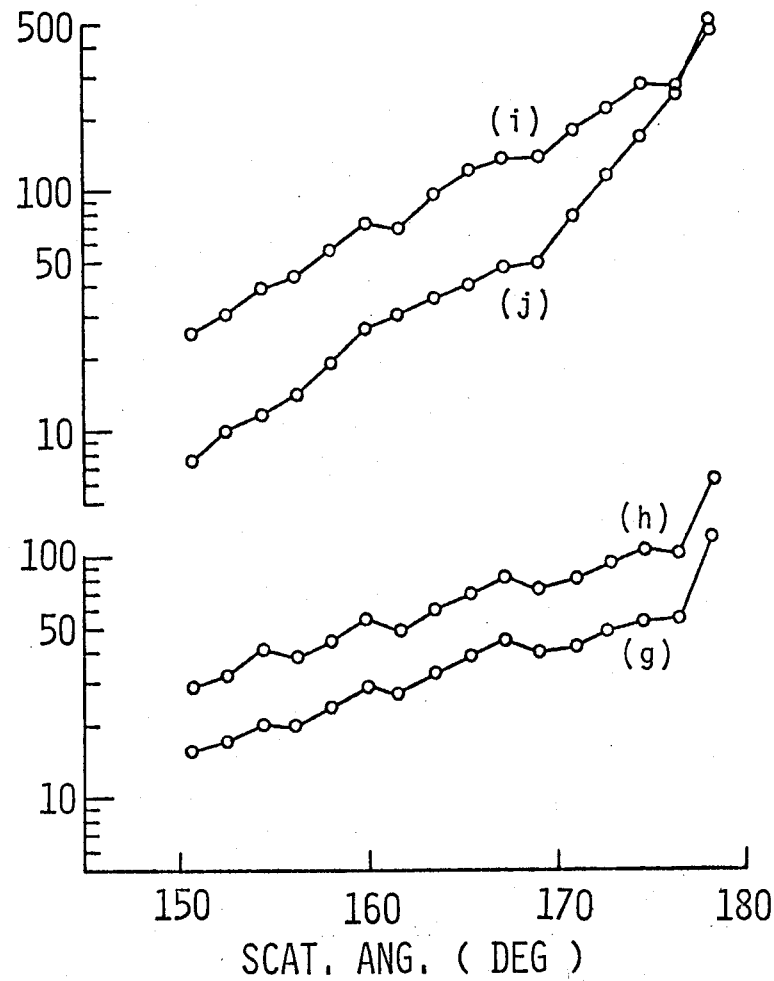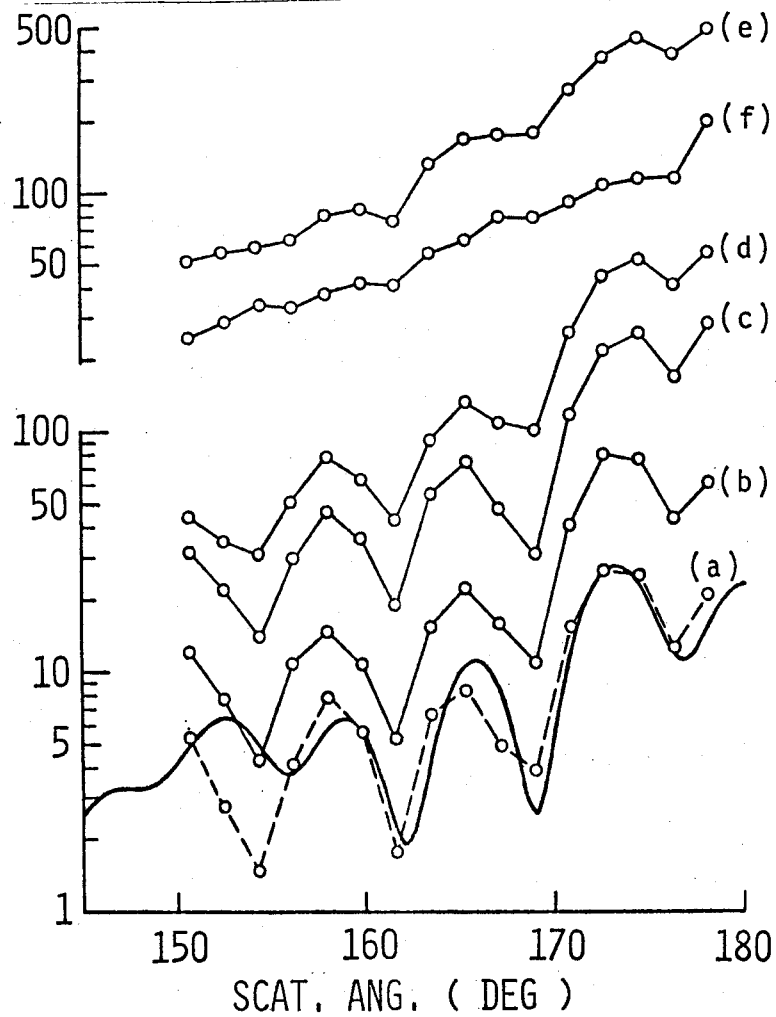
Fig.6-7 Backward scattering patterns of 3.20 μmφ latex spheres :
particle concentrations in weight %, (a) 0.0001,
(b) 0.0003, (c) 0.001, (d) 0.003, (e) 0.01, (f) 0.03,
(g) 0.1, (h) 0.3, (i) 1.0, (j) 10.0

173

174

S.S.
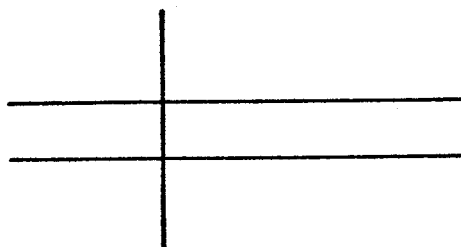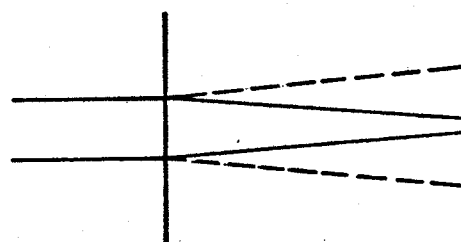
FOMS

M.S.
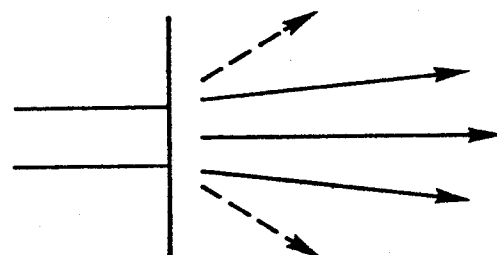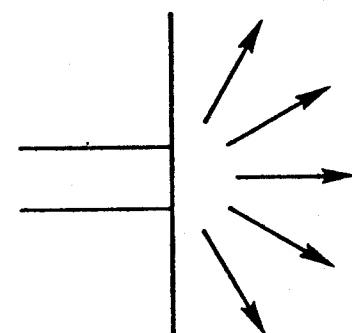
DIFF.

Fig.6-8 Concept of four phases of scattering :
         single scattering (S.S.), first order multiple
         scattering (FOMS), multiple scattering (M.S.),
         diffusion (DIFF.)
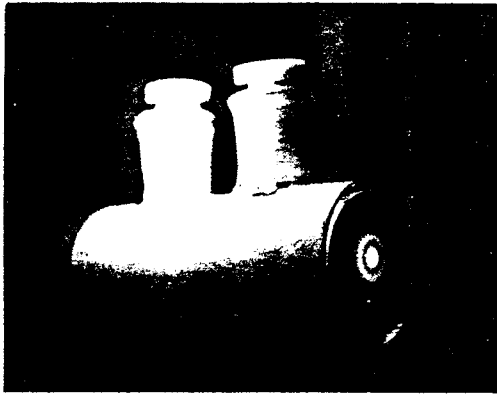
(a)

(c)
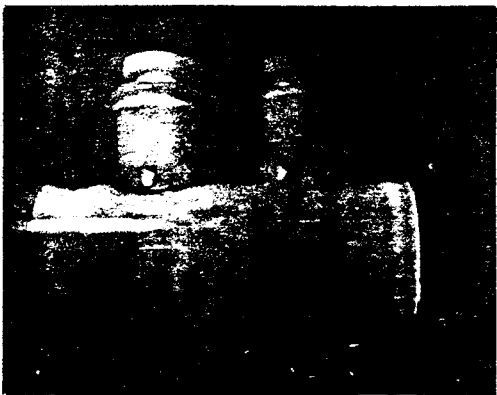
(b)
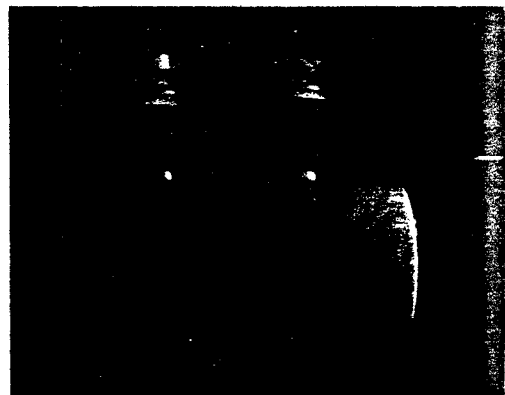
(d)

Fig.6-9 Dark and bright bands on dense solution of latex spheres :
collimated beam of He-Ne laser on 2.02 µmϕ spheres,
(a) frontal view of 10 % solution, attenuation of incident
beam ND = 2.3, f 16, 1/60 sec. (b) side view of 10 % sol.
ND = 0, f 16, 1/15 sec. (c) frontal view of 1 % solution,
ND = 2.3, f 16, 1/60 sec. (d) side view of 1 % sol.
ND = 1.0, f 16, 1/8 sec.
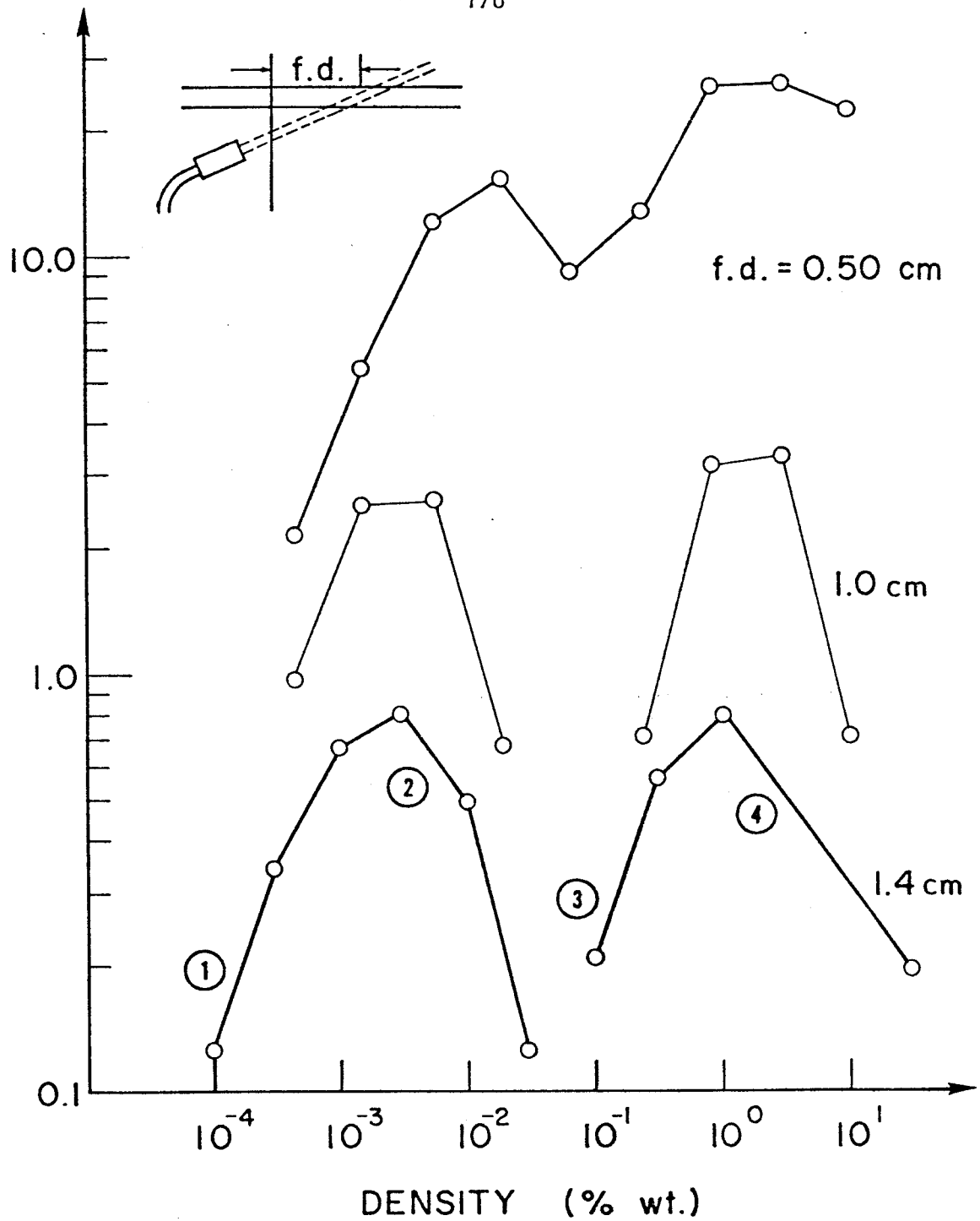
Fig.6-10 Four phases of scattering : Scattered intensity vs.
scatterer density with different focal depths,
① single scattering, ② first order multiple
scattering, ③ multiple scattering, ④ diffusion
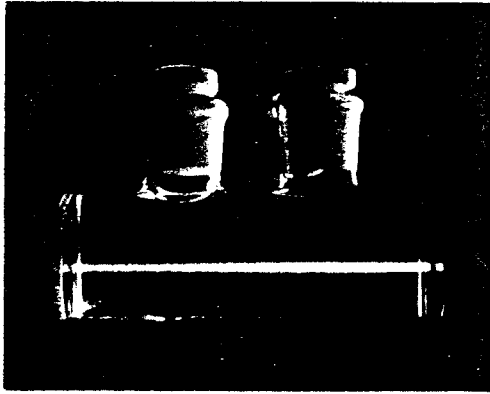
(a)
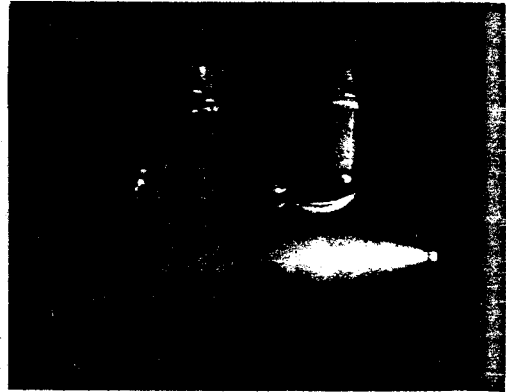
(b)
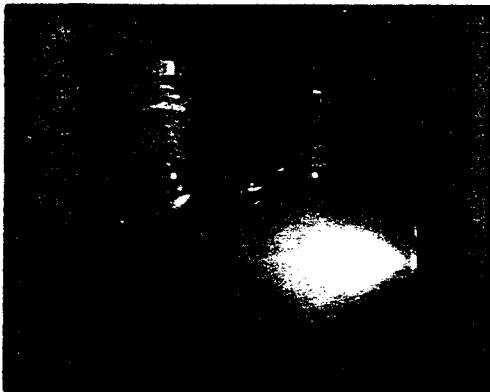
(c)

(d)

Fig.6-11   Visual observation of different phases of scattering :
collimated He-Ne laser impinged on aqueous solutions
of 2.02 $\mu m\phi$ latex spheres,   (a) particle concentration
$\rho = 0.001$ % wt., f 16, 1/8 sec,   (b) $\rho = 0.01$ % wt.
f 16, 1/60 sec,   (c) $\rho = 0.03$ % wt., f 16, 1/8 sec,
(d) $\rho = 0.1$ % wt., f 16, 1/15 sec.   See Fig.6-9 for
the cases of 1 % and 10 % solutions.
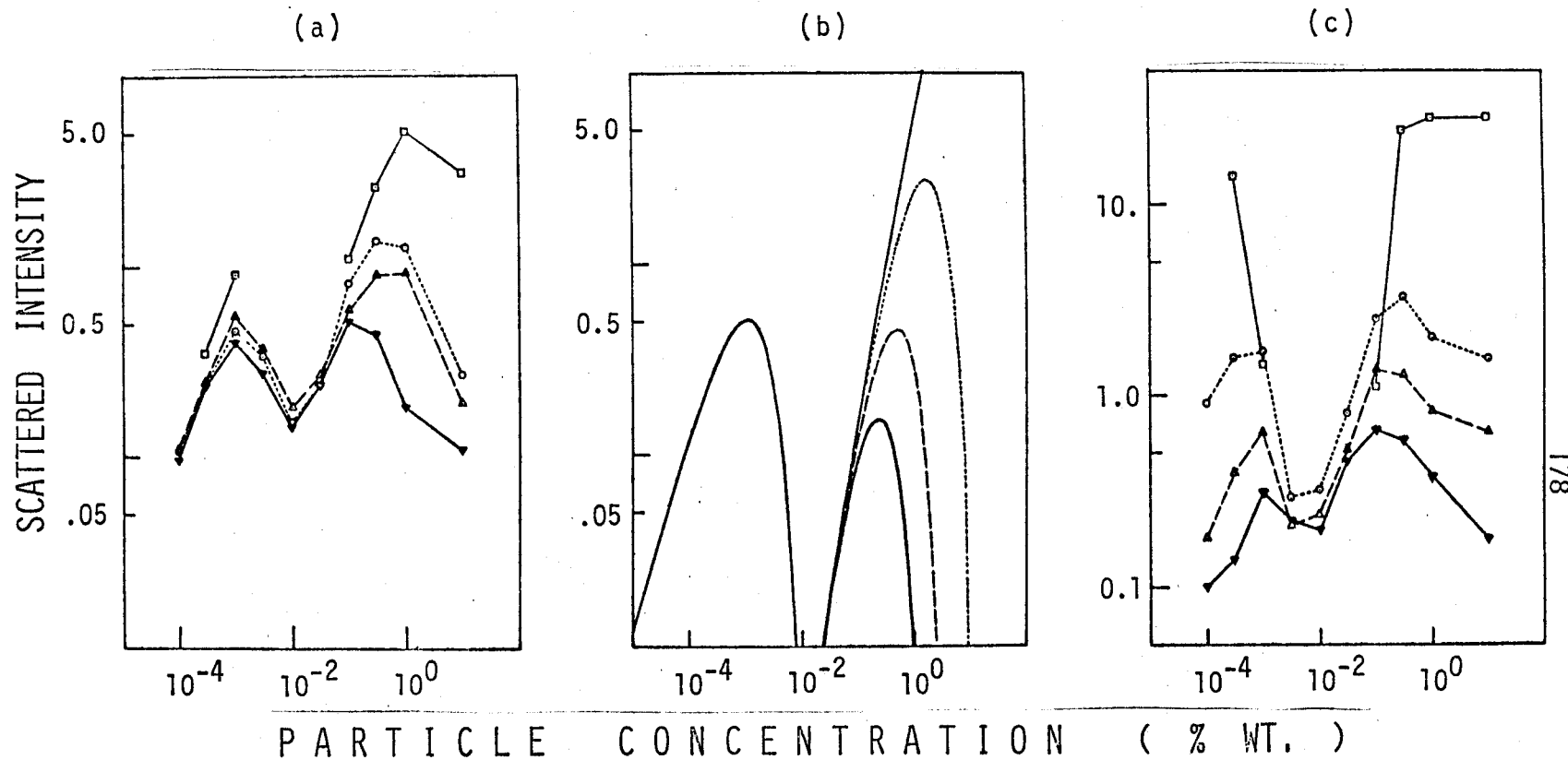
Fig.6-12 Scattered intensity vs. scatterer density : 0.481 μmφ latex spheres,
scattered angles, 1.83° (———), 11.0° (·····), 20.2° (-----),
29.3° (———), (a) range-gated measurements, (b) theoretical
calculations, (c) non- range-gated measurements

178
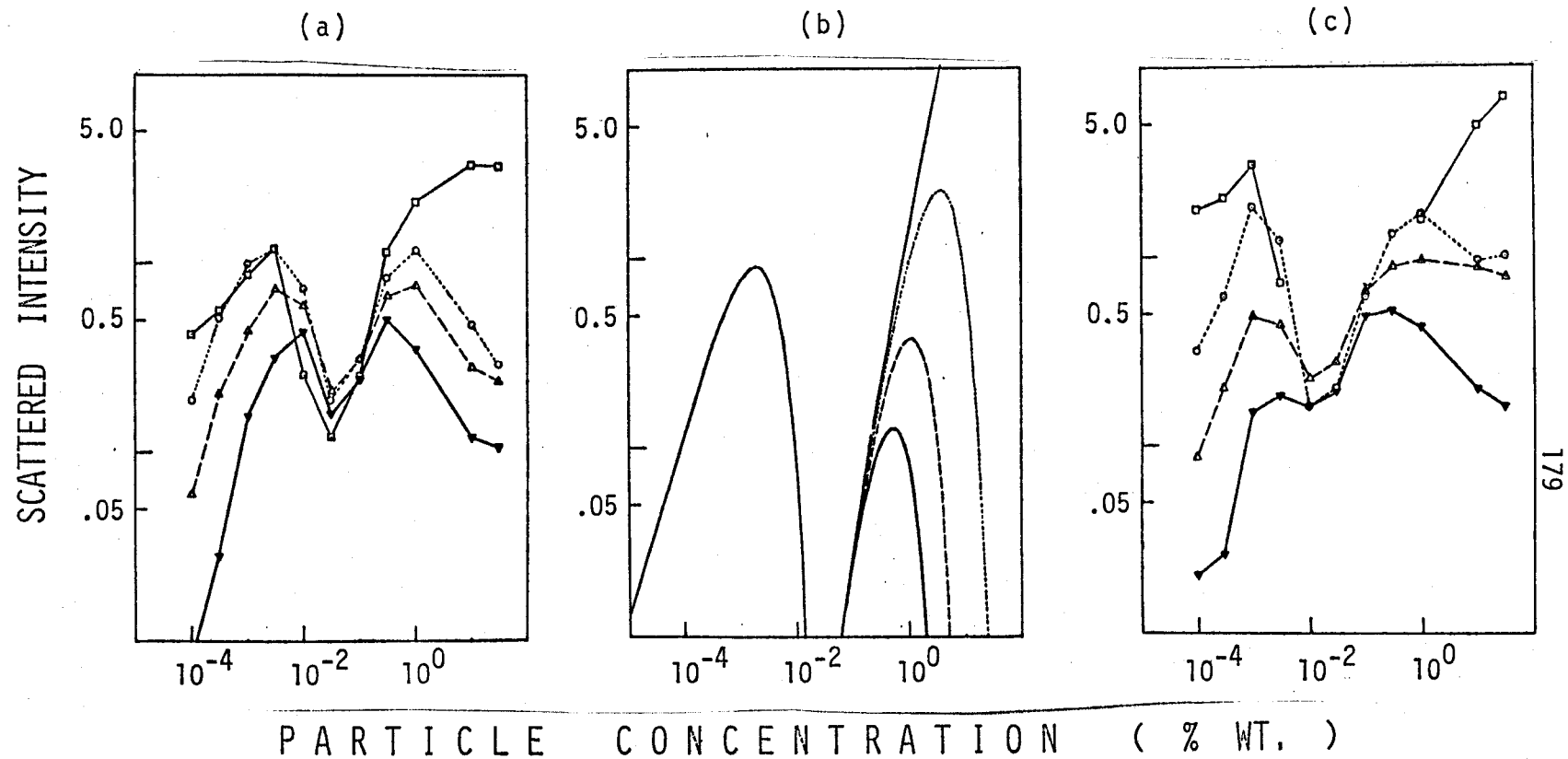
Fig.6-13 Scattered intensity vs. scatterer density : 2.02 μmφ latex spheres, scattered angles, 1.83° (———), 11.0° (·····), 20.2° (-----), 29.3° (———), (a) range-gated measurements, (b) theoretical calculations, (c) non-range-gated measurements, 1.83° case was lowered down by 1/3
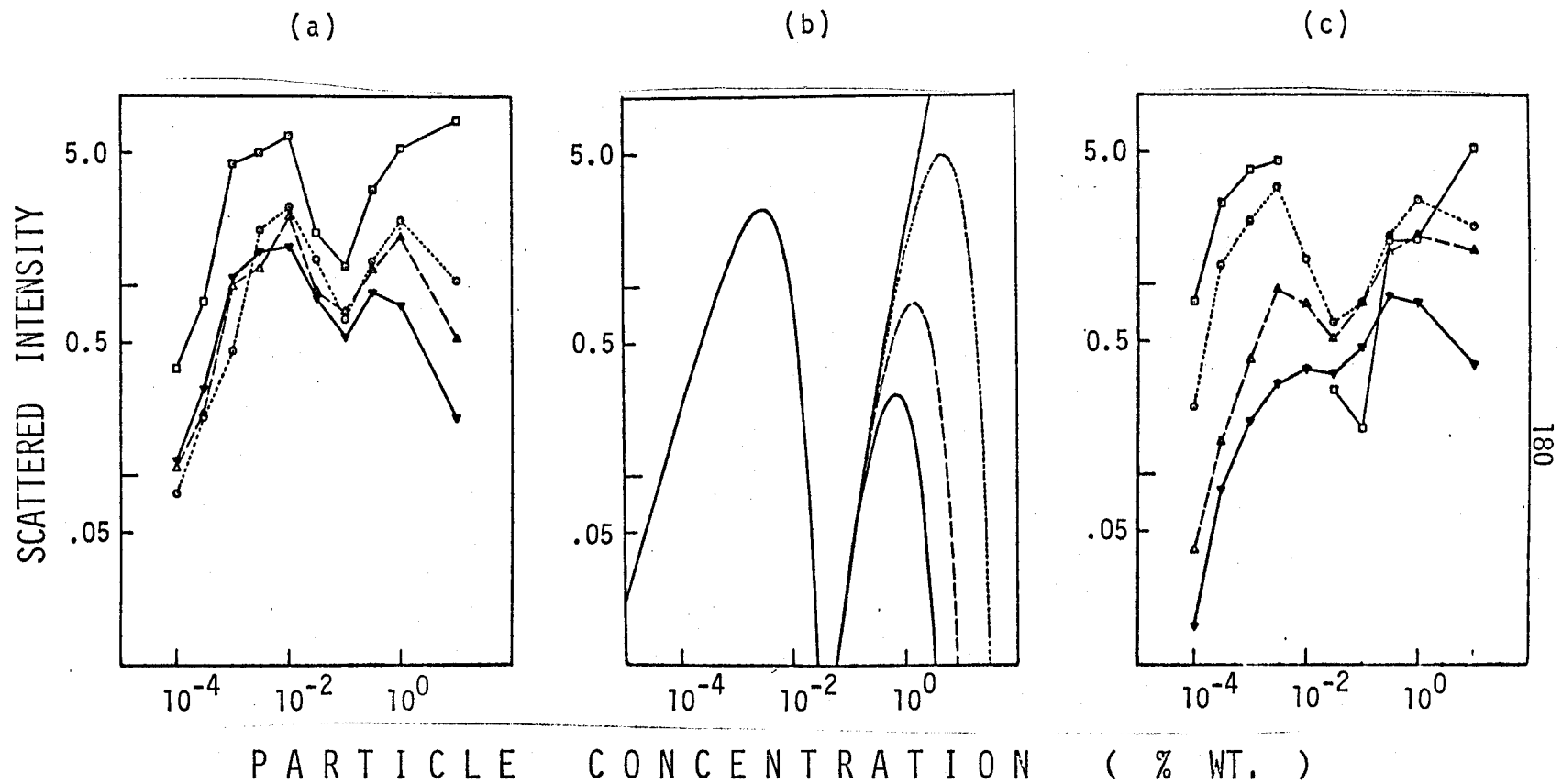
Fig.6-14 Scattered intensity vs. scatterer density : 3.20 μmφ latex spheres, scattered angles, 1.83° (———), 11.0° (·····), 20.2° (-----), 29.3° (———), (a) range-gated measurements, (b) theoretical calculations, (c) non-range-gated measurements, 1.83°case was lowered down by 1/10

dia.	std. dev. / mean	σ_t	calculated ρ_{max}	measured ρ_{max}
(μm)	(%)	(μm^2)	(cm^{-3})	(cm^{-3})
0.481	0.374	0.186	1.89E8	1.64E8
2.02	0.668	7.96	4.41E6	6.78E6
3.20	5.94	20.1	1.74E6	2.80E6

Table 6-1

Maxima of Scattered Intensity for Tenuous Media

$$\rho_{max} = \frac{1}{2\,\sigma_t\,c\,\Delta t} \ln \left(\frac{t_0 + \Delta t}{t_0 - \Delta t}\right)$$

where

$$c\,\Delta t = 3 \ (mm), \quad c\,t_0 = 28.6 \ (mm) \ .$$

Calculated ρ_{max}

dia.	average radial distance r = 1.43 θ (cm)			
(μm)	0.137	0.320	0.503	0.640
0.481	1.09E12	1.99E11	8.05E10	4.97E10
2.02	3.36E10	6.16E9	2.49E9	1.54E9
3/20	1.18E10	2.15E9	8.92E8	5.39E8

$$\rho_{max} = \frac{2tc}{r^2 \sigma_s (1-\bar{\mu})} \qquad \text{where tc = 2.86 (cm)}$$

Measured ρ_{max}

dia.	radial distance of observation (cm)			
(μm)	.046-.23	.23-.41	.41-.59	.55-.73
0.481	1.64E11	4.92E10	8.20E10	3.28E10
2.02	6.78E9	2.26E9	2.26E9	1.13E9
3.20	2.81E9	5.61E8	5.61E8	2.81E8

Table 6-2

Maxima of Scattered Intensity for Dense Media
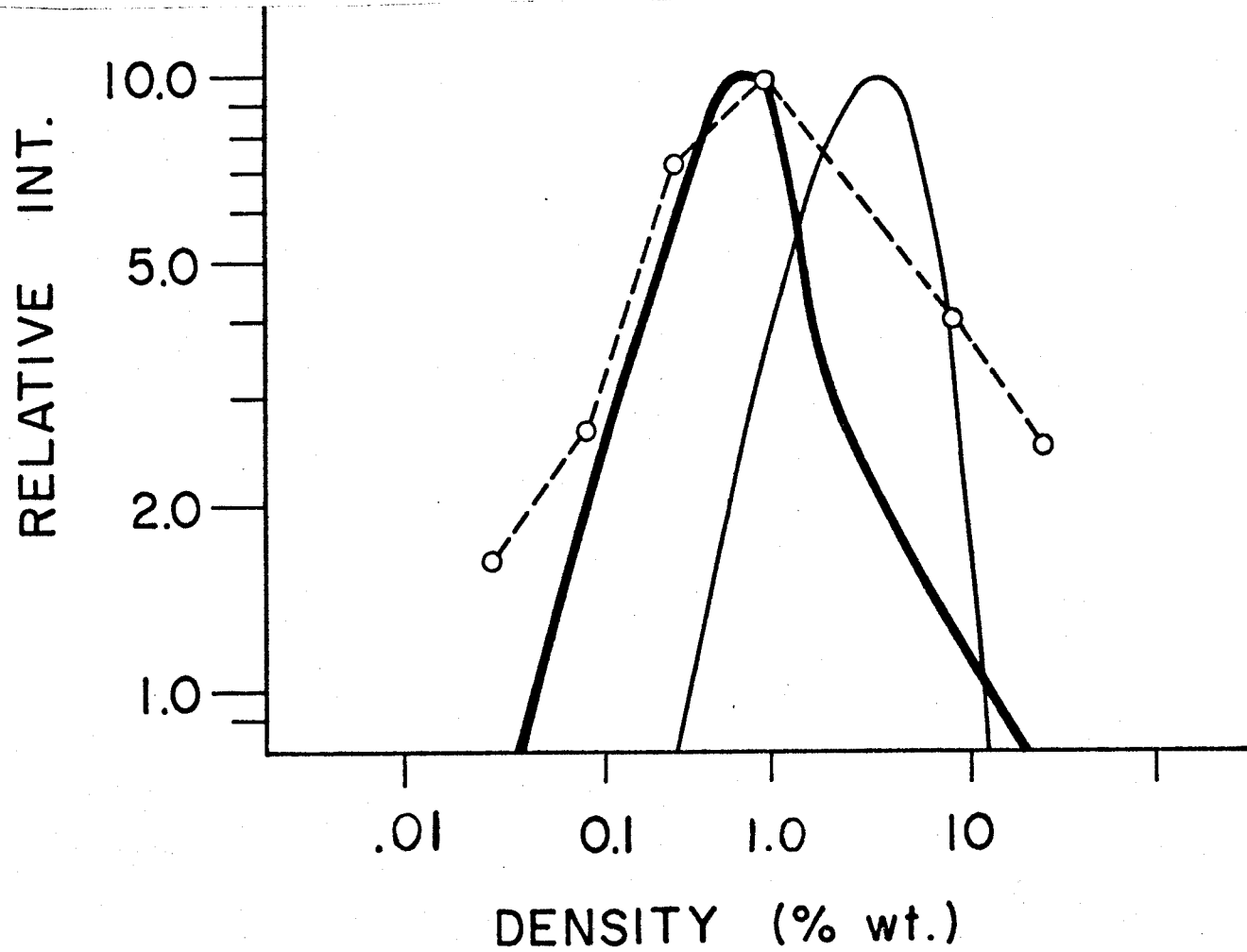
Fig.6-15 Comparison of different solutions and measurement : 2.02 μmφ latex spheres,
         solid curves ; theoretical calculations, solutions of diffusion equation
         for plane wave incidence (——), and point source (——),
         dashed line ; measurement at scattered angle θ = 11.0°

Chapter VII

MEASUREMENT OF LIGHT VELOCITY IN DIFFUSE MEDIA

VII.1   INTRODUCTION

Measurement of light velocity is an old and new subject. Starting from Galileo's attempt, it has been a significant area in physical science (Froome, 1969). The accuracy of measurement has been steadily improved with the progress of science and technology (Halliday, 1960, p. 1001). The accuracy can be used as an indicator to show the accelerated growth of today's science. Almost a century has passed after the theory of relativity was verified and still active studies are being conducted on the velocity of light.

However, it is rather surprising that (as far as we know) no report has been found on the slowing rate of light velocity in diffuse media. Just recently, Ishimaru theoretically predicted that light is slowed down to $1/\sqrt{3}$ of the case without scatterers. In order to measure such a large velocity as light, we must use a long base line or measure a small time interval. The measurement using a reflector on the lunar surface is an example of the former. The picosecond resolution of the range-gating technique enables the latter.

In Chapter VI, we discussed the different phases of scattering along with the analysis on the correlation between theory and measurement. Based on the analysis, in this chapter, scattering

models are constructed for our observation geometry with tenuous and dense media. According to the models, the slowing rate of the light velocity in diffuse media is obtained by measuring the difference in arrival-time of pulses scattered from tenuous and dense media. The slowing rate measured is shown to be very close to the predicted value, $\sqrt{3}$.

VII.2   THEORY

VII.2.1   Received Pulse Shape for Dense and Tenuous Media

The intensity profile of the scattered pulse through the range-gating shutter is given by the following convolution:

$$I_{rec}(t) = \int_{-\infty}^{\infty} I_d(t') \, S(t - t') \, dt' \qquad (7-1)$$

where $I_d(t)$ is the diffuse intensity and $S(t)$ is the transmission of the range-gating shutter. As was seen in Section VI.2.2, $S(t)$ is approximated by the rectangular function with the width Δt (~ 10 psec).

Thus we have

$$I_{rec}(t) = \int_{t-\Delta t}^{t+\Delta t} I_d(t') \, dt' \qquad (7-2)$$

If the time-scale of the $I_d(t)$ is much larger than Δt, the received intensity profile $I_{rec}(t)$ approximates the scattered pulse shape $I_d(t)$.

$I_d(t)$ for dense medium was obtained in Chapter V, which was characterized by the sharp rise and slow decay. Here, $I_d(t)$ for tenuous medium is obtained from the geometry of the system. See Fig. 7-1. Beams with diameter a and b represent those of the incident pulse and the receiving cone of the detector, respectively. The range-gated scattered intensity is proportional to the overlapping volume between the scattering volume AB'D'C and the sampling volume (shown by a dark rectangle box in Fig. 7-1). As the sampling volume is
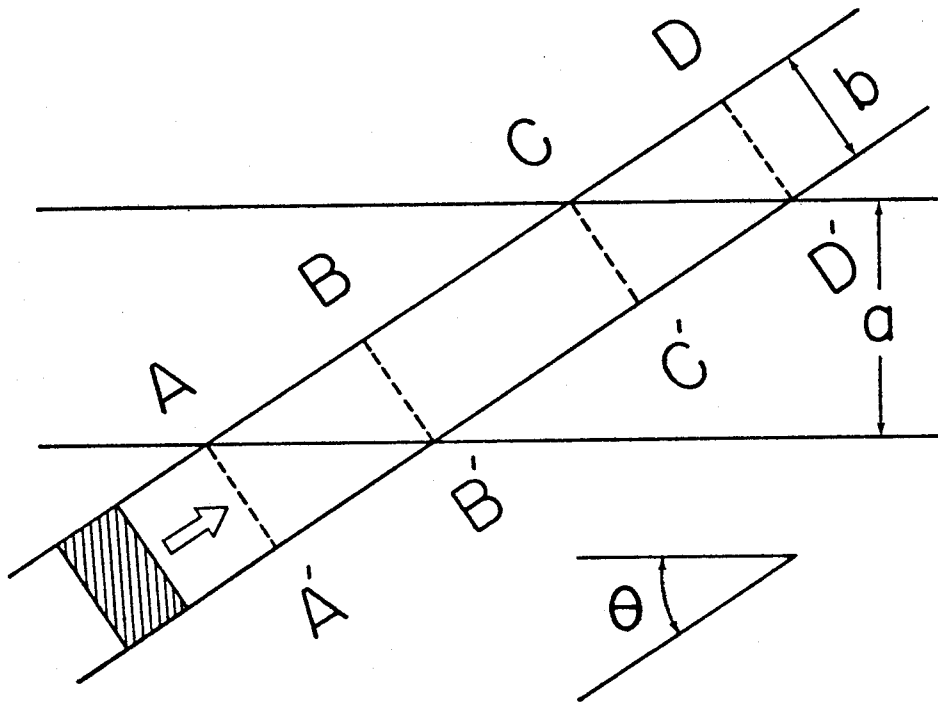
Fig.7-1 Geometry of range-gated scattering volume in tenuous medium :
incident laser beam with beamwidth a, and receiving pattern
with thickness b, scattering angle or observation angle θ

moved along the receiving cone, full overlap occurs in the region BC-B'C' while in AB-A'B' and CD-C'D' the overlap is partial. The lengths of each region are

$$AB = CD = b/\tan\Theta$$

$$BC = a/\sin\Theta - b/\tan\Theta$$

where Θ is the scattering angle.

Therefore, $I_d(t)$ for tenuous medium can be approximated by the trapezoid with the following parallel sides. The top side is given by

$$BC/c = (\frac{a}{\sin\Theta} - \frac{b}{\tan\Theta})/c \qquad (7-3)$$

and bottom side is

$$AD/c = (\frac{a}{\sin\Theta} + \frac{b}{\tan\Theta})/c \qquad (7-4)$$

where c is the group velocity of light in the medium which suspends the scatterers.

VII.2.2   Velocity of Light in Diffusive Media

The diffusion equation for the point source located at the origin was given in Eq. (5-46) which is

$$(\nabla^2 - q^2) U_d (\bar{r};\omega_1,\omega_2) = - \frac{3}{4\pi} \alpha_{tr} P_i(\omega_1,\omega_2)\delta(\bar{r}) \qquad (7-5)$$

It can be transformed into the time domain, yielding

$$\left(\nabla^2 - \frac{3}{c^2}\frac{\partial^2}{\partial t^2} - \frac{1}{D^2}\frac{\partial}{\partial t} - 3\rho^2\sigma_{tr}\sigma_a\right)U_d(\bar{r};t) = -\frac{3}{4\pi}\left(\frac{1}{c}\frac{\partial}{\partial t}\right.$$

$$\left. + \rho\sigma_{tr}\right)P_0\delta(t)\delta(\bar{r}) \qquad\qquad (7\text{-}6)$$

where D^2 is the diffusion coefficient and is given by

$D^2 = cl_d/3$, $l_d = \{\rho(\sigma_{tr} + \sigma_a)\}^{-1}$ and l_d is the diffusion mean free

path (Morse, 1953, p. 178). P_0 is the total energy radiated at the

origin and is given by

$$\iint P_i(\omega_1,\omega_2)\, e^{-i(\omega_1-\omega_2)t}\, d\omega_1\, d\omega_2 = P_0\delta(t) \qquad\qquad (7\text{-}7)$$

Eq. (7-6) shows "the propagation and diffusion characteristics of a

pulse wave. The second term shows the propagation with the velocity

of $c/\sqrt{3}$, which is consistent with the diffusion phenomena. The

third term shows the diffusion and the fourth term indicates the

absorption." (Ishimaru, 1978b).

In the following sections, this "slowed down speed of light" is

measured.

VII.3   EXPERIMENTS

VII.3.1   Experimental Facility

The range-gating system described in Section IV.3.1 was used. As discussed in Section IV.3.2(f), the scattering cell of the horizontal cylindar replaces the vertical one. See. Fig. 7-2.

VII.3.2   Scattered Pulse Shape Measurement for Tenuous and Dense Medium

Since the pathlength of the infrared gating pulse determines the sampling time of the scattered intensity, we can measure the scattered intensities as a function of time by changing the IR pathlength (dashed line in Fig. 7-2). Thus by scanning the prism PR_2, we can trace the intensity profile of the scattered pulse in time. As can be seen in Fig. 7-1, in the case of tenuous media, this operation corresponds to sampling different depths along the path of the scattered light toward the detector. This is where the term "range-gating" comes from. In other words, the pulse shape obtained represents the spatial profile of the scattered intensity as well as the temporal profile. In the case of dense medium, it represents only the temporal profile.

Note that as shown in Eq. (7-1), the profiles mentioned above are the convolutions of the scattered intensity and the transmission of the range-gating shutter.

Since the reference signal is available as described in Section IV.3.1, we can compare the magnitudes of the scattered pulses between
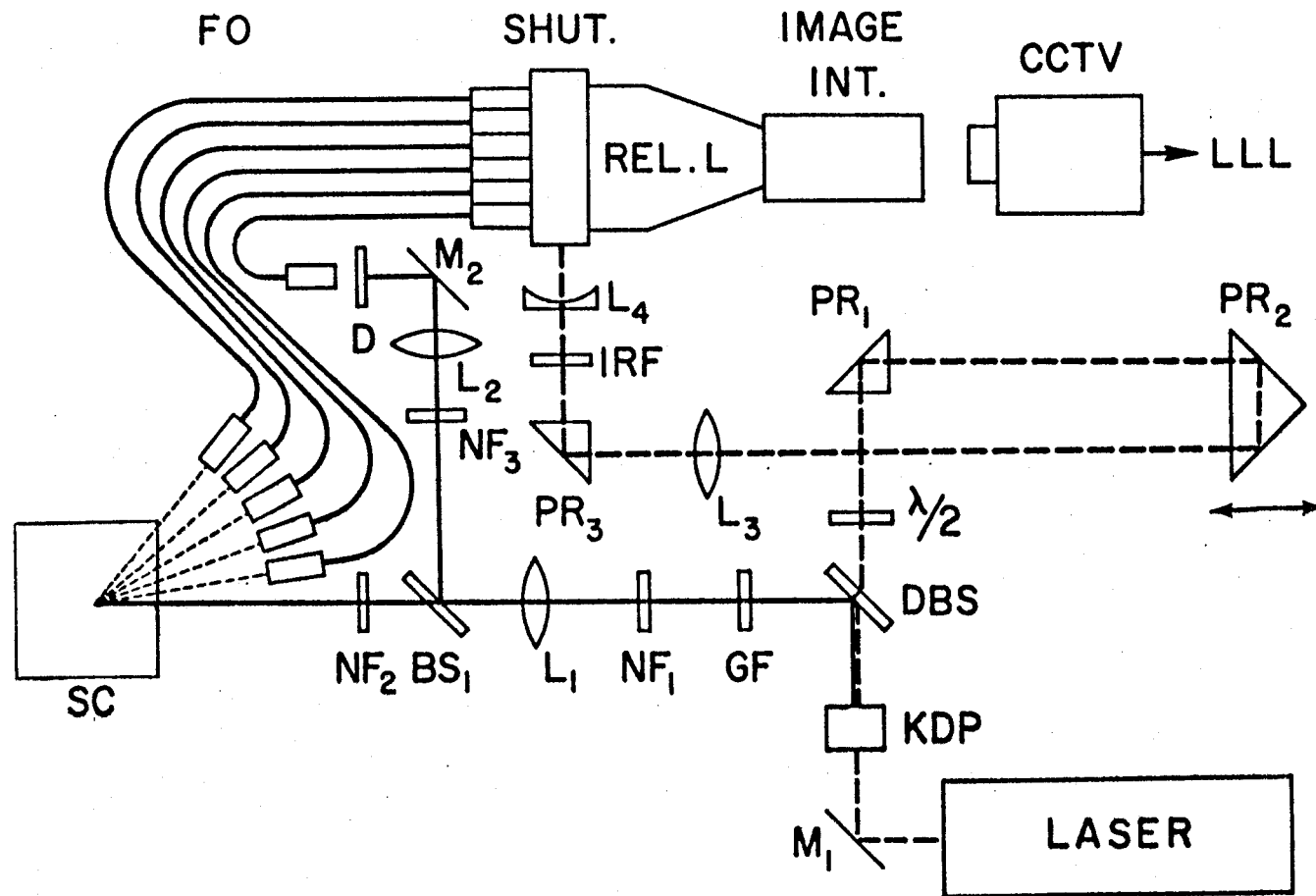
Fig.7-2 Schematic of off-axis backscattered pulse shape measurement

the tenuous and dense media cases. The measurements are conducted at the scattering angle $\Theta = 2.76° \sim 21.6°$ and with the concentration $\rho = 10^{-4}\% \sim 10\%$ by weight.

VII.3.3   Measurement of Light Velocity in Diffusive Media

Fig. 7-3 illustrates the measurement. When the medium is tenuous, the incident light-pulse travels along the path L_1 and the light scattered at an angle Θ travels back to the detector along the path L_2 . The light traveled in any other path can be eliminated by the narrow receiving pattern of the detector and the range-gating technique. The traveling time of the pulse is given by

$$t_a = (L_1 + L_2)/v_a \tag{7-8}$$

where $v_a = c/n$ is the group velocity of light in the tenuous medium and n is the refractive index of the medium.

When the medium is very dense, the light received by the detector is predominantly the one which diffused the shortest distance L_3 along the boundary. In the medium with high $\rho\sigma_t$, a small increase in pathlength attenuates the light considerably.

Although the direction of the propagation along the boundary does not coincide with the acceptance angle of the detector, the almost isotropic scattering of the diffusion phenomena allows us to measure the diffused intensity. In the dense medium, the pulse shape changes as it propagates such as pulse broadening and tailing. The diffusion time t_b is defined as the period taken for the peak of the pulse to reach the detector. It is given by
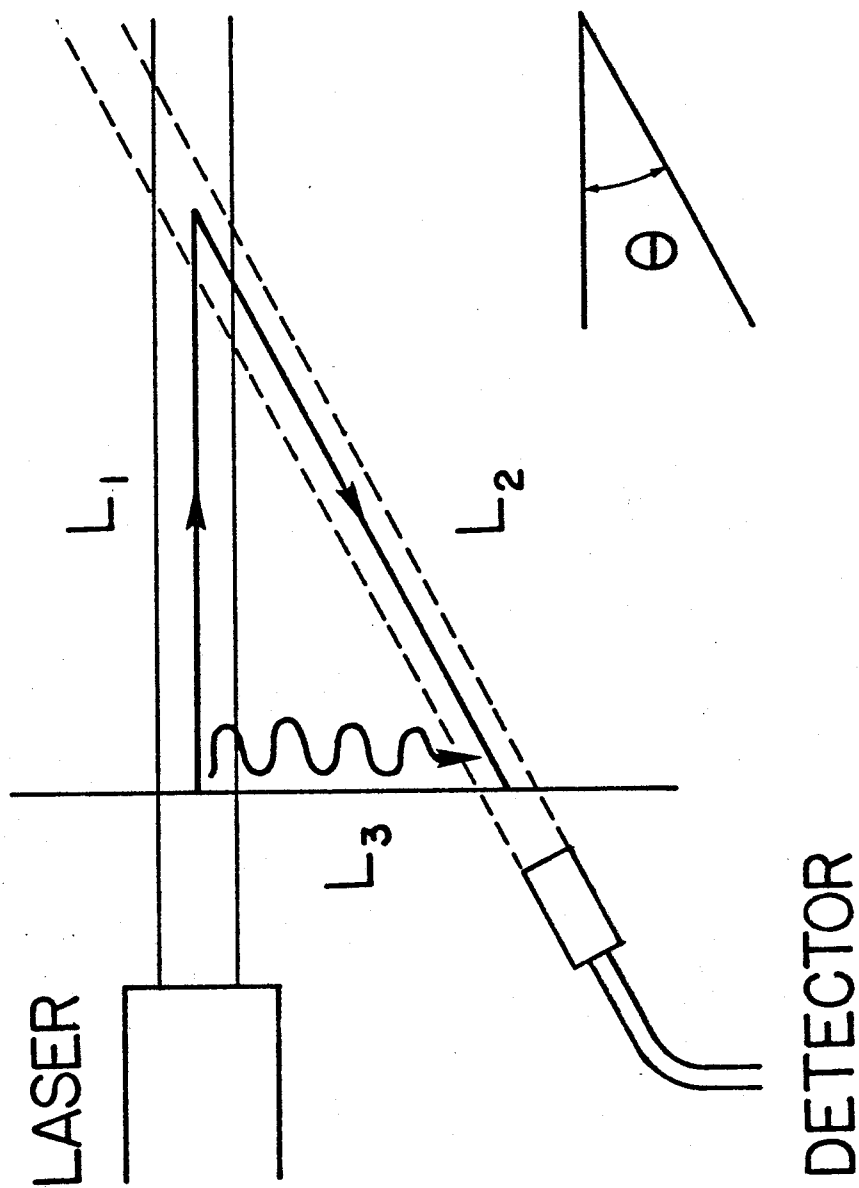
Fig. 7-3 Geometry of light velocity measurement

$$t_b = L_3/v_b \qquad\qquad (7\text{-}9)$$

where v_b is the velocity of interest at which the peak of the pulse propagates.

As was seen in the previous section (VII.3.2), the intensity profile of the scattered pulse can be obtained by changing the pathlength of the infrared range-gating pulse. Therefore, we can determine the IR pathlength at which the scattered intensity reaches the peak value. Two such pathlengths are measured, one for a tenuous medium (l_a) and another for a dense medium (l_b). The difference in these pathlengths corresponds to the time difference between t_a and t_b, i.e.,

$$(l_a - l_b)/v_{IR} = t_a - t_b \qquad\qquad (7\text{-}10)$$

where v_{IR} is the velocity of the infrared gating pulse which travels in the air. Therefore, by measuring the difference in the IR pathlengths, $l_d = l_a - l_b$ we can obtain the velocity of light in the diffuse medium, i.e.,

$$v_b = L_3 \left(\frac{L_1 + L_2}{v_a} - \frac{l_d}{v_{IR}} \right)^{-1} \qquad\qquad (7\text{-}11)$$

Noting that $v_a = c/n$ and $v_{IR} = c$, the factor of the slowing down by diffusion is given by

$$\frac{v_b}{c} = \frac{L_3}{n(L_1 + L_2) - l_d} \qquad\qquad (7\text{-}12)$$

As was discussed in Section VII.2.1, the intensity profile observed is not the scattered pulse itself. It is the convolution of the scattered pulse and the gating-pulse. Their pulse width can be comparable sometimes. However, it should be noted that while the convolution broadens the pulse shape, it does not change the relative position of the two pulse-peaks between the cases of tenuous and dense media.

VII.4   RESULTS AND DISCUSSION

VII.4.1   Shapes of Scattered Pulses

Figs. 7-4(a) ~ (j) show the intensity profile of the received signals measured as a function of time. Each figure consists of a set of pulses with different scatterer densities which range from 10^{-4}% to 10% by weight. A log-scale was used for the ordinate to present the results of tenuous and dense media in the same graph. Each data point is the average of 3-7 shots of the laser. The standard deviation in intensity is within 10% of the average value, while the uncertainty in the temporal location is ±0.017 psec. The time origin (t = 0) was defined as the instance at which the peak of the incident pulse passes the boundary of the scattering medium. It was obtained by subtracting the time duration $t = (L_1 + L_2)/v$ from the center time of the trapezoidal pulse shape measured in the case of tenuous media, See Fig. 7-3 and Section VII.2.1 for the definitions of parameters and more discussions. The center times of the trapezoids were very stable and no fluctuation was observed in the measurement. At the top of each figure are shown the two calculated arriving-times of the pulse peak. The calculations are based on the assumptions of the regular group velocity of light in the medium and the slowed-down velocity due to the diffusion discussed in Section VII.2.2. Thus, the left and right marks correspond to $t = L_3/v$ and $t = \sqrt{3}\, L_3/v$, respectively. At the bottom of each figure, are shown the two time-durations which correspond to the parallel sides of the trapezoid calculated by Eqs. (7-5) and (7-6).

As was discussed in Section VII.2.1, the difference in the received pulse shape is evident between the tenuous and dense media. They are characterized by the trapezoides in the former case, and the rapid rise and the slow asymptotic decay in the latter case.

An interesting transition in their shapes can be seen as the scattering angle (Θ in Fig. 7-3) changes or equivalently the radial distance (L_3) of the observation point changes. First, the transition in the bottom two curves is studied, which are the measurements with the tenuous media. The measured widths of the parallel sides of the trapezoidal curves are well correlated to the theoretical calculations. The slightly wider sides of the measurement are due to the finite width of the sampling volume or the finite shutter open duration. Note that the decrease in the lateral sides of the trapezoids is steeper if they were shown in a linear scale.

Next, the transition in the pulse shapes for dense media is studied. The pulses are shown in the top three curves for $\Theta = 2.76°\sim 8.25°$ and in the top two curves for $\Theta = 16.4°\sim 21.6°$. There is no significant reason for not measuring the third curves for the latter angle range. They were not particularly necessary for the light velocity measurement which was the major purpose at the beginning.

The characteristic shapes predicted theoretically in Chapter V are verified. Fig. 7-5 shows the comparison between theory and measurement at different observation angles ($\Theta = 4.13°$, 8.25°) with different densities ($\Theta = 1\%$, 10% wt.). The theoretical curves are obtained by applying the formula of range-gating, Eqs. (8-5)(8-6) to

the diffusion solution for the beam wave case, Eq. (5-54). The agreement is good except for the low intensity parts where the measurements are less accurate due to the low signal to noise ratio, dark current of the detector, etc.

In addition to the agreement in the general shape, the theory well describes the inversion of the pulse peak positions for the 10% wt. and 1% wt. cases when the receiving angle changes from $\Theta = 4.13°$ to $\Theta = 8.25°$. The inversion can be better understood in Fig. 6-13(a). At the angles close to the backward normal, the scattered intensity increases as the scatterers density increases, while at other angles the intensity decreases in the higher density.

Concerning the curves for dense media in Figs. 7-4(a) $\sim$ (j), some points listed below are not fully understood. (1) A pulse-broadening is observed only for 10% wt. and 1% wt. densities at the smaller angles $\Theta = 4.13° \sim 8.25°$. No noticeable broadening appears in other conditions. (2) The relative positions of two pulse peaks for 10% wt. and 1% wt. densities are again reversed at $\Theta = 16.4° \sim 21.6°$. (3) In the larger angles ($\Theta = 16.4° \sim 21.6°$), the arriving-time of the pulse peak for 1% wt. density is consistently later than that for 10% wt. density.

These results imply that in the large angle region the diffusion mechanism may be different from the ones we have analyzed so far. The computer program based on the diffusion solution for the beam wave incidence, fails to calculate a reasonable impulse response for the conditions equivalent to the measurements in this range. Difficulties

in explaining the behavior of the scattered intensity in the large
angle region were also encountered in the analysis of the backward
scattering patterns in Section VI.4.1

VII.4.2 Velocity of Light in Diffuse Medium

The table 7-1 shows the result of the light velocity measurement
described in Section VII.2.2. In the table, Θ, L_3, $L_1 + L_2$, l_d and
α are the scattering angle, the radial distance of the observation
point, the propagation path of the light pulse when the medium is
tenuous, the difference in the pathlength of the IR shutter-activating
pulse and the slowing rate of the light velocity which is of ultimate
interest. See Fig. 7-3 for the illustration.

Since the propagation distance L_3 for the diffuse light is
short in the first five angles, the results are not as accurate as
the latter five angles. However, four data out of five show a greater
slowing rate than $\sqrt{3}$. According to the small sampling theory using
the Student's t distribution, the 99% confidence interval for all
ten data and the last five data are 1.85 ± 0.35 and 1.75 ± 0.081,
respectively. Although this is not the direct measurement of the light
velocity such as the transmitting velocity, and the number of data is
not many, the results evidently show the slowing phenomena and the
slowing rate obtained is very close to the theoretically predicted
value, $\sqrt{3}$. See Fig.7-6.

Regardless of diffusion, light propagates slower in the material
of the particles ($n = 1.59$ for $\lambda = 0.53$ μm) than the suspending medium
(water, $n = 1.33$). However, the slowing rate due to the higher

refractive index of the particle material would be 1.19, even if all the spaces are filled with the material, or the packing factor $H = 1$. The particle densities used in these experiments were much less, $H \leq 0.1$. Therefore, at least with statistical significance, we can conclude that the velocity of light in a diffuse medium is decreased by the factor $1/\sqrt{3}$ from its group velocity in the suspending medium of the scatterers.

As can be seen in Figs. 7-4(a) $\sim$ (j), the rising periods of the pulses are well correlated to those calculated which are shown at the top of each figure as the widths of the two arriving-times. The more rapid rise for the shorter L_3 can be seen. Note the sharp rise in the log-scale of the ordinate.
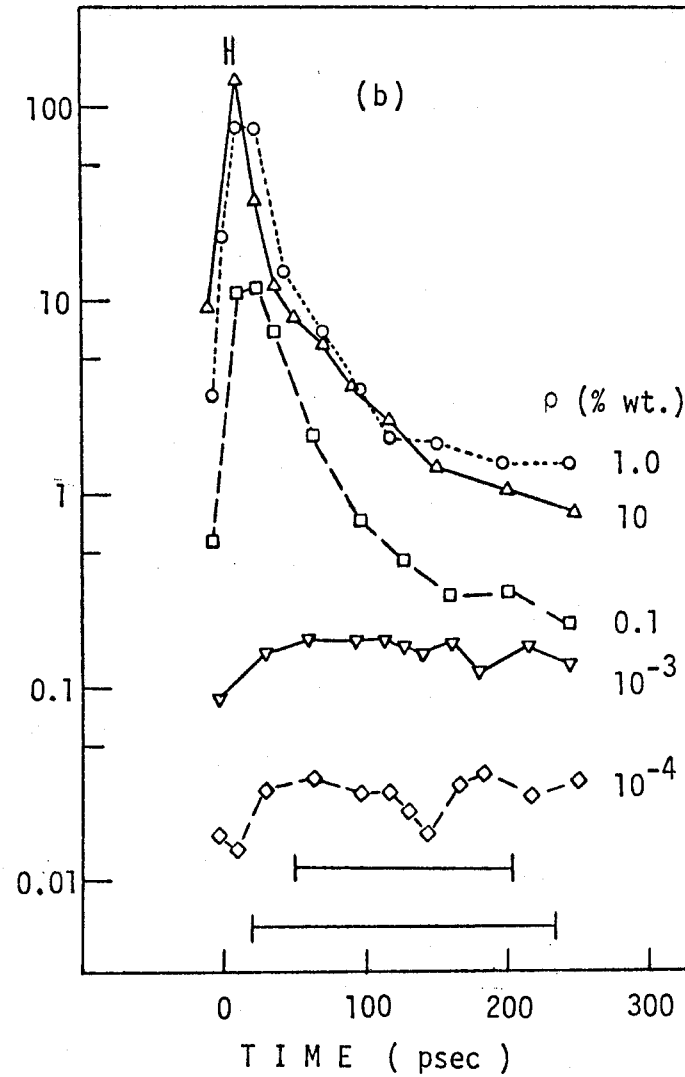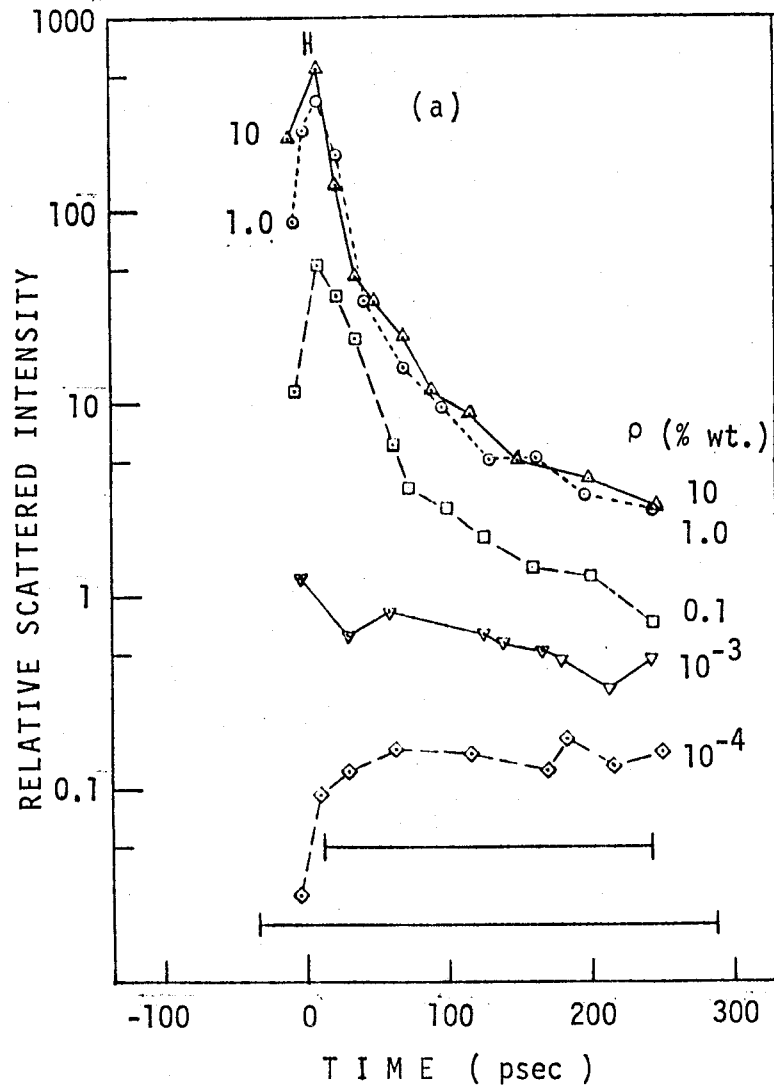
Fig.7-4   Intensity profiles of off-axis backscattered pulses : (a) θ = 2.76°, (b) θ = 4.13°
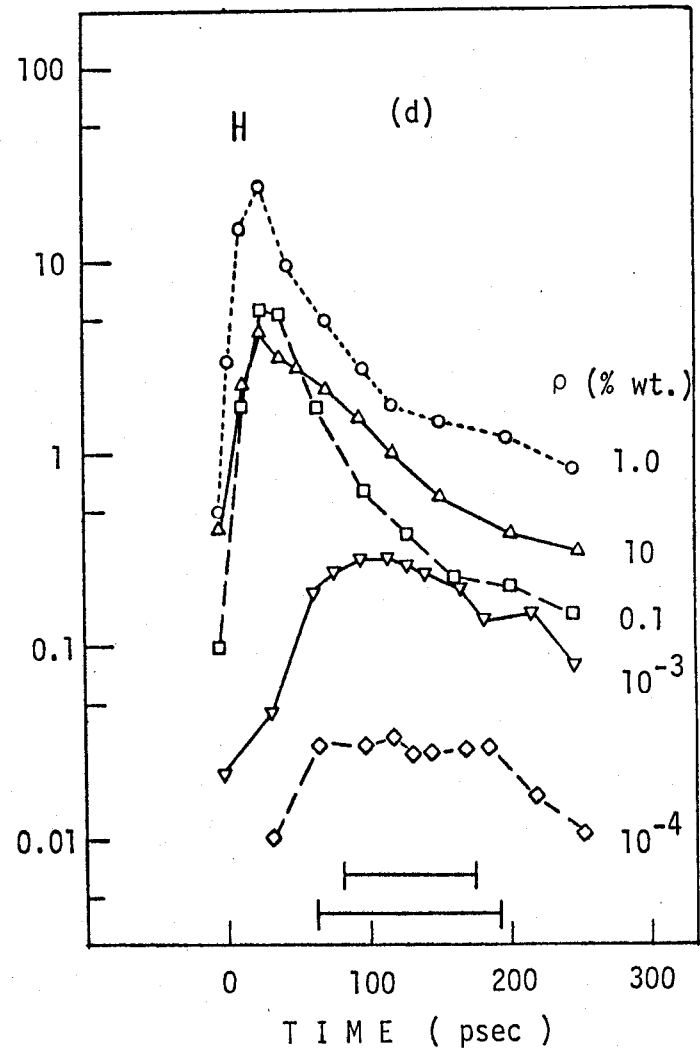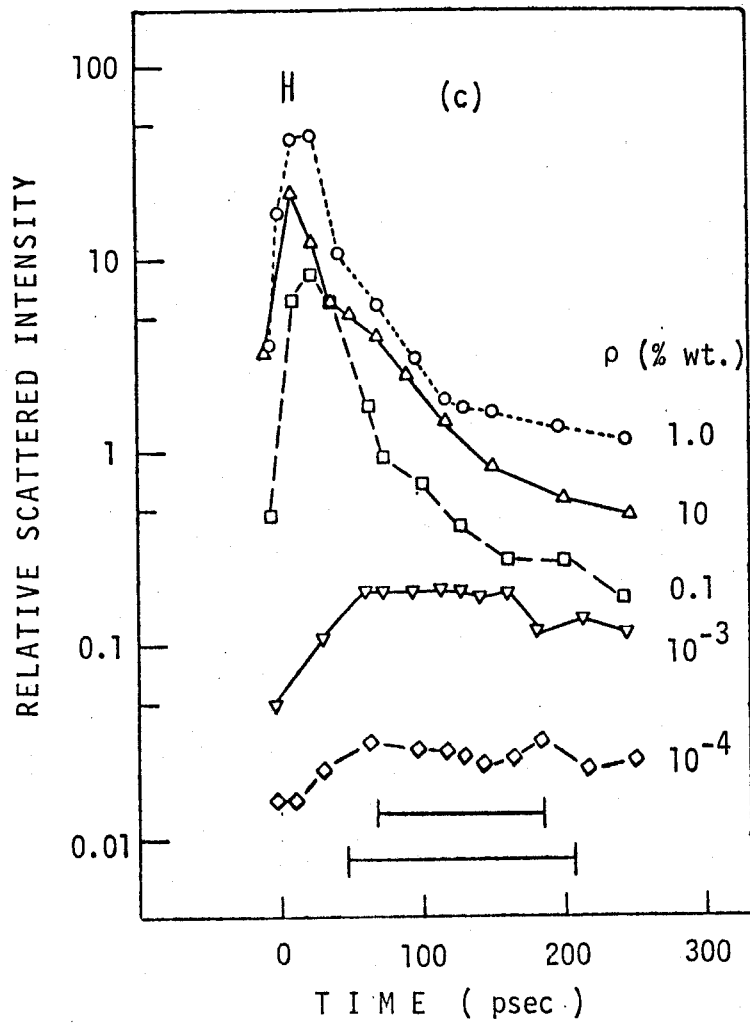
Fig.7-4 Intensity profiles of off-axis backscattered pulses : (c) θ = 5.51°, (d) θ = 6.88°
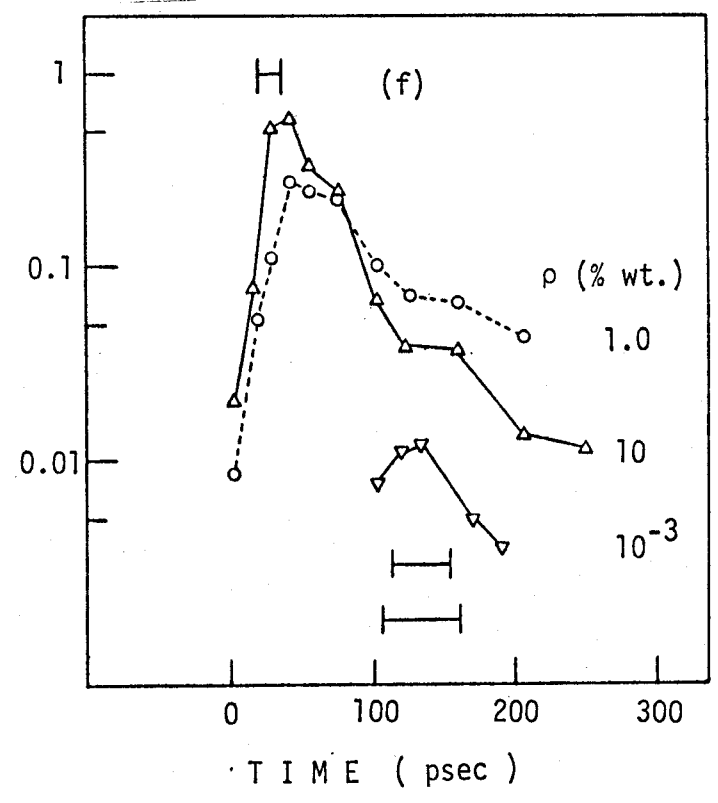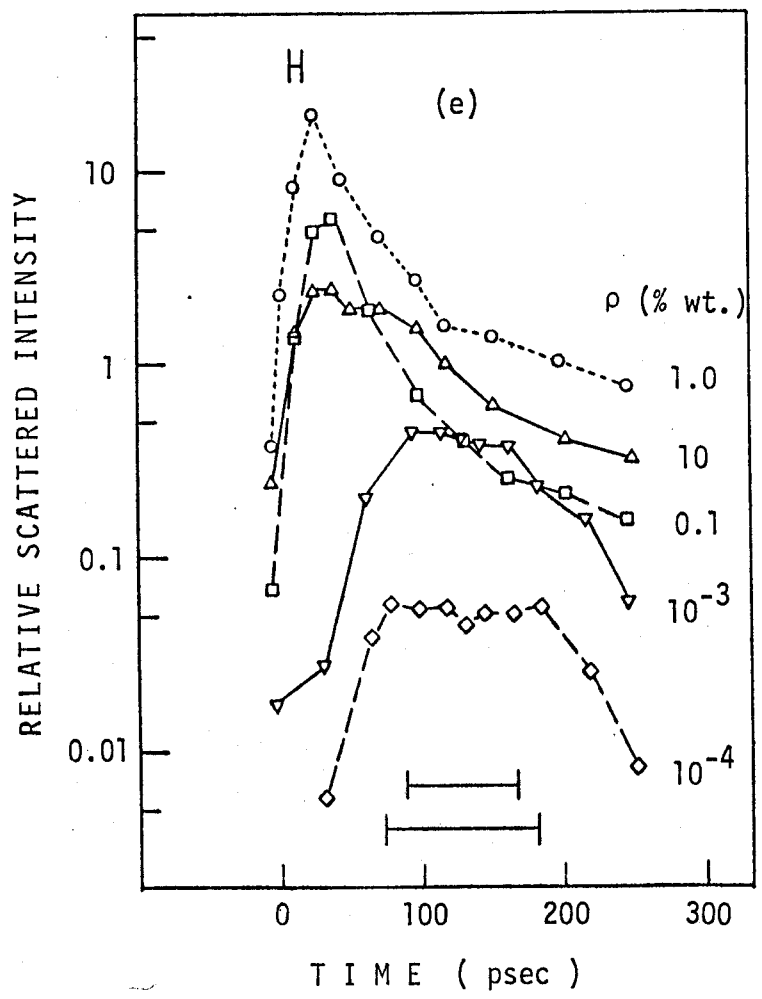
Fig.7-4 Intensity profiles of off-axis backscattered pulses : (e) θ = 8.25°, (f) θ = 16.4°
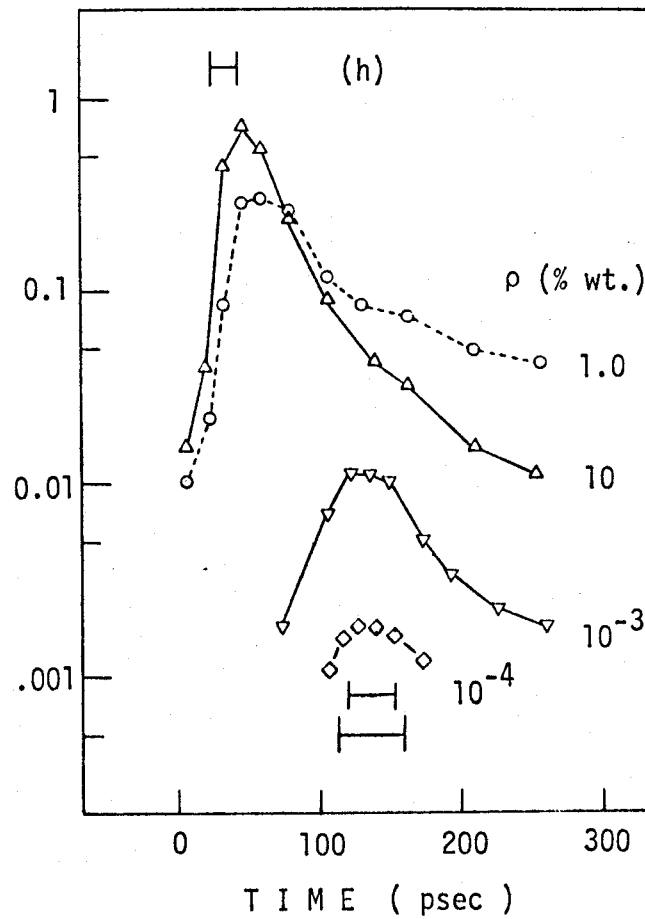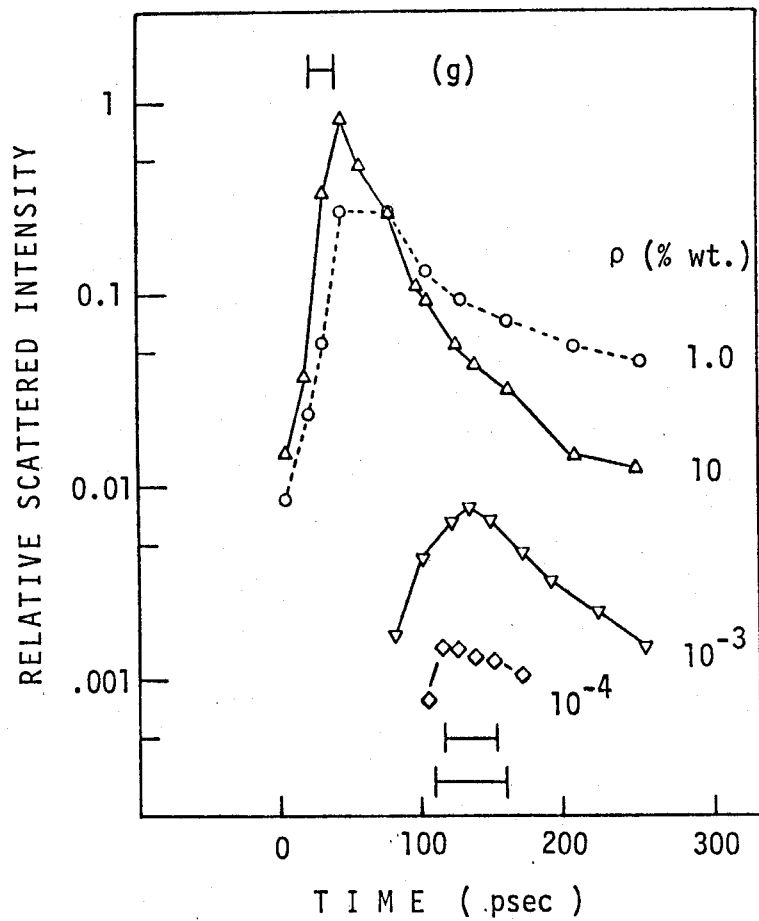
Fig.7-4   Intensity profiles of off-axis backscattered pulses : (g) θ = 17.7°, (h) θ = 19.0°
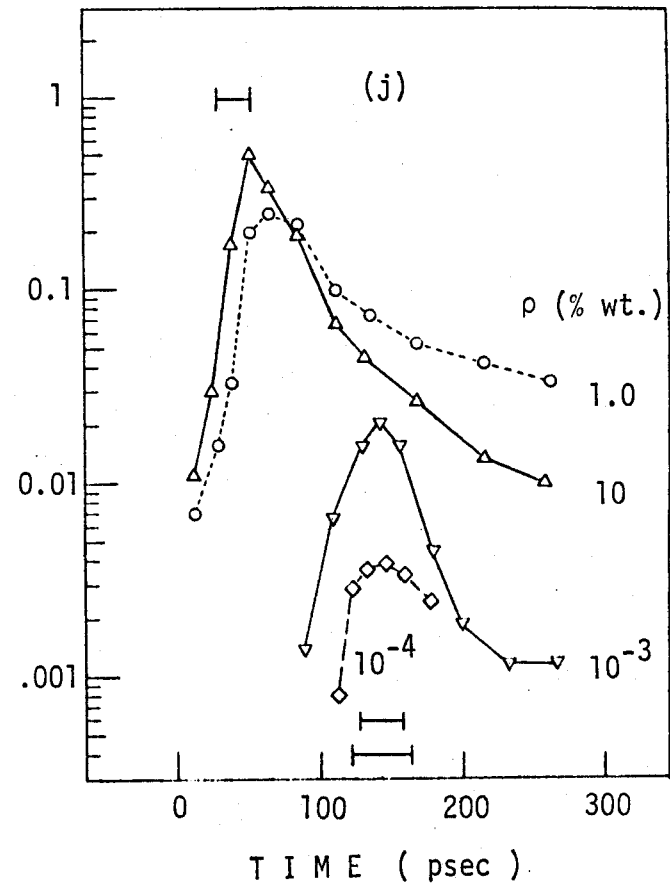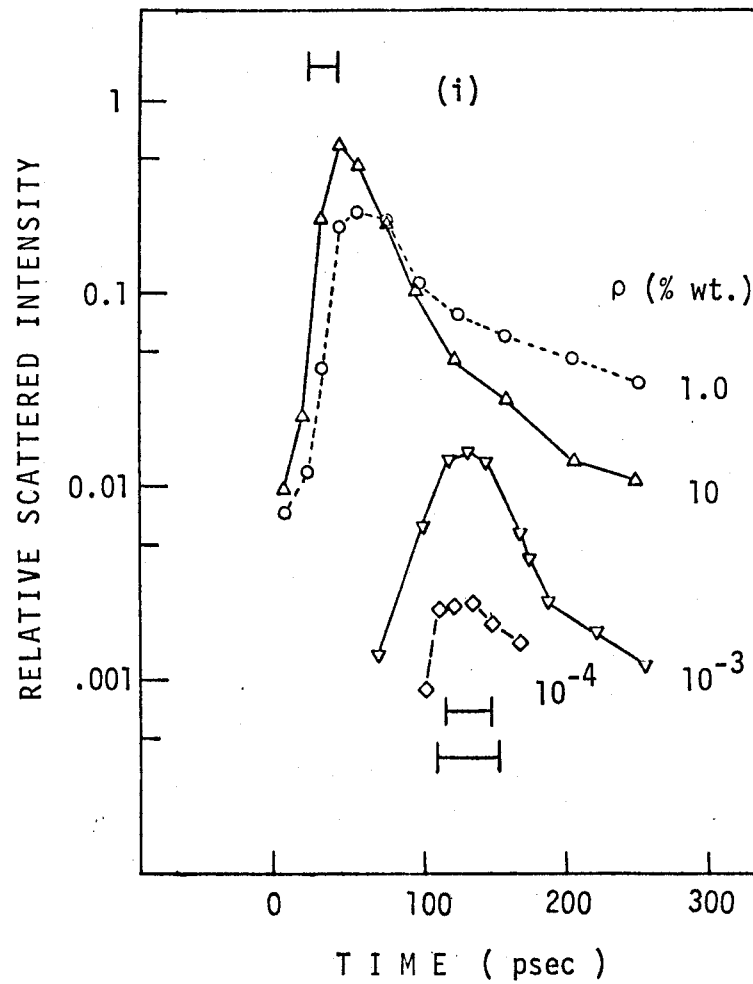
Fig.7-4 Intensity profiles of off-axis backscattered pulses : (i) θ = 20.3°, (j) θ = 21.6°
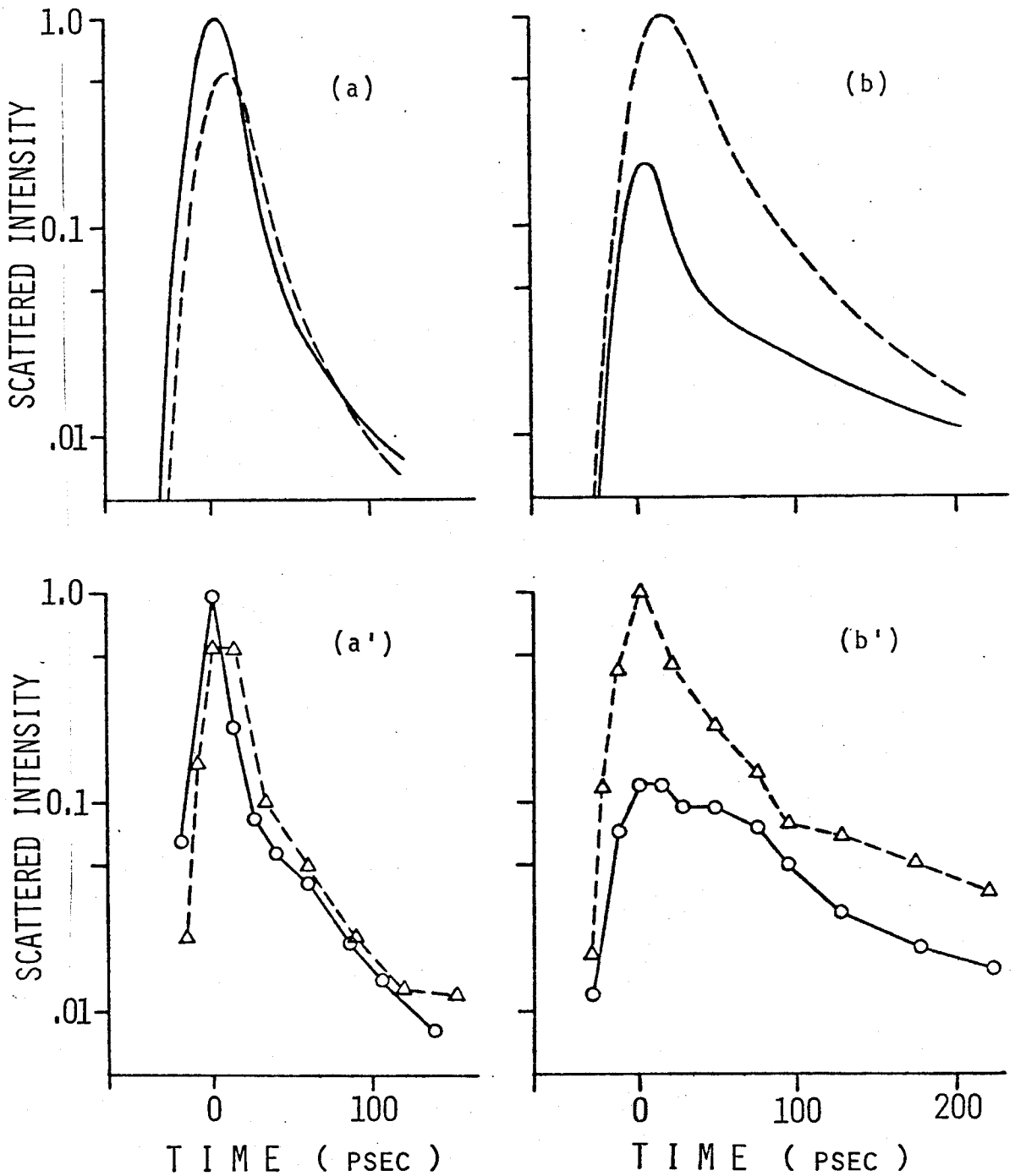
Fig.7-5 Agreement between theory (a),(b), and measurement (a'),(b')
in off-axis backscattered pulse shapes from dense media :
2.02 µmφ latex spheres, density ρ = 10 % wt. (————) and
1 % wt. (-----), beam width W = 10 psec.
(a),(a') θ = 2.76°, (b),(b') θ = 8.25°

θ (deg.)	L_3 (mm)	$L_1 + L_2$ (mm)	1_d (mm)	Slowing rate α
2.76	.769	28.5	36.5	1.37
4.13	1.16	28.5	35.0	1.88
5.51	1.54	28.6	34.5	1.73
6.88	1.94	28.7	32.5	2.20
8.25	2.33	28.9	30.5	2.56
16.4	4.85	30.2	29.0	1.73
17.7	5.30	30.6	28.0	1.80
19.0	5.77	30.9	27.5	1.77
20.3	6.25	31.3	27.0	1.76
21.6	6.74	31.8	27.0	1.71

Table 7-1

Slowing Rate of Light Velocity in Diffuse Medium

$$\left(\begin{array}{l} \text{99\% confidence limits for } \alpha \text{ is} \\ 1.75 \pm 0.081 \text{ for lower five data} \\ 1.85 \pm 0.35 \text{ for all ten data} \end{array} \right)$$
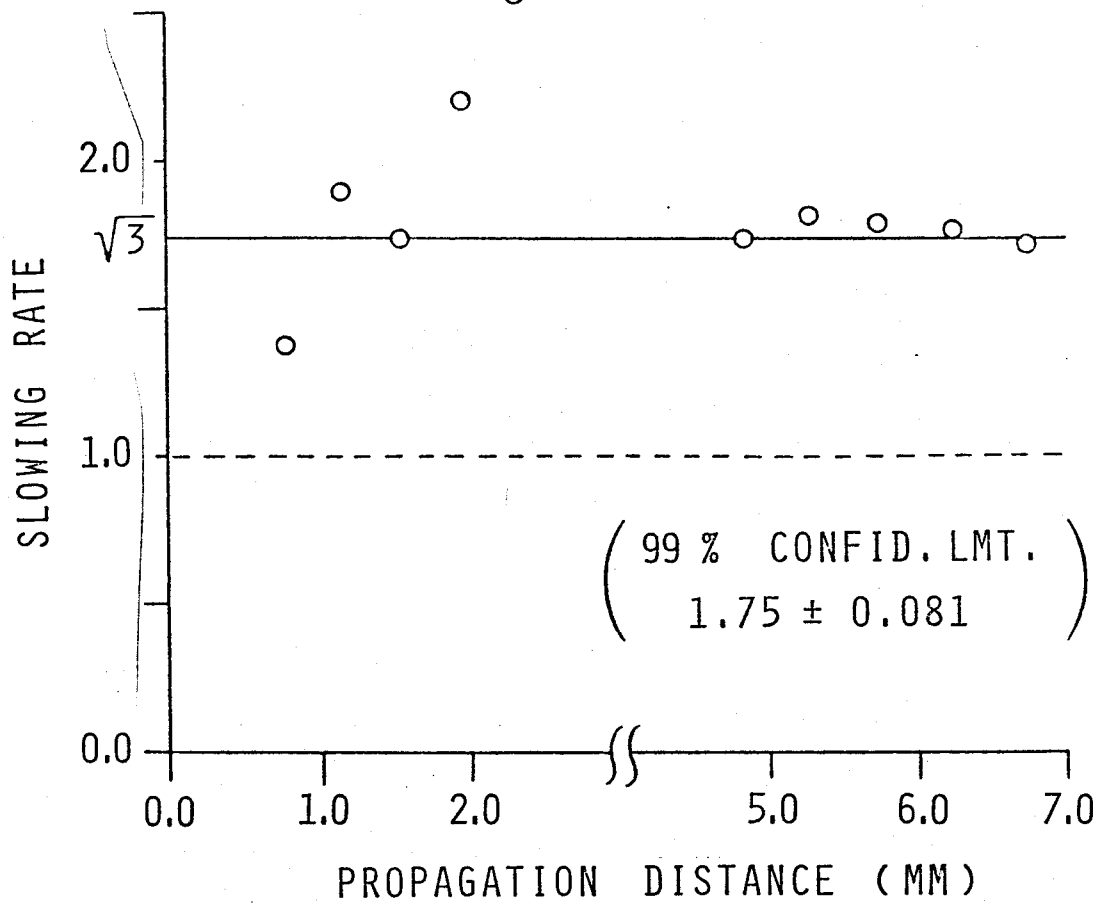
Fig.7-6 Slowing rate of velocity of light in diffuse media :
circles are measurements, solid and dashed lines show
positions of √3 and 1.0 for comparison

Chapter VIII

REMOTE SENSING OF DENSE MEDIA BY PICOSECOND PULSE BACKSCATTERING

VIII.1   INTRODUCTION

Optical pulse propagation in dense random media represents a
class of scattering problem that is important in many practical appli-
cations, such as remote sensing in meteorology, astronomy and biology.
Although CW studies in dense media have been reported (Ishimaru, 1978a,
p. 175), (Reynolds, 1976), very few attempts have been made to treat
the problem of backscattering of a short optical pulse from a dense
distribution of scatterers. Recently, the general formulation for
backscattering of a pulse from a dense medium was obtained by applying
the diffusion approximation to the time-dependent equation of transfer
(Ishimaru, 1978b).

With the advent of lasers capable of generating ultrashort pulses
with durations of the order of picoseconds, and even fractions of a
picosecond (Bradley, 1977, p. 36), a new field of experimental studies
in time-dependent light scattering has become possible. Applying
picosecond optical range-gating techniques (Duquay, 1971)(Bruckner,
1976, 1978a) to light scattering measurements, it is now possible to
record the intensity profile of a backscattered pulse on a picosecond
time scale.

For several years, there has been significant interest in the
possible   deterious effects of micro-aggregates in transfused blood

when administered in massive amounts as large blood transfusions. It has been proposed that these aggregates consist of platelets, white blood cells and fibrin (Solis, 1974).

Currently, there is no satisfactory technique for identifying, sizing and quantifying such micro-aggregates. The evidence for their clinical significance is largely based on the demonstration of such material in the pulmonary capillaries of experimental animals which have undergone massive transfusions of whole blood. The primary technique which has been used for quantification of such material in blood is the screen filtration pressure measurement (Arrington, 1974). This is an indirect technique which measures the pressure required to push blood through a filter of standard size at a fixed rate. It is currently the best method available but is not useful in quantitating size and amount of particulate material and is obviously subject to a number of variables. Therefore, the technique which provides a better evaluation of micro-aggregate size and number, is desirable. Since our ultimate goal is the measurement in vivo, the technique should be applicable to a dense medium such as whole human blood at normal hematocrits.

In previous chapters, a theory was developed for the backscattering from random media (Chapter V), the range of validity for the diffusion approximation was investigated (Chapter VI), and pulses scattered in the off-axis backward directions ($\theta \neq 180°$) were measured (Chapter VII). This chapter presents the development of a remote-sensing technique for dense media by picosecond pulses scattered in the backward normal

direction (θ = 180°).

The range-gating technique is formulated and the received pulse shape is calculated using the diffusion solution obtained in Chapter V. A good agreement between theory and measurement is shown both in the shape and magnitude of the scattered pulse. The analysis of the backscattered pulse shape shows the sensitivity of this technique to the scatterers' absorption characteristics and diffusion optical distance ($\tau_d = \rho\sigma_{tr}z$) of the scattering medium. Finally, the feasibility of this technique for the remote sensing of platelet aggregation and dense cataracts is demonstrated.

VIII.2   THEORY

VIII.2.1   Principle of Measurement

The principle of the backscattered picosecond pulse measurement is illustrated in Figs. 8-1, and 8-2. The picosecond shutter consists of a rectangular cell filled with carbon disulfide (CS_2) placed between two crossed polarizers, P_1 and P_2 whose axes are 45° to the horizontal. Since the polarizers are crossed, the shutter is usually closed. The signal light in the visible wavelength (λ = 0.53 μm) is a plane wave propagating in the z-direction with the signal information (backscattered pulse shape) contained along the z-direction. It impinges on the shutter normally and the shutter-activating infrared (IR) pulse passes through the CS_2 in the x-direction. The intense electric field of the IR pulse induces a narrow zone of birefringence in the CS_2 which makes a narrow transparent window through the crossed polarizers at the position of the IR pulse. Since the IR pulse travels at the speed of light, the transparent window moves across the shutter at the same speed. Thus, we observe the streak record of the incoming signal along the path of the IR pulse across the shutter face.

VIII.2.2   Formulation of Range-Gating Technique

Fig. 8-2 shows the geometry of the problem. The temporal behavior of the backscattered pulse is resolved by means of a transversely gated laser-driven Kerr effect streak shutter (Bruckner, 1978a, 1976). The Kerr medium (CS_2 in the present case) is rendered birefringent on
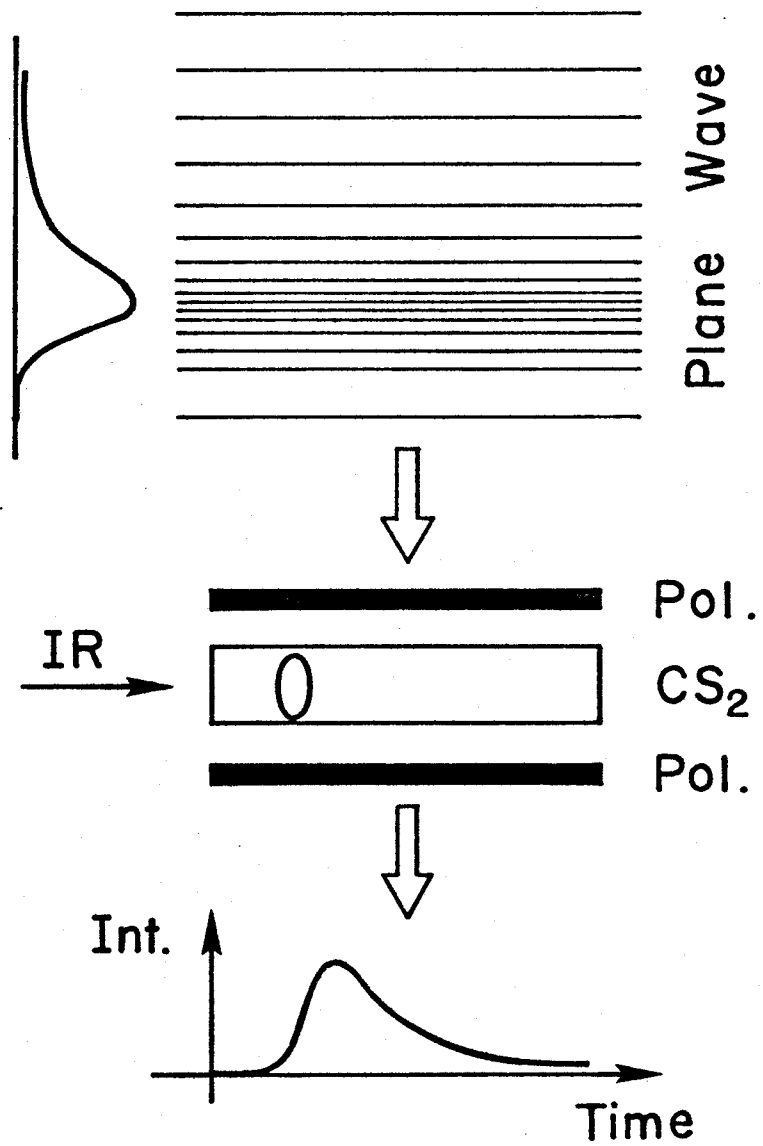
Fig.8-1 Principle of backscattered pulse shape measurement

SIGNAL PULSE
$S(x,y,z;t)$

GATING
PULSE
$I_{IR}(t)$

STREAK
SHUTTER

$-d$

$+d$
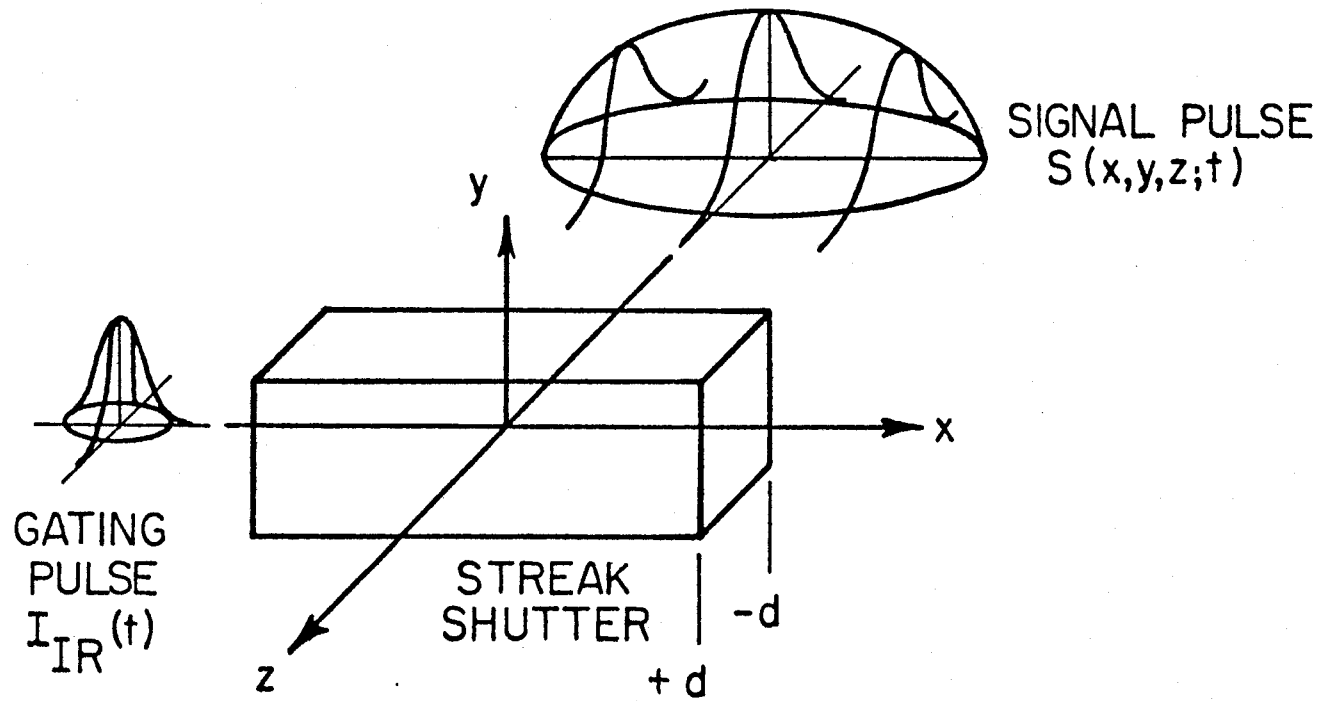
Fig.8-2   Geometry of range-gating shutter

a picosecond time scale by a powerful ultrashort infrared pulse travelling in the x-direction, obtained from a Nd:glass laser. The beam-expanded backscattered pulse is incident on the shutter along the z-axis, as shown. The transmitted signal is a cross-correlation of the gating pulse and signal pulse. Details of the experimental setup are given in Section VIII.3.

The intensity function of the signal pulse propagating in the z-direction and normally incident upon the Kerr shutter is given by

$$S(x,y,z;t) = f_1(x)g_1(y)[G(\tau)*I(\tau)]_{\tau=t-z/v_g} \qquad (8-1)$$

where f_1 and g_1 are intensity profiles of the signal pulse in the x- and y-directions, v_g is the group velocity of light in the shutter and $[G*I]$ is the backscattered signal given as a convolution of the impulse response $G(t)$ of the scatterers and the incident pulse shape $I(t)$ evaluated at $t - z/v_g$.

An infrared (IR) pulse travelling at the speed of light induces a narrow zone of birefringence at its position in the shutter which is normally closed, thus rendering it momentarily open at its location. Thus, the transmission of the shutter driven by the IR pulse is given by

$$T(x,y,z;t) = I(t - x/v_g)g_2(y)h_2(z) \qquad (8-2)$$

where $I(t - x/v_g)$, $g_2(y)$ and $h_2(z)$ are transmission profiles of the transparent zone in x-, y- and z-directions respectively. Note that the profile in x-direction is the intensity profile of the

incident pulse $I(t)$ appearing in Eq. (8-1). This is because the transmission of the shutter is assumed proportional to the square of the IR gating pulse and the incident pulse was derived from the IR pulse by second harmonic generation, which also scales approximately as the square of the IR pulse intensity. Thus, $T(t) \propto I_{IR}^2(t) \propto I(t)$. Combining Eqs. (8-1) and (8-2), the gated signal intensity recorded on the x-y plane can be shown to be:

$$D(x,y) = \int_{-\infty}^{\infty} dt \int_{-d}^{d} S(x,y,z;t) \, T(x,y,z;t)$$

$$= f_1(x) g_1(y) g_2(y) \int_{-d}^{d} dz \, h_2(z) \, [G(\tau) * R_I(\tau)]_{\tau = \frac{x-z}{v_g}}$$

$$\simeq f_1(x) g_1(y) g_2(y) \int_{-\infty}^{\infty} dz \, h_2(z) \, [G(\tau) * R_I(\tau)]_{\tau = \frac{x-z}{v_g}}$$

$$= f_1(x) g_1(y) g_2(y) \, [h_2(\tau) * G(\tau) * R_I(\tau)]_{\tau = \frac{x}{v_g}} \qquad (8-3)$$

where $R_I(t)$ is the autocorrelation function of $I(t)$, and the integrand is a fast decaying function in z. In our measurement system, the intensity variation in the x-direction is sampled and $f_1(x)$ is almost constant across the sampling width. Therefore, the intensity profile of the range-gated backscattered pulse is given by

$$D(x) = C_1 [h_2(\tau) * G(\tau) * R_I(\tau)]_{\tau = \frac{x}{v_g}}$$

$$= C_2 \mathcal{F}^{-1} [h_2(\omega) I_d(0,-\hat{z};\omega) \, S(\omega)] \qquad (8-4)$$

where C_1 and C_2 are constants and $H_2(\omega)$, $I_d(\omega)$ and $S(\omega)$ are the Fourier transforms of $h_2(t)$, $G(t)$ and $R_I(t)$, respectively.

Assuming that $I(t)$ and $h_2(t)$ are approximated by Gaussian functions, $D(x)$ can be expressed as a function of measurable parameters;

$$D(x) = C_3 \frac{\Delta\tau^2 w}{v_g} \int_{\infty}^{\infty} I_d(\omega) \, e^{-\left(\frac{\Delta\tau^2}{2} + \frac{w^2}{4v_g^2}\right)\omega^2} \, e^{i\frac{x}{v_g}\omega} \, d\omega \qquad (8\text{-}5)$$

where

$$I(t) = e^{-\left(\frac{t}{\Delta\tau}\right)^2}, \quad h_2\left(\frac{z}{v_g}\right) = e^{-\left(\frac{z/v_g}{w/v_g}\right)^2} = e^{-\left(\frac{z}{w}\right)^2},$$

C_3 is a constant, $\Delta\tau$ is the incident pulse duration, and w is the beam width of the IR gating pulse. $I_d(\omega)$ is given in Eq. (8-10) derived in the next section.

$D(x)$ represents the time-resolved backscattered pulse as seen through the Kerr shutter, where the spatial variable x along the axis of the shutter corresponds to time. The backscattered time resolved pulse at $z = 0$ will now be defined as I_s, where

$$I_s(t) = D(x)\big|_{x=v_g t} \qquad (8\text{-}6)$$

VII.2.3   Backscattering from Dense Medium

Since in measurement the beam width of the incident wave is collimated widely ($\sim$ 20 mm dia.), it is approximated as a plane wave. The diffusion solution for the plane wave incidence was obtained in Sections V.2.4 and V.2.5 as asymptotic cases of the beam wave solution. Here, the same result is derived from the diffusion equation for a plane wave incidence, which is considerably simpler than the beam wave incidence.

The diffusion equation and boundary conditions describing the propagation of the average intensity $U_d(z)$ for a plane wave pulse incident on a semi-infinite slab consisting of a random dense distribution of anisotropic scatterers is given by (Ishimaru, 1978b)

$$\left(\frac{\partial^2}{\partial z^2} - q^2 \right) U_d = Q_o$$

$$U_d - h \frac{\partial}{\partial z} U_d + \frac{Q_1}{2\pi} = 0, \quad \text{at } z = 0 \qquad (8\text{-}7)$$

$$U_d = 0 \qquad , \quad \text{at } z = \infty$$

where Q_o and Q_1 represent the isotropic and anisotropic source contributions within the medium.

$$Q_o = - \frac{3}{4\pi} F_o \rho \sigma_s (\alpha_{tr} + \bar{\mu}\alpha) e^{-\alpha z}$$

$$Q_1 = F_o \rho \sigma_s \frac{\bar{\mu}}{\alpha_{tr}} e^{-\alpha z} \qquad (8\text{-}8)$$

and F_o is the source photon flux at $r = z = 0$, $\bar{\mu}$ is the average value of the cosine of the scattering angle ($-1 \le \bar{\mu} \le 1$) where -1 is purely backscattering, $+1$ is purely forward scattering, and 0 represents isotropic scattering. The microscopic scattering and absorption cross-sections are σ_s and σ_a, ρ is the density of scatterers, and

$$q^2 = 3\alpha_a \alpha_{tr} \quad ,$$

$$h = \frac{2}{3\alpha_{tr}} \quad ,$$

$$\alpha = \rho(\sigma_s + \sigma_a) - i\frac{\omega_d}{c}$$

$$\alpha_{tr} = \rho[\sigma_s(1 - \bar{\mu}) + \sigma_a] - i\frac{\omega_d}{c}$$

$$\alpha_a = \rho\sigma_a - i\frac{\omega_d}{c}$$

Note that equation (8-7) is derived from the two frequency equation of transfer, where

$$\omega_d = \omega_1 - \omega_2$$

and the phase velocity within the medium at each frequency is approximately equal to the velocity of light c . Detailed discussion is given elsewhere (Ishimaru, 1978b).

Solving the diffusion equation, the solution for the average intensity in a dense medium is given by

$$U_d(z) = \frac{3}{4\pi}\frac{F_o\rho\sigma_s}{q^2-\alpha^2}\{(\alpha_{tr} + \bar{\mu}\alpha)e^{-\alpha z} - \frac{3\alpha_{tr} + (2+3\bar{\mu})\alpha + 6\bar{\mu}\alpha_a}{3\alpha_{tr} + 2q}\alpha_{tr}e^{-qz}\} \quad (8-9)$$

This agrees with Eq. (5-36) exactly, which was obtained through a different approach in Section V.2.5.

Using Eq. (8-9), the specific intensity improved to include the effect of first order multiple scattering at the boundary of the scattering medium, was given in Eq. (5-68):

$$I_d \ (z = 0, \ -\hat{z}; \omega_1, \omega_2)$$

$$= \frac{3}{4\pi} F_o \ [\ \frac{\rho \sigma_b}{6\alpha} + (\rho \sigma_s)^2 \ \frac{\bar{\mu}q - \alpha_{tr}}{q^2 - \alpha^2} \{ \frac{2\alpha + 3\bar{\mu}\alpha + 3\alpha_{tr} + 6\bar{\mu}\alpha_a}{(2q + 3\alpha_{tr})(q + \alpha)}$$

$$- \frac{\bar{\mu}q + \alpha_{tr}}{2\alpha \ \alpha_{tr}} \ \} \ ] \tag{8-10}$$

Definitions of parameters and detailed discussion on the derivation are given in Section V.2.8. Note that the first and the second term of the square bracket [·] corresponds to the first order multiple scattering and diffusion, respectively.

Since this is an intensity in the frequency domain, the Fourier transform of Eq. (8-10) gives the impulse response in the time-domain, i.e.,

$$G(t) = \int_{-\infty}^{\infty} I_d(\bar{r}, \hat{s}; \omega_d) e^{-i\omega_d t} \ d\omega_d \tag{8-11}$$

These results coupled with the picosecond range-gating technique given in the previous section will be the basis of our analytical evaluation of the experimentally obtained time-resolved backscattered pulse on the interface plane of a scattering medium at $z = 0$.

VIII.3   EXPERIMENTS

VIII.3.1   Experimental Facility

The apparatus used in Chapters VI and VII is modified. Its

schematic diagram is shown in Fig. 8-3. A mode-locked Nd:glass

laser, LASER generates a train of ~100 IR pulses (λ = 1.06 μm),

each of ~10 psec duration (FWHM) and carrying a peak power density

of ~200 MW/cm^2 . Frequency doubling occurs in a KDP crystal adjusted

to yield ~10% conversion efficiency. The green pulses are separated

from the IR pulses by a dichroic beam splitter DBS. The vertically

polarized green pulses are directed by prism PR_1 toward a polarizing

beam splitter cube PBS, which reflects vertically polarized light

but transmits horizontally polarized light. The quarter-wave retar-

der plate, λ/4, serves to circularly polarize the green pulses

impinging on the scatterers contained in the scattering cell SC.

The backscattered pulses are randomly polarized, which allows them to

pass through the polarizing beamsplitter. The presence of the retar-

der plate assures that the scattered light from the first few mean

free paths in the medium will also be transmitted by PBS. After

passing through the field stop aperture FS, the beam of signal pulses

is expanded by a pair of cylindrical lenses L_1 and L_2, to a trans-

verse width of ~5 cm before entering the picosecond shutter.

In the meantime, the IR pulses, polarized vertically by the half-

wave retarder plate λ/2, traverse a variable optical delay line, con-

sisting of three right angle prisms PR_2-PR_4, to equalize the IR and

green pathlengths and thus assure proper gating synchronization. The
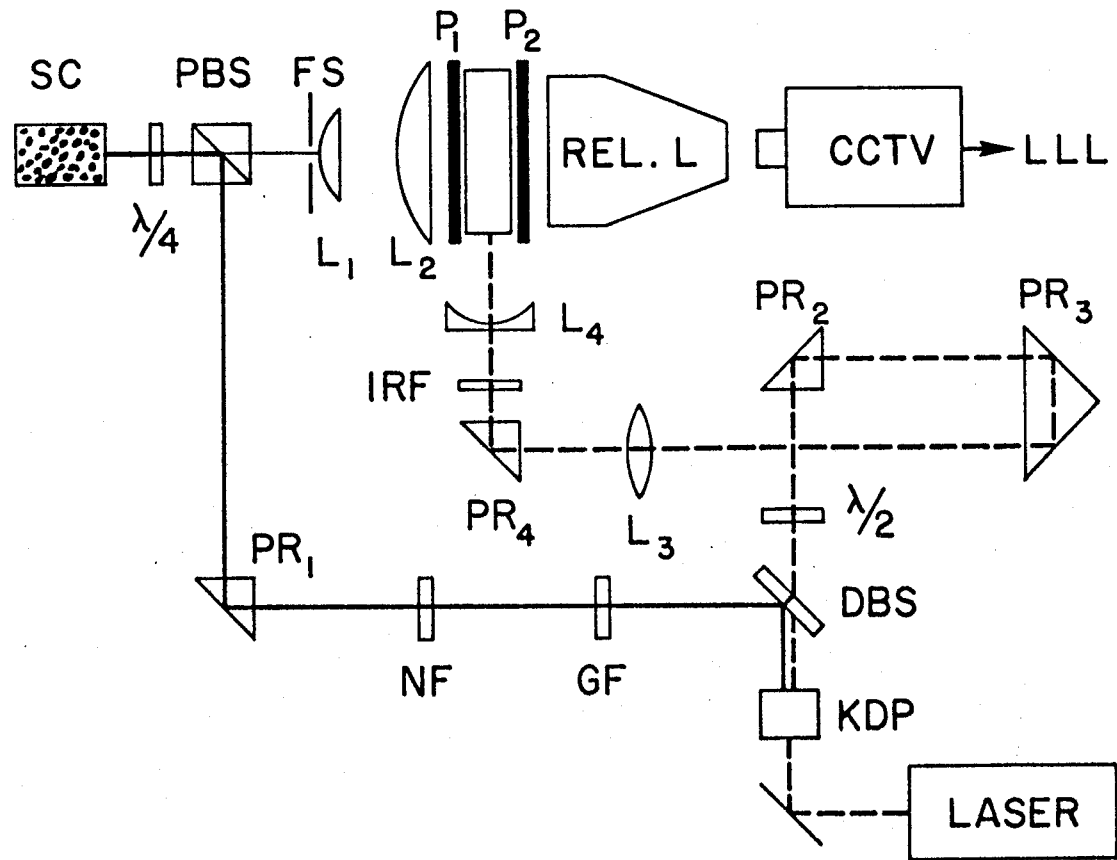
Fig.8-3 Schematic of on-axis backscattered pulse shape measurement

picosecond shutter consists of a rectangular quartz cell containing carbon disulfide (CS_2) placed between two crossed polarizers P_1 and P_2 whose polarization axes are at 45° to the horizontal (Duguay, 1969). The beam of IR pulses is rendered vertically polarized by a half-wave retardation plate, $\lambda/2$, and its diameter is reduced to ~2 mm by the pair of lenses L_3 and L_4. In the CS_2 each IR pulse induces a narrow zone of birefringence which travels through the Kerr liquid at the speed of light. At the location of the IR pulse, the shutter transmits light incident at a right angle to its path. A portion of the beam-expanded signal pulse is thus transmitted along the IR path at a position which is proportional to the signal pulse delay. In this way, one can observe a time-resolved streak record of the incident signal through the shutter. The peak transmission factor is ~1%, with an on-off contrast ratio of ~1000. The output from the shutter is detected and processed by a low-light-level video detector system described in Section IV.3.2(3). Note the image intensifier was not used in this experiment. Since each pulse train consists of ~100 pulses, the final record is a multiple exposure of the same event.

VII.3.2   Sample Scatterers

The scattering media were aqueous suspensions of latex micro-spheres obtained from Dow Chemical Corp. with diameters of 0.481 μm, 2.02 μm, 3.2 μm, 5.7 μm and 45.4 μm. They were provided in concentrated solutions with the density, 30% by weight for 2.02 μm spheres and 10% wt. for other spheres. Sample suspensions of desired density

were prepared by diluting the concentrated solutions with 0.01% detergent water. The detergent, sodium dodecyl sulfate, was added to distilled and deionized water as a surfactant to prevent aggregation of the particles. The suspensions were contained in cylindrical spectrophotometric cells with 22 mm diameter and 50 mm pathlength.

To simulate an impulse response of a measurement system, a diffusely reflecting plate was used in place of the scattering cell. It was a white, 5 cm x 5 cm barium sulfate plaque obtained from Photo Research. It was designed for a reflectance standard and has diffuse reflectance nearly 100%.

VIII.3.3 Data Processing

The time-resolved intensity profiles of the backscattered pulses, obtained from the detector system in Fig. 8-3, were recorded with an oscilloscope. An example of the recorded signals is shown in Fig. 8-4. The curves were digitized and stored on magnetic tapes for further processing. The intensity axis of the recroded pulse (ordinate) was linear over the intensity range of interest, but the time axis (abscissa) was not linear due to the imaging characteristics of a video detector. The calibration factors for this nonlinearity were obtained by measuring the time shift of the recorded pulse as a function of a known change in the pathlength of the IR gating pulse. Since the laser output intensity fluctuates from shot to shot, from 10 to 20 data curves were collected for each scattering medium.
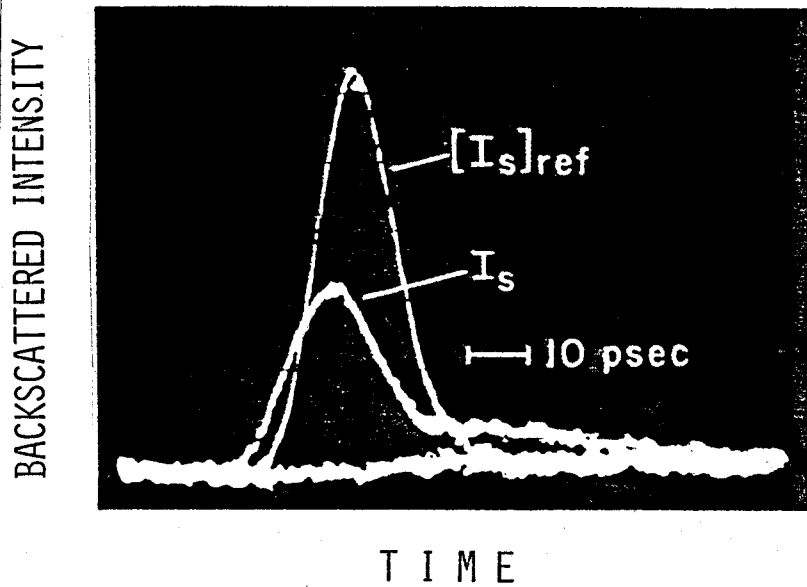
Fig.8-4 Typical recorded signals : backscattering from
a diffusely reflecting plate, $[I_s]_{ref}$, and
a solution of latex spheres, I_s

VIII.4   RESULTS AND DISCUSSION

VIII.4.1   Agreement between Theory and Measurement

Fig. 8-4 shows an example of the recorded signals. They are the superimposed intensity profiles of backscattered pulses from a diffusely reflecting plate and a suspension of 0.481 μm latex spheres. The pulse shape from the diffusely reflecting plate is smooth and closely follows the average outline of the more noisy profiles obtained with a mirror as the target, except for a slight tailing. Therefore, it was concluded that the pulse shape of the diffusely reflecting plate closely represents the impulse response of our measurement system.

After normalization of each curve by the peak intensity of the impulse response, an average and a standard deviation were calculated at each point on the time axis sampled in the digitizing process. The width of the double curves in the following figures (a) define the standard deviation of the data. Fig. 8-5(a) shows the normalized backscattered pulse shapes from suspensions of 0.481 μm latex spheres having concentrations of 10%, 1% and 0.1% by weight and from the diffusely reflecting reference plate. Fig. 8-5(b) shows the backscattered pulses calculated by Eqs. (8-6), (8-5) and (8-10), where the scattering and absorption parameters were calculated using MIE solutions modified to include size distributions of scatterers. Figs. 8-6 ～ 8-11 show a similar comparison between experiment (a) and theory (b) for latex spheres with diameters of 2.02 μm (ρ = 0.3%, 3%, 30% wt.), 2.02 μm (hereafter, ρ = 0.1%, 1%, 10% wt.), 3.20 μm,

5.7 μm, 5.7 μm (absorbing) and 45.4 μm, respectively. These sizes investigated correspond to those of biological particles of interest. Their correspondence is as follows: 0.481 μm and 3.20 μm are the typical diameters of microwave induced cataracts in an eye of a rabbit (Bruckner, 1978a). 0.481 μm and 45.4 μm are the typical diameters of a spherical equivalent of a platelet and a platelet aggregate (Ishimaru, 1976). 5.7 μm is the diameter of a spherical equivalent of a red blood cell (Reynolds, 1975). 2.02 μm is a representative diameter of general biological microparticles. Measurements are not shown for 0.1% solution of 2.02 μm spheres and 0.1% and 1% solutions of 45.4 μm spheres, where the signal was below the noise level.

Discrepancies can be seen between measurement and calculation, particularly in the cases of the lowest density (ρ = 0.1% wt.) where the validity of the diffusion approximation is questionable. They are the time-shifts of the pulses and the separation of the effect of first order multiple scattering (FOMS) from that of diffusion. Both appear in theoretical calculations but not in measurements. Otherwise, the agreement between theory and experiment in the pulse shapes is good. Note the difference in the pulse shape for the least concentration between the cases of 0.481 μm, 2.02 μm spheres and 3.20 μm, 5.7 μm spheres. As was theoretically predicted in Section V.4.6, FOMS becomes comparable to diffusion for 3.20 μm or larger spheres.

The general pulse shape is characterized by a rapid rise and slow asymptotic decay. The response to a decrease in scatterer

concentration is that of pulse broadening and an intensity increase in the asymptotic decay. Except for the case of 45.4 μm spheres, pulse broadening for a 10% solution was a few picoseconds, while the broadening for a 1% solution is approximately 5 to 10 picoseconds. In general, pulse broadening increases as the concentration is decreased and for a 0.1% solution the pulse broadening extends for several tens of picoseconds.

Despite the fluctuation in the intensity of the incident light, the agreement in the relative magnitude of the pulse is also good. Fig. 8-12 shows the result of the regression analysis for the peak values of the measured and calculated pulses. The correlation coefficient obtained (ρ_{xy} = 0.894) is considered to be high for this experiment which was originally designed for the qualitative analysis.

During approximately the first 20 psec the backscattered pulse shapes seem to be dominated by the impulse response of the measurement system rather than that of the scattering medium of interest. The impulse response of the measurement system is mainly determined by the cross-correlation function of the laser pulse shape and the shutter transmission function. To remove the influence of the laser pulse shape and shutter response, and thus more fully characterize the scattering and absorption properties of the medium, a laser and gating system of much shorter pulse duration and resolution, respectively, will be required.

The following hypotheses are considered to explain the above

discrepancies between theory and experiment. The backscattering from the boundary region of scatterers may be larger than that calculated by the FOMS approximation. If so, the impulse response of measurement system is predominant at the time origin of the backscattered pulse and the effect of the diffusion appears only in the asymptotic tale of the pulse. This clarifies the difference in the measured pulse shapes for the least concentration between the cases of 0.481 μm, 2.02 μm spheres and 3.2 μm, 5.7 μm spheres. Since in the latter cases, the diffusion tail appears late and small, the observed pulse shape without a tail is due to the scattering at the boundary of the scattering medium. While, in the former cases, the diffusion tail is large and close enough to merge in the pulse shape due to the scattering at the boundary.

Another plausible hypothesis to explain the discrepancies is the following. There may be a different mechanism of scattering which cannot be described by the asymptotic expansion of the FOMS and diffusion approximations. This scattering corresponds to the "multiple scattering" region named in Section VI.4.1, which was placed between the FOMS and diffusion regions. See Section VI.4 for detailed discussions. A new theory may be required to fill this gap or "missing link."

VIII.4.2 Sensitivity for Scatterers Characteristics

Figs. 8-6 ~ 8-10 show that the shape of the backscattered pulse is sensitive to the change of particle concentration but not to the change of particle size itself in the range of 0.481 ~ 5.7 μm. It

should be remembered that with a tenuous medium scattering patterns are very sensitive to the change of the scatterers size. The scattering patterns for 0.481 μm, 2.02 μm and 3.20 μm spheres were shown to be completely different in Section IV.4.2. See Figs. 4-5, 4-6 and 4-7. This insensitivity to a particle size is attributed to the multiple scattering effect which averages out the distinct scattering patterns of individual scatterers and make the macroscopic scattering isotropic.

However, as was theoretically predicted in Section V.4.3, an effect of the scatterers' absorption characteristics on the back-scattered pulse shape can be expected. To examine this effect, experiments were conducted with absorbing and non-absorbing scatterers. They are respectively blue dyed latex spheres and regular white latex spheres, both with 5.7 μm diameters, and the incident light is green ($\lambda = 0.53$ m). Fig. 8-13 shows the comparison of their measurements. The effect of absorption can clearly be observed in the reduced pulse height maxima and the almost completely diminished diffusion tail. The theoretical discussions made in Section V.4.3 are thus verified. The agreement with the theory can be confirmed in the comparison between the measurement and calculation shown in Figs. 8-13 and 8-14.

The results presented in this section suggest the applicability of this technique to remote sensing problems. Particularly it will be useful to investigate the density or the absorption characteristics of dense media.

VIII.4.3 Dependence on Diffusion Optical Distance

Fig. 8-15 shows the comparison of the measurements with 0.481 μm and 45.4 μm dia latex spheres. The backscattered pulse shapes are similar between 0.1% wt. solution of 0.481 μm spheres and 10% wt. solution of 45.4 μm spheres. Between these two cases, all the parameters such as particle sizes, cross sections, particle densities, etc. are different except for the diffusion optical distance per unit distance, $\tau_d/z = \rho\sigma_{tr}$. Note the closeness in $\rho\sigma_{tr}$ (4.61 cm^{-1} and 5.39 cm^{-1}) and the difference in the regular optical distance, $\tau/z = \rho\sigma_t$ (30.5 cm^{-1} and 74.1 cm^{-1}). This verifies experimentally the results of the numerical analysis presented in Section V.4.1 and V.4.3 which showed the dependence on τ_d. Also, it justifies the choice of τ_d as the normalization constant in the analysis of diffuse scattering.

The results shown in this section suggest the following applications. (1) Since the backscattering from dense media is dependent on $\tau_d = \rho\sigma_{tr}$ z, the physical change which causes the change in any one of the parameters, ρ , σ_{tr} and z can be detected by observing the backscattered pulse shape. This is applied to detect the change in microwave induced cataracts _in vivo_. The changes of interest are the density of cataracts, the size of constituent protein particles and the thickness of the cataractous lesion.

If two of the three parameters, ρ , σ_{tr} and z are known, another parameter can be estimated from the backscattered pulse shape. For example, in remote-sensing of fog by lidar, the density of the

fog ρ can be estimated by knowing the average cross section $\langle\sigma_{tr}\rangle$ of the fog particles and the penetration depth z of the light.

VIII.4.4 Detection of Platelet Aggregates

Finally, a theoretical basis is given for our ultimate goal, i.e., the detection of platelet aggregates in a transfusion blood.

If scatterers are aggregated in a closed system, the density of the scatterers does not change in terms of the fractional weight or the fractional volume. However, the diffusion optical distance changes considerably due to the change in the optical cross sections of the scatterers. This is because the volume of the scatterer is proportional to the cube of the scatterers' size while the cross section is approximately proportional to the square. Therefore, if the scatterers are aggregated, a change in the shape of the backscattered pulse is expected.

An example is shown in Fig. 8-16(a) and (b) which are the backscattered pulse shapes from 0.481 μm spheres and 45.4 μm spheres both with the 10% wt. density. The conditions of (a) and (b) simulate those before and after the aggregation of platelets, respectively. This distinct difference in shape suggests a promising applicability of this technique to the detection of scatterer aggregation in dense media. If other parameters are constant or known, this technique can be also used to evaluate the degree of aggregation.

(a)

MEASUREMENT

(b)

THEORY
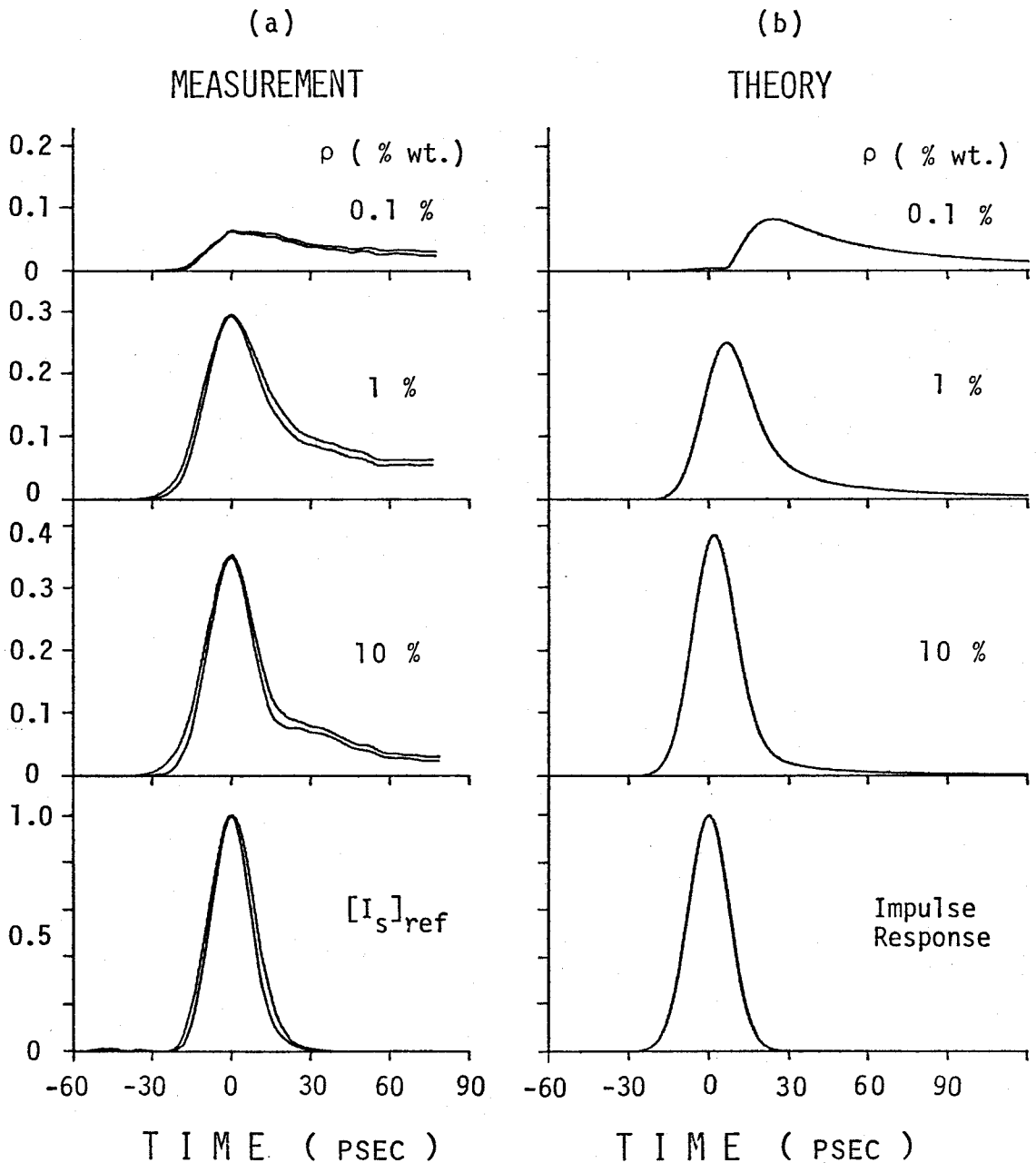
Fig.8-5 Backscattered pulse shapes from 0.481 μmφ latex spheres :
normalized by peak value of bottom curve, i.e., $I_s(t) / [I_s(0)]_{ref}$

(a) measurements; aqueous solutions of spheres (above three curves),
and diffusely reflecting plate (bottom curve). Dual curves
represent range of fluctuation of measured pulse shapes.
(b) theoretical calculations; 0.481 μmφ latex spheres (above three
curves), and impulse response (bottom curve), wave length
λ = 0.53 μm, beam width BW = 3 mm, pulse length PL = 10 psec.

(a)

MEASUREMENT

(b)

THEORY
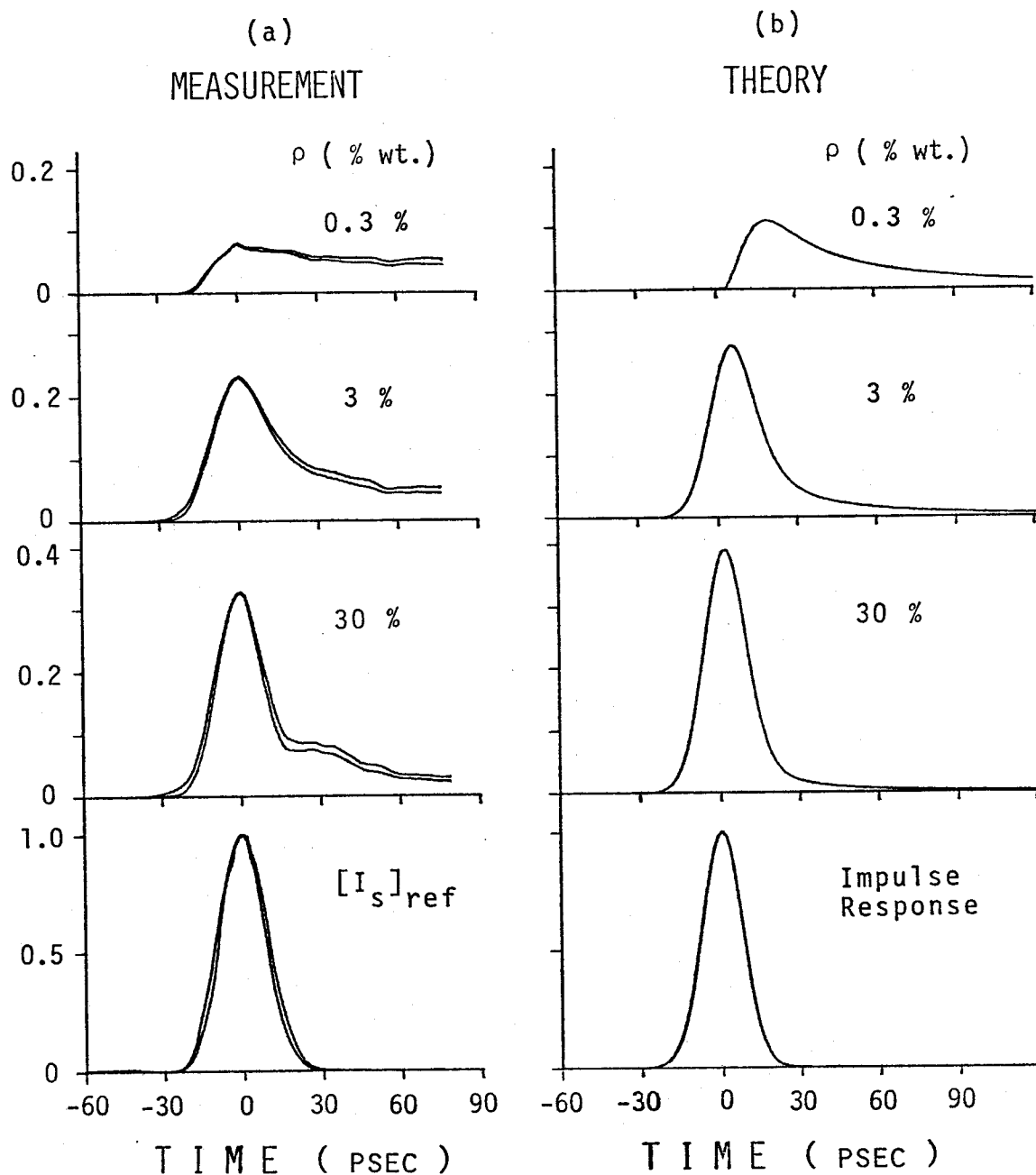
Fig.8-6 Backscattered pulse shapes from 2.02 μmφ latex spheres (30%) : normalized by peak value of bottom curve, i.e., $I_s(t)$ / $[I_s(0)]_{ref}$

(a) measurements; aqueous solutions of **spheres** (above three curves), and diffusely reflecting plate (bottom curve). Dual curves represent range of fluctuation of measured pulse shapes.

(b) theoretical calculations; 2.02 μmφ **latex** spheres (above three curves), and impulse response (bottom curve), wavelength λ = 0.53 μm, beam width BW = 3 mm, **pulse** length PL = 10 psec.

(a)

MEASUREMENT

(b)

THEORY
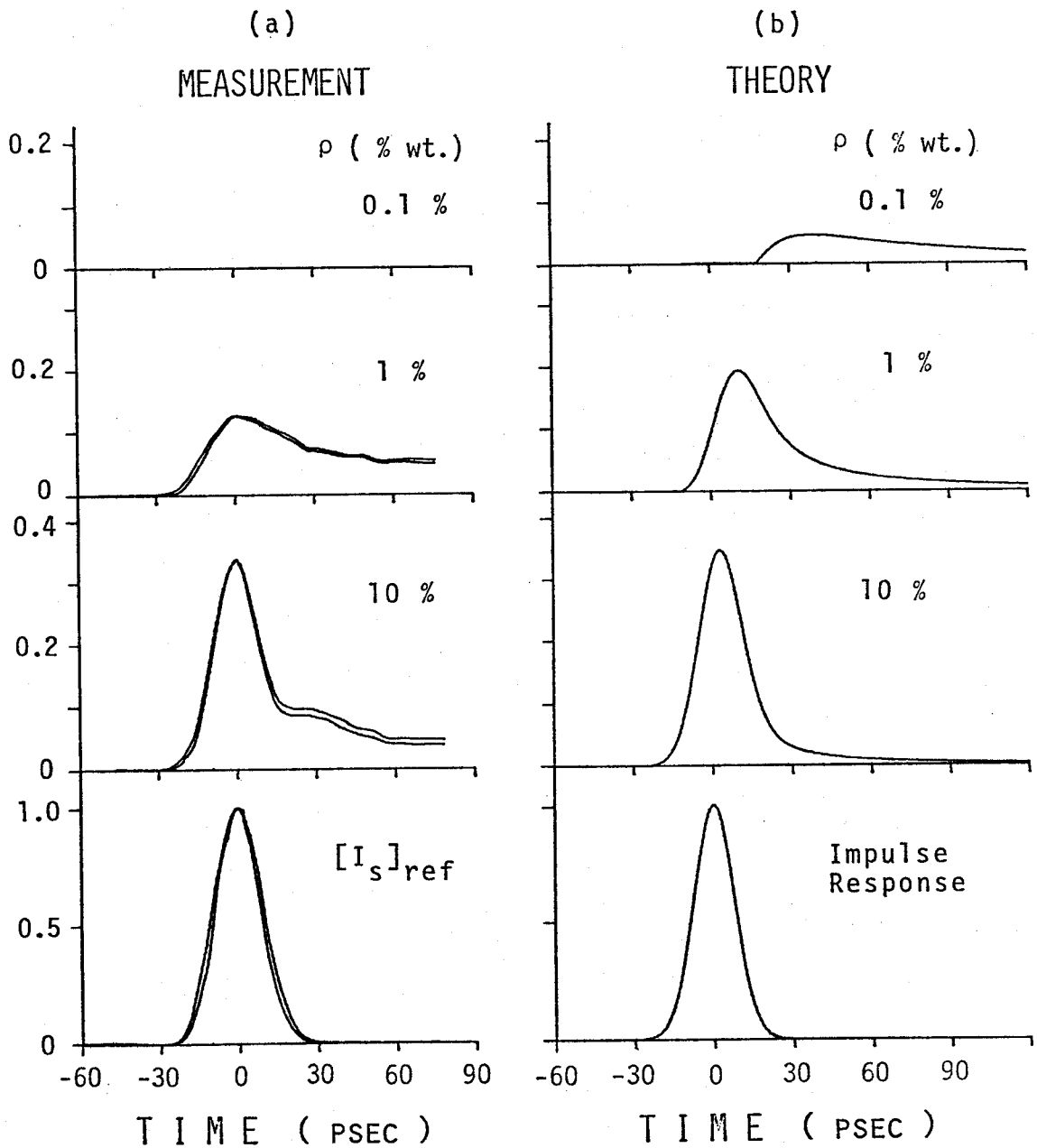
Fig.8-7 Backscattered pulse shapes from 2.02 μmφ latex spheres (10%) : normalized by peak value of bottom curve, i.e., $I_s(t)$ / $[I_s(0)]_{ref}$

(a) measurements; aqueous solutions of spheres (above three curves), and diffusely reflecting plate (bottom curve). Signal level of 0.1 % solution was too low to measure.

(b) theoretical calculations; 2.02 μmφ latex spheres (above three curves), and impulse response (bottom curve), wavelength λ = 0.53 μm, beam width BW = 3 mm, pulse length PL = 10 psec.
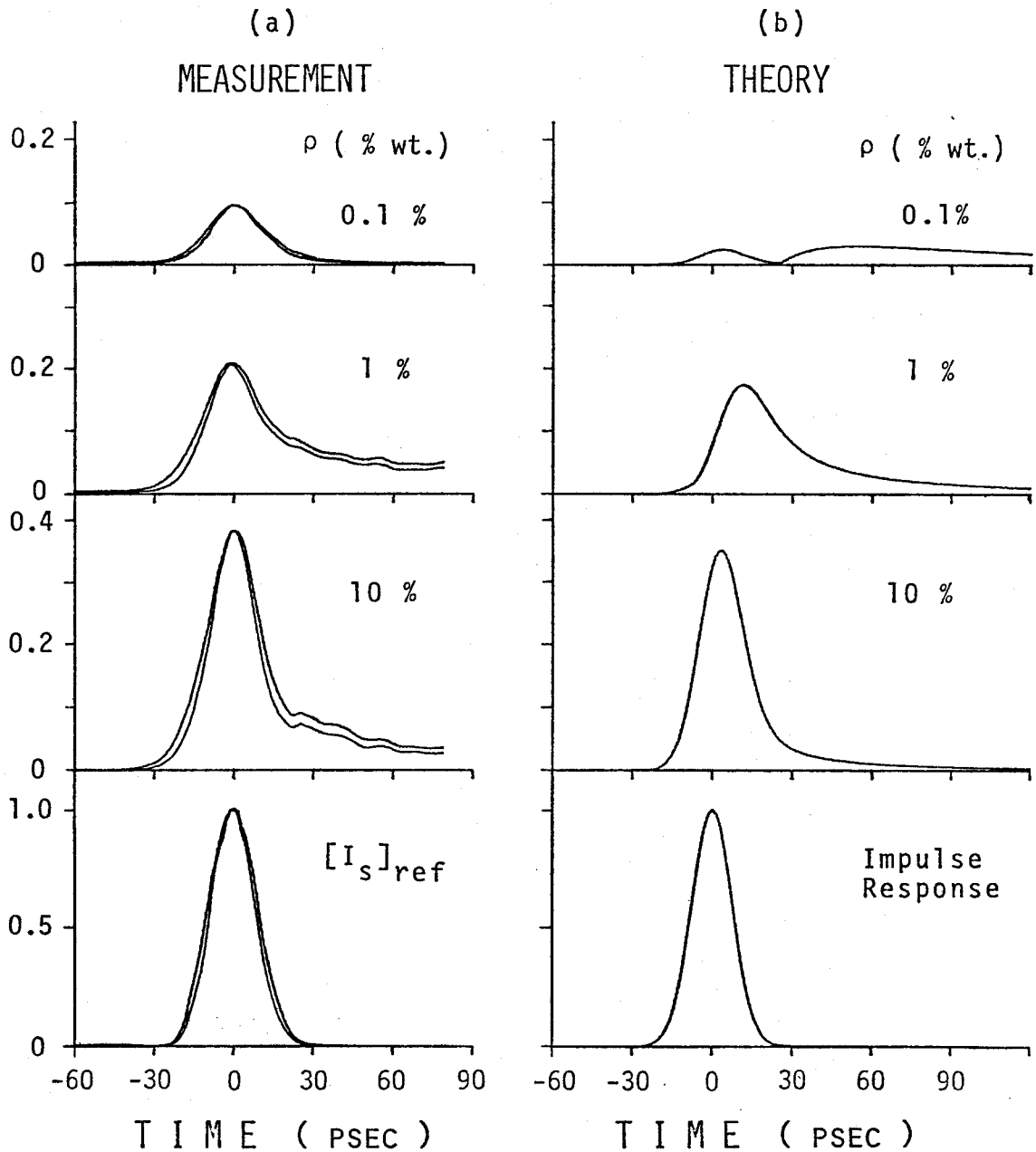
Fig.8-8 Backscattered pulse shapes from 3.20 μmφ latex spheres :
normalized by peak value of bottom curve, i.e., $I_s(t) / [I_s(0)]_{ref}$
(a) measurements; aqueous solutions of spheres (above three curves),
    and diffusely reflecting plate (bottom curve). Dual curves
    represent range of fluctuation of measured pulse shapes.
(b) theoretical calculations; 3.20 μmφ latex spheres (above three
    curves), and impulse response (bottom curve), wavelength
    $\lambda = 0.53$ μm, beam width BW = 3 mm, pulse length PL = 10 psec.

(a)

MEASUREMENT

(b)

THEORY
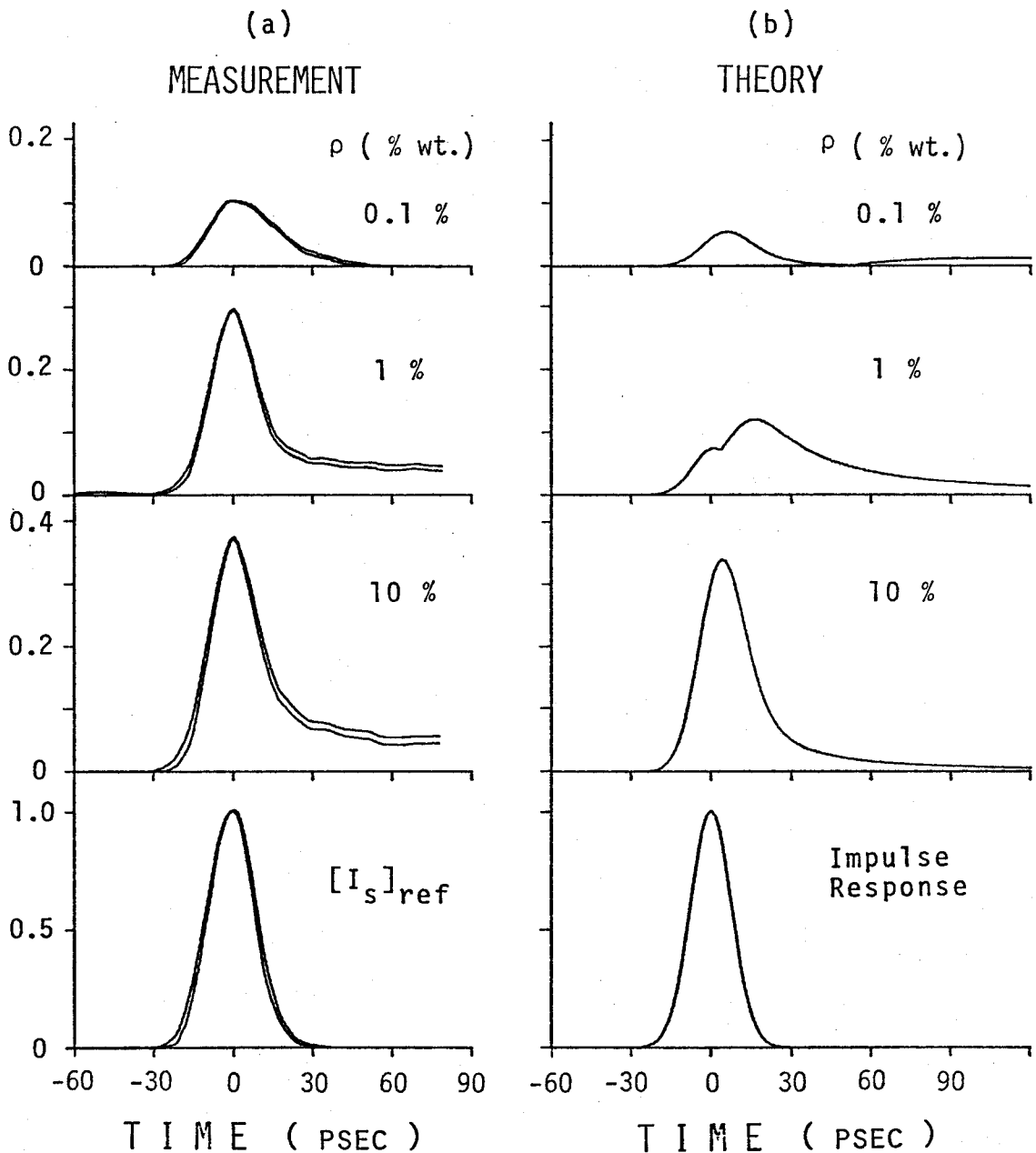
Fig.8-9 Backscattered pulse shapes from white 5.7 $\mu m\phi$ latex spheres : normalized by peak value of bottom curve, i.e., $I_s(t)$ / $[I_s(0)]_{ref}$

(a) measurements; aqueous solutions of spheres (above three curves), and diffusely reflecting plate (bottom curve). Dual curves represent range of fluctuation of measured pulse shapes.

(b) theoretical calculations; 5.7 $\mu m\phi$ latex spheres (above three curves), and impulse response (bottom curve), non-absorbing spheres, albedo W_o= 1.0, λ = 0.53 μm, BW = 3 mm, PL = 10 psec.
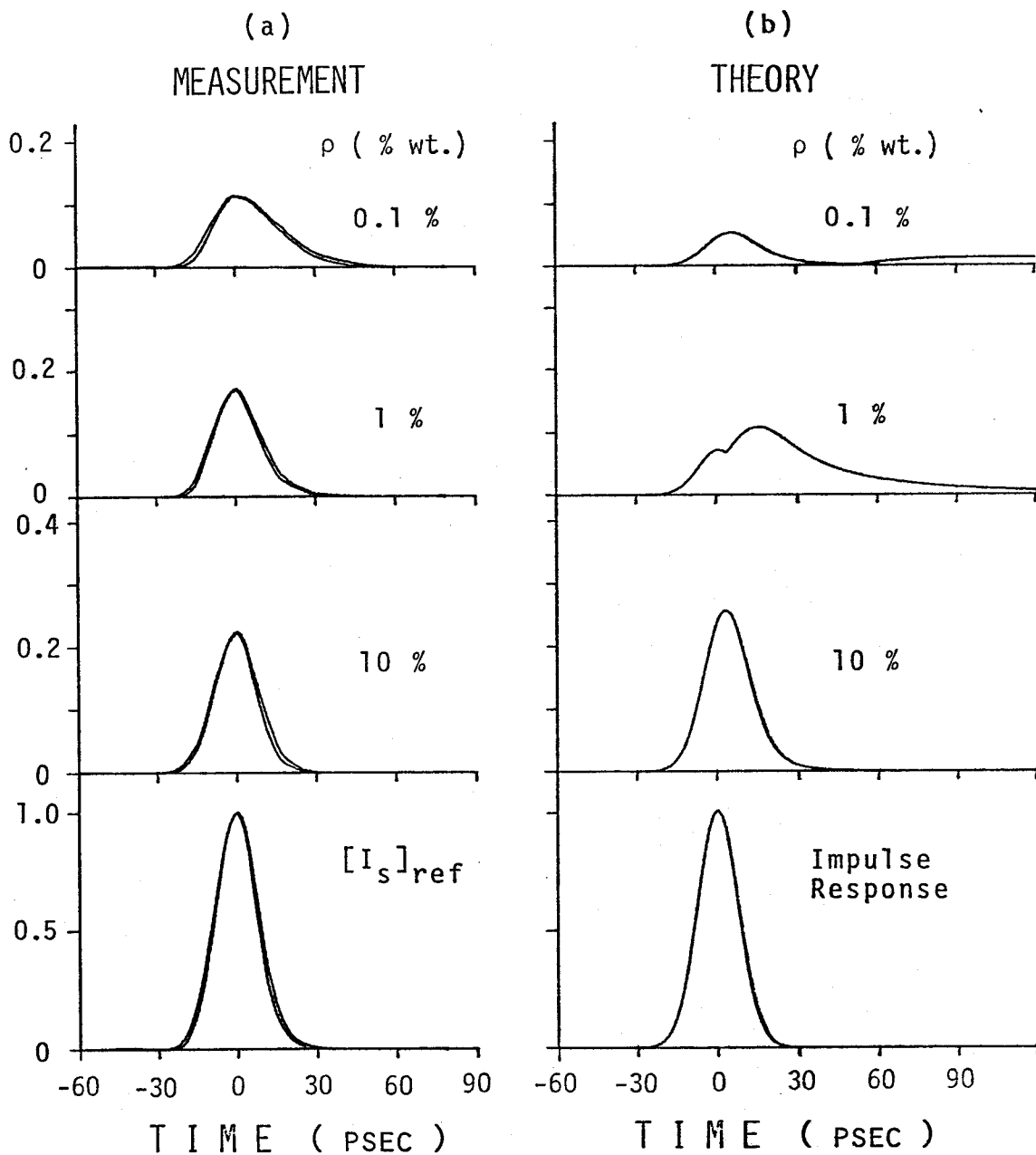
Fig.8-10 Backscattered pulse shapes from blue 5.7 μmϕ latex spheres :
normalized by peak value of bottom curve, i.e., $I_s(t) / [I_s(0)]_{ref}$
(a) measurements; aqueous solutions of spheres (above three curves),
and diffusely reflecting plate (bottom curve). Dual curves
represent range of fluctuation of measured pulse shapes.
(b) theoretical calculations; 5.7 μmϕ latex spheres (above three
curves), and impulse response (bottom curve), absorbing spheres
$n_i = 0.0001$, $W_o = 0.992$, $\lambda = 0.53$ μm, BW = 3 mm, PL = 10 psec.
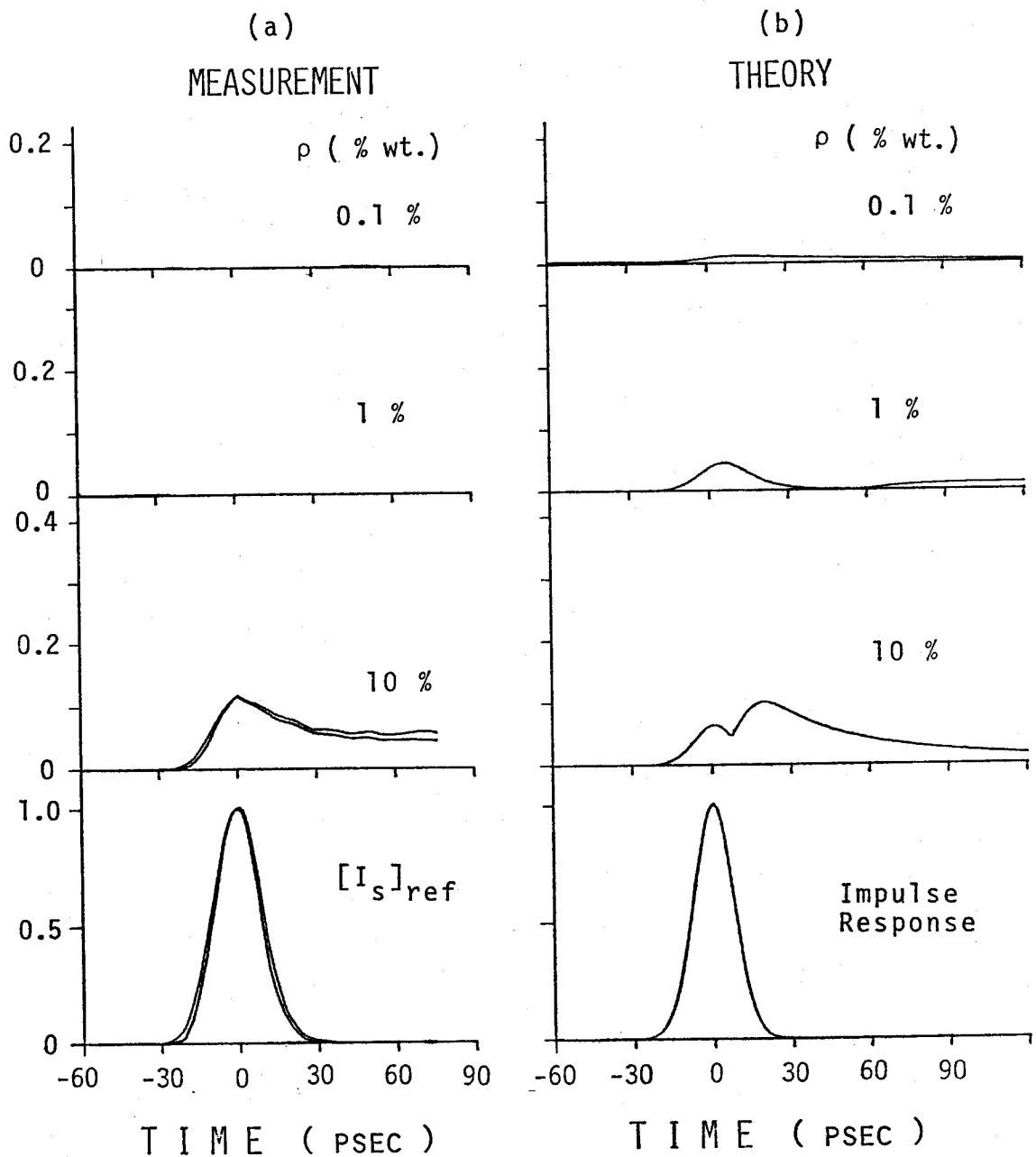
Fig.8-11 Backscattered pulse shapes from 45.4 μmφ latex spheres : normalized by peak value of bottom curve, i.e., $I_s(t)$ / $[I_s(0)]_{ref}$

(a) measurements; aqueous solutions of spheres (above three curves), and diffusely reflecting plate (bottom curve). Signal level of 0.1 % and 1 % solutions was too low to measure.

(b) theoretical calculations; 45.4 μmφ latex spheres (above three curves), and impulse response (bottom curve), wavelength λ = 0.53 μm, beam width BW = 3 mm, pulse length PL = 10 psec.
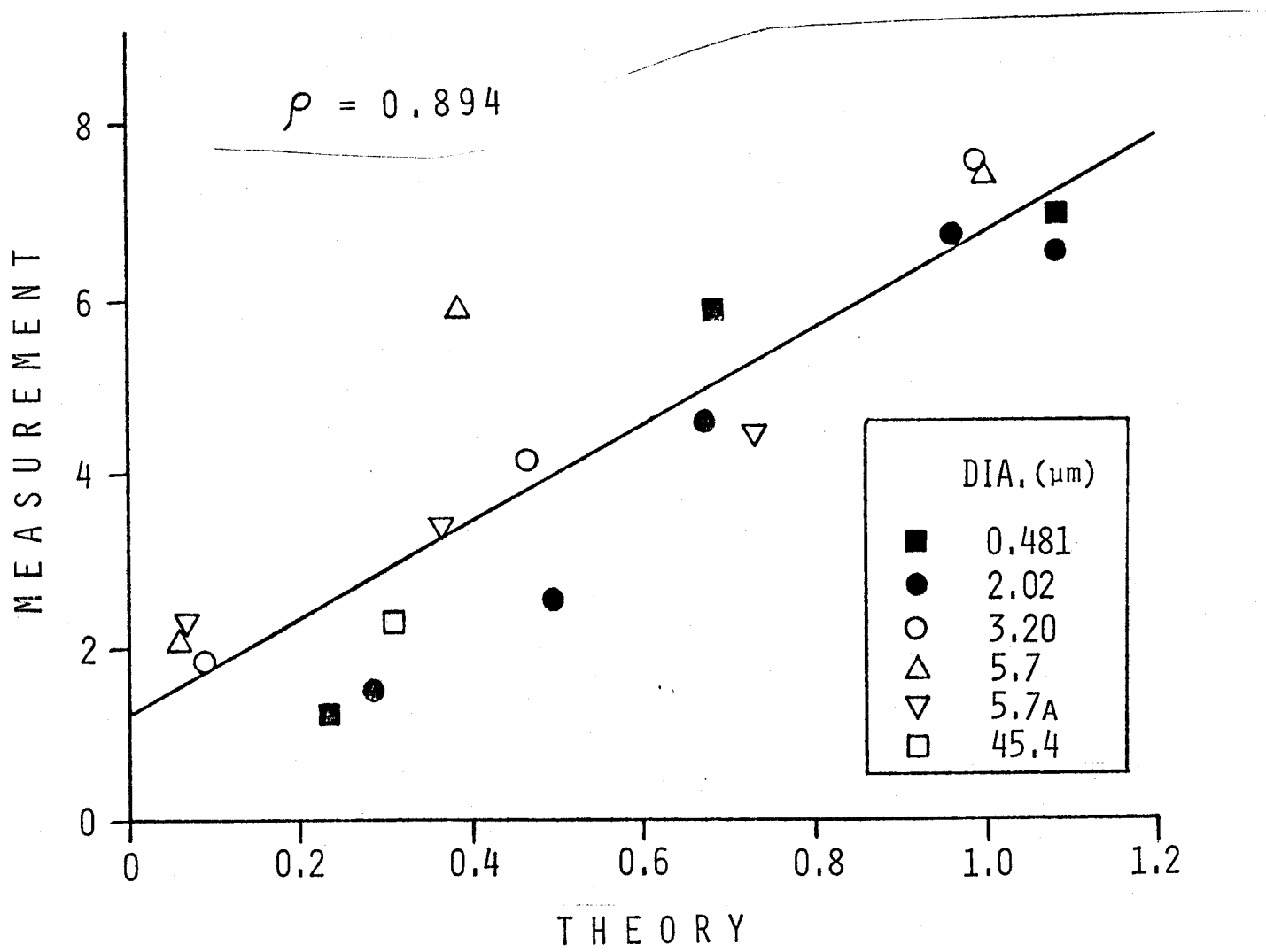
Fig.8-12 Correlation of peak pulse intensity between theory and measurement
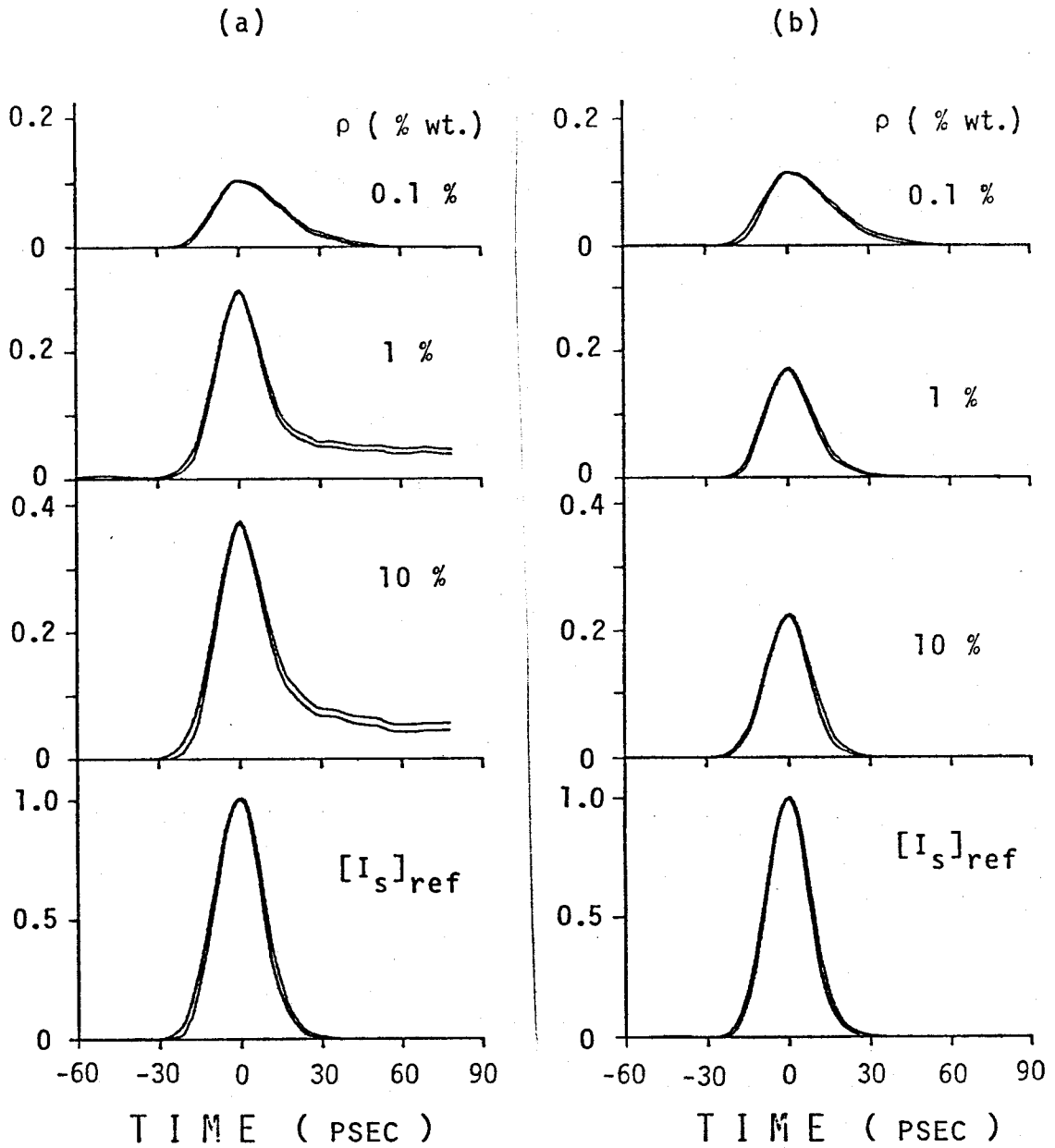
Fig.8-13 Effect of absorption of scatterers : measurement
5.7 μmφ latex spheres, (a) non-absorbing (white),
(b) absorbing (blue)
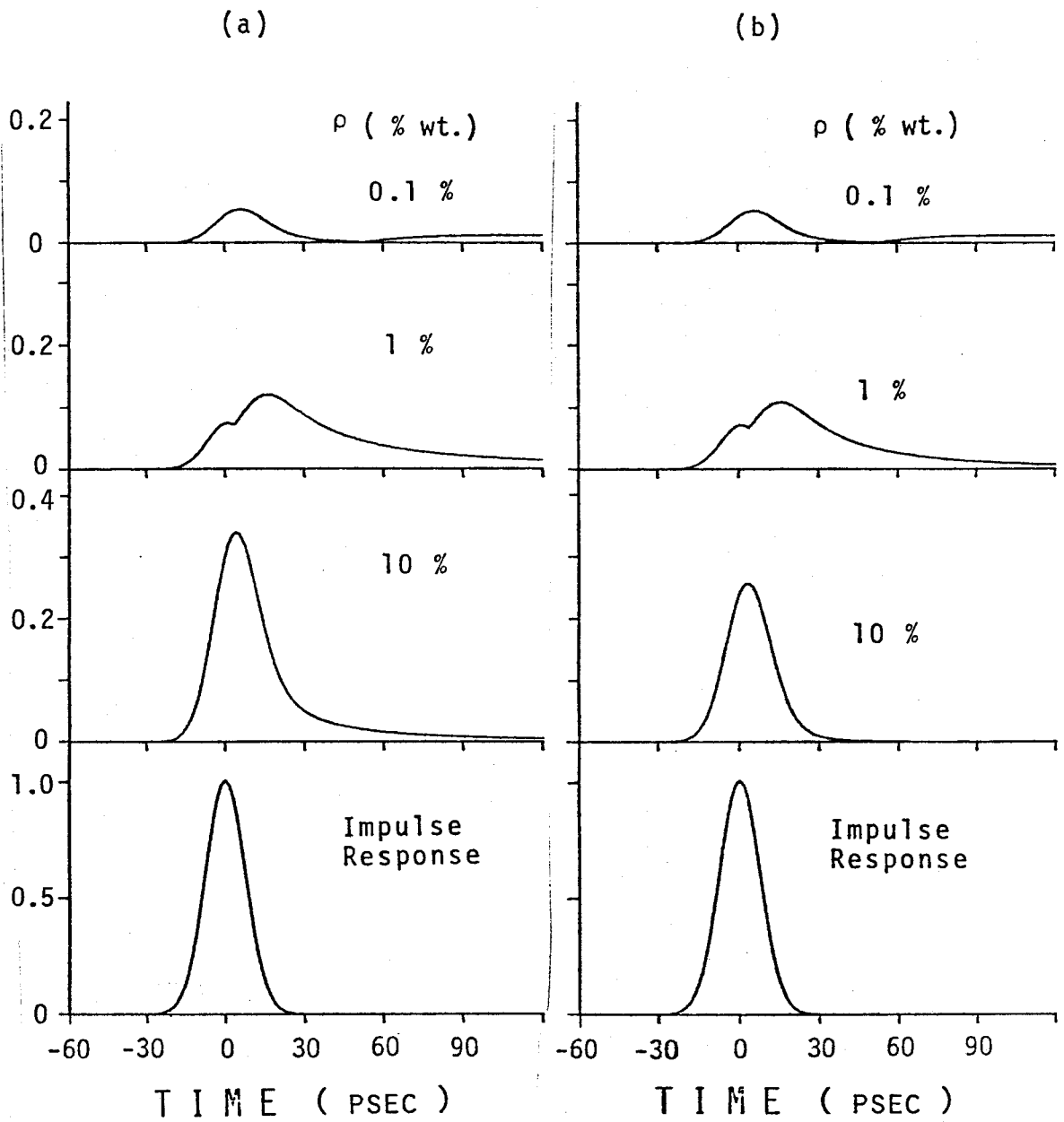
Fig.8-14 Effect of absorption of scatterers : theory
5.7 $\mu m\phi$ latex spheres, (a) non-absorbing (n_i = 0.0,
W_o = 1.0), (b) absorbing (n_i = 0.0001, W_o = 0.992)
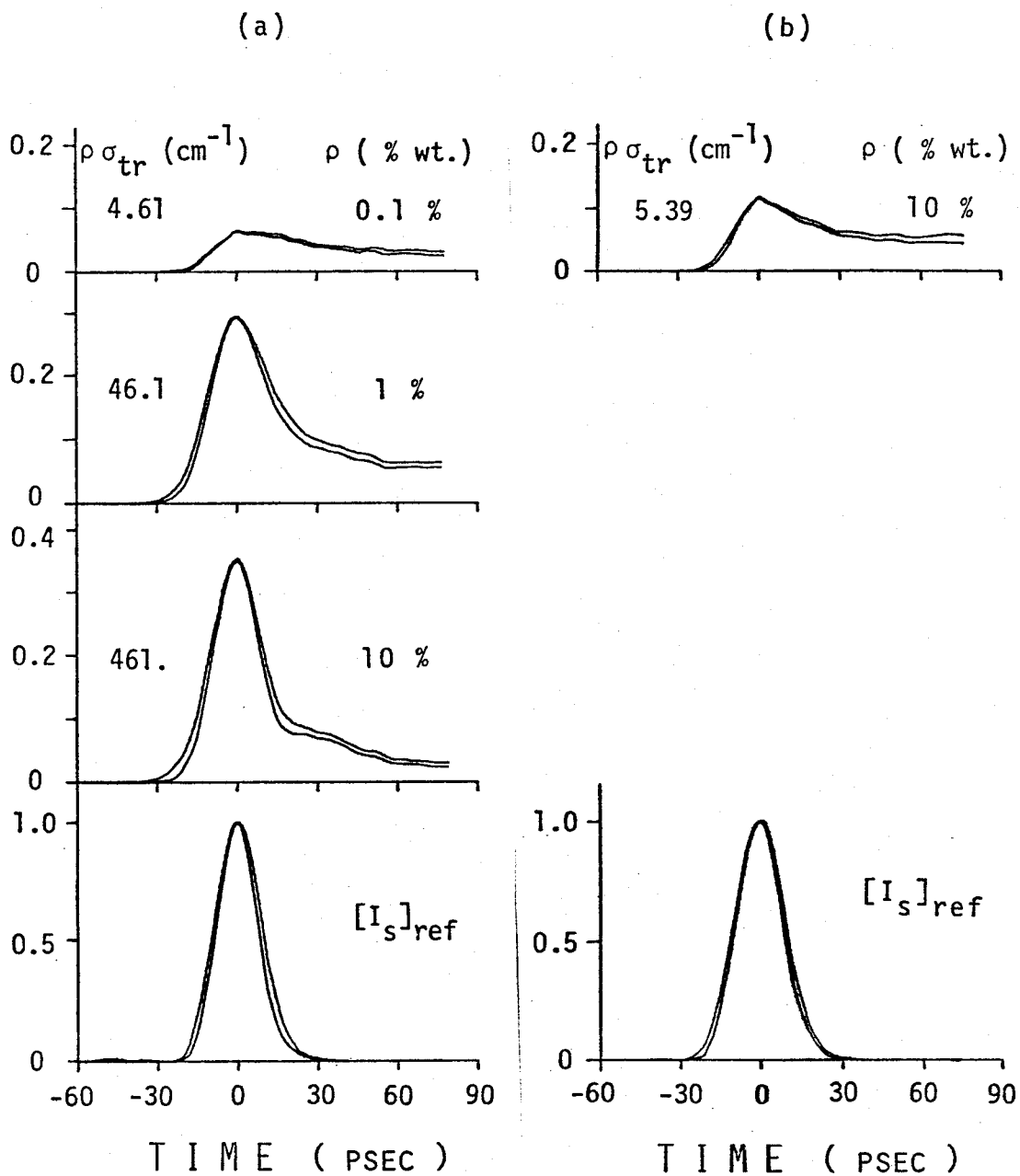
Fig.8-15 Dependence on diffusion optical distance : measurements
of 0.481 μmφ (a), and 45.4 μmφ (b), latex spheres

(a)   0.481 μm spheres

(b)   45.4 μm spheres

ρ (% wt.)

10 %

$[I_s]_{ref}$

ρ (% wt.)

10 %

$[I_s]_{ref}$

TIME (PSEC)

TIME (PSEC)
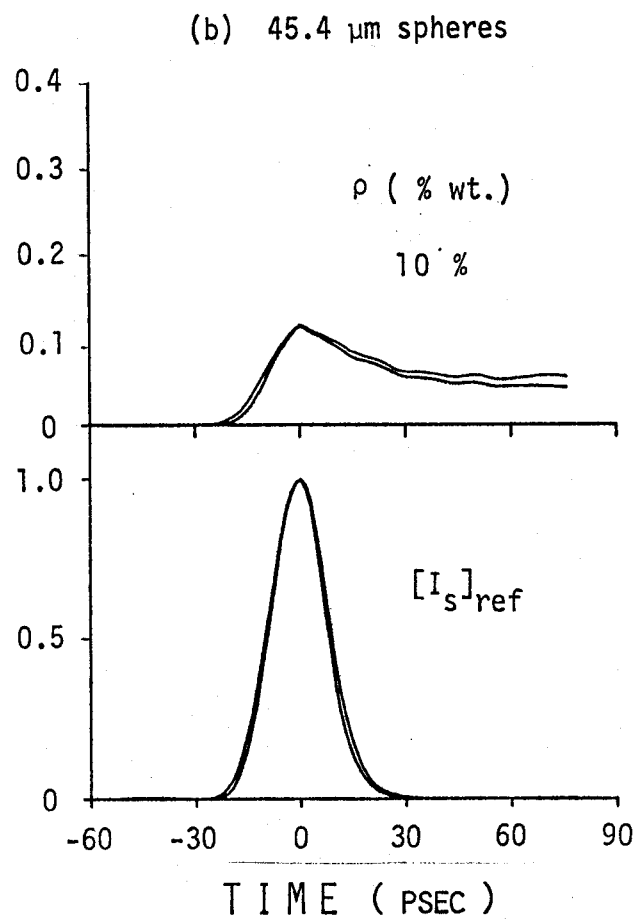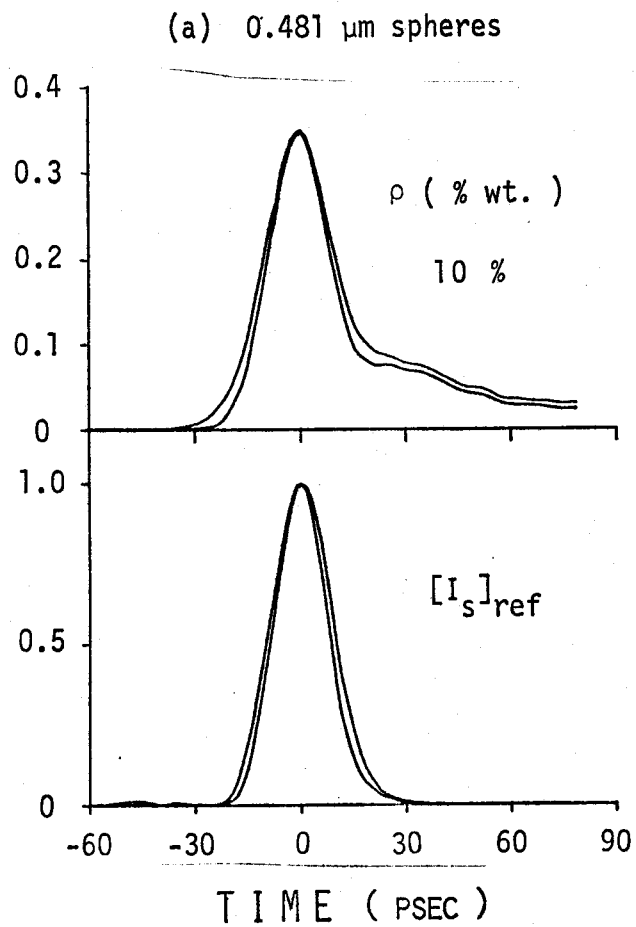
Fig.8-16   Detection of aggregation of scatterers : measurements
of 0.481 μmφ (a), and 45.4 μmφ (b), latex spheres

Chapter IX

SUMMARY AND CONCLUSIONS

OUTLINE

This thesis discussed the development of the following three remote sensing techniques. The preceding chapters were devoted to the theoretical analysis of their methods and the experimental verification of their applicability. They are,

(1) Fourier Transform Inversion Technique: This technique determines the size distribution of tenuous scatterers from the forward scattering pattern.

(2) Backward Scattering Pattern Analysis: This technique determines the average size and variance of tenuous scatterers from the backward scattering pattern.

(3) Pulse Backscattering from Dense Medium: This technique evaluates the optical parameters and condition-changes of scatterers in a dense medium by means of backscattered pulses.

These techniques are applied to the non-invasive probing of biological particles, namely bacteria in urine, cataracts in an eye, and platelets in blood, respectively.

RESULTS

(1) A modification of the Rayleigh-Debye approximation was proposed to extend its range of validity. The derivation of the modification was given in two different methods. The improvement due to the modification was demonstrated by comparing the scattering patterns for spheres calculated by the modified Rayleigh-Debye approximation, regular Rayleigh-Debye approximation and the exact Mie solution. The improvement is evident, particularly in the scattering angles for the extrema of scattered intensity.

(2) An inversion technique was developed which determines the size distribution of tenuous scatterers from the forward scattering pattern. This technique is applicable for 1, 2, and 3 dimensional scattering (diffractions). It does not require matrix-inversion or a priori knowledge of functional forms of the size distribution, and it can take advantage of other techniques in spectral analysis such as the Fast Fourier Transform or digital filtering technique.

Susceptibility to noise was checked by adding the random noise to the scattered intensity pattern simulated by the Rayleigh-Debye approximation. Typical error for 10% noise was within a few % for mean and standard deviation in the estimation of Gaussian distribution using 1024 points FFT.

Size distributions were determined for the latex spheres with known sizes and bacteria in homogeneous and highly aggregated conditions. The range of validity of this technique was extended by the

modification discussed above. A resolution comparable to the wavelength of the probing light was demonstrated. In the case of prolate spheroidal bacteria, the determined size was found to be that of the minor axis of the spheroids. With aggregated bacteria, a large peak and small periodic peaks ~~were recovered~~ corresponding to the bacteria *appeared in the obtained size dist.* in singlets and multiplets, respectively.

(3) A technique was developed which determines an average size and variance of the scatterers from the backward scattering pattern. Using the solution of the equation of transfer under the first order multiple scattering (FOMS) approximation, a time-dependent specific intensity was obtained as a function of geometrical and illuminating conditions. An experimental system was constructed which can measure backward scattering patterns while eliminating extraneous scattering by the range-gating technique.

Measurements with and without range-gating showed the noise-suppression of more than two orders of magnitude. Scattering patterns were measured with latex spheres of 0.481 µm, 2.02 µm and 3.20 µm diameters where the wavelength of probing light is 0.53 µm. With range-gating, they agreed with Mie calculations very well. Without range-gating, the patterns were severely distorted by the forward scattering due to the reflection from the backwall of the scattering cell.

Reduction of the multiple scattering effect by range-gating was demonstrated. The density range of single scattering and FOMS is extended by an order of magnitude from the non-range-gated case. The

valid range of FOMS is further extended if the multiple scattering effect is included as a decrease of measured turbidity. The usefulness of the range-gating technique was also shown in eliminating the correction for the change of scattering volumes.

(4) The equation of transfer was solved under the two-frequency diffusion approximation and a closed form expression was obtained for beam wave pulse incidence on a slab of dense random media. It was shown that the solution is general and includes the cases of the semi-infinite medium, the plane wave incidence and the point source, as its asymptotic cases. The validity of the diffusion approximation was theoretically investigated by examining the sign of the impulse response at the time-origin. A new parameter "diffusion optical distance," $\tau_d = \rho \sigma_{tr} z$, was proposed.

Through the numerical analysis, the following were obtained. The pulse shapes scattered at backward angles are characterized by a rapid rise and slow asymptotic decay. The decay, called a diffusion tail, is approximated by $\exp(- C\tau_d)$, where C is a constant. The normalization with τ_d enables us to present the scattered pulse shapes in a universal curve for different observation geometries and scatterer properties except for the absorption characteristics. The effect of scatterer absorption appears in the scattered pulse shape as an attenuation of peak intensity and as suppression of the diffusion tail. The pulse broadening is greater for the point source than for the plane wave incidence by 3 ~ 4 orders of magnitude. The effects of diffusion, particularly in the diffusion tail, appear more

pronounced for point source than for the plane wave incidence. The beam wave case has the property of these two cases. A closed form expression was obtained for the backscattered specific intensity which includes the effect of FOMS near the boundary of the scattering media where the diffusion approximation is not valid. It was shown that the effect of FOMS is significant around the time-origin of the scattered pulse for particles larger than 3.20 μm among those used in experiments.

(5) The dependence of scattered intensity on the scatterer density was investigated. Backward scattering patterns and visual observation of the collimated beam in a scattering medium suggested the four different phases of scattering. Their distinctions were shown clearly when the scattered intensity is plotted as a function of scatterer density. Two peaks appeared in the low and high density regions. The four phases were found to correspond to the ascending and descending slopes of each peak.

The two peaks were well described by the solution of the equation of transfer under the time-dependent FOMS and the two-frequency diffusion approximations, respectively. The locations of the peaks calculated were generally in good agreement with measurement.

(6) By the optical range-gating technique, pulse shapes scattered in the off-axis backward directions were measured in the picosecond range. Trapezoidal and exponentially decaying pulse shapes were observed for tenuous and dense media. The pulse shapes agreed well

with the solutions of the equation of transfer under the time-dependent FOMS and two-frequency diffusion approximations, respectively.

The slowing rate of light velocity in diffuse media is obtained by measuring the difference in arrival-time of the pulse peaks scattered from tenuous and dense media. The 99% confidence interval for the slowing rate measured at five different propagation distances was 1.75 ± 0.081 which is very close to the theoretically predicted value of $\sqrt{3}$.

(7) Backscattered pulse shapes were observed on-axis with picosecond resolution. The range-gating technique was formulated mathematically. The agreement between theoretical calculation and measurement was very good both in the shape and the magnitude of the backscattered pulses. The correlation coefficient between theory and measurement was 0.894 for the peak intensity of the pulses. The effect of scatterer absorption was seen in the reduced pulse heights and considerably diminished diffusion tails. The pulse shapes were found to be dependent on the diffusion optical distance rather than the regular optical distance. These results verified the theoretical analysis made above. Furthermore, they showed the feasibility of this technique to assess the aggregation of scatterers in a closed system such as the platelet aggregates in transfusion blood.

CONCLUSIONS

(1) The three remote sensing techniques proposed are feasible. They
     are applicable to the medical problems specified.

(2) The scattering patterns calculated by the Rayleigh-Debye approxi-
     mation are considerably improved, if the approximation is modified
     to include the refractive index of the scatterer in the Fourier
     transform kernel.

(3) The range-gating technique is useful in backward scattering
     pattern measurements.

(4) Light scattering can be classified into four categories according
     to the scatterer density.

(5) Light is slowed down in diffuse media by the factor $1/\sqrt{3}$.

(6) The two-frequency diffusion approximation is a valid mathematical
     approach to the description of the backscattering of optical
     pulses from dense random media.

FUTURE STUDY

Progressing technology is now producing the laser which is capable of generating optical pulses shorter than a picosecond. With the shorter pulses, the latter two remote sensing techniques proposed in this thesis become more powerful. Further study should be conducted to refine these techniques with the shorter pulses.

As to the practical applications, the techniques are still in the stage of development. Further effort is also required to implement these techniques in clinical applications, such as reliability study, safety study, etc.

BIBLIOGRAPHY

Arrington, P. and J. McNamara (1974). Ann. Surg. 179, 519.

Bradley, D. J. (1977). "Ultrashort Light Pulses" Ed. Shapiro, S.L. Springer-Verlag, New York.

Brigham, E. O. (1974). "The Fast Fourier Transform." Prentice-Hall Englewood Cliffs.

Bruckner, A. P. (1976). Proc. SPIE 94, 41.

Bruckner, A. P. (1978a). Appl. Opt. 17, 3177.

Bruckner, A. P., D. C. Auth, A. R. Tokuda, and K. Shimizu (1978b). Technical Report, SAM-TR-78.

Bucher, E. A. and R. M. Lerner (1973). Appl. Opt. 12, 2401.

Chandrasekhar, S. (1950). "Radiative Transfer." Oxford Univ. Press, London, and Dover, New York.

Cohen, J. (1972). "The Staphylococci." John Wiley & Sons, New York.

Cooke, D. D. and M. Kerker (1973). J. Coll. Int. Sci. 42, 150.

DeMaria, A. J., W. H. Glenn, Jr., M. J. Brienza, and M. E. Mack (1969), Proc. IEEE 57, 2.

Duguay, M. A. and J. W. Hansen (1969). Appl. Phys. Lett. 15, 192.

Duguay, M. A. and A. T. Mattick (1971). Appl. Opt. 10, 2162.

Erhukumov, L. M., I. G. Zarnitsina, and P. I. Kirsch (1973). Radiofiz, 16, 573.

Franklin, J. N. (1970). J. Math. Anal. Appl. 31, 682.

Froome, K. D. and L. Essen (1969). "The Velocity of Light and Radio Waves." Academic, London and New York.

Fymat, A. L. (1979). Appl. Opt. 18, 126.

Goodman, J. W. (1968). "Introduction to Fourier Optics." McGraw Hill, San Francisco.

Halliday, D. and R. Resnick (1960). "Physics." John Wiley & Sons, New York.

Hong, S. T. and A. Ishimaru (1976). Radio Sci. 11, 551.

Hong, S. T., I. Sreenivasiah, and A. Ishimaru (1977). IEEE Trans. Antennas Propag. AP-25, 822.

IMSL (1978). "IMSL Subroutine Library." University of Washington, Seattle, Washington.

Ishimaru, A. (1974). Lecture notes at University of Washington, Seattle, Washington.

Ishimaru, A. and S. T. Hong (1975). Radio Sci. 10, 637.

Ishimaru, A. (1976). Grant Application for NIH Grant No. HL-19993-01.

Ishimaru, A. (1977). Proc. IEEE 65, 1030.

Ishimaru, A. (1978a). "Wave propagation and scattering in random media, Volumes I and II." Academic, New York.

Ishimaru, A. (1978b). JOSA 68, 1045.

Keitz, H. A. E. (1971). "Light Calculations and Measurements." Macmillan, London.

Kerker, M. (1969). "The Scattering of Light." Academic, New York.

Kratohvil, J. P. and C. Smart (1965). J. Coll. Int. Sci. 20, 875.

Kraut, E. A. (1967). "Fundamentals of Mathematical Physics." McGraw Hill, New York.

Liu, C. H. and K. C. Yeh (1975). Radio Sci. 10, 1055.

Molcho, J. (1975). Ph.D. Thesis, University of Washington, Seattle, Washington.

Morse, P. M. and H. Feshback (1953). "Methods of Theoretical Physics." McGraw Hill, New York.

Oppenheim, A. V. and R. W. Schafer (1975). "Digital Signal Processing." Prentice-Hall, Englewood Cliffs.

Reynolds, L. O. (1975). Ph.D. Thesis, University of Washington, Seattle, Washington.

Reynolds, L. O., C. C. Johnson, and A. Ishimaru (1976). Appl. Opt. 15, 2059.

Schmidt, P. W. and O. L. Brill (1965). "Electromagnetic Scattering." Gordon and Breach, New York.

Shifrin, K. S. and A. Y. Perelman (1965). "Electromagnetic Scattering." Gordon and Breach, New York.

Shimizu, K. (1976). M.S. Thesis, University of Washington, Seattle, Washington.

Shimizu, K. and A. Ishimaru (1978). Opt. Eng. 17, 129.

Shimizu, K., A. Ishimaru, L. O. Reynolds, and A. P. Bruckner (1979). Appl. Opt. to be published.

Solis, R. T., et al. (1974). Transfusion 14, 538.

Sreenivasiah, I., A. Ishimaru, and S. T. Hong (1976). Radio Sci. 11, 775.

Sunak, H. R. D. and W. A. Gambling (1974). Opt. Commun. 11, 277.

Uscinski, B. J. (1974). Proc. R. Soc. Lond. A336, 379.

Van deHulst, H. C. (1957). "Light Scattering by Small Particles." John Wiley & Sons, New York.

Wolfgang, J. K. and S. T. Davis (1972). "Microbiology." Meredith.

Wyatt, P. J. (1972). J. Coll. Int. Sci. 39, 479.

Appendix III.A   Derivation of Eq. (3-19)

(Inversion Formula for 3-Dimensional Case)

The field at a spherical scatterer with the radius a is given by

$$E(r,a) = rect(r,a) = \begin{cases} 1 & 0 \le r \le a \\ 0 & r > a \end{cases}$$

As can be seen in Eq. (3-15), the inverse transform of the scattered intensity is the autocorrelation function of the above field, i.e.,

$$S^{-1}[I(k_r,a)] = R_E(r,a) = \frac{1}{6}(r - 2a)^2(r + 4a)rect(r,2a)$$

where the transform S^{-1} was defined in Eq. (3-12). Applying the differential operation, we have

$$\frac{\partial^2}{\partial r^2} S^{-1}[I(k_r a)] = r \, rect(r,2a) + (r^2 - 4a^2)\delta(r) + \frac{1}{6}(r^3 - 12ra^2$$

$$+ 16a^3)\delta'(r)$$

where $(r^2 - 4a^2)\delta(r - 2a) = 0$

and $(r^3 - 12ra^2 + 16a^3)\delta'(r - 2a) = 0$

Therefore,

$$\frac{\partial}{\partial r} \frac{1}{r} \frac{\partial^2}{\partial r^2} S^{-1}[I(k_r,a)] = -\delta(r - 2a) + f_1(r)\delta(r) + f_2(r)\delta'(r)$$

$$+ f_3(r)\delta''(r)$$

where f_1, f_2, f_3 are functions of r .

                                                                                Q.E.D.

Appendix III.B   Proof of Eq. (3-21)

(Elimination of Differential Operation in 3-Dimensional Case)

The differential equation for the spherical Bessel function is given by

$$\frac{d^2y}{dr^2} + \frac{2}{r}\frac{dy}{dr} + \left\{ k^2 - \frac{n(n+1)}{r^2} \right\} \ y = 0$$

and the solution is $y = C_1 \ j_n(kr) + C_2 n_n(kr)$ where C_1 and C_2 are constants.

Hence, the spherical Bessel function of order 0, or $j_0(kr)$ satisfies the equation

$$\frac{d^2y}{dr^2} = -\frac{2}{r}\frac{dy}{dr} - k^2 y \tag{3B-1}$$

As was shown in Eq. (3-19), the size distribution of scatterers is given by

$$C_3 n\left(\frac{r}{2}\right) + C_4 \delta(r) = \frac{\partial}{\partial r}\frac{1}{r}\frac{\partial^2}{\partial r^2} \ S^{-1}[I(k)]$$

$$= \int_0^\infty I(k) \ \frac{\partial}{\partial r} \left\{ \frac{1}{r}\frac{\partial^2}{\partial r^2} j_0(kr) \right\} \ k^2 \ dk \triangleq A \tag{3B-2}$$

Using Eq. (3B-1), we have

$$\left(\frac{1}{r} y''\right)' = \left(-\frac{2}{r^2} y' - \frac{k^2}{r} y\right)' = \left(\frac{8}{r^3} - \frac{k^2}{r}\right) y' + \frac{3k^2}{r^2} y \tag{3B-3}$$

where $y' = \frac{\partial}{\partial r} j_0(kr) = -k \ j_1(kr)$.

Substituting (3B-3) in (3B-2), we have the spherical Bessel transform converted into the Fourier-cosine and -sine transforms, i.e.,

$$A = \int_0^\infty \left(\frac{8k^2}{r^4} - \frac{k^4}{r^2} \right) I(k) \cos kr \, dk$$

$$+ \int_0^\infty \left(\frac{4k^3}{r^3} - \frac{8k}{r^5} \right) I(k) \sin kr \, dk \qquad (3B-4)$$

Since $I(k)$ is an even function with respect to k, Eq. (3B-4) is combined into the regular Fourier transform, i.e.,

$$A = \int_0^\infty f_e(k) \cos kr \, dk + \int_0^\infty f_0(k) \sin kr \, dk$$

$$= \frac{1}{2} \int_{-\infty}^\infty \{ f_e(k) + i f_0(k) \} e^{-ikr} \, dk$$

where $f_e(k)$ and $f_0(k)$ are even and odd functions. Therefore, finally we obtain

$$n\left(\frac{r}{2}\right) \propto \mathcal{F}^{-1} \left[\left\{ \left(\frac{4k^2}{r^4} - \frac{k^4}{2r^2} \right) + i \left(\frac{2k^3}{r^3} - \frac{4k}{r^5} \right) \right\} I(k) \right] \Bigg|_{r > 0}$$

Q.E.D.

Appendix III.C   Extrema of Scattering Pattern for Spheroids

Fig. Al shows scattering patterns of a sphere and spheroids with different axial ratios (e) using the Rayleigh-Debye approximation. Here, an axial ratio is defined as the ratio of one axis and an axis of revolution.

The locations of extrema for prolate spheroids (e > 1) coincide with those of spheres (e = 1), but those for oblate spheroids (e < 1) do not. This phenomenon can be interpreted as follows. When a prolate spheroid rotates in all the directions uniformly, it forms a sphere with a concentric inhomogeneity. Its core is a sphere with a radius equal to the minor axis of the prolate spheroid. Considering a degree of overlap, the core is most dense and therefore gives the largest contribution in scattering.
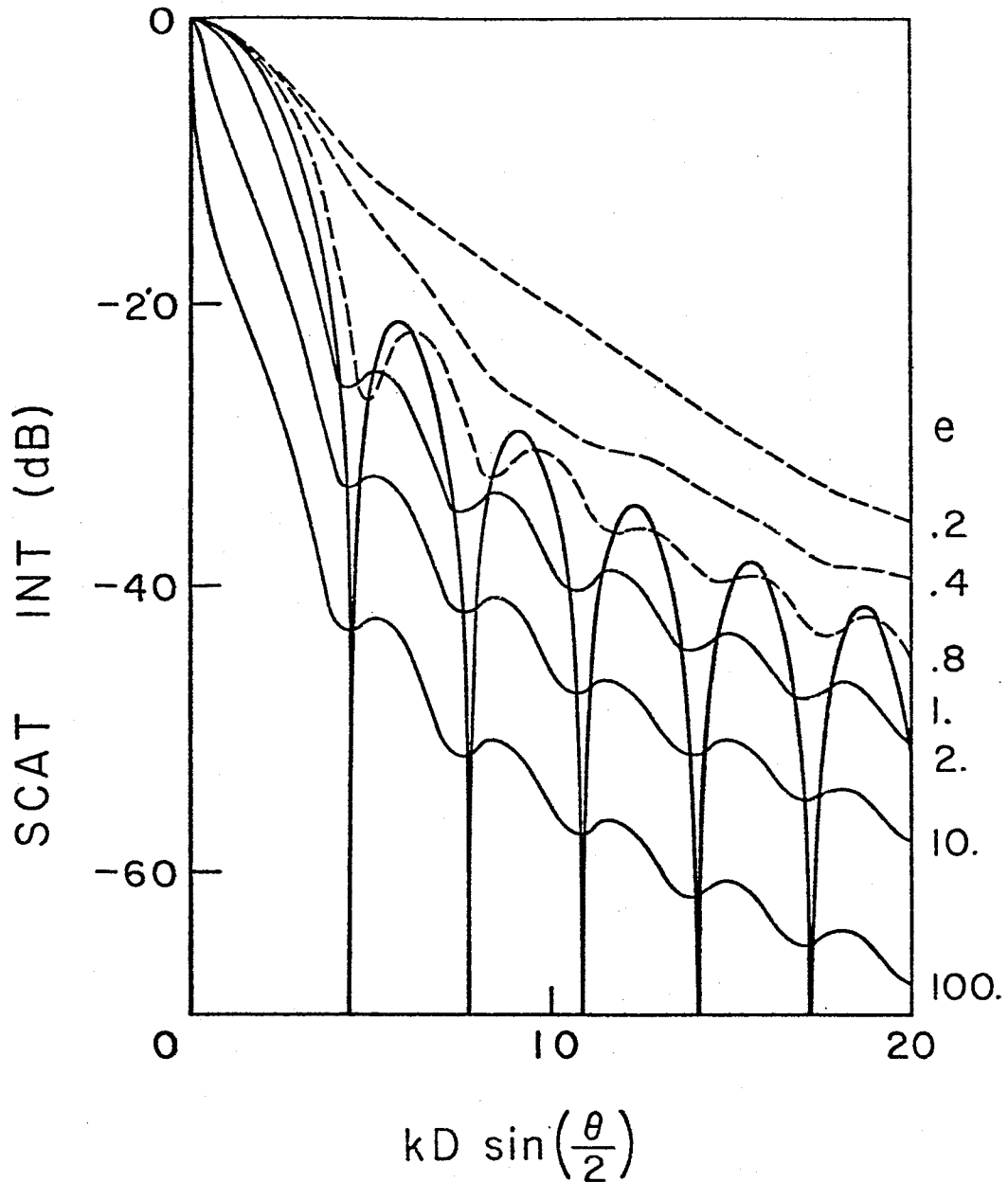
Fig.A-1 Scattering patterns of randomly oriented spheroids
by Rayleigh-Debye approximation :
e (axial ratio) = one axis / axis of revolution
e > 1 ; prolate spheroid,   e = 1 ; sphere
e < 1 ; oblate spheroid

Appendix V.A.   Derivation of Eq. (5-43)

(Saddle Point Technique for Evaluation of Integral)

The integral to be evaluated is

$$I = \int_0^\infty f(\gamma) J_0(\lambda r) \exp(-\gamma z) \frac{\lambda}{\gamma} d\lambda$$

$$= \frac{1}{2} \int_{-\infty}^\infty f(\lambda) H_0^{(2)}(\lambda r) \exp(-\gamma z) \frac{\lambda}{\gamma} d\lambda$$

where $\gamma^2 = \lambda^2 - k^2$, $q^2 = -3\alpha_a \alpha_{tr} = -k^2$

Using the asymptotic form for the Hankel function of the 2nd kind,

$$H_0^{(2)}(\lambda r) \sim \sqrt{\frac{2}{\pi \lambda r}} \exp(-j\lambda r + j\frac{\pi}{4})$$

we have

$$I \approx \frac{\exp(j\pi/4)}{\sqrt{2\pi}} \int_{-\infty}^\infty f_1(\lambda) \exp(-j\lambda r - \sqrt{\lambda^2 - k^2}\, z) d\lambda$$

where $f_1(\lambda) = \sqrt{\frac{\lambda}{r}}\ \frac{f(\sqrt{\lambda^2 - k^2})}{\sqrt{\lambda^2 - k^2}}$

changing the variables

$$\lambda = k \sin\alpha \ , \ z = R \cos\Theta \ , \ r = R \sin\Theta$$

we have

$$I \approx \frac{\exp(j\frac{\pi}{4})}{\sqrt{2\pi}} \int_C f_2(\alpha) \exp[kR\, f_3(\alpha)]\ d\alpha$$

where

$$f_2(\alpha) = f_1(k \sin\alpha) \, k \cos\alpha = \left(\frac{k \sin\alpha}{R \sin\theta} \right)^{1/2} \frac{f(jk \cos\alpha)}{j}$$

$$f_3(\alpha) = -j \cos(\alpha - \theta)$$

Change in the integration path and the steepest descent contour (SDC) are shown in Fig. 5A-1.
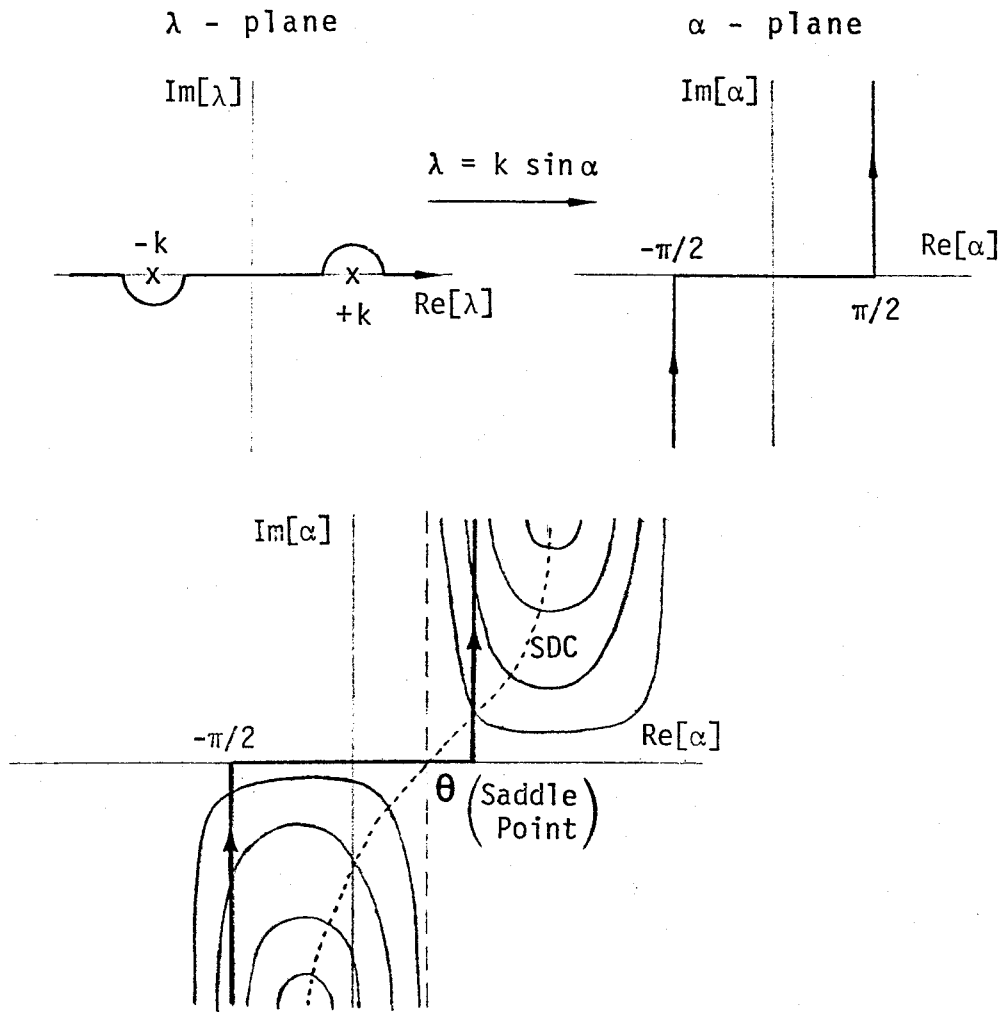
Fig.5A-1 Method of steepest descent contour :
θ ; saddle point
SDC (-----) ; steepest descent contour

Saddle point α_s is given by

$$\frac{\partial}{\partial \alpha} f_3(\alpha) = j \sin(\alpha - \Theta) = 0 \qquad\qquad \alpha_s = \Theta$$

We choose ϕ so that $-e^{j2\phi} f''(\alpha_s)$ is real positive and the integration contour C follows the SDC. In this case

$$\phi = \pi/4$$

Using the method of steepest descents or the saddle point technique (Ishimaru, 1974, p. 338), we have

$$I = \frac{\exp(j\pi/4)}{\sqrt{2\pi}} \int_C f_2(\alpha) \exp[kRf_3(\alpha)]\, d\alpha$$

$$\approx \frac{\exp(j\pi/4)}{\sqrt{2\pi}} f_2(\alpha_s) \exp[kRf_3(\alpha_s) + j\phi] \sqrt{\frac{2\pi}{-\exp(j2\phi)f''(\alpha_s)kR}}$$

$$= \frac{\exp(j\pi/4)}{\sqrt{2\pi}} \frac{\sqrt{k}}{\sqrt{R}} \frac{f(jk\cos\Theta)}{j} \exp\left(-jkR + j\frac{\pi}{4}\right) \sqrt{\frac{2\pi}{kR}}$$

$$= f(jk\cos\Theta) \frac{\exp(-jkR)}{R} = f(q\cos\Theta) \frac{e^{-qR}}{R}$$

$$= f\left(q\frac{z}{R}\right) \frac{\exp(-qR)}{R}$$

Appendix P : Computer Programs

App.P-1 Fourier transform inversion technique for measured data : determination of size-distribution of scatterers from measured scattering pattern

```
      PROGRAM  INVMES (INPUT,OUTPUT,PUNCH)
C        INVERSION FOR MEASURED DATA              OCT. 1978   K.SHIMIZU
C          SIZE DISTRIBUTION ESTIMATION FROM SCATTERING PATTERN
C        IOMIT : OMIT LOWER ANGLE DATA (1), HIGHER ANGLE (2), OR NOT (3)
C
      REAL  KS,KSLMT
      DIMENSION  SIK(1030),KS(1030),R(1030)
      DIMENSION  X(515),Y(515)
      DATA  N,M,NOUT,RMAX,YMAX  / 512, 9, 200, 1.5, 5.0 /
      DATA  IWIND,IPUNCH,IFILT  / 1, 1, 0 /
      DATA  PI,WL,RFMED / 3.14159265358979, 0.6328, 1.33 /
10    FORMAT(1H1)
11    FORMAT(E17.10,E17.10)
12    FORMAT(///30X,*SCATTERING PATTERN*)
14    FORMAT(///30X,*SIZE DISTRIBUTION --- ESTIMATED*)
15    FORMAT(///30X,*SIZE DISTRIBUTION --- FILTERED*)
16    FORMAT(///10X,*N=*,I5,5X,*BAND=+-*,F8.2,/15X,*I/P WINDOW=*,I2,5X
     1,*O/P FILTER=*,I2)
17    FORMAT(/10X,*MEAN=*,E12.5,5X,*STD.DEV.=*,E12.5)
18    FORMAT(10X,E12.5,5X,E12.5)
19    FORMAT(10(/),30X,*XXXXX  DATA ARE PUNCHED IN CARDS   XXXXX*)
C     --- READ IN MEASURED DATA
      I=1
21    READ 11,  X(I),Y(I)
      IF  ( X(I) .LT. 0.0 ) GO TO 22
      I=I+1
      GO TO 21
22    NDATA=I-1
      PRINT 10
      PRINT 18,  ( X(I),Y(I),I=1,NDATA )
30    CONTINUE
C     --- INTERPOLATE DATA FOR 2**M
      AK=2.*PI*RFMED/WL
      YNORM=Y(1)
      DO 31  I=1,NDATA
      X(I)=AK*2.0*SIN(X(I)*PI/360.)
31    Y(I)=10.*ALOG10(Y(I)/YNORM)
      KSLMT=X(NDATA)
      NHLF=N/2
      DO 32  I=1,NHLF
32    KS(I)=X(1)+(KSLMT-X(1))*FLOAT(2*I-1)/FLOAT(N)
      CALL INTPOLT(X,Y,NDATA,KS,SIK,NHLF)
      PRINT 10
      PRINT 18,  ( KS(I),SIK(I),I=1,20)
      PRINT 10
      CALL PLOTA(KS,NHLF,SIK,NHLF)
      CALL PLOT3(1H*,KS,SIK,NHLF)
      CALL PLOT3(1HX,X,Y,NDATA)
      CALL PLOT4(1,1H )
      IF ( IPUNCH .EQ. 0 )  GO TO 35
      XEND=-10.0
      YEND=0.0
      PUNCH 18,  (KS(J),SIK(J),J=1,NHLF)
      PUNCH 18,  XEND,YEND
      PUNCH 18,  (X(J),Y(J),J=1,NDATA)
```

```
            PUNCH 18, XEND,YEND
35      DO 36  I=1,NHLF
36      SIK(I)=10.**(SIK(I)/10.)
C   --- WINDOWING TO REDUCE THE LEAKAGE
        IF(IWIND.EQ.0)  GO TO 53
        DO 51  J=1,NHLF
        ARG=PI*FLOAT(NHLF-J+1)/FLOAT(NHLF)
        WIND=0.42-0.5*COS(ARG)+0.08*COS(ARG*2.)
        SIK(NHLF+J)=SIK(J)*WIND
51      KS(NHLF+J)=KS(J)
        DO 52  J=1,NHLF
        SIK(J)=SIK(N-J+1)
52      KS(J)=-KS(N-J+1)
53      CONTINUE
        PRINT 10
        CALL AUTOPLT(KS,SIK,N)
        PRINT 12
C   --- SIZE DISTRIBUTION ESTIMATION
        CALL ESTDERV (SIK,KS,R,N,M,KSLMT,X,Y,NOUT,RMAX)
        DO 61  J=1,NOUT
        X(J)=X(J)/2.
61      Y(J)=-Y(J)
        IF (IPUNCH.EQ.0) GO TO 62
        PUNCH 18, (X(J),Y(J), J=1,NOUT)
        PUNCH 18, XEND,YEND
62      CONTINUE
        PRINT 10
        CALL FIXPLOT(X,Y,NOUT,0.0,RMAX,0.0,YMAX)
        PRINT 14
        NSTOP=NOUT/10
        DO 63  J=1,NSTOP
63      Y(J)=0.0
        PRINT 10
        CALL AUTOPLT(X,Y,NOUT)
        PRINT 14
C   --- FILTERING THE ESTIMATED SIZE DISTRIBUTION
        IF (IFILT.EQ.0)  GO TO 64
        CALL FILTER(X,Y,NHLF)
        PRINT 10
        CALL AUTOPLT(X,Y,NHLF)
        PRINT 15
64      CONTINUE
C   --- MEAN AND STD.DEV. OF ESTIMATED DISTRIBUTION
        SUM1=0.0
        SUM2=0.0
        NSTOP=NOUT/12
        DO 72  J=NSTOP,NOUT
        SUM1=SUM1+X(J)*Y(J)
72      SUM2=SUM2+Y(J)
        XAV=SUM1/SUM2
        SUM1=0.0
        DO 73  J=NSTOP,NOUT
73      SUM1=SUM1+(X(J)-XAV)**2*Y(J)
        XSTDEV=SQRT(SUM1/SUM2)
        PRINT 10
        PRINT 16, N,KSLMT,IWIND,IFILT
        PRINT 17, XAV,XSTDEV
        IF (IPUNCH.EQ.0) GO TO 81
        PUNCH 16, N,KSLMT,IWIND,IFILT
        PUNCH 17, XAV,XSTDEV
        PRINT 19
81      CONTINUE
        PRINT 10
        STOP
        END
        SUBROUTINE  INTPOLT(X,Y,N,XC,YC,NC)
        DIMENSION  X(N),Y(N),XC(NC),YC(NC),C(90,3),BPAR(4)
        BPAR(1)=1.
        BPAR(2)=6.*(Y(2)-Y(1))/(X(2)-X(1))**2
        BPAR(3)=0.
        BPAR(4)=0.
```

```
        IC=N-1
        CALL ICSICU(X,Y,N,BPAR,C,IC,IER1)
        CALL ICSEVU(X,Y,N,C,IC,XC,YC,NC,IER2)
        RETURN
        END
        SUBROUTINE   ESTDERV (SIK,K,R,N,M,KLMT,X,Y,NOUT,RMAX)
C        SIZE DISTRIBUTION ESTIMATION FOR 3 DIMENSION
C           BY TAKING DERIVATIVES AFTER FFT
        REAL   K,KLMT
        COMPLEX   CSI
        DIMENSION   SIK(N),K(N),R(N),X(NOUT),Y(NOUT)
        DIMENSION   CSI(1030),BPAR(4),C(1030,3),D(1)
10      FORMAT(1H1)
11      FORMAT(///30X,*PROCESS OF ESTIMATION*)
        DO 30   J=1,N
        ARG=SIK(J)*K(J)
30      CSI(J)=CMPLX(ARG,0.)
        CALL FASTFT(CSI,M,KLMT,R)
        NM1=N-1
        DO 40   J=1,NM1
        R(J)=R(J+1)
40      SIK(J)=AIMAG(CSI(J+1))/(2.*R(J))
        PRINT 10
        CALL AUTOPLT(R,SIK,NM1)
        PRINT 11
        BPAR(1)=0.
        BPAR(2)=0.
        BPAR(3)=0.
        BPAR(4)=0.
        IC=NM1-1
        DO 50   J=1,NOUT
50      X(J)=2.*(R(1)+(RMAX-R(1))*FLOAT(J-1)/FLOAT(NOUT-1))
        CALL ICSICU(R,SIK,NM1,BPAR,C,IC,IER1)
        CALL DCSEVU(R,SIK,NM1,C,IC,X,Y,NOUT,D,0,IER2)
        DO 60   J=1,NOUT
60      IF  ( Y(J) .GT. 0.0 ) Y(J)=0.0
        IC=NOUT-1
        CALL ICSICU(X,Y,NOUT,BPAR,C,IC,IER3)
        CALL DCSEVU(X,Y,NOUT,C,IC,X,Y,NOUT,D,0,IER4)
        DO 70   J=1,NOUT
70      IF  ( Y(J) .LT. 0.0 ) Y(J)=0.0
        DO 80   J=1,NOUT
80      Y(J)=Y(J)/X(J)
        CALL ICSICU(X,Y,NOUT,BPAR,C,IC,IER5)
        CALL DCSEVU(X,Y,NOUT,C,IC,X,Y,NOUT,D,0,IER6)
        DO 90   J=1,NOUT
90      IF  ( Y(J) .GT. 0.0 ) Y(J)=0.0
        PRINT 10
        CALL AUTOPLT(X,Y,NOUT)
        PRINT 11
        RETURN
        END
        SUBROUTINE   FASTFT (C,M,B,T)
C        THIS ROUTINE CALCULATES FAST FOURIER TRANSFORM
C
C
C                     N
C        C(OUT) =    SUM   C(IN) * EXP( I*W(J)*T(K) ) * DW
C              K     J=1         J
C
C        W(J)=(J-1)*DW-B*(N-1)/N,   T(K)=(K-1)*DT,
C        DW=2*B/N,   DT=PI/B,   N=2**M,   (-B,B)=BAND WIDTH
C        NOTE :  SPECIAL CONSIDERATIONS ON THE SYMMETRY
C
        COMPLEX  C,CARG
        DIMENSION  C(1030),T(1030),IWK(20)
        PI=3.14159265358979
        N=2**M
        FRCTN=1.-1./FLOAT(N)
        CALL FFT2(C,M,IWK)
        CALL FFRDR2(C,M,IWK)
        ARG1=2.*B/FLOAT(N)
```

```
      DO 1  J=1,N
      ARG2=-FLOAT(J-1)*FRCTN*PI
      CARG=CMPLX( COS(ARG2),SIN(ARG2) )
      C(J)=ARG1*CARG*C(J)
      T(J)=FLOAT(J-1)*PI/B
1     CONTINUE
      RETURN
      END
      SUBROUTINE  FILTER(X,Y,N)
      DIMENSION  X(N),Y(N)
      RETURN
      END
      SUBROUTINE  FIXPLOT (X,Y,N,XMIN,XMAX,YMIN,YMAX)
C       PLOTTING IN FIXED SCALE
      DIMENSION  X(N),Y(N),IMAGE(561),NSCALE(5)
      NSCALE(1)=0
      CALL PLOT1(NSCALE,5,10,10,10)
      CALL PLOT2(IMAGE,XMAX,XMIN,YMAX,YMIN)
      CALL PLOT3(1H*,X,Y,N)
      CALL PLOT4(1,1H )
      RETURN
      END
      SUBROUTINE  AUTOPLT(X,Y,N)
C       PLOTTING AUTOMATICALLY SCALED
      DIMENSION  X(N),Y(N)
      CALL PLOTA(X,N,Y,N)
      CALL PLOT3(1H*,X,Y,N)
      CALL PLOT4(1,1H )
      RETURN
      END
```

App.P-2 Fourier transform inversion technique for simulated data : analysis of the technique with simulated scattering patterns

```
      PROGRAM   INVSIM (INPUT,OUTPUT,PUNCH)
C
C         INVERSION FOR SIMULATED DATA              OCT. 1978   K.SHIMIZU
C             SIZE DISTRIBUTION ESTIMATION FROM SCATTERING PATTERN
C         IOMIT : OMIT LOWER ANGLE DATA (1), HIGHER ANGLE (2), OR NOT (0)
C
      REAL   KS,KSLMT
      DIMENSION  SIK(1030),KS(1030),R(1030),A(150),SDIST(150)
      DIMENSION  X(515),Y(515)
      DATA   N,M,NOUT,RMAX,YMAX   / 128, 7, 200, 3.0, 1500. /
      DATA   NDIST,AVE,STDEV,SNR /101, 2.0, 0.18, 0.00 /
      DATA   IWIND,IPUNCH,IFILT,IOMIT,NCUT / 1, 1, 0, 0, 1000 /
      DATA   PI,WL,RFMED / 3.14159265358979, 0.6328, 1.33 /
10    FORMAT(1H1)
11    FORMAT(///30X,*SIZE DISTRIBUTION --- GIVEN*)
12    FORMAT(///30X,*SCATTERING PATTERN*)
13    FORMAT(///30X,*RESULT OF TRANSFORM*)
14    FORMAT(///30X,*SIZE DISTRIBUTION --- ESTIMATED*)
15    FORMAT(///30X,*SIZE DISTRIBUTION --- FILTERED*)
16    FORMAT(///10X,*N=*,I5,5X,*BAND=+-*,F8.2,/15X,*I/P WINDOW=*,I2,5X
     1,*O/P FILTER=*,I2/15X,*DATA OMIT=*,I2,5X,*CUTOUT NO.=*,I5)
17    FORMAT(/30X,*(GIVEN DISTRIBUTION)*,9X,*MEAN=*,E12.5,5X,
     1*STD.DEV.=*,E12.5/30X,*(ESTIMATED DISTRIBUTION)*,5X,*MEAN=*
     2,E12.5,5X,*STD.DEV.=*,E12.5,5X,*SNR=*,F8.4)
18    FORMAT(10X,E12.5,5X,E12.5)
19    FORMAT(10(/),30X,*XXXXX  DATA ARE PUNCHED IN CARDS  XXXXX*)
C   --- SIZE DISTRIBUTION
      ARG1=SQRT(2.*PI)*STDEV
      DO 31  I=1,NDIST
      A(I)=1.00+FLOAT(I-1)*0.02
      ARG2=-0.5*((A(I)-AVE)/STDEV)**2
31    SDIST(I)=EXP(ARG2)/ARG1
```

```
C
      PRINT 10
      CALL AUTOPLT(A,SDIST,NDIST)
      PRINT 11
      XEND=-10.0
      YEND=0.0
      IF ( IPUNCH .EQ. 0 ) GO TO 32
      PUNCH 18, ( A(J),SDIST(J), J=1,NDIST )
      PUNCH 18, XEND,YEND
32    CONTINUE
C     --- GENERATION OF SCATTERING PATTERN
C         KS=WAVENO  CORRESPONDS TO  SCATT.ANG.=0-60 (DEG)
      WAVENO=2.*PI*RFMED/WL
      KSLMT=WAVENO
      CALL SCATPAT(KS,SIK,N,A,SDIST,NDIST,KSLMT)
C     --- MODIFICATION OF SCATTERING PATTERN
      NHLF=N/2
      NCUTH=NCUT/2
      NCUTH1=NCUTH+1
      IF(IOMIT-1) 45,41,43
41    DO 42  I=1,NCUTH
42    SIK(I)=SIK(NCUTH1)*(KS(NCUTH1)/KS(I))**4
      GO TO 45
43    DO 44  I=NCUTH1,NHLF
44    SIK(I)=SIK(NCUTH)*(KS(NCUTH)/KS(I))**4
45    CONTINUE
      YNORM=SIK(1)
C     --- NOISE ADDITION (IF UNWANTED, SET SNR=0.0  OR ADD,  GO TO 48)
      IX=2**24+3
      CALL RAND(15,IX,0,NHLF,R)
      DO 46  J=1,NHLF
      R(J)=2.*R(J)-1.0
46    SIK(J)=(1.+SNR*R(J))*SIK(J)
48    CONTINUE
C     --- PLOTTING THE FORWARD SCATTERING PATTERN
      DO 56  I=1,NHLF
      X(I)=KS(I)
      IF ( SIK(I) .EQ. 0.0 )  SIK(I)=1.0E-10
56    Y(I)=10.*ALOG10(SIK(I)/YNORM)
      PRINT 10
      CALL AUTOPLT(X,Y,NHLF)
      PRINT 12
      IF ( IPUNCH .EQ. 0 )  GO TO 58
      PUNCH 18, (X(J),Y(J),J=1,NHLF)
      PUNCH 18, XEND,YEND
58    CONTINUE
C     --- WINDOWING TO REDUCE THE LEAKAGE
      IF(IWIND.EQ.0)  GO TO 53
      DO 51  J=1,NHLF
      ARG=PI*FLOAT(NHLF-J+1)/FLOAT(NHLF)
      WIND=0.42-0.5*COS(ARG)+0.08*COS(ARG*2.)
      SIK(NHLF+J)=SIK(J)*WIND
51    KS(NHLF+J)=KS(J)
      DO 52  J=1,NHLF
      SIK(J)=SIK(N-J+1)
52    KS(J)=-KS(N-J+1)
53    CONTINUE
      PRINT 10
      CALL AUTOPLT(KS,SIK,N)
      PRINT 12
C     --- SIZE DISTRIBUTION ESTIMATION
      CALL ESTDERV (SIK,KS,R,N,M,KSLMT,X,Y,NOUT,RMAX)
      DO 61  J=1,NOUT
      X(J)=X(J)/2.
61    Y(J)=-Y(J)
      IF (IPUNCH.EQ.0) GO TO 62
      PUNCH 18, (X(J),Y(J), J=1,NOUT)
      PUNCH 18, XEND,YEND
62    CONTINUE
      PRINT 10
      CALL FIXPLOT(X,Y,NOUT,0.0,RMAX,0.0,YMAX)
```

```
      PRINT 14
      NSTOP=NOUT/10
      DO 63  J=1,NSTOP
63    Y(J)=0.0
      PRINT 10
      CALL AUTOPLT(X,Y,NOUT)
      PRINT 14
C     --- FILTERING THE ESTIMATED SIZE DISTRIBUTION
      IF (IFILT.EQ.0)  GO TO 64
      CALL FILTER(X,Y,NHLF)
      PRINT 10
      CALL AUTOPLT(X,Y,NHLF)
      PRINT 15
64    CONTINUE
C     --- MEAN AND STD.DEV. OF ESTIMATED DISTRIBUTION
      SUM1=0.0
      SUM2=0.0
      NSTOP=NOUT/5
      DO 72  J=NSTOP,NOUT
      SUM1=SUM1+X(J)*Y(J)
72    SUM2=SUM2+Y(J)
      XAV=SUM1/SUM2
      SUM1=0.0
      DO 73  J=NSTOP,NOUT
73    SUM1=SUM1+(X(J)-XAV)**2*Y(J)
      XSTDEV=SQRT(SUM1/SUM2)
      PRINT 10
      PRINT 16, N,KSLMT,IWIND,IFILT,IOMIT,NCUT
      PRINT 17, AVE,STDEV,XAV,XSTDEV,SNR
      IF (IPUNCH.EQ.0) GO TO 81
      PUNCH 16, N,KSLMT,IWIND,IFILT,IOMIT,NCUT
      PUNCH 17, AVE,STDEV,XAV,XSTDEV,SNR
      PRINT 19
81    CONTINUE
      PRINT 10
      STOP
      END
      SUBROUTINE  SCATPAT(KS,SIK,N,A,SDIST,NDIST,KSLMT)
C       SCATTERING PATTERN BY RAYLEIGH-DEBYE APPROXIMATION
C       INPUT : N,A(NDIST),SDIST(NDIST),NDIST,KSLMT
C       OUTPUT : KS(N),SIK(N)
      REAL  KS,KSLMT
      DIMENSION  KS(N),SIK(N),A(NDIST),SDIST(NDIST)
      SCAT(Z)=3.*(SIN(Z)-Z*COS(Z))/Z**3
      PI=3.14159265358979
      NHLF=N/2
      DO 10  J=1,NHLF
      KS(J)=FLOAT(2*J-1)*KSLMT/FLOAT(N)
10    SIK(J)=0.0
      DO 30  I=1,NDIST
      V=4.*PI*A(I)**3/3.
      DO 20  J=1,NHLF
      ARG=A(I)*KS(J)
      SIKA=(V*SCAT(ARG))**2
20    SIK(J)=SIK(J)+SIKA*SDIST(I)
30    CONTINUE
      RETURN
      END
      SUBROUTINE  ESTDERV (SIK,K,R,N,M,KLMT,X,Y,NOUT,RMAX)
C       SIZE DISTRIBUTION ESTIMATION FOR 3 DIMENSION
C         BY TAKING DERIVATIVES AFTER FFT
      REAL  K,KLMT
```

                              .
                              .
                              .

              rests are same as App.P-1

                              .
                              .
                              .

App.P-3 Solution of diffusion equation for beam wave incidence
         on semi-infinite medium

```
      PROGRAM  BEAMWVE(OUTPUT,TAPE6=OUTPUT,PUNCH)
C     UNITS ARE IN CENTIMETERS
C     IPUNCH= NO PUNCH(0), IMPULSE RESP.(1), IMP.RESP. $ SPECTRUM(2)
C     BW= HALF WIDTH OF E-1 POINTS (NOT FULL WIDTH)
C     ANGD= SCATT. ANGLE IN DEGREE,  FOR BACKSCATT.  ANGD=180.
      COMPLEX  CSI,CT,CA,CTR
      DIMENSION  CSI(260),W(260),T(260),SIMAG(260),SIPHSE(260)
      DIMENSION  X(31),YR(31)
      COMMON  /PARM/ RDIST,BW,BWNRM,AMU,ANGR,RG
      COMMON  /CS/ CT,CA,CTR
      EXTERNAL  FXR,FXI
      DATA  IPUNCH,N,M,ITAPER,P  / 0, 128, 7, 1, 50. /
      DATA  AMU,H,RHO,SCATCS,ABSCS/0.886,0.00,2.26E10,7.95E-8,0.0/
      DATA  RDIST,BW,ANGD  / 0.0457567, 0.1, 178.1666667 /
      DATA  WLMT,ALMT,BLMT,RTOL/1.50,0.0,0.30,0.001/
      DATA  IRG / 1 /
10    FORMAT(1H1)
101   FORMAT(//45X,*REAL PART OF INTEGRAND*,10X,*W=*,F6.3)
111   FORMAT(/10X,*N=*,I4,5X,*RAD.DIST.(CM)=*,F8.5,5X,*E-1 B.W.(CM)=*
     1,F8.3,5X,*REC.ANG.(DEG)=*,F8.3/10X,*RHO(/CC)=*,E12.5,5X
     2,*H(PACK.FACT.)=*,F5.3,5X,*MU=*,F8.5)
112   FORMAT(10X,*TR.C-S(CM**2)=*,E12.5,5X,*TOT.C-S=*,E12.5,5X
     1,*SCAT.C-S=*,E12.5,5X,*ABS.C-S=*,E12.5//)
12    FORMAT(30X,*NORM.COEFF.(RHO*SIGMATR*CMED)=*,E12.5,*  (/SEC)*)
131   FORMAT(30X,*NORMALIZED ANG.FREQ. (OMEGA.O/NORM.COEFF)*////)
132   FORMAT(40X,*NORMALIZED TIME (T*NORM.COEFF)*)
133   FORMAT(1H1,5X,*(IMPULSE RESP.)/(NORM.COEFF.)*)
14    FORMAT(////7X,*NORMALIZED*,2X,*SPECTRUM OF SPECIFIC INTENSITY*
     1,*  ITERATION*/8X,*ANG.FREQ.*,4X,*(MAGNITUDE)*,4X,*(PHASE(DEG))*
     2,4X,*REAL IMAG.*/)
151   FORMAT(6X,F9.3,5X,2(E12.5,3X),2I5)
152   FORMAT(9X,F6.3,5X,2(E12.5,3X))
16    FORMAT(///17X,*NORMALIZED*,11X,*IMPULSE RESPONSE*/20X,*TIME*,11X,
     1*(REAL)*,8X,*(IMAGINARY)*/)
17    FORMAT(15X,F10.3,5X,E12.5,5X,E12.5)
18    FORMAT(1H1,10(/),20X,*XXXXX  DATA ARE PUNCHED IN CARDS  XXXXX*)
C     CONSTANTS
      PI=3.14159265358979
      C=3.0E10
      RFRMED=1.33
      CMED=C/RFRMED
      NHLF=N/2
      ANGR=ANGD*PI/180.
      SCACS=SCATCS
C
      SCATCS=SCACS*(1.0-H)
      TOTLCS=SCATCS+ABSCS
      TRSPCS=(1.0-AMU)*SCATCS+ABSCS
      BWNRM=RHO*TRSPCS*BW
      ANRM=RHO*TRSPCS*CMED
C     SETTING THE NORMALIZED FREQ.(OMEGA)
      DW=2.*WLMT/FLOAT(N)
      FRCTN=1.-1./FLOAT(N)
      DO 31  I=1,NHLF
      W(I)=FLOAT(I-1)*DW-FRCTN*WLMT
31    W(N+1-I)=-W(I)
C
C     --- SPECTRUM ---
C
      PRINT 10
      PRINT 14
      ARG1=-SCATCS*BWNRM**2/TRSPCS
      ARG2=-(RDIST/BW)**2
      ARG2=AMU*EXP(ARG2)/BWNRM**2
```

```
      ARGR1=TOTLCS/TRSPCS
      ARGR2=ABSCS/TRSPCS
      DO 51   I=1,NHLF
      CT=CMPLX(ARGR1,-W(I))
      CA=CMPLX(ARGR2,-W(I))
      CTR=CMPLX( 1., -W(I))
      PL=5.E-12
      PW=0.15
      ARGW=0.5*PL**2+0.25*(PW/CMED)**2
      WD=RHO*TRSPCS*CMED*W(I)
      RG=EXP(-ARGW*WD**2)
      IF ( IRG .EQ. 0 )  RG=1.0
      CALL QUAD(ALMT,BLMT,RTOL,ERR,1,SIR,FXR,IERR,0)
      CALL QUAD(ALMT,BLMT,RTOL,ERR,1,SII,FXI,IERI,0)
      CSI(I)=ARG1*(CMPLX(SIR,SII)-COS(ANGR)*ARG2*RG/CTR)
      CSI(N+1-I)=CONJG(CSI(I))
      SIMAG(I)=CABS(CSI(I))
      SIR=REAL(CSI(I))
      SII=AIMAG(CSI(I))
      IF ( SIR .EQ. 0.0  .AND.  SII .EQ. 0.0 )  SIR=SII=1.0
      SIPHSE(I)=ATAN2(SII,SIR)*180./PI
      PRINT 151, W(I),SIMAG(I),SIPHSE(I),IERR,IERI
51    CONTINUE
      DO 52   J=1,31
      X(J)=ALMT+FLOAT(J-1)*(BLMT-ALMT)/30.
52    YR(J)=FXR(X(J))
      CALL AUTOPLT(X,YR,31)
      PRINT 101,  W(NHLF)
      CALL AUTOPLT(W,SIMAG,NHLF)
      PRINT 131
      PRINT 12, ANRM
      IF (IPUNCH .NE. 0)  PUNCH 111, N,RDIST,BW,ANGD,RHO,H,AMU
      IF (IPUNCH .EQ. 2)  PUNCH 152, (W(K),SIMAG(K),SIPHSE(K),K=1,NHLF)
C
C       ---  IMPULSE RESPONSE  ---
C
      IF (ITAPER .EQ. 0)  GO TO 62
      CALL CTAPER(CSI,N,P)
62    CONTINUE
      CALL INVFT(CSI,M,WLMT,T)
      DO 63   I=1,N
63    SIMAG(I)=REAL(CSI(I))
      PRINT 10
      PRINT 133
      CALL PLOTA(T,N,SIMAG,N)
      CALL PLOT3(1H*,T,SIMAG,N)
      CALL PLOT4(1,1H )
      PRINT 132
      PRINT 111, N,RDIST,BW,ANGD,RHO,H,AMU
      PRINT 112, TRSPCS,TOTLCS,SCATCS,ABSCS
      PRINT 12, ANRM
      PRINT 10
      PRINT 17, (T(K),CSI(K),K=1,N)
      IF (IPUNCH.EQ.0)  GO TO 64
      PUNCH 16
      PUNCH 17, (T(K),CSI(K),K=1,N)
      PRINT 18
64    CONTINUE
99    CONTINUE
      PRINT 10
      STOP
      END
```

```
      FUNCTION  FXR(X)
      COMPLEX  CT,CA,CTR,Y,CARG1,CARG2,CARG3,C1,C2,C3,C4,CFX
      REAL   MMBSJO,MMBSJ1
      COMMON  /PARM/ RDIST,BW,BWNRM,AMU,ANGR,RG
      COMMON  /CS/ CT,CA,CTR
      Y=CSQRT(X**2+3.*CA*CTR)
      ARG1=RDIST*BWNRM*X/BW
      ARG2=MMBSJO(ARG1,IDUMMY)
      ARG3=MMBSJ1(ARG1,IDUMMY)
      ARG4=-(BWNRM*X/2.)**2
      ARG4=EXP(ARG4)
      C1=AMU*Y-CTR
      C2=2.*Y+3.*CTR
      C3=Y+CT
      C4=CTR+AMU*CT
      CARG1=C1/(C2*C3)
      CARG2=CARG1/CTR
      CARG3=(1.5*C4/C3+AMU*Y/CTR)/C2
      CARG1=ARG2*ARG4*CARG1*X
      CARG2=ARG3*ARG4*CARG2*X**2
      CARG3=ARG2*ARG4*CARG3*X
      CFX=CARG1+SIN(ANGR)*CARG2+COS(ANGR)*CARG3
      FXR=REAL(CFX)*RG
      RETURN
      END
      FUNCTION  FXI(X)
      COMPLEX  CT,CA,CTR,Y,CARG1,CARG2,CARG3,C1,C2,C3,C4,CFX
      REAL   MMBSJO,MMBSJ1
      COMMON  /PARM/ RDIST,BW,BWNRM,AMU,ANGR,RG
      COMMON  /CS/ CT,CA,CTR
      Y=CSQRT(X**2+3.*CA*CTR)
      ARG1=RDIST*BWNRM*X/BW
      ARG2=MMBSJO(ARG1,IDUMMY)
      ARG3=MMBSJ1(ARG1,IDUMMY)
      ARG4=-(BWNRM*X/2.)**2
      ARG4=EXP(ARG4)
      C1=AMU*Y-CTR
      C2=2.*Y+3.*CTR
      C3=Y+CT
      C4=CTR+AMU*CT
      CARG1=C1/(C2*C3)
      CARG2=CARG1/CTR
      CARG3=(1.5*C4/C3+AMU*Y/CTR)/C2
      CARG1=ARG2*ARG4*CARG1*X
      CARG2=ARG3*ARG4*CARG2*X**2
      CARG3=ARG2*ARG4*CARG3*X
      CFX=CARG1+SIN(ANGR)*CARG2+COS(ANGR)*CARG3
      FXI=AIMAG(CFX)*RG
      RETURN
      END
      SUBROUTINE  AUTOPLT(X,Y,N)
C     PLOTTING AUTOMATICALLY SCALED
      DIMENSION  X(N),Y(N)
      PRINT 10
10    FORMAT(1H1)
      CALL PLOTA(X,N,Y,N)
      CALL PLOT3(1H*,X,Y,N)
      CALL PLOT4(1,1H )
      RETURN
      END
      SUBROUTINE  CTAPER (C,N,P)
C     SPLIT-COS-BELL TAPERING   P: % OF SERIES TO BE TAPERED (IN %)
      COMPLEX  C
      DIMENSION  C(N)
      PI=3.14159265358979
      IF ((P .LE. 0.0) .OR. (P .GT. 100.))  RETURN
      M=INT(0.01*P*FLOAT(N)+0.5)/2
      DO 10  I=1,M
      W=0.5-0.5*COS(PI*(FLOAT(I)-0.5)/FLOAT(M))
      C(I)=C(I)*W
```

```
10      C(N+1-I)=C(N+1-I)*W
        RETURN
        END
        SUBROUTINE  INVFT(C,M,B,T)
C        THIS ROUTINE CALCULATES INVERSE FOURIER TRANSFORM
C
C                          N
C        C(OUT) = 1/2*PI (  SUM  C(IN) *EXP( -I*W(J)*T(K))  )*DW
C                K         J=1         J
C
C
C        W(J)=(J-1)*DW-B*(N-1)/N,   T(K)=(K-N/2)*DT
C        DW=2*B/N,   DT=PI/B,   N=2**M,   (-B,B)=BAND WIDTH
C        NOTE :  SPECIAL CONSIDERATIONS ON THE SYMMETRY OF FREQ. AND TIME
C
        COMPLEX  C,CA,CB,CARG
        DIMENSION  C(1030),CA(1030),CB(1030),T(1030),IWK(20)
        PI=3.14159265358979
        N=2**M
        FRCTN=1.-1./FLOAT(N)
        NHLF=N/2
        DO 1  I=1,N
        CA(I)=C(I)
1       CB(I)=CONJG(C(I))
        CALL FFT2(CA,M,IWK)
        CALL FFRDR2(CA,M,IWK)
        CALL FFT2(CB,M,IWK)
        CALL FFRDR2(CB,M,IWK)
        ARG1=B/(PI*FLOAT(N))
        DO 2  I=1,NHLF
        ARG2=-FLOAT(NHLF-I)*FRCTN*PI
        CARG=CMPLX(COS(ARG2),SIN(ARG2))
        C(I)=ARG1*CARG*CA(NHLF+1-I)
2       T(I)=-FLOAT(NHLF-I)*PI/B
        DO 3  I=1,NHLF
        ARG2=FLOAT(I)*FRCTN*PI
        CARG=CMPLX(COS(ARG2),SIN(ARG2))
        C(NHLF+I)=ARG1*CARG*CONJG(CB(I+1))
3       T(NHLF+I)=FLOAT(I)*PI/B
        RETURN
        END
```

App.P-4 Solution of diffusion equation for quasi-spherical wave incidence on semi-infinite medium

```
        PROGRAM  SPHRWVE(OUTPUT,TAPE6=OUTPUT,PUNCH)
C        UNITS ARE IN CENTIMETERS
C        IPUNCH= NO PUNCH(0), IMPULSE RESP.(1), IMP.RESP. S SPECTRUM(2)
C        FBW= NOMINAL BEAM WIDTH (TO KEEP FLUX(1.0)*BW**2 CONSTANT)
C          AFFECTS ONLY ON MAGNITUDE OF OUTPUT
C        ANGD= SCATT. ANGLE IN DEGREE,  FOR BACKSCATT.  ANGD=180.
C        (ROBS,PHID)= POLAR COORDINATE OF OBSERVATION POINT  (CM,DEG)
        COMPLEX  CSI,CT,CA,CTR,CQ,CARG,C1,C2,C3,CNOM,CDEN,CSI1,CSI2
        DIMENSION  CSI(260),W(260),T(260),SIMAG(260),SIPHSE(260)
        DATA   IPUNCH,N,M,ITAPER,P  / 1, 256, 8, 1, 50. /
        DATA   AMU,H,RHO,SCATCS,ABSCS/0.930,0.10,1.95E6,3295.0E-8,0.0/
        DATA   WLMT,ANGD,ROBS,PHID,FBW  / 4.0000,150.,1.000, 90.0, 0.01 /
10      FORMAT(1H1)
111     FORMAT(/10X,*N=*,I4,5X,*RHO(/CC)=*,E12.5,5X,*H(PACK.FACT.)=*
       1,F5.3,5X,*MU=*,F8.5,5X,*REC.ANG.(DEG)=*,F8.3
       2/10X,*DIST.OF OBS.(CM) =*,F10.5,5X,*ANGLE OF OBS.(DEG) =*,F8.3)
112     FORMAT(10X,*TR.C-S(CM**2)=*,E12.5,5X,*TOT.C-S=*,E12.5,5X
       1,*SCAT.C-S=*,E12.5,5X,*ABS.C-S=*,E12.5//)
12      FORMAT(30X,*NORM.COEFF.(RHO*SIGMATR*CMED)=*,E12.5,*  (/SEC)*)
```

```
131    FORMAT(30X,*NORMALIZED ANG.FREQ. (OMEGA.D/NORM.COEFF)*////)
132    FORMAT(40X,*NORMALIZED TIME (T*NORM.COEFF)*)
133    FORMAT(1H1,5X,*(IMPULSE RESP.)/(NORM.COEFF.)*)
14     FORMAT(///7X,*NORMALIZED*,2X,*SPECTRUM OF SPECIFIC INTENSITY*
      1/8X,*ANG.FREQ.*,4X,*(MAGNITUDE)*,4X,*(PHASE(DEG))*)
151    FORMAT(6X,F9.3,5X,2(E12.5,3X))
152    FORMAT(9X,F6.3,5X,2(E12.5,3X))
16     FORMAT(///17X,*NORMALIZED*,11X,*IMPULSE RESPONSE*/20X,*TIME*,11X,
      1*(REAL)*,8X,*(IMAGINARY)*/)
17     FORMAT(15X,F10.3,5X,E12.5,5X,E12.5)
18     FORMAT(1H1,10(/),20X,*XXXXX  DATA ARE PUNCHED IN CARDS  XXXXX*)
C       CONSTANTS
       PI=3.14159265358979
       C=3.0E10
       RFRMED=1.33
       CMED=C/RFRMED
       NHLF=N/2
       PHIR=PHID*PI/180.
       ANGR=(ANGD-PHID)*PI/180.
       SCATCS=SCATCS*(1.-H)
       TOTLCS=SCATCS+ABSCS
       TRSPCS=(1.0-AMU)*SCATCS+ABSCS
       ANRM=RHO*TRSPCS*CMED
       BWNRM=RHO*TRSPCS*FBW
       RNRM=RHO*TRSPCS*ROBS
       DW=2.*WLMT/FLOAT(N)
C       SETTING THE NORMALIZED FREQ.(OMEGA)
       FRCTN=1.-1./FLOAT(N)
       DO 31  I=1,NHLF
       W(I)=FLOAT(I-1)*DW-FRCTN*WLMT
31     W(N+1-I)=-W(I)
C
C       ---  SPECTRUM  ---
C
       PRINT 10
       PRINT 14
       ARGR1=TOTLCS/TRSPCS
       ARGR2=ABSCS/TRSPCS
       X=COS(PHIR)
       DO 51  I=1,NHLF
       CT=CMPLX(ARGR1,-W(I))
       CA=CMPLX(ARGR2,-W(I))
       CTR=CMPLX( 1., -W(I))
       CQ=CSQRT(3.*CA*CTR)
       CARG=0.5*BWNRM**2*CEXP(-CQ*RNRM)*SCATCS*AMU/(RNRM*TRSPCS*CTR)
       C1=CTR*(CT+1.5*AMU*CT+1.5*CTR)/(AMU*CQ**2)
       C2=1.5*CTR/CQ
       C3=(CT/CQ)**2
       CNOM=X*(X**2+C1)
       CDEN=(X+C2)*(X**2-C3)
       CSI1=(CTR+(CQ+1./RNRM)*COS(ANGR))*CNOM/CDEN
       CSI2=(3.*X**2+C1)/CDEN-CNOM*(3.*X**2+2.*C2*X-C3)/CDEN**2
       CSI2=CSI2*SIN(PHIR)*SIN(ANGR)/RNRM
       CSI(I)=-CARG*(CSI1+CSI2)
       CSI(N+1-I)=CONJG(CSI(I))
       SIMAG(I)=CABS(CSI(I))
       SIR=REAL(CSI(I))
       SII=AIMAG(CSI(I))
       SIPHSE(I)=ATAN2(SII,SIR)*180./PI
       PRINT 151, W(I),SIMAG(I),SIPHSE(I)
51     CONTINUE
       CALL AUTOPLT(W,SIMAG,NHLF)
       PRINT 131
       PRINT 12, ANRM
       IF (IPUNCH .NE. 0)  PUNCH 111, N,RHO,H,AMU,ANGD,ROBS,PHID
       IF (IPUNCH .EQ. 2)  PUNCH 152, (W(K),SIMAG(K),SIPHSE(K),K=1,NHLF)
C
C       ---  IMPULSE RESPONSE  ---
C
       IF (ITAPER .EQ. 0)  GO TO 62
       CALL CTAPER(CSI,N,P)
```

```
      62     CONTINUE
             CALL INVFT(CSI,M,WLMT,T)
             DO 63  I=1,N
      63     SIMAG(I)=REAL(CSI(I))
             PRINT 10
             PRINT 16
             PRINT 17, (T(K),CSI(K),K=1,N)
             PRINT 133
             CALL PLOTA(T,N,SIMAG,N)
             CALL PLOT3(1H*,T,SIMAG,N)
             CALL PLOT4(1,1H )
             PRINT 132
             PRINT 111, N,RHO,H,AMU,ANGD,ROBS,PHID
             PRINT 112, TRSPCS,TOTLCS,SCATCS,ABSCS
             PRINT 12, ANRM
             IF (IPUNCH.EQ.0)  GO TO 64
             PUNCH 16
             PUNCH 17, (T(K),CSI(K),K=1,N)
             PRINT 18
      64     CONTINUE
      99     CONTINUE
             PRINT 10
             STOP
             END
             SUBROUTINE  AUTOPLT(X,Y,N)
      C        PLOTTING AUTOMATICALLY SCALED
             DIMENSION  X(N),Y(N)
                                  .
                                  .
                                  .
                                  .
             rests  are  same  as App.P-3
                                  .
                                  .
                                  .
                                  .
```

App.P-5 Solution of diffusion equation for a point source

```
             PROGRAM  PNTSRCE (OUTPUT,PUNCH)
      C        UNITS ARE IN CENTIMETERS
      C        IPUNCH= NO PUNCH(0), IMPULSE RESP.(1), IMP.RESP. S SPECTRUM(2)
      C        BW= HALF WIDTH OF E-1 POINTS (NOT FULL WIDTH)
      C        ANGD= SCATT. ANGLE IN DEGREE,  FOR BACKSCATT.  ANGD=180.
      C        HPL= HALF PULSE LENGTH OF E-1 POINTS (SEC)
      C        HPW= HALF PULSE WIDTH OF E-1 POINTS (CM)
             COMPLEX  CSI,CT,CA,CTR,CQ
             DIMENSION  CSI(260),W(260),T(260),SIMAG(260),SIPHSE(260)
             DIMENSION  X(31),YR(31),YI(31)
             DATA  IPUNCH,N,M,ITAPER,P  / 1, 256, 8, 1, 50. /
             DATA  AMU,H,RHO,SCATCS,ABSCS/0.930,0.10,1.95E6,3295.0E-8,0.0/
             DATA  WLMT,RDST,IRG,HPL,HPW  / 0.800, 1.00000, 0, 5.E-12, 0.15 /
      10     FORMAT(1H1)
      111    FORMAT(/10X,*N=*,I4,5X,*RHO(/CC)=*,E12.5,5X,*H(PACK.FACT.)=*
             1,F5.3,5X,*MU=*,F8.5,5X,*RAD.DIST.(CM)=*,F8.3)
      112    FORMAT(10X,*TR.C-S(CM**2)=*,E12.5,5X,*TOT.C-S=*,E12.5,5X
             1,*SCAT.C-S=*,E12.5,5X,*ABS.C-S=*,E12.5//)
      12     FORMAT(30X,*NORM.COEFF.(RHO*SIGMATR*CMED)=*,E12.5,*  (/SEC)*)
      131    FORMAT(30X,*NORMALIZED ANG.FREQ. (OMEGA.0/NORM.COEFF)*///)
      132    FORMAT(40X,*NORMALIZED TIME (T*NORM.COEFF)*)
      133    FORMAT(1H1,5X,*(IMPULSE RESP.)/(NORM.COEFF.)*)
      14     FORMAT(///7X,*NORMALIZED*,2X,*SPECTRUM OF SPECIFIC INTENSITY*
             1/8X,*ANG.FREQ.*,4X,*(MAGNITUDE)*,4X,*(PHASE(DEG))*)
      151    FORMAT(6X,F9.3,5X,2(E12.5,3X))
      152    FORMAT(9X,F6.3,5X,2(E12.5,3X))
```

```
16      FORMAT(///17X,*NORMALIZED*,11X,*IMPULSE RESPONSE*/20X,*TIME*,11X,
       1*(REAL)*,8X,*(IMAGINARY)*/)
17      FORMAT(15X,F10.3,5X,E12.5,5X,E12.5)
18      FORMAT(1H1,10(/),20X,*XXXXX  DATA ARE PUNCHED IN CARDS   XXXXX*)
C       CONSTANTS
        PI=3.14159265358979
        C=3.0E10
        RFRMED=1.33
        CMED=C/RFRMED
        NHLF=N/2
        SCACSN=SCATCS*(1.-H)
        TOTLCS=SCACSN+ABSCS
        TRSPCS=(1.0-AMU)*SCACSN+ABSCS
        ANRM=RHO*TRSPCS*CMED
        RNRM=RHO*TRSPCS*RDST
C       SETTING THE NORMALIZED FREQ.(OMEGA)
        DW=2.*WLMT/FLOAT(N)
        FRCTN=1.-1./FLOAT(N)
        DO 31  I=1,NHLF
        W(I)=FLOAT(I-1)*DW-FRCTN*WLMT
31      W(N+1-I)=-W(I)
C
C
C       ---   SPECTRUM   ---
C
        PRINT 10
        PRINT 14
        ARG1=(RHO*TRSPCS)**2
        ARGR1=TOTLCS/TRSPCS
        ARGR2=ABSCS/TRSPCS
        DO 51  I=1,NHLF
        CT=CMPLX(ARGR1,-W(I))
        CA=CMPLX(ARGR2,-W(I))
        CTR=CMPLX( 1., -W(I))
        CQ=CSQRT(3.*CA*CTR)
        CSI(I)=ARG1*CTR*CEXP(-CQ*RNRM)/RNRM
        IF ( IRG .EQ. 0 )  GO TO 41
        ARGRG=0.5*HPL**2+0.25*(HPW/CMED)**2
        WD=RHO*TRSPCS*CMED*W(I)
        RG=EXP(-ARGRG*WD**2)
        CSI(I)=CSI(I)*RG
41      CSI(N+1-I)=CONJG(CSI(I))
        SIMAG(I)=CABS(CSI(I))
        SIR=REAL(CSI(I))
        SII=AIMAG(CSI(I))
        IF ( SIR .EQ. 0.0  .AND.  SII .EQ. 0.0 )  SIR=SII=1.0
        SIPHSE(I)=ATAN2(SII,SIR)*180./PI
        PRINT 151, W(I),SIMAG(I),SIPHSE(I)
51      CONTINUE
        CALL AUTOPLT(W,SIMAG,NHLF)
        PRINT 131
        PRINT 12, ANRM
        IF (IPUNCH .EQ. 2)  PUNCH 152, (W(K),SIMAG(K),SIPHSE(K),K=1,NHLF)
C
C       ---   IMPULSE RESPONSE   ---
C
        IF (ITAPER .EQ. 0)  GO TO 62
        CALL CTAPER(CSI,N,P)
62      CONTINUE
        CALL INVFT(CSI,M,WLMT,T)
        DO 63  I=1,N
63      SIMAG(I)=REAL(CSI(I))
        PRINT 10
        PRINT 16
        PRINT 17, (T(K),CSI(K),K=1,N)
        PRINT 133
        CALL PLOTA(T,N,SIMAG,N)
        CALL PLOT3(1H*,T,SIMAG,N)
        CALL PLOT4(1,1H )
        PRINT 132
        PRINT 111, N,RHO,H,AMU,RDST
```

```
           PRINT 112, TRSPCS,TOTLCS,SCACSN,ABSCS
           PRINT 12, ANRM
           IF (IPUNCH.EQ.0)  GO TO 64
           PUNCH 17, (T(K),CSI(K),K=1,N)
           PRINT 18
     64    CONTINUE
     99    CONTINUE
           PRINT 10
           STOP
           END
           SUBROUTINE  AUTOPLT(X,Y,N)
     C      PLOTTING AUTOMATICALLY SCALED
           DIMENSION  X(N),Y(N)
```

.
.
.
.

rests are same as App.P-3

.
.
.
.

App.P-6 Solution of diffusion equation for plane wave incidence on semi-infinite medium : Effects of range-gating and first order multiple scattering are included.

```
           PROGRAM  PLANINC (OUTPUT,PUNCH)
     C
     C     CALCULATION OF BACKSCATTERED-PULSE-SHAPE FOR PLANE WAVE PULSE
     C      INCIDENT ON SEMI-INFINITE DIFFUSION MEDIUM      NOV. 1978
     C     PL=PULSE LENGTH, FULL (NOT HALF) WIDTH OF E-1 POINTS (SEC)
     C     BW=BEAMWIDTH OF RANGE GATING PULSE, F.W. OF E-1 POINTS (CM)
     C     IPRINT= NUMBER OF DATA TO BE PRINTED OR NO PRINTING
     C     IPUNCH= PUNCH(1) OR NOT(0)
     C     IWIND= WINDOWING(1) OR NOT(0)
     C     UNITS ARE IN CM (CENTIMETERS)
     C
           COMPLEX  CSI,CRG,CT,CTR,CA,CQ,CARG,CARG1,CARG2,CARG3,CARG4
           COMPLEX  CSIA,CRGA
           DIMENSION  CSI(260),CRG(260),W(260),T(260),YA(260),YB(260)
           DIMENSION  CSIA(260),CRGA(260)
           DATA  N,M,IPRINT,IPUNCH,IWIND / 256, 8, 20, 1, 1 /
           DATA  AMU,H,RHO,SCATCS,ABSCS /0.928,1.000,1.95E7,3427.5E-8, 0.0 /
           DATA  WLMT,PL,BW,BACKCS  / 2.5E12, 10.E-12, 0.3, 3945.46E-8 /
     10    FORMAT (1H1)
     11    FORMAT (5X,E12.5,5X,4E14.5)
     12    FORMAT (1H1,10(/),30X,*XXXXX  DATA ARE PUNCHED IN CARDS  XXXXX*)
           PI=3.14159265358979
           C=3.0E10
           RFMED=1.62
           V=C/RFMED
           HPL=PL/2.0
           HBW=BW/2.0
           NHLF=N/2
           NPRINT=NHLF+IPRINT
     C     --- SPECTRUM OF SCATT. INT.
           DO 90  III=1,3
           RHO=RHO/10.
           H=H/10.
           SCACSN=SCATCS*(1.-H)
           TOTLCS=SCACSN+ABSCS
           TRSPCS=(1.0-AMU)*SCACSN+ABSCS
```

```
      RT=RHO*TOTLCS
      RTR=RHO*TRSPCS
      RA=RHO*ABSCS
      DW=2.*WLMT/FLOAT(N)
      FRCTN=1.-1./FLOAT(N)
      DO 31  J=1,N
      W(J)=FLOAT(J-1)*DW-FRCTN*WLMT
      DK=W(J)/V
      CT=CMPLX(RT,-DK)
      CTR=CMPLX(RTR,-DK)
      CA=CMPLX(RA,-DK)
      CQ=CSQRT(3.*CTR*CA)
      CARG1=RHO*BACKCS/(6.*CT)
      CARG2=(RHO*SCACSN)**2
      CARG2=CARG2*(AMU*CQ-CTR)/(CQ**2-CT**2)
      CARG3=(2.+3.*AMU)*CT+3.*CTR+6.*AMU*CA
      CARG3=CARG3/((2.*CQ+3.*CTR)*(CQ+CT))
      CARG4=(AMU*CQ+CTR)/(2.*CT*CTR)
      CSI(J)=CARG2*(CARG3-CARG4)
      CSIA(J)=CARG1
C    --- RANGE-GATING
      ARG=0.5*HPL**2+0.25*(HBW/V)**2
      ARG=-ARG*W(J)**2
      CRG(J)=CSI(J)*EXP(ARG)*PL**2*BW/V
      CRGA(J)=CSIA(J)*EXP(ARG)*PL**2*BW/V
31    CONTINUE
      IF  ( IPRINT .EQ. 0 )  GO TO 32
      PRINT 10
      PRINT 11,  ( W(I),CSI(I),CRG(I),I=NHLF,NPRINT)
32    CONTINUE
      DO 36  J=1,N
      YA(J)=CABS(CSI(J))
36    YB(J)=CABS(CRG(J))
      CALL AUTOPLT(W,YA,N)
      CALL AUTOPLT(W,YB,N)
C    --- BLACKMAN WINDOW TO REDUCE THE LEAKAGE
C          FOR IMPULSE RESPONSE ONLY,  NOT FOR THE RANGE-GATED
      IF ( IWIND .EQ. 0 )  GO TO 38
      NHLF=N/2
      DO 37  J=1,NHLF
      ARG=PI*FLOAT(J)/FLOAT(NHLF)
      WIND=0.42-0.5*COS(ARG)+0.08*COS(ARG*2.)
      CSI(J)=CSI(J)*WIND
      CSIA(J)=CSIA(J)*WIND
      CSI(N+1-J)=CSI(N+1-J)*WIND
37    CSIA(N+1-J)=CSIA(N+1-J)*WIND
38    CONTINUE
C    --- INVERSE FOURIER TRANSFORM
      CALL INVFT(CSI,M,WLMT,T)
      CALL INVFT(CSIA,M,WLMT,T)
      CALL INVFT(CRG,M,WLMT,T)
      CALL INVFT(CRGA,M,WLMT,T)
      DO 33  J=1,N
      YA(J)=REAL(CSI(J))
      IF ( YA(J) .LT. 0.0 )  YA(J)=0.0
      YA(J)=YA(J)+REAL(CSIA(J))
      IF ( YA(J) .LT. 0.0 )  YA(J)=0.0
      YB(J)=REAL(CRG(J))
      IF ( YB(J) .LT. 0.0 )  YB(J)=0.0
      YB(J)=YB(J)+REAL(CRGA(J))
      IF ( YB(J) .LT. 0.0 )  YB(J)=0.0
33    CONTINUE
      CALL AUTOPLT(T,YA,N)
      CALL AUTOPLT(T,YB,N)
      IF  ( IPRINT .EQ. 0 )  GO TO 34
      PRINT 10
      PRINT 11,  ( T(I),CSI(I),CRG(I),I=NHLF,NPRINT)
34    CONTINUE
      IF  ( IPUNCH .EQ. 0 )  GO TO 35
      PUNCH 11,  ( T(I),CSI(I),CRG(I),I=1,N )
```

```
       PRINT 12
35     CONTINUE
90     CONTINUE
       PRINT 10
       STOP
       END
       SUBROUTINE  INVFT(C,M,B,T)
C       THIS ROUTINE CALCULATES INVERSE FOURIER TRANSFORM
C
C
C                            N
C        C(OUT) = 1/2*PI ( SUM  C(IN) *EXP( -I*W(J)*T(K)) )*OW
C                  K         J=1    J
C
C      W(J)=(J-1)*OW-B*(N-1)/N,  T(K)=(K-N/2)*OT
C      OW=2*B/N,  OT=PI/B,  N=2**M,  (-B,B)=BAND WIDTH
C      NOTE : SPECIAL CONSIDERATIONS ON THE SYMMETRY OF FREQ. AND TIME
C
       COMPLEX  C,CA,CB,CARG
       DIMENSION  C(1030),CA(1030),CB(1030),T(1030),IWK(20)
       PI=3.14159265358979
       N=2**M
       FRCTN=1.-1./FLOAT(N)
       NHLF=N/2
       DO 1  I=1,N
       CA(I)=C(I)
1      CB(I)=CONJG(C(I))
       CALL  FFT2(CA,M,IWK)
       CALL  FFRDR2(CA,M,IWK)
       CALL  FFT2(CB,M,IWK)
       CALL  FFRDR2(CB,M,IWK)
       ARG1=B/(PI*FLOAT(N))
       DO 2  I=1,NHLF
       ARG2=-FLOAT(NHLF-I)*FRCTN*PI
       CARG=CMPLX(COS(ARG2),SIN(ARG2))
       C(I)=ARG1*CARG*CA(NHLF+1-I)
2      T(I)=-FLOAT(NHLF-I)*PI/B
       DO 3  I=1,NHLF
       ARG2=FLOAT(I)*FRCTN*PI
       CARG=CMPLX(COS(ARG2),SIN(ARG2))
       C(NHLF+I)=ARG1*CARG*CONJG(CB(I+1))
3      T(NHLF+I)=FLOAT(I)*PI/B
       RETURN
       END
       SUBROUTINE  AUTOPLT(X,Y,N)
C        PLOTTING AUTOMATICALLY SCALED
       DIMENSION  X(N),Y(N)
       PRINT 10
10     FORMAT(1H1)
       CALL  PLOTA(X,N,Y,N)
       CALL  PLOT3(1H*,X,Y,N)
       CALL  PLOT4(1,1H )
       RETURN
       END
```

App.P-7 Mie theory modified for asymmetrical size-distribution of spherical scatterers

```
      PROGRAM MIE(INPUT,OUTPUT,TAPE5=INPUT,TAPE6=OUTPUT,PUNCH)
C
C     MAIN PROGRAM MIE -- CALLS SUBROUTINE DAMIE
C     MODIFIED FOR ASYMMETRIC SIZE DISTRIBUTION BY  K.SHIMIZU   MAY 1977
C
C     THE PROGRAM CALCULATES ANGULAR SCATTERED INTENSITY AND
CC       SCATTERING PARAMETERS (C-S. AND EFF.FACT.)
C     GAUSSIAN QUADRATURE INTEGRATION FOR SIZE DISTRIBUTION
C     RFR,RFI = REAL AND IMAGINARY PARTS OF REFRACTIVE INDEX OF SPHERE
C     RFMED = REFRACTIVE INDEX OF BACKGROUND MEDIUM (REAL)
C     WVLENG = WAVELENGTH IN VACUO (MICRON)
C     JX = NO. OF ANGLES IN 0-90,  AJX = ANGLE STEP SIZE
C     TD1(1) = FIRST ANGLE IN DEGREES ... USUALLY 0.0
C     R = AVERAGE RADIUS OR MODE OF DISTRIBUTION (MICRON)
C     PDR = FULL 3DB-WIDTH OF SIZE DISTRIBUTION IN % OF MODE RADIUS
C     PDR = 2.86*STD.DEV/RADIUS    (NOT DIAMETER)
C     PDRL,PDRR=S.D.WIDTH OF LEFT & RIGHT OF MODE RADIUS (PDR=PDRL+PDRR)
C     IF SIZE DIST.IS NOT NEEDED, SET N=1,LPDR=RPDR=ZI(1)=0.0,WEI(1)=1.0
C     GAUSS DATA ORDER   ZI(I),WEI(I)=(0.0),RIGHT,LEFT,RIGHT,L,R,L, .....
C     IPUNCH = DATA PUNCH(1) OR NOT(0)
C     IRANGE = SCATTERING RANGE, WHOLE(0), FORWARD(1), BACKWARD(2)
C
      COMMON IRANGE
      DIMENSION   SIVV1(100),SIVV2(100),SIVV(200),SIVVN(200)
      DIMENSION   TD1(100),TD2(100),TD(200),ELTRMX(4,100,2)
      DIMENSION   ZI(15),WEI(15),DIST(15)
      DIMENSION   NS(5),IMAGE(1000),X(200),Y(200)
      DATA  (ZI(I),I=1,15)/0.0,0.201194093997435,-0.201194093997435,
     1     0.394151347077563,-0.394151347077563,0.570972172608539,
     2     -0.570972172608539,0.724417731360170,-0.724417731360170,
     3     0.848206583410427,-0.848206583410427,0.937273392400706,
     4     -0.937273392400706,0.987992518020485,-0.987992518020485/
      DATA  (WEI(I),I=1,15)/0.202578241925561,2*0.198431485327111,
     1     2*0.186161000115562,2*0.166269205816994,2*0.139570677926154,
     2     2*0.107159220467172,2*0.070366047488108,2*0.030753241996117/
11    FORMAT(1H1)
12    FORMAT(15X,*MIE SCATTERING - - - SIZE DISTRIBUTED*)
13    FORMAT(//18X,*(INPUT)*/20X,*AVERAGE RADIUS=*,F10.6/20X,*3DB-WIDTH*
     1,* OF DISTRIBUTION IN % OF AVE.RADIUS*/25X,*LEFT =*,F7.2,
     2* %     RIGHT =*,F7.2,* %*
     2 /20X,*NO. OF SAMPLE POINTS FOR S.D. INTEGRATION   N=*,I3)
14    FORMAT(20X, *WAVELENGTH(MICRON)=*,F10.6,5X,*RFMED=*,F10.6,
     1    /20X,*WAVENUMBER=*,E12.5,5X,*AV.SIZE PARAMETER=*,E12.5)
15    FORMAT(20X,*SPHERE INDEX=(*,F10.8,*)-I(*,E11.5,*)*)
16    FORMAT(//18X,*(OUTPUT)*/20X,*AVERAGED TOTAL CROSS-SECTION =*,E12.5,
     1/20X,*AVERAGED ABSORPTION C-S (MICRON**2)=*,E12.5
     1/20X,*AVERAGED MEAN COS(THETA) =*,E12.5)
165   FORMAT(20X,*AREA UNDER S.D. CURVE =*,F8.5)
17    FORMAT(///27X,*ANGLE*,7X,*S.I.VERT.*,6X,*NORM.SIV(DB)*/)
18    FORMAT(25X,F7.2,5X,E12.5,5X,E12.5)
19    FORMAT(25X,*NORMALIZED SCATTERED INTENSITY VERT.  (DB)*/
     1        70X,*NORMALIZATION DENOMINATOR =*,E12.5//)
C
      PI=3.14159265358979
      IPUNCH=0
      IRANGE=0
      TD1(1)=0.0
      JX=31
      AJX=3.0
      R=1.010
      RFR=1.58
      RFI=0.0
```

```
      RFMED=1.33
      WVLENG=0.53
C
      DO 90  N=1,15,14
      PORL=1.0
      PORR=1.0
      IF (N.NE.1)  GO TO 25
      PORL=PORR=0.0
      ZI(1)=0.0
      WEI(1)=1.0
25    CONTINUE
      RRFR=RFR/RFMED
      RRFI=RFI/RFMED
      WAVENO=2.0*PI*RFMED/WVLENG
      SQKINV=(1.0/WAVENO)**2
      C=1.0823922
      DO 31  J=1,JX
      TD1(J)=FLOAT(J-1)*AJX+TD1(1)
      SIVV1(J)=0.0
      SIVV2(J)=0.0
31    CONTINUE
      DISSUM=0.0
      CEXT=0.0
      CSCAT=0.0
      AMU=0.0
      I=1
312   NPI=N+I
      IODD=(FLOAT(NPI)/2.0-FLOAT(NPI/2))*3.0
      IF (IODD) 90,313,314
313   DR=R*2.*PORL/100.0
      GO TO 315
314   DR=R*2.*PORR/100.0
315   RI=R+DR*ZI(I)/C
      SP=WAVENO*RI
      CALL DAMIE(SP,RRFR,RRFI,TD1,JX,QEXT,QSCAT,CTBRQS,ELTRMX)
      DIST(I)=(1.-ZI(I)**2)**2
      DISSUM=DISSUM+DIST(I)*WEI(I)
      CEXT=CEXT+WEI(I)*(QEXT*PI*RI**2)*DIST(I)
      CSCAT=CSCAT+WEI(I)*(QSCAT*PI*RI**2)*DIST(I)
      AMU=AMU+WEI(I)*DIST(I)*CTBRQS/QSCAT
      IF(IRANGE.EQ.2)  GO TO 33
      DO 32  J=1,JX
32    SIVV1(J)=SIVV1(J)+WEI(I)*SQKINV*ELTRMX(2,J,1)*DIST(I)
      IF(IRANGE.EQ.1)  GO TO 35
33    CONTINUE
      DO 34  J=1,JX
      TD2(J)=180.0-TD1(J)
34    SIVV2(J)=SIVV2(J)+WEI(I)*SQKINV*ELTRMX(2,J,2)*DIST(I)
35    CONTINUE
      IF (I.EQ.N)  GO TO 38
      I=I+1
      GO TO 312
38    CONTINUE
C     DATA ARRANGEMENT
      IF(IRANGE.EQ.2)  GO TO 52
      JN=JX
      DO 51  J=1,JN
      TD(J)=TD1(J)
      SIVV(J)=SIVV1(J)/DISSUM
      ARG=SIVV(J)/SIVV(1)
51    SIVVN(J)=10.*ALOG10(ARG)
      XMAX=0.0
      XMIN=-56.0
      YMAX=0.0
      YMIN=-90.0
      IF (IRANGE.NE.2)  GO TO 54
52    JN=JX
      DO 53  J=1,JN
      TD(J)=TD2(J)
      SIVV(J)=SIVV2(J)/DISSUM
```

```
        ARG=SIVV(J)/SIVV(1)
 53     SIVVN(J)=10.*ALOG10(ARG)
        XMAX=10.0
        XMIN=-7.5
        YMAX=-150.0
        YMIN=-180.0
 54     IF (IRANGE.NE.0)  GO TO 56
        JN=2*JX-1
        JXM1=JX-1
        DO 55  J=1,JXM1
        JA=JX+J
        JB=JX-J
        TD(JA)=TD2(JB)
        SIVV(JA)=SIVV2(JB)/DISSUM
        ARG=SIVV(JA)/SIVV(1)
 55     SIVVN(JA)=10.*ALOG10(ARG)
        XMAX=0.0
        XMIN=-56.0
        YMAX=0.0
        YMIN=-180.0
 56     CONTINUE
        SPAV=WAVENO*R
        CEXT=CEXT/DISSUM
        CSCAT=CSCAT/DISSUM
        CABS=CEXT-CSCAT
        AMU=AMU/DISSUM
       .PRINT 11
        PRINT 12
        PRINT 13, R,PDRL,PDRR,N
        PRINT 14, WVLENG,RFMED,WAVENO,SPAV
        PRINT 15, RFR,RFI
        PRINT 16, CEXT,CABS,AMU
        PRINT 165, DISSUM
C     --PRINTING DATA.  TO AVOID,ADD  GO TO 71
        PRINT 17
        PRINT 18,  (TD(J),SIVV(J),SIVVN(J),J=1,JN)
 71     CONTINUE
C     --PLOTTING.  TO AVOID, ADD  GO TO 73
        DO 72  J=1,JN
        Y(J)=-TD(J)
 72     X(J)=SIVVN(J)
C       PLOTTING WITH VARIABLE AXES
        PRINT 11
        CALL PLOTA(X,JN,Y,JN)
        CALL PLOT3(1H*,X,Y,JN)
        CALL PLOT4(36,36H            SCATTERING ANGLE***DEGREE)
C       PLOTTING WITH FIXED AXES
        NS(1)=1
        NS(2)=NS(3)=NS(4)=0
        NS(5)=2
        PRINT 11
        CALL PLOT1(NS,3,15,7,13)
        CALL PLOT2(IMAGE,XMAX,XMIN,YMAX,YMIN)
        CALL PLOT3(1H*,X,Y,JN)
        CALL PLOT4(31,31H        SCATTERING ANGLE***DEGREE)
        PRINT 19, SIVV(1)
        PRINT 13, R,PDRL,PDRR,N
        PRINT 15, RFR,RFI
 73     CONTINUE
        IF (IPUNCH) 76,76,74
 74     PUNCH 13, R,PDRL,PDRR,N
        PUNCH 15, RFR,RFI
        PUNCH 18,  (TD(J),SIVV(J),SIVVN(J),J=1,JN)
        PRINT 75
 75     FORMAT(1H1,10(/),20X,*XXXXX   DATA ARE PUNCHED IN CARDS  XXXXX*)
 76     CONTINUE
 90     CONTINUE
        STOP
        END
```

```
      SUBROUTINE DAMIE (X,RFR,RFI,THETD,JX,QEXT,QSCAT,CTBRQS,ELTRMX)   AMIE   1
C     MODIFIED FOR CDC 6400 - D A CHRISTENSEN                          AMIE   2
C     REFRACTIVE INDEX RF= CMPLX(RFR,-RFI)                             AMIE   3
C     MODIFIED FOR FORWARD/BACKWARD SELECTION    APR. 1977
    5 FORMAT( 9X,* THE VALUE OF THE SCATTERING ANGLE IS GREATER THAN    AMIE   4
     1 90.0 DEGREES. IT IS *,F15.4)                                    AMIE   5
    6 FORMAT (// 9X,* PLEASE READ COMMENTS.*//)                        AMIE   6
    7 FORMAT(// 9X,*THE VALUE OF THE ARGUMENT JX IS GREATER THAN 100*) AMIE   7
    8 FORMAT(// 9X,* THE VALUE OF RFI . X IS GREATER THAN 80.0. IT IS*, AMIE   8
     1 F15.4)                                                          AMIE   9
      COMMON IRANGE
      REAL    X,RX,RFR,RFI,QEXT,QSCAT,T(5),TA(4),TB(2),TC(2)           AMIE  10
      REAL    TD(2),TE(2),CTBRQS                                       AMIE  11
      REAL    ELTRMX(4,100,2),PI(3,100),TAU(3,100),CSTHT(100),SI2THT(100)AMIE 12
     1,THETD(100)                                                      AMIE  13
      COMPLEX    RF,RRF,RRFX,WM1,FNA,FNB,TC1,TC2,WFN(2),ACAP(2)         AMIE  14
      COMPLEX    FNAP,FNBP                                             AMIE  15
      EQUIVALENCE (WFN(1),TA(1)),(FNA,TB(1)),(FNB,TC(1))               AMIE  16
      EQUIVALENCE(FNAP,TD(1)),(FNBP,TE(1))                             AMIE  17
      IF ( JX .LE. 100 ) GO TO 20                                      AMIE  18
      WRITE(6,7)                                                       AMIE  19
      WRITE(6,6)                                                       AMIE  20
      CALL EXIT                                                        AMIE  21
   20 RF = CMPLX(RFR,-RFI)                                             AMIE  22
      RRF = 1.0  /RF                                                   AMIE  23
      RX = 1.0  /X                                                     AMIE  24
      RRFX = RRF * RX                                                  AMIE  25
      DO 30 J = 1,JX                                                   AMIE  26
      IF ( THETD(J) .LT. 0.0   ) THETD(J) = ABS(THETD(J))             AMIE  27
      IF ( THETD(J) .GT. 0.0   ) GO TO 23                              AMIE  28
      CSTHT(J) = 1.0                                                   AMIE  29
      SI2THT(J) = 0.0                                                  AMIE  30
      GO TO 30                                                         AMIE  31
   23 IF ( THETD(J) .GE. 90.0   ) GO TO 25                             AMIE  32
      T(1) = ( 3.14159265358979    * THETD(J))/180.0                   AMIE  33
      CSTHT(J) = COS(T(1))                                             AMIE  34
      SI2THT(J) = 1.0   - CSTHT(J)**2                                  AMIE  35
      GO TO 30                                                         AMIE  36
   25 IF ( THETD(J) .GT. 90.0   ) GO TO 28                             AMIE  37
      CSTHT(J) = 0.0                                                   AMIE  38
      SI2THT(J) = 1.0                                                  AMIE  39
      GO TO 30                                                         AMIE  40
   28 WRITE(6,5) THETD(J)                                              AMIE  41
      WRITE(6,6)                                                       AMIE  42
      CALL EXIT                                                        AMIE  43
   30 CONTINUE                                                         AMIE  44
      DO 35 J = 1,JX                                                   AMIE  45
      PI(1,J) = 0.0                                                    AMIE  46
      PI(2,J) = 1.0                                                    AMIE  47
      TAU(1,J) = 0.0                                                   AMIE  48
      TAU(2,J) = CSTHT(J)                                              AMIE  49
   35 CONTINUE                                                         AMIE  50
      T(1) = COS(X)                                                    AMIE  51
      T(2) = SIN(X)                                                    AMIE  52
      WM1 = CMPLX( T(1),-T(2))                                         AMIE  53
      WFN(1) = CMPLX(T(2),T(1))                                        AMIE  54
      WFN(2) = RX * WFN(1) - WM1                                       AMIE  55
      T(1) = RFI * X                                                   AMIE  56
      IF ( T(1) .GT. 80.0   ) GO TO 40                                 AMIE  57
      T(3) = 0.5   * EXP(T(1))                                         AMIE  58
      T(4) = 0.25 /T(3)                                                AMIE  59
      T(1) = T(3) + T(4)                                               AMIE  60
      T(2) = T(3) - T(4)                                               AMIE  61
      T(3) = T(2)**2                                                   AMIE  62
      T(2) = T(1) * T(2)                                               AMIE  63
      T(1) = T(3)                                                      AMIE  64
      T(3) = RFR * X                                                   AMIE  65
      T(4) = SIN(T(3))                                                 AMIE  66
      T(3) = COS(T(3))                                                 AMIE  67
      T(1) = T(1) + T(4)**2
```

```
      T(3) = T(3) * T(4)                                          AMIE  68
      T(3) = T(3) * T(4)                                          AMIE  69
      ACAP(1) =  CMPLX(T(3),T(2))/T(1)                            AMIE  70
      GO TO 50                                                    AMIE  71
   40 ACAP(1) =  CMPLX( 0.0  ,1.0   )                             AMIE  72
      WRITE(6,8) T(1)                                             AMIE  73
      WRITE(6,6)                                                  AMIE  74
   50 ACAP(2) = - RRFX + (1.0  /(RRFX - ACAP(1)))                 AMIE  75
      TC1 = ACAP(2) * RRF + RX                                    AMIE  76
      TC2 = ACAP(2) * RF + RX                                     AMIE  77
      FNA = (TC1*TA(3) - TA(1))/(TC1*WFN(2) - WFN(1))             AMIE  78
      FNB = ( TC2*TA(3) - TA(1))/(TC2 * WFN(2) - WFN(1))          AMIE  79
      FNAP = FNA                                                  AMIE  80
      FNBP = FNB                                                  AMIE  81
      T(1) = 1.50                                                 AMIE  82
      TB(1) = T(1) * TB(1)                                        AMIE  83
      TB(2) = T(1) * TB(2)                                        AMIE  84
      TC(1) = T(1) * TC(1)                                        AMIE  85
      TC(2) = T(1) * TC(2)                                        AMIE  86
      IF (IRANGE.EQ.2) GO TO 602
      DO 601  J=1,JX
      ELTRMX(1,J,1) = TB(1) * PI(2,J) + TC(1) * TAU(2,J)          AMIE  88
      ELTRMX(2,J,1) = TB(2) * PI(2,J) + TC(2) * TAU(2,J)          AMIE  89
      ELTRMX(3,J,1) = TC(1) * PI(2,J) + TB(1) * TAU(2,J)          AMIE  90
      ELTRMX(4,J,1) = TC(2) * PI(2,J) + TB(2) * TAU(2,J)          AMIE  91
  601    CONTINUE
      IF (IRANGE.EQ.1)  GO TO 603
  602 DO 60  J=1,JX
      ELTRMX(1,J,2) = TB(1) * PI(2,J) - TC(1) * TAU(2,J)          AMIE  92
      ELTRMX(2,J,2) = TB(2) * PI(2,J) - TC(2) * TAU(2,J)          AMIE  93
      ELTRMX(3,J,2) = TC(1) * PI(2,J) - TB(1) * TAU(2,J)          AMIE  94
      ELTRMX(4,J,2) = TC(2) * PI(2,J) - TB(2) * TAU(2,J)          AMIE  95
   60 CONTINUE                                                    AMIE  96
  603    CONTINUE
      QEXT = 2.0   * ( TB(1) + TC(1))                             AMIE  97
      QSCAT =(TB(1)**2 + TB(2)**2 + TC(1)**2 + TC(2)**2)/0.75     AMIE  98
      CTBRQS = 0.0                                                AMIE  99
      N = 2                                                       AMIE 100
   65 T(1) = 2*N - 1                                              AMIE 101
      T(2) = N - 1                                                AMIE 102
      T(3) = 2 * N + 1                                            AMIE 103
      DO 70 J = 1,JX                                              AMIE 104
      PI(3,J) = (T(1)*PI(2,J)*CSTHT(J)-N*PI(1,J))/T(2)            AMIE 105
      TAU(3,J) = CSTHT(J)*(PI(3,J)-PI(1,J))-T(1)*SI2THT(J)*PI(2,J)+  AMIE 106
     1 TAU(1,J)                                                   AMIE 107
   70 CONTINUE                                                    AMIE 108
      WM1 = WFN(1)                                                AMIE 109
      WFN(1) = WFN(2)                                             AMIE 110
      WFN(2) = T(1)*RX*WFN(1) - WM1                               AMIE 111
      ACAP(1) = ACAP(2)                                           AMIE 112
      ACAP(2) = -N * RRFX + (1.0  /(N*RRFX-ACAP(1)))              AMIE 113
      TC1 = ACAP(2)*RRF + N*RX                                    AMIE 114
      TC2 = ACAP(2)*RF  + N*RX                                    AMIE 115
      FNA = (TC1*TA(3)-TA(1))/(TC1*WFN(2) - WFN(1))               AMIE 116
      FNB = (TC2*TA(3)-TA(1))/(TC2*WFN(2) - WFN(1))               AMIE 117
      T(5) = N                                                    AMIE 118

      T(4) = T(1)/(T(5)*T(2))                                     AMIE 119
      T(2) = (T(2)*(T(5) + 1.0  ))/T(5)                           AMIE 120
      CTBRQS = CTBRQS + T(2)*(TD(1)*TB(1) + TD(2)*TB(2) + TE(1)*TC(1) +  AMIE 121
     1 TE(2)*TC(2)) + T(4)*(TD(1)*TE(1) + TD(2)*TE(2))            AMIE 122
      QEXT = QEXT + T(3)*(TB(1)+TC(1))                            AMIE 123
      T(4) = TB(1)**2 + TB(2)**2 + TC(1)**2 + TC(2)**2            AMIE 124
      QSCAT = QSCAT + T(3) *T(4)                                  AMIE 125
      T(2) = N*(N+1)                                              AMIE 126
      T(1) = T(3)/T(2)                                            AMIE 127
      K = (N/2)*2                                                 AMIE 128
      IF (IRANGE.EQ.2)  GO TO 802
```

```
      DO 801  J=1,JX
      ELTRMX(1,J,1)=ELTRMX(1,J,1)+T(1)*(TB(1)*PI(3,J)+TC(1)*TAU(3,J))    AMIE 130
      ELTRMX(2,J,1)=ELTRMX(2,J,1)+T(1)*(TB(2)*PI(3,J)+TC(2)*TAU(3,J))    AMIE 131
      ELTRMX(3,J,1)=ELTRMX(3,J,1)+T(1)*(TC(1)*PI(3,J)+TB(1)*TAU(3,J))    AMIE 132
      ELTRMX(4,J,1)=ELTRMX(4,J,1)+T(1)*(TC(2)*PI(3,J)+TB(2)*TAU(3,J))    AMIE 133
801   CONTINUE
      IF (IRANGE.EQ.1)  GO TO 803
802   DO 80  J=1,JX
      IF ( K .EQ. N ) GO TO 75                                          AMIE 134
      ELTRMX(1,J,2)=ELTRMX(1,J,2)+T(1)*(TB(1)*PI(3,J)-TC(1)*TAU(3,J))    AMIE 135
      ELTRMX(2,J,2)=ELTRMX(2,J,2)+T(1)*(TB(2)*PI(3,J)-TC(2)*TAU(3,J))    AMIE 136
      ELTRMX(3,J,2)=ELTRMX(3,J,2)+T(1)*(TC(1)*PI(3,J)-TB(1)*TAU(3,J))    AMIE 137
      ELTRMX(4,J,2)=ELTRMX(4,J,2)+T(1)*(TC(2)*PI(3,J)-TB(2)*TAU(3,J))    AMIE 138
      GO TO 80                                                          AMIE 139
   75 ELTRMX(1,J,2)=ELTRMX(1,J,2)+T(1)*(-TB(1)*PI(3,J)+TC(1)*TAU(3,J))   AMIE 140
      ELTRMX(2,J,2)=ELTRMX(2,J,2)+T(1)*(-TB(2)*PI(3,J)+TC(2)*TAU(3,J))   AMIE 141
      ELTRMX(3,J,2)=ELTRMX(3,J,2)+T(1)*(-TC(1)*PI(3,J)+TB(1)*TAU(3,J))   AMIE 142
      ELTRMX(4,J,2)=ELTRMX(4,J,2)+T(1)*(-TC(2)*PI(3,J)+TB(2)*TAU(3,J))   AMIE 143
   80 CONTINUE                                                          AMIE 144
803   CONTINUE
      IF( T(4) .LT. 1.0E-14 ) GO TO 100                                 AMIE 145
      N = N + 1                                                         AMIE 146
      DO 90 J = 1,JX                                                    AMIE 147
      PI(1,J) = PI(2,J)                                                 AMIE 148
      PI(2,J) = PI(3,J)                                                 AMIE 149
      TAU(1,J) = TAU(2,J)                                               AMIE 150
      TAU(2,J) = TAU(3,J)                                               AMIE 151
   90 CONTINUE                                                          AMIE 152
      FNAP = FNA                                                        AMIE 153
      FNBP = FNB                                                        AMIE 154
      GO TO 65                                                          AMIE 155
100   CONTINUE
      IF (IRANGE.EQ.2)  GO TO 121
      K=1
101   DO 120  J=1,JX
      DO 115 I = 1,4                                                    AMIE 158
      T(I) = ELTRMX(I,J,K)                                              AMIE 159
  115 CONTINUE                                                          AMIE 160
      ELTRMX(2,J,K) = T(1)**2 + T(2)**2                                 AMIE 161
      ELTRMX(1,J,K) = T(3)**2 + T(4)**2                                 AMIE 162
      ELTRMX(3,J,K) = T(1)*T(3) + T(2)*T(4)                             AMIE 163
      ELTRMX(4,J,K) = T(2)*T(3) - T(4)*T(1)                             AMIE 164
  120 CONTINUE                                                          AMIE 165
      IF (IRANGE.EQ.1 .OR. K.EQ.2)  GO TO 122
121   K=2
      GO TO 101
122   CONTINUE
      T(1) = 2.0   * RX**2                                              AMIE 166
      QEXT = QEXT * T(1)                                                AMIE 167
      QSCAT = QSCAT * T(1)                                              AMIE 168
      CTBRQS = 2.0   * CTBRQS * T(1)                                    AMIE 169
      RETURN                                                            AMIE 170
      END                                                               AMIE 171
```

V I T A

Name: Koichi Shimizu

Born: May 10, 1950, Otaru, Hokkaido, Japan

Father: Masatoshi Shimizu

Mother: Aiko Shimizu

Secondary
School: Choryo Senior High School, Otaru, Hokkaido, Japan

		Degree
College:	Hokkaido University	B.Eng., 1973
	University of Washington, Seattle	M.S.E.E., 1976